HIGH-RESOLUTION SIMULATIONS OF COMPRESSIBLE TURBULENT FLOWS

A DISSERTATION
SUBMITTED TO THE DEPARTMENT OF MECHANICAL ENGINEERING
AND THE COMMITTEE ON GRADUATE STUDIES
OF STANFORD UNIVERSITY
IN PARTIAL FULFILLMENT OF THE REQUIREMENTS
FOR THE DEGREE OF
DOCTOR OF PHILOSOPHY

Hang Song
August 2024

This dissertation is online at: https://purl.stanford.edu/db520mm2402

I certify that I have read this dissertation and that, in my opinion, it is fully adequate in scope and quality as a dissertation for the degree of Doctor of Philosophy.

Sanjiva Lele, Primary Adviser

I certify that I have read this dissertation and that, in my opinion, it is fully adequate in scope and quality as a dissertation for the degree of Doctor of Philosophy.

Alex Aiken

I certify that I have read this dissertation and that, in my opinion, it is fully adequate in scope and quality as a dissertation for the degree of Doctor of Philosophy.

Gianluca Iaccarino

I certify that I have read this dissertation and that, in my opinion, it is fully adequate in scope and quality as a dissertation for the degree of Doctor of Philosophy.

Parviz Moin

Approved for the Stanford University Committee on Graduate Studies.

Stacey F. Bent, Vice Provost for Graduate Education

This signature page was generated electronically upon submission of this dissertation in electronic format.

Abstract

Computational fluid dynamics plays a critical role in a wide variety of disciplines. In recent years, high-performance computing (HPC) has undergone rapid developments and has enabled many large-scale simulations conducted with high grid resolution or high-fidelity physical models. Meanwhile, new challenges have also been introduced to the research community. From the perspective of computational research in fluid mechanics, several questions need to be addressed: How can we further improve the simulation quality? How can we efficiently utilize modern HPC resources? What can we learn from higher-resolution simulations? In this dissertation, the answers to these three questions will be provided based on the author's research experience in compressible turbulent flows.

First, a robust, high-resolution computational framework is established. The simulation framework is based on compact finite difference methods. The aliasing error in the nonlinear inviscid flux is effectively reduced, and the spectral resolution of the viscous flux is significantly enhanced especially in the high-wavenumber range. As a result, artificial solution filtering, which was previously necessary for numerical stabilization, can now be avoided. The simulation framework is compatible with various equation-of-state models, transport models, and shock-capturing methods. It also supports simulations on both Cartesian and curvilinear meshes. Detailed analysis of the numerical performance of the simulation framework is presented.

Additionally, a direct parallel linear solver algorithm for the linear systems arising from compact numerical schemes is presented. The design of the parallel solution process considers both shared-memory and distributed-memory hierarchies and is suitable for multi-GPU (graphics processing unit) computation. The algorithm supports a cyclic banded system with variable grid partitioning and has a much lower cost along with a smaller communication footprint compared to existing methods. This algorithm has demonstrated scalability of up to 24576 GPUs in a fluid mechanics simulation.

Furthermore, two aspects of the physics of compressible turbulent flows are discussed. The compressibility effects are investigated using direct numerical simulations of solenoidally forced compressible isotropic turbulence. The Reynolds number based on the longitudinal Taylor-micro-scale is approximately 170 for all simulations, and the turbulent Mach number ranges from 0.2 to 0.7. Data over approximately 10 eddy-turnover times at a statistically stationary state is collected for

each case for analysis. Various statistical quantities are measured, and the decomposed motions are studied based on analytically derived budget equations. Finally, the transonic shock buffet on a laminar supercritical airfoil is investigated using a wall-resolved large-eddy simulation. The airfoil is configured at an angle-of-attack of 4 degrees in a freestream with a Mach number of 0.735. The chord-length-based Reynolds number is 1 million. Data over approximately 267 convective time units are collected for analysis. The dominant frequencies in the fluctuations of lift and drag coefficients are identified. The space-time correlations at the peak frequencies are studied using spectral proper orthogonal decomposition.

Acknowledgments

My pursuit of a PhD has been similar to climbing a steep mountain. I am grateful that my journey has not been lonely. Throughout this challenging ascent, I have been fortunate to receive the companionship, encouragement, and support of many incredible people. Their presence has been a source of confidence and strength, inspiring me and motivating me to overcome each obstacle along the way.

Above all, I am deeply thankful to my parents, Jie Bai and Xiutian Song, for their unwavering love and warm support. They have been present for every significant moment in my life, sharing in my achievements and challenges. Their encouragement has been indispensable in reaching this milestone, and their love has made this accomplishment even more special.

I am also profoundly grateful to my PhD advisor, Prof. Sanjiva K. Lele, for his invaluable mentorship and kind support. It is a great honor to be part of his research group and to have conducted my PhD research here. His expertise and dedication have been crucial in guiding me toward my achievements. In addition, his encouragement has inspired me to develop broader academic interests and motivated me to explore further research across various fields. Beyond the workplace, I also deeply appreciate all his suggestions and support regarding my long-term career plans.

I would like to acknowledge my oral examination and thesis reading committee members Prof. Alison L. Marsden, Prof. Parviz Moin, Prof. Alex Aiken, and Prof. Gianluca Iaccarino. Beyond their roles as committee members, I greatly appreciate and have enjoyed our conversations on topics related to my research as well as those aligned with my broader interests. I would also like to thank Prof. Eric Darve at Stanford University. From him, I have learned the basics of parallel programming and numerical linear algebra. I am also grateful to him for the helpful discussions and comments on the design of the parallel linear solver presented in this thesis. Furthermore, I would like to sincerely acknowledge Student Services in the Department of Mechanical Engineering at Stanford University – Alyssa J. Cicat, Soo Ji Kim, and Michelle L. Rice, as well as Prof. Allison M. Okamura and Prof. Ellen Kuhl as the Director of Graduate Studies and Chair of the Department of Mechanical Engineering at Stanford University respectively for their tremendous help during the thesis submission process as well as my entire graduate studies.

I would like to express my heartfelt thanks to my professors and course instructors during my

master's studies at the University of Southern California (USC), Prof. Paul D. Ronney, Prof. Larry G. Redekopp, Prof. Veronica Eliasson, Prof. Iván Bermejo-Moreno, Prof. Mitul Luhar, Prof. Satwindar S. Sadhal, Prof. Julian A. Domaradzki, Dr. Henry Abakians, and Dr. David C. Wilcox, as well as my professors at the South China University of Technology (SCUT) where I did my undergraduate study, Prof. Jianghong Wu and Prof. Yingzi Kang. They have cultivated my passion for scientific research and inspired me to remain curious and continue exploring knowledge. It is a real pleasure that many of them have also observed my progress throughout my PhD journey.

Furthermore, I am grateful to scientists in the broader research community who have provided me with invaluable support, insightful discussions, and helpful suggestions about my research work and career. It is a great privilege to highlight them. I would like to sincerely thank Dr. Britton J. Olson (Lawrence Livermore National Laboratory) for collaborating on significantly extending the work on the parallel linear solver; Dr. Jacqueline H. Chen (Sandia National Laboratory) for the helpful discussions on the numerical methods and physics of turbulence; Prof. Hussein Aluie (the University of Rochester), Prof. Diego Donzis (TAMU), Prof. Sharath Girimaji (TAMU), and Prof. Tim Colonius (Caltech) for the valuable discussions on the topics of compressible turbulence; Prof. Lin Fu (HKUST) for the instructions on using and designing high-order nonlinear shock-capturing schemes; Prof. Lluís Jofre Cruanyes (Barcelona Tech – UPC) for the detailed implementations of real-gas equation-of-state and transport models; Prof. Soshi Kawai for the discussions on many topics including numerical methods, dense-gas flows, and aerodynamics; Prof. Philipp Schlatter (FAU & KTH) for the collaborations on the effects of mixed-precision operations in computational-fluid-dynamic solvers and the valuable suggestions on the topics of wall-bounded turbulence during the Center for Turbulence Research (CTR) Summer Program.

Closely related to my thesis work, I would like to acknowledge all my collaborators. Most of them are from the extended academic family of the Flow Physics and Aeroacoustics Laboratory (FPAL), i.e., the Lele Research Group. First, I am very much appreciative to Dr. Aditya S. Ghate, Dr. Akshay Subramaniam, and Dr. Man-Long Wong, my three academic big brothers, for the close discussions and collaborations on different topics presented in this thesis. I am also immensely grateful for their mentorship during my early PhD studies. I am deeply thankful to Dr. Kristen V. Matsuno and Dr. Jacob R. West for their direct and dedicated involvement in the development of the computational code, *PadeLibs*, which was used to conduct all the simulations presented in this thesis. This is truly an amazing team that naturally formed based on our common interests, and the outcome we have accomplished together is among the achievements during my PhD that I am most proud of. Additionally, I would like to acknowledge Lucy J. Brown for providing much useful feedback on *PadeLibs* from a user's perspective during its early-stage development. I would also like to thank Anjini Chandra and Steven Dai for the collaborative work on the dense-gas boundary layer and shear layer flows respectively including testing the computational code and verifying results. Furthermore, I would like to express my heartfelt thanks to Anjini Chandra and Andy Wu for their tremendous

help in proofreading, verifying, and reviewing my thesis and other related manuscripts. Moreover, I am exceedingly grateful to other current and former lab-mates I have closely interacted with during my PhD journey – Dr. Gao Jun (Gary) Wu, Ryan Hass, Alboreno Voci, Olivia Martin, Zoe Barbeau, Kevin Cherng, Dr. Michael F. Howland, Dr. Michael C. Adler, and Dr. Aaron Wienkers.

I am deeply grateful to my special and beloved Miss Yi Liu. Her patience, understanding, and encouragement have been a constant source of strength and inspiration. I deeply appreciate the countless ways she has supported me. Additionally, I thank my cousins, Dr. Hongyan Sun and Peng Liu, for their persistent encouragement. Throughout my PhD journey, I have also received significant moral support from my friends. I would like to greatly acknowledge the immense and enduring support from Dr. Harshavardhan Mylapilli, Dr. Dejuan Kong, and Dr. Zhengyu Huang, as well as the kind company and tremendous help from Anjiang Wei, Qi Jiang, Chloe Choi, Dr. Jack Guo, Omkar Shende, Ahmed Elnahhas, Tim Flint, Jonathan Pham, Carlos Gonzalez, Kimberly Liu, Rahul Agrawal, Christopher Williams, Dr. Kevin P. Griffin, Dr. Zhenghong Zhou, Qiheng Zheng, Junlin Mu, Dr. Bin Xia, Kenneth Lu, Yilin Shen, Joshua Dong, Caidan Cao, Yushi (Jasmine) Shao, Tian Xie, Youdi Pan, Zichao Wang, Yuetong Zhang, Wenling Gao, Dr. Zengrong Hao, Dr. Haosen Xu, Jiatian Huang, Yu Liang, Sen Lin, Quandong Huang, Xingda Zhang, Dr. Xiangyu Gao, Dr. Si Shen, Andrew Lawson, Dr. Ashkan Davani, Dr. Shrey Trivedi, Dr. Eugene Kong, Dr. Jakrapop Wongwiwat, Blake DuBois, Julian D. Heinrich, Richard Cheng, Julie Ng, Teng Yeung, and others. I extend my deepest thanks to all my friends for their unconditional support throughout my PhD journey.

Last but not least, I would like to acknowledge all the research support. The research presented in this thesis is partially supported by the National Science Foundation (NSF-OAC-2103509) and the National Aeronautics and Space Administration (NASA-80NSSC22M0108). The computational code development and simulations use the computing resources managed by the XSEDE / ACCESS program, the Texas Advanced Computing Center (TACC), and the Oak Ridge Leadership Computing Facility (OLCF) at the Oak Ridge National Laboratory (ORNL) via the ASCR Leadership Computing Challenge (ALCC), Innovative and Novel Computational Impact on Theory and Experiment (INCITE), and SummitPLUS allocations. The geometry of the OALT25 laminar supercritical airfoil used in the work that is presented in this thesis is provided by ONERA.

Contents

List of Tables

List of Figures

Chapter 1

Introduction

1.1 Background

Turbulence involves energy transfer over a wide range of time and length scales and is governed by highly nonlinear dynamics [126]. Numerical simulations play a critical role in fundamental studies of turbulence physics as well as in engineering applications involving turbulent flows. However, conducting high-quality numerical simulations of turbulent flows is challenging.

In the past decades, Reynolds-averaged Navier-Stokes (RANS) has been widely used as a low-cost solution to address engineering problems [174]. In practice, RANS simulations can be applied to estimate turbulent flows at large Reynolds numbers with a relatively small number of grid points. If the flow configuration contains a homogeneous direction, this direction can be reduced in a RANS simulation. However, the solution from a RANS simulation only represents the mean flow, and all effects of turbulence are modeled. Accordingly, the accuracy of a RANS solution largely depends on the quality of the turbulence closure model. If the computational mesh can sufficiently resolve all the mean flow and modeled turbulence quantities, the RANS solution becomes grid independent [174]. Therefore, the requirements of numerical methods for RANS simulations focus on robustness and efficiency.

For a higher-quality solution, eddy-resolving simulations are considered. If turbulent motions at all scales are well-resolved, a turbulence closure model is not needed, and the simulation is known as a direct numerical simulation (DNS). In studies of the fundamental physics of turbulence, DNS have and will continue to be extensively adopted as the most reliable simulation approach. However, DNS has a stringent requirement on grid resolution. Its capability is strictly limited by the accessibility of compute power. For many engineering problems, DNS is not an affordable solution approach. As a compromise, a more efficient and practical simulation approach is to resolve the range of length scales that carry the most energetic turbulent motions while modeling the effects of smaller scale motions. Simulation approaches associated with this concept, such as large-eddy simulations (LES), have

gained increasing interest in engineering applications. In these simulations, the turbulence closure models are adaptive with respect to the computational grid size. The simulation results do not show grid-independence until the mesh resolution reaches the DNS regime. Nevertheless, quantities of interests, such as lift and drag coefficients, can achieve convergence within acceptable tolerance for engineering applications. The solution of an eddy-resolving simulation contains both large-scale coherent flow structures and turbulent flow structures over a wide range of length scales, with the smallest resolved scale being supported by the computational mesh resolution. Consequently, the solution of an eddy-resolving simulation is more sensitive to the quality of numerical methods compared to a RANS simulation.

In compressible turbulent flows, the fluid's thermodynamic behavior and conservation of energy are fully coupled in the system of governing equations. The flow contains acoustic waves and entropy waves. Associated with these, dilatational motion, density fluctuations, and extra pressure fluctuations are generated. Under supersonic conditions, the flow can also develop shocks. All these flow features interact with turbulent flow structures. In studies of compressible turbulence, these interactions are commonly referred to as compressibility effects which are characterized by the turbulent Mach number. From a physical viewpoint, compressibility effects enable bidirectional energy transfer between turbulent kinetic energy and internal energy. Statistically, compressibility effects cause intermittency in compressible turbulence and impact the energy cascade. From a simulation point of view, some of the waves, especially at a high Mach number, are locally highly anisotropic. The thicknesses of the strong compression waves and shock waves are under-resolved at a subgrid scale, but along the wave tangential direction, the wave structure may create coherent structures. To well resolve or capture these waves in a unified simulation framework is challenging. On one hand, sufficient numerical dissipation is needed for shock-capturing. On the other hand, the propagation of acoustic waves can be excessively damped by numerical dissipation. As a result, robustness for simulations of compressible turbulent flows is necessary but is no longer the only criterion to be achieved using dissipative methods. From this perspective, high-order numerical frameworks with highly localized use of numerical dissipation for shock-capturing are considered as promising solutions.

Compact finite difference methods, besides high-order convergence, have been demonstrated to have significantly higher spectral resolution in the linear regime compared to corresponding explicit schemes [89]. However, traditional applications in simulations of compressible turbulent flows using compact finite difference methods have encountered serious numerical instability issues. This is primarily due to the accumulation of aliasing errors in the calculations of nonlinear inviscid fluxes as well as a lack of spectral resolution in the high-wavenumber regime in the assembly of viscous fluxes in the compressible Navier-Stokes equations. As a brute-force solution, a low-pass numerical filter is applied regularly as the simulation progresses to remove the spectral energy near the Nyquist wavenumber. Previous practice has demonstrated that the solution filtering can effectively maintain

simulation robustness, and it can be shown that filtering the solution can still preserve the formal order of grid convergence. However, it is concerning that solution filtering does not stabilize the simulation by essentially reducing the aliasing error in the assembly of nonlinear inviscid fluxes or enhancing the spectral resolution in the assembly of viscous fluxes. The stabilization is achieved by introducing an extra numerical damping mechanism at the small scales. For LES, the filtering effects are dominant over the effects of the turbulence closure model near the Nyquist wavenumber.

For a large-scale simulation, the computational grid is decomposed and data are stored in different distributed memory partitions during the simulation runtime. For modern high-performance computing, the use of graphics processing units (GPUs) has significantly accelerated the overall computation speed and enabled the affordability of larger scale simulations. However, a prerequisite of efficiently utilizing GPU power is that the solution process can be largely parallelized. For simulations on structured meshes using explicit numerical schemes, the dominant communication cost for each partition is to exchange data with neighboring partitions for the numerical stencils. In contrast, using compact finite difference methods requires solving a banded linear system across the distributed memory partitions along the dimension to be solved. If the computational domain is periodic, the linear system contains non-zero cyclic entries. For large-scale simulations using compact numerical schemes, the dominant computational cost is in solving the linear system. Many traditional linear solution algorithms have been designed for shared memory parallelism. For distributed computing, data transpose or re-partitioning based on all-to-all communication is required. However, a simulation with this treatment will not achieve scalability when a large number of GPUs are used. This issue has been the limiting factor for the efficient application of compact numerical schemes to large-scale simulations on modern high-performance computing architectures.

1.2 Research highlights

This dissertation is motivated by three major challenges related to numerical studies of compressible turbulent flows:

- Demands of advancing fundamental understanding of compressible turbulent flows
- Requirements of increasing simulation resolution while improving robustness in simulations using high-order numerical schemes
- Difficulties in efficiently utilizing of modern high-performance computing resources

The simulation framework based on high-order compact finite difference methods is presented in Ch. 2. The simulation framework advances the conservative variables at collocated grid points and assembles fluxes at the edge-staggered grid points based on the interpolations of primitive variables and staggered derivative operations. As a result, the aliasing error in the nonlinear inviscid fluxes of the compressible Navier-Stokes system is effectively reduced. Meanwhile, the assembly of

viscous fluxes has significantly improved spectral resolution in the high-wavenumber regime and a non-zero spectral response at the Nyquist wavenumber. All this improvement leads to a significant benefit – solution filtering is no longer needed for the purpose of stabilizing simulations using compact finite difference methods. Besides Cartesian meshes, the framework also supports simulations on curvilinear meshes for local mesh refinement or simulations of flows involving complex geometries. Furthermore, simulations of flows containing both shocks and turbulence are discussed. The application of localized artificial diffusivity (LAD) models [75, 76] and approximate Riemann solvers [157] with nonlinear upwind-biased interpolation schemes [141] are demonstrated. The computational capability of the framework is also extended to simulations of real-gas flows. Compressible turbulent flows of CO_2 under transcritical conditions are discussed in Ch. 3. The pressure-volume-temperature relation is calculated with the Peng-Robinson equation-of-state model [119], and the viscosity and thermal conductivity are calculated based on a temperature and pressure dependent transport model [25]. The demonstrative simulations for the framework involve flow with shocks in high-speed turbulent mixing and heat transfer within wall-bounded turbulence.

A direct parallel linear solver algorithm to solve the cyclic banded linear systems arising from compact numerical schemes is presented in Ch. 4. The algorithm is based on the cyclic reduction and parallel cyclic reduction algorithms which serve as prototype elimination patterns. The design of the algorithm considers hierarchical parallelism with both shared-memory and distributed-memory access. This algorithm has demonstrated a significantly lower communication footprint during the solution process compared to other linear solver approaches. The algorithm also supports flexible grid partitioning and naturally solves the system with non-zero cyclic entries and arbitrary system size. The parallel performance is demonstrated in a representative fluid mechanics simulation. The parallel linear solver algorithm has achieved scalability of up to 24576 GPUs on the *Summit* supercomputer.

Finally, numerical investigations of two fluid mechanics problems are conducted. The compressibility effects are studied using DNS of solenoidally-forced compressible isotropic turbulence. The details are presented in Ch. 5. The mesh size of all DNS is $1024 \times 1024 \times 1024$. The Reynolds number based on the longitudinal Taylor microscale is approximately 170 for all cases, and the turbulent Mach number ranges from 0.2 to 0.7. The probability density functions of the quantities of interest and their variations as functions of the turbulent Mach number are investigated. The decomposed flow motions corresponding to the analytically derived budget equations are also studied. The shock buffet on a laminar supercritical airfoil (OALT25) in transonic flow is investigated using a wall-resolved LES. This work is presented in Ch. 6. The freestream Mach number is 0.735, and the chord-length-based Reynolds number is 1 million. The airfoil is configured with an angle-of-attack of 4 degrees. The simulation resolves the laminar boundary layer separation and flow naturally transitioning to turbulence near the leading edge. The oscillation of the main shock is well-captured using hybrid central-Riemann fluxes and a nonlinear shock-capturing scheme. In

addition, the simulation resolves the turbulent vortex shedding and propagation of acoustic waves. The simulation data over a range of approximately 267 convective time units are collected for analysis. Signal processing indicates that the fluctuations of the lift and drag coefficients contain two dominant frequencies. Further analysis identifies that the dominant frequencies are due to the main shock buffet and turbulent vortex shedding respectively. A modal analysis using spectral proper orthogonal decomposition (SPOD) is conducted to investigate the space-time correlations during shock buffet. The SPOD captures the low-rank behavior at the two dominant frequencies, and the first SPOD mode shapes are shown. It is also observed from the evolution of the SPOD mode shapes that several feedback paths exist in the shock buffet system.

1.3 Major accomplishments

- Developed a robust computational framework with low aliasing error and high spectral resolution for simulations of compressible turbulent flows using compact finite difference methods on both Cartesian and curvilinear meshes.
- Presented a strategy for using hybrid central-Riemann fluxes for simulations of compressible turbulent flows containing shocks with the use of the approximate Riemann fluxes localized to shock structures.
- Generalized the computational framework to simulations of real-gas flows.
- Designed a direct parallel linear solver algorithm to solve the cyclic banded linear systems arising from compact numerical schemes for modern high-performance computing architectures with heterogeneous memory access; and demonstrated the scalability of the proposed parallel linear solver algorithm on state-of-the-art high-performance computing systems.
- Investigated and quantified compressibility effects in solenoidally-forced isotropic turbulence; derived a system of velocity-variance budget equations to study the decomposed motions in compressible isotropic turbulence; and established power-law scaling with the turbulent Mach number for various turbulence statistical quantities.
- Conducted a wall-resolved LES for studies of transonic laminar shock buffet; measured and identified the dominant frequencies in a transonic laminar shock buffet system; and observed possible feedback mechanisms in the transonic laminar shock buffet system.

Chapter 2

Robust High-Resolution Simulation Framework Without Filtering

A robust high-order compact finite difference framework is proposed for simulations of compressible turbulent flows with high spectral resolution using a fully collocated variable storage paradigm. Both inviscid and viscous fluxes are assembled at the edge-staggered grid locations. Nonlinear robustness is attained as a consequence of the intrinsic reduction of aliasing errors in the inviscid fluxes due to the spectral behavior of the compact interpolation schemes. Additional robustness is provided by enhancing the spectral resolution of the viscous flux and its divergence at small scales using purely staggered numerical differentiation. Demonstrative simulations have shown numerical stability of the compact finite difference discretization without any type of solution filtering on both Cartesian and curvilinear meshes. For simulations on a curvilinear mesh, a general metric evaluation approach that satisfies the geometric conservation law is proposed. Additional approaches to combining the proposed scheme with approximate Riemann solvers and artificial diffusivities for shock-capturing are also discussed. Along with theoretical analysis, rigorous evaluation and validation of the methodology on canonical tests, including classic two-dimensional simulations, direct numerical simulations, and large-eddy simulations, are used to confirm robustness and accuracy.

The study illustrated in this chapter is partially published in Ref. [146], and the full content has been submitted for journal publication.

2.1 Introduction

High-order numerical schemes are an economical strategy used in conducting high-resolution numerical simulations of turbulent flows. They are widely applied for their rapid grid convergence accompanied by an affordable increase in computational cost. In turbulent flows, the structure of turbulent eddies spans a wide range of length scales. Additionally, in compressible flows, the thermodynamic behavior of a fluid is strongly coupled with the flow. As a result, acoustic waves [10], shocks [151] and eddy shocklets [88], and fluctuations of transport properties [47, 102] commonly exist as flow features. Such wave structures need to be resolved or captured while maintaining the spatio-temporal accuracy of turbulent vortical structures at various scales and enforcing numerical conservation. Meanwhile, due to the energy cascade in turbulent flows, the turbulent kinetic energy is transferred from large scales to smaller and smaller scales successively until it is dissipated by molecular viscosity at the Kolmogorov length scale, η. The Kolmogorov length scale is the smallest length scale of turbulent eddies [80]. For direct numerical simulations (DNS), the Kolmogorov length scale is fully resolved by the computational mesh. However, considering computational cost, the Kolmogorov length scale is often set close to the limit of the mesh resolution, $k_{\max}\eta \sim \mathcal{O}(1)$ [177, 72], where $k_{\max}$ is the maximum wavenumber supported by the computational mesh. For inhomogeneous turbulent flows, local mesh refinement or mesh stretching may be required to adapt to the local Kolmogorov length scale and, for wall-bounded turbulence in particular, the viscous length scale imposed by the wall [178, 122, 22]. In large-eddy simulations (LES), the mesh resolution is usually configured within the inertial subrange where the local turbulent motion shows statistically universal behavior and can be modeled. The solution of an LES is interpreted as a set of filtered quantities that resolves the large turbulent eddies carrying most of the turbulent kinetic energy. The residual effects beyond the mesh-supported resolution are represented by a subgrid-scale (SGS) model. Due to the nature of turbulence, the SGS model imposes mesh-adaptive dissipation, and many popular SGS models are formulated as eddy viscosity models [144, 104, 167, 109] based on the Boussinesq approximation [13]. Both viscous dissipation and SGS model dissipation are predominately associated with the most finely resolved flow structures.

Capturing or resolving features at small scales requires numerical schemes to have satisfactory spectral behavior in addition to high-order grid convergence. Spectral methods and pseudo-spectral methods are widely used in computational fluid dynamics [68]. For an infinitely differentiable profile, the spectral representation converges faster than any power of the grid size [116]. The numerical errors are mainly ascribed to the Gibbs phenomenon for an insufficiently smooth profile and potential aliased interactions in nonlinear operations. Alternatively, compact finite difference methods [89] provide a more flexible approach to addressing complexities in boundary conditions and can be applied in combination with a variety of numerical schemes such as shock-capturing schemes. Compact numerical schemes are implicitly formulated to access more information across the entire domain. As a result, the leading-order truncation error is much smaller than that of explicit schemes [89].

Compact finite difference methods have demonstrated remarkable successes in DNS and LES of incompressible and compressible turbulent flows [72, 85, 54, 129], computational aeroacoustics [10, 28], and simulations of multiphysics flows and nonlinear wave propagation [53, 139].

Preserving numerical stability while maintaining high-order accuracy and spectral resolution has become a major challenge in simulating compressible turbulent flows. One of the primary contributors to numerical instability is the aliasing error. The dynamics of compressible turbulence are highly nonlinear over a broad-band spectrum. Given a finite grid resolution, the nonlinear interactions associated with high-wavenumber modes will cause aliasing errors that are more significant for higher-order numerical schemes [83]. Therefore, dealiasing treatments are required in flux assembly. A reformulation of the nonlinear advection terms, known as the skew-symmetric form, has been proposed and demonstrated to effectively reduce aliasing errors [9, 8]. Significant efforts have been made to further establish numerical conservation with higher-order and non-dissipative schemes [39, 121, 16]. For simulations of high-speed flows, the skew-symmetric form has been successfully and widely used [120]. The aliasing error of a product term can be analytically quantified from Fourier analysis, and the exact solution to calculating a product in Fourier space involves conducting a dealiased convolution. Nevertheless, this is impractical for large-scale simulations due to the high computational cost. The product should be directly computed in physical space with the aliasing error reduced or removed. A phase-shift method has been attempted in simulations of turbulence using the Fourier spectral method [118], where a shift in physical space of the multiplier fields is conducted to partially or completely cancel the aliasing error in quadratic term calculations. The zero-padding approach is equivalent to the dealiased convolution where the product is computed with sufficiently upsampled resolution, and the result is then downsampled back to the original resolution. As a consequence, all aliasing errors are projected to the extended high-wavenumber modes and eventually truncated after downsampling. However, the increase in the memory footprint of this approach makes it relatively inefficient in large-scale computations. An approach analogous to zero-padding involves filtering the high wavenumber components that cause aliasing interactions before calculating the product [115]. For spectral methods, this treatment is equivalent to applying zero-padding on a coarser resolution without final downsampling. The aliasing error produced by multiplication can be completely removed, although some unaliased nonlinear interactions are also inevitably excluded by filtering. This approach does not require changing the grid resolution and thus can be conducted at a relatively low cost. As an extra advantage, it preserves the conservation form of the nonlinear fluxes.

Another critical contributor to numerical instability is the numerical discretization of diffusive fluxes. This issue particularly exists in simulations of turbulent flows with collocated finite difference methods. Collocated central difference schemes for first derivatives have a trivial response to the mode at the Nyquist wavenumber and have poor spectral behavior close to the Nyquist wavenumber. As a result, the dispersion error from the divergence of advection fluxes occurs as

spurious high-wavenumber, including grid-to-grid, oscillations. These oscillations are supposed to be dissipated by the diffusion mechanism. However, due to the insufficient spectral resolution in the high-wavenumber regime of collocated central difference schemes, when computed by applying the first derivative scheme twice, these oscillations will pile up. Some improvements have been made by evenly appending more grid points to the stencil to optimize the dispersion relation in the high-wavenumber regime [94, 35]. It can be proved, however, that the trivial Nyquist wavenumber response is unavoidable in collocated central difference schemes [89]. One treatment of the diffusion term is to reformulate the flux divergence using the differentiation product rule to recover the Laplacian term and inner product of the gradients of the diffusivity coefficient and flow variable such as velocity and temperature; this has a much improved spectral response in high-wavenumber regimes including at the Nyquist wavenumber. Nevertheless, the conservation form is broken. Numerical filters have also been utilized in LES and under-resolved simulations [129, 76]. As an extra note, this type of filtering is directly applied to the solution variables for the sake of robustness and should be distinguished from the dealiasing filtering for the calculation of nonlinear terms [115], the explicit filtering in grid-independent LES [12], or test filters in numerical models [104, 29]. Based on the transfer function behavior, a practical filtering operation can completely remove grid-to-grid oscillations and largely weaken near-Nyquist high-wavenumber features while preserving the low-wavenumber and moderate-wavenumber features. Serious evaluation of the impact of solution filtering is required to establish the accuracy of the method [129, 76, 74].

Staggered grids, on the other hand, have considerably enhanced behavior in high-wavenumber feature capturing. The staggered first derivative scheme used in the divergence operator has a non-trivial response to the Nyquist wavenumber mode due to phase shifting. The staggered grid approach was originally proposed for solving the pressure-velocity decoupling issue in incompressible flow simulations [61] and has been widely used as a standard approach [117]. An improvement in robustness has also been demonstrated in simulations of compressible turbulent flows using compact finite difference methods [107]. However, the storage of variables on a staggered grid can be complicated. Variables are stored at nodal points and edges along each direction to be consistent with flux assembly. Further variable transformations are needed in compressible flow simulations. Additionally, the fluxes have to be assembled at different locations for different governing equations in the system.

While finite difference methods are formulated on a structured mesh, problems involving complex geometries or local mesh refinement can be actualized via an invertible mapping [127]. A uniform Cartesian grid, known as the computational domain or reference domain, is generated and mapped to a curvilinear mesh, known as the physical domain or actual domain. The mapping is defined by a metric tensor and its inverse. The primitive variables are constructed using a basis in the physical domain, and the differential operations are conducted in the reference domain. Due to the metric tensor, extra nonlinear interactions are created. The analysis has shown that the calculation

of the metric tensor must be consistent with the divergence operator to cancel the numerical error that causes numerical instability; this is also known as the geometric conservation law (GCL) [156]. Further works have shown the GCL-consistent computations in conjunction with collocated compact finite difference methods and shock capturing schemes [165, 111].

This work proposes an improved finite difference framework for simulations of compressible turbulent flows. The divergence operations are based on staggered schemes while all conservative variables are stored at collocated grid points. This framework is particularly favorable to high-order compact numerical schemes and reduces the aliasing error in nonlinear flux assembly and high-wavenumber viscous dissipation. The formulations on both uniform Cartesian mesh and curvilinear mesh are constructed. The metric generation approach is constructed in accordance with the numerical schemes and is proved to be GCL-consistent. The elementary numerical schemes are described in Sec. 2.2. The overall computational framework for the compressible Navier-Stokes system is described in Sec. 2.3. Lastly, some benchmark tests and demonstrative examples are provided in Sec. 2.4.

2.2 Numerical schemes

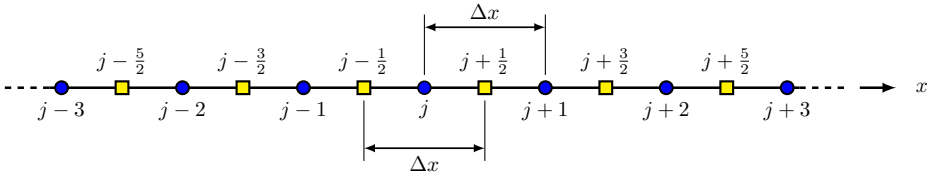

Figure 2.1: Schematic of one-dimensional discretization with a uniform mesh.

In this section, the elementary numerical schemes used in the proposed computational framework and their properties are described. A uniform mesh is generated with grid spacing Δx as shown in Fig. 2.1. A smooth profile, $f(x)$, is discretized on the given computational mesh with $f_j = f(x_j)$ at the nodal grid points. Based on the derivations in Ref. [89] and Ref. [107], a family of tridiagonal collocated compact finite difference schemes for evaluation of the first derivative can be written as

$$\alpha f'_{j-1} + f'_j + \alpha f'_{j+1} = a\frac{f_{j+1} - f_{j-1}}{2\Delta x} + b\frac{f_{j+2} - f_{j-2}}{4\Delta x} \tag{2.1}$$

where f'_j represents the numerically evaluated first derivative of $f(x)$ at x_j. This set of schemes is formally fourth-order accurate for a generic value of α with the following constraints on the coefficients a and b.

$$a = \frac{2}{3}(\alpha + 2) \tag{2.2}$$

$$b = \frac{1}{3}(4\alpha - 1) \tag{2.3}$$

Additionally, as shown in Fig. 2.1, a set of edge grid points are located at a half grid-spacing offset and staggered from the nodal grid points. The smooth profile $f(x)$ evaluated at the edge-staggered grid points can be denoted as $f_{j\pm1/2} = f(x_j \pm \Delta x/2)$. A family of tridiagonal staggered compact finite difference schemes for the first derivative evaluation can be expressed as

$$\alpha f'_{j-1} + f'_j + \alpha f'_{j+1} = a\frac{f_{j+1/2} - f_{j-1/2}}{\Delta x} + b\frac{f_{j+3/2} - f_{j-3/2}}{3\Delta x} \tag{2.4}$$

where fourth-order accuracy is preserved for a generic value of α with the following constraints on a and b.

$$a = \frac{3}{8}(-2\alpha + 3) \tag{2.5}$$

$$b = \frac{1}{8}(22\alpha - 1) \tag{2.6}$$

A family of tridiagonal compact staggered interpolation schemes can be written as

$$\alpha f^I_{j-1} + f^I_j + \alpha f^I_{j+1} = a\frac{f_{j+1/2} + f_{j-1/2}}{2} + b\frac{f_{j+3/2} + f_{j-3/2}}{2} \tag{2.7}$$

where f^I_j denotes the numerically interpolated values of $f(x)$ at x_j. The family of compact interpolations is formally fourth-order accurate if the following constraints are satisfied.

$$a = \frac{1}{8}(10\alpha + 9) \tag{2.8}$$

$$b = \frac{1}{8}(6\alpha - 1) \tag{2.9}$$

Due to the symmetry of the expression, Eq. (2.4) and Eq. (2.7) can be used to calculate corresponding results both from collocated (nodal) to edge-staggered points and from edge-staggered to collocated points with a shift of $\pm1/2$ in the grid index. A scheme degenerates to an explicit method upon choosing $\alpha = 0$. For $\alpha \neq 0$, a tridiagonal linear system needs to be solved. For a large scale computation, an effective parallel direct solution method is described in Ref. [147]. The leading-order truncation error can vanish if a specific value of α is set in each scheme, and sixth-order schemes will be formulated with the most compact stencil. The coefficients of the sixth-order compact schemes are listed in Tab. 2.1.

Scheme	Equation	α	a	b
collocated finite difference	(2.1)	1/3	14/9	1/9
staggered finite difference	(2.4)	9/62	63/62	17/62
central interpolation	(2.7)	3/10	3/2	1/10

Table 2.1: Coefficients of the 6th-order compact schemes.

The spectral response can be investigated from Fourier analysis. Assume that a one-dimensional periodic domain defined on $x \in [0, L)$ is discretized on a uniform mesh with N grid points. The grid spacing is $\Delta x = L/N$, so that $x_j = j\Delta x$ for $j \in \{j \in \mathbb{N} \mid j < N\}$. The discrete Fourier representation of f_j is given by

$$f_j = \sum_{n=-N/2}^{N/2-1} \widehat{f}_n e^{2\pi i n j/N} \tag{2.10}$$

where $\widehat{f}_n \in \mathbb{C}$ is the discrete Fourier transform of $f(x)$, and $i = \sqrt{-1}$ is the imaginary unit. A wavenumber, k_n, is introduced as $k_n = 2\pi n/L$. For $L = N\Delta x$ and $n \in [-N/2, N/2)$, it can be shown that $k_n \Delta x \in [-\pi, \pi)$. Additionally, the modes with respect to $k_{\pm N/2}\Delta x = \pm\pi$ are equivalent, and such $k_{\pm N/2}$ is known as the Nyquist wavenumber. The exponent on the right-hand side of Eq. (2.10) yields $2\pi i n j/N = i k_n x_j$.

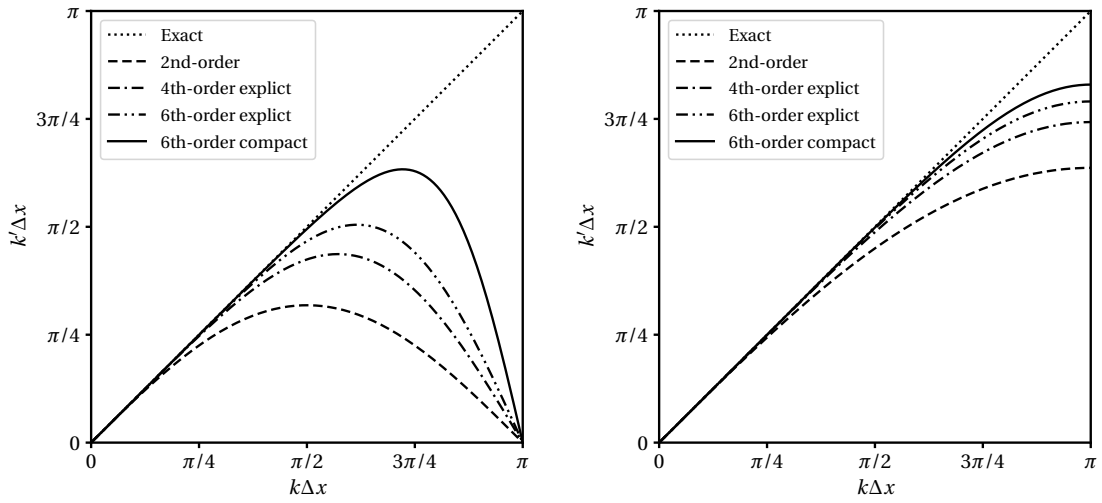

Figure 2.2: Modified wavenumber profiles of some central difference schemes: (a) collocated schemes; (b) staggered schemes.

The Fourier representation of the first derivative can be analytically written as

$$\left.\frac{df}{dx}\right|_{x_j} = \sum_{n=-N/2}^{N/2-1} i k_n \widehat{f}_n e^{i k_n x_j} \tag{2.11}$$

and an identical expression can be formulated for the numerical calculation of the first derivatives.

$$f'_j = \sum_{n=-N/2}^{N/2-1} i k'_n \widehat{f}_n e^{i k_n x_j} \tag{2.12}$$

where k'_n is known as the modified wavenumber [89, 98], and the spectral error is indicated by the discrepancy between k'_n and k_n. For simplicity, the subscript n is dropped while discussing single-mode behavior, so that $k \in \{k_n \mid n \in \mathbb{Z} \wedge n/N \in [-1/2, 1/2)\}$ and $k' \in \{k'_n \mid n \in \mathbb{Z} \wedge n/N \in [-1/2, 1/2)\}$. Substituting the expression in Eq. (2.10) into the finite difference schemes in Eq. (2.1) and Eq. (2.4), the modified wavenumbers can be obtained as

$$k'\Delta x = \frac{a\sin(k\Delta x) + \frac{1}{2}b\sin(2k\Delta x)}{1 + 2\alpha\cos(k\Delta x)} \tag{2.13}$$

and

$$k'\Delta x = \frac{2a\sin\left(\frac{1}{2}k\Delta x\right) + \frac{2}{3}b\sin\left(\frac{3}{2}k\Delta x\right)}{1 + 2\alpha\cos(k\Delta x)} \tag{2.14}$$

respectively. For central difference schemes, the modified wavenumbers are all real-valued, $k' \in \mathbb{R}$. As shown in Eq. (2.13), at the Nyquist wavenumber, $k'\Delta x = 0$ holds for all collocated central difference schemes, while for staggered central difference schemes, $k'\Delta x = \frac{7-10\alpha}{3-6\alpha}$ at the Nyquist wavenumber. The modified wavenumbers of the collocated and staggered sixth-order compact finite difference schemes are plotted in Fig. 2.2. For reference, the modified wavenumber profiles for the second-order central difference schemes and sixth-order explicit central difference schemes are also plotted. By comparison, the staggered schemes have significantly improved spectral behavior compared to the collocated schemes especially in the high-wavenumber regime. For both types of schemes shown in Fig. 2.2, the sixth-order compact difference schemes have the most accurate modified wavenumbers. The modified wavenumber of the collocated sixth-order compact scheme is relatively accurate for $k\Delta x < \pi/2$, and $k'/k = \frac{28}{9\pi} \approx 0.990$ for $k\Delta x = \pi/2$. Beyond $k\Delta x \approx 2.267$, k' starts to decrease with k, and large discrepancies occur. The modified wavenumber of the staggered sixth-order compact scheme has a broader accurate wavenumber regime. k' monotonically increases with k over the entire spectral domain. $k'/k = \frac{206\sqrt{2}}{93\pi} \approx 0.997$ for $k\Delta x = \pi/2$, and $k'/k \approx 0.83$ at the Nyquist wavenumber.

Using the discrete Fourier representation in Eq. (2.10), the exact value at a staggered grid point is

$$f_{j+1/2} = \sum_{n=-N/2}^{N/2-1} \widehat{f}_n e^{2\pi i n(j+1/2)/N} \tag{2.15}$$

Analogously, substituting the Fourier representation in an interpolation scheme, an expression equivalent to the following form can be obtained.

$$f^I_{j+1/2} = \sum_{n=-N/2}^{N/2-1} T(k_n\Delta x)\widehat{f}_n e^{2\pi i n(j+1/2)/N} \tag{2.16}$$

where $T(k\Delta x)$ is known as the transfer function [89]. The subscript n is dropped for simplicity in the discussion of the transfer function consistently with what is defined in the previous discussion so that

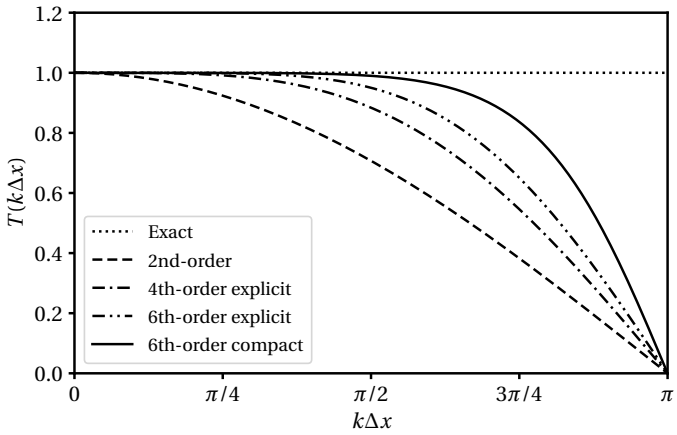

Figure 2.3: Transfer functions of several central interpolation schemes.

k is an instantiation of the set of discrete wavenumbers, $k \in \{k_n \mid n \in \mathbb{Z} \wedge n/N \in [-1/2, 1/2)\}$. This indicates that a numerical interpolation is equivalent to the exact interpolation of a filtered profile. For a central interpolation scheme, the transfer function is also real valued, $T(k\Delta x) \in \mathbb{R}$. The analytical expression of the transfer function for the interpolation scheme formulated in Eq. (2.7) is given as follows.

$$T(k\Delta x) = \frac{a\cos\left(\frac{1}{2}k\Delta x\right) + b\cos\left(\frac{3}{2}k\Delta x\right)}{1 + 2\alpha\cos(k\Delta x)} \tag{2.17}$$

and its profile is shown in Fig. 2.3 in comparison with the second-order and fourth-order explicit central interpolation schemes. Comparing the three profiles for the transfer function, all interpolation schemes preserve the mean value, and the sixth-order compact interpolation shows the best spectral behavior in preserving the mode amplitude for $k\Delta x < \pi/2$. At $k\Delta x = \pi/2$, the values of the transfer functions for the second-order scheme, explicit fourth-order scheme, explicit sixth-order scheme and compact sixth-order scheme are approximately 0.707, 0.884, 0.950 and 0.990, respectively. In the high wavenumber regime, the transfer function profile decreases and eventually reaches zero at the Nyquist wavenumber. These filtering effects embedded in the numerical interpolation schemes favor flux dealiasing, which is fully discussed in Sec. 2.3.

The linear response of the numerical dispersion and dissipation is discussed using a model advection-diffusion equation, shown as follows:

$$\frac{\partial \phi}{\partial t} + \nabla \cdot [\boldsymbol{v}(\theta)\phi] = \nabla \cdot [\nu \nabla \phi] \tag{2.18}$$

The model problem is defined on a two dimensional periodic domain for $\boldsymbol{x} = (x, y) \in [0, L_x) \times [0, L_y)$. $\phi(x, y, t)$ is the dependent variable. $\boldsymbol{v}(\theta) = V\left(\hat{\boldsymbol{e}}_x \cos\theta + \hat{\boldsymbol{e}}_y \sin\theta\right)$ is the advective velocity, where V and θ are constant, and $\hat{\boldsymbol{e}}_x$ and $\hat{\boldsymbol{e}}_y$ form a constant orthogonal basis of a Cartesian coordinate

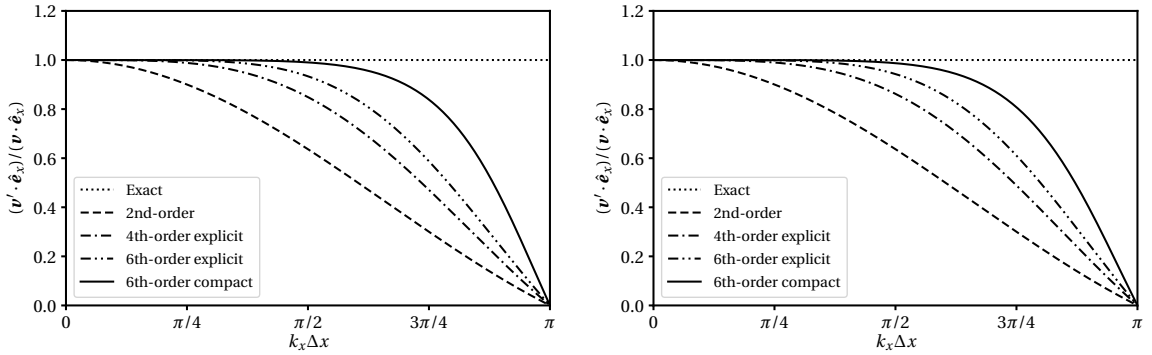

Figure 2.4: Profiles of the modified spectral advection velocities in one-dimensional computations: (a) collocated difference schemes; (b) staggered difference schemes combined with central interpolation schemes. As $k_x \Delta x \to 0$, the plots show asymptotic behavior.

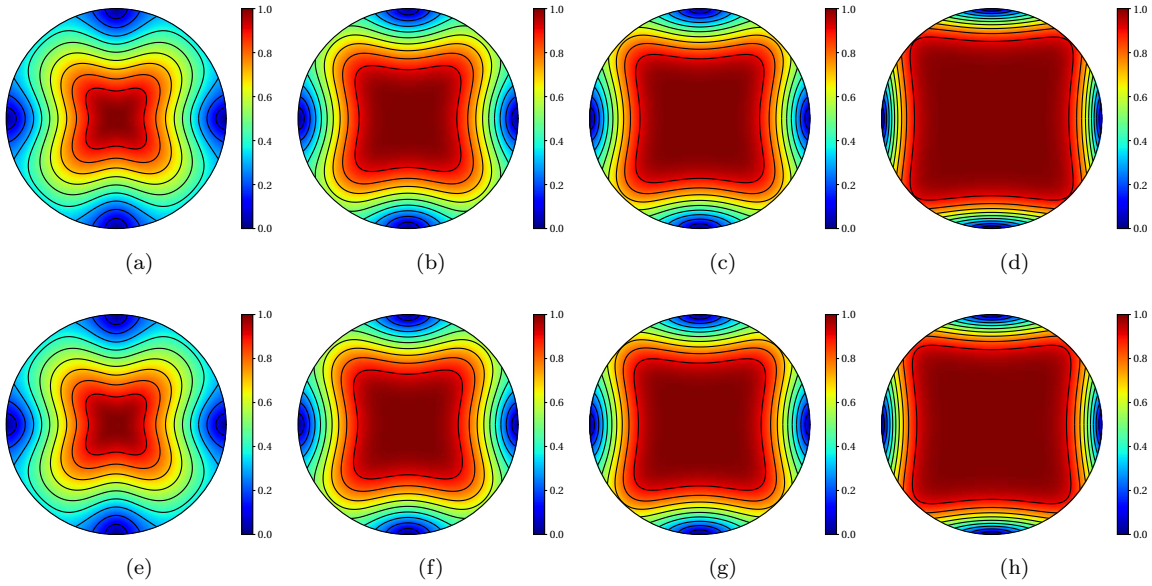

Figure 2.5: Relative spectral advective speed, $(\boldsymbol{v}' \cdot \hat{\boldsymbol{e}}_l) \,/\, (\boldsymbol{v} \cdot \hat{\boldsymbol{e}}_l)$, shown in $|k|\delta$–φ polar coordinate system, where $\hat{\boldsymbol{e}}_l = \hat{\boldsymbol{e}}_x \cos\theta + \hat{\boldsymbol{e}}_y \sin\theta$ and $\varphi = \theta$: (a) collocated second-order difference; (b) collocated fourth-order explicit difference; (c) collocated sixth-order explicit difference; (d) collocated sixth-order compact difference; (e) staggered second-order difference with interpolation; (f) staggered fourth-order explicit difference with interpolation; (g) staggered sixth-order explicit difference with interpolation; (h) staggered sixth-order compact difference with interpolation. The isocurves are generated based on a linear scale. As $k \to 0$, the contours show asymptotic behavior.

system. ν is a constant diffusivity. Eq. (2.18) is expressed in conservation form, where $\boldsymbol{v}\phi$ is the linear advective flux, and $\nu\nabla\phi$ is the linear diffusive flux. The computational domain is discretized with a uniform mesh containing N_x and N_y grid points in x and y dimensions respectively. A two-dimensional discrete Fourier transform can be denoted as

$$\phi(\boldsymbol{x}_{pq}, t) = \sum_{m=-N_x/2}^{N_x/2-1} \sum_{n=-N_y/2}^{N_y/2-1} \widehat{\phi}_{mn}(t) e^{i\boldsymbol{k}_{mn}\cdot\boldsymbol{x}_{pq}} \tag{2.19}$$

where $\boldsymbol{x}_{pq} = x_p\hat{\boldsymbol{e}}_x + y_q\hat{\boldsymbol{e}}_y$ represents two-dimensional coordinates, and $\boldsymbol{k}_{mn} = k_{xm}\hat{\boldsymbol{e}}_x + k_{yn}\hat{\boldsymbol{e}}_y$ is the wavenumber vector. The spatial coordinates can be calculated as $x_p = L_x p/N_x$ and $y_q = L_y q/N_y$ respectively, and the two components of the wavenumber vector are defined as $k_{xm} = 2\pi m/L_x$ and $k_{yn} = 2\pi n/L_y$ respectively. In the following discussion of single-mode behavior, the subscripts m and n are dropped as in previous discussions, so that without a subscript, a quantity can be interpreted as an instantiation of the set of all admissible values, $k_x \in \{k_{xm} \mid m \in \mathbb{Z} \wedge m/N_x \in [-1/2, 1/2)\}$, $k_y \in \{k_{yn} \mid n \in \mathbb{Z} \wedge n/N_y \in [-1/2, 1/2)\}$, $\widehat{\phi} \in \{\widehat{\phi}_{mn} \mid m, n \in \mathbb{Z} \wedge m/N_x, n/N_y \in [-1/2, 1/2)\}$, and $\boldsymbol{k} = k_x\hat{\boldsymbol{e}}_x + k_y\hat{\boldsymbol{e}}_y$.

Considering the errors caused by the schemes, the numerical solution to a semi-discretized form of Eq. (2.18) is consistent with the following modified ordinary differential equation in Fourier space.

$$\frac{d\widehat{\phi}}{dt} + i\boldsymbol{k}\cdot\boldsymbol{v}'\widehat{\phi} = -\nu' k^2 \widehat{\phi} \tag{2.20}$$

where $k^2 = \boldsymbol{k}\cdot\boldsymbol{k}$, and $\boldsymbol{v}'$ and ν' can be interpreted as the modified spectral advective velocity and modified spectral diffusivity respectively. According to the definition of the modified wavenumber in Eq. (2.12), $\boldsymbol{v}'$ and ν' account for the effects of the modified wavenumber. Their expressions are given in the following equations.

$$\boldsymbol{v}'(\theta, \boldsymbol{k}) = V\left(\hat{\boldsymbol{e}}_x \frac{k_x''}{k_x}\cos\theta + \hat{\boldsymbol{e}}_y \frac{k_y''}{k_y}\sin\theta\right) \tag{2.21}$$

$$\nu'(\boldsymbol{k}) = \nu\left(\frac{k_x'^2 + k_y'^2}{k^2}\right) \tag{2.22}$$

where k_x'' and k_y'' can be interpreted as the effective modified wavenumbers corresponding to the combination of all the discrete operators, including interpolation and differentiation, along the x- and y-directions respectively and treated as functions of k_x and k_y respectively consistently with the one-dimensional analysis. For staggered differential operations, interpolation schemes are required to evaluate advective fluxes. Therefore, the effective modified wavenumbers should consider both the transfer function and the modified wavenumber from the staggered differentiation,

$k''_x\Delta x = T(k_x\Delta x)k'_x\Delta x$ and $k''_y\Delta y = T(k_y\Delta y)k'_y\Delta y$. For collocated differential operations, interpolation schemes are not needed. Accordingly, effective modified wavenumbers of a collocated scheme are equal to its modified wavenumbers, $k''_x\Delta x = k'_x\Delta x$ and $k''_y\Delta y = k'_y\Delta y$. Mapping to a polar coordinate system, the wavenumber vector can be written as $\boldsymbol{k} = |k|\,(\hat{\boldsymbol{e}}_x\cos\varphi + \hat{\boldsymbol{e}}_y\sin\varphi)$, where φ defines an angle of observation. Consistent with the scaling of the wavenumber components in each dimension, the dimensionless wavenumber magnitude can be expressed as $|k|\,\delta$, where $\delta(\varphi) = \sqrt{\Delta x^2\cos^2\varphi + \Delta y^2\sin^2\varphi}$. If $\Delta x = \Delta y$, then δ is independent of φ, and the wavenumber magnitude is scaled by the uniform grid spacing.

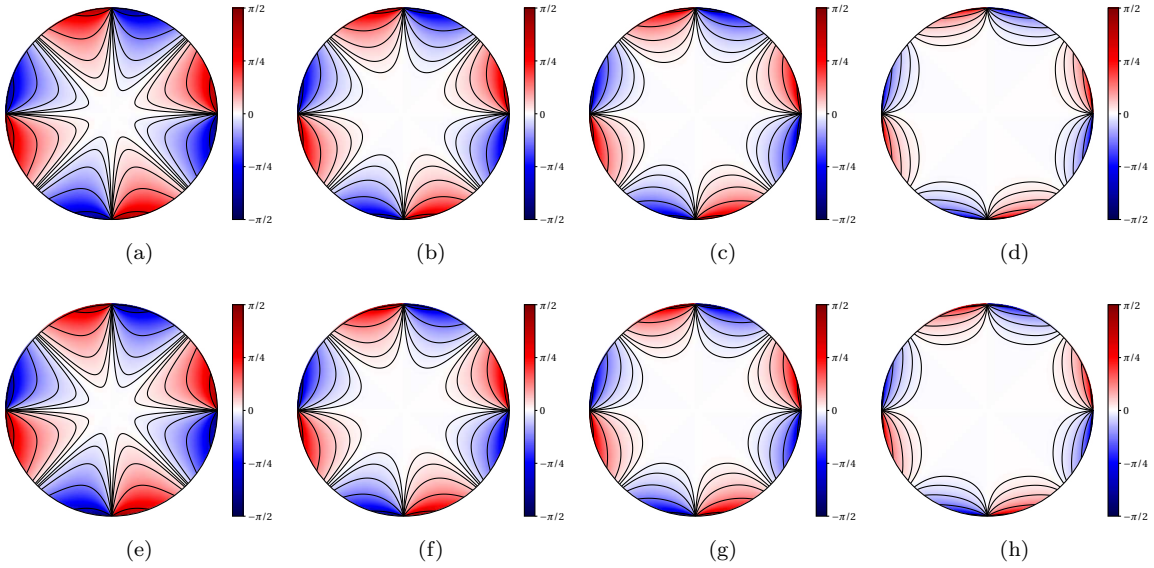

Figure 2.6: Errors of the modified spectral advective velocity angles, $\theta' - \theta$ where $\theta'(\boldsymbol{k})$ is the polar angle of the modified spectral advective velocity, $\boldsymbol{v}'$, i.e., $\boldsymbol{v}' = |\boldsymbol{v}'|\,(\hat{\boldsymbol{e}}_x\cos\theta' + \hat{\boldsymbol{e}}_y\sin\theta')$. The errors are shown in $|k|\delta$–φ polar coordinate system with $\varphi = \theta$: (a) collocated second-order difference; (b) collocated fourth-order explicit difference; (c) collocated sixth-order explicit difference; (d) collocated sixth-order compact difference; (e) staggered second-order difference with interpolation; (f) staggered fourth-order explicit difference with interpolation; (g) staggered sixth-order explicit difference with interpolation; (h) staggered sixth-order compact difference with interpolation. The isocurves are generated based on a logarithmic scale. As $|\boldsymbol{v}'| \to 0$, the contours show asymptotic behavior.

The two-dimensional spectral dispersion is characterized by the modified spectral advective velocity, $\boldsymbol{v}'$. For an exact differentiation, $\boldsymbol{v}' = \boldsymbol{v}$ for all resolved Fourier modes. For a numerical solution, $\boldsymbol{v}'$ has non-constant spectral behavior with respect to the advective direction, θ, and the wave orientation, φ. If $\theta = \varphi = 0$, the model problem becomes one-dimensional. The numerical dispersion in the linear advection is shown in Fig. 2.4. It can be seen that among the listed collocated schemes, the sixth-order compact finite difference scheme best resolves the advection of the modes for $k_x\Delta x < \pi/2$. However, the advection of the Nyquist wavenumber mode cannot be

resolved by the collocated central difference schemes, and the mode will become a standing wave. In comparison, for higher-order schemes, a staggered scheme has spectral behavior nearly identical to that of the collocated scheme of the same order even though the staggered numerical differential operations have significantly improved modified wavenumbers. For the second-order discretizations, the spectral behavior of the staggered and collocated schemes are completely identical. This behavior occurs because the interpolation is also considered as a step of the staggered calculation that suppresses the overall high-wavenumber features. The leading-order truncation error for the model problem of each scheme is derived in A.1 and listed in Tab. A.1 to quantify the response of numerical errors with respect to the local solution features in physical space. For a two-dimensional configuration, the anisotropy is shown in Fig. 2.5 and Fig. 2.6. For the linear system, without loss of generality, let $\theta = \varphi$ and $\Delta x = \Delta y$. Accordingly, the contours in Fig. 2.5 are equivalent to $|\boldsymbol{v}'| \,/\, |\boldsymbol{v}|$. Most of the contours in Fig. 2.5 present square-like shapes. This is because a Cartesian mesh only defines a rectangular domain and is not perfectly isotropic. As a result, the corresponding spectral domain is also rectangular. As a fair comparison, only $|k|\,\delta \leq \pi$ is considered. Due to the spectral behavior of the collocated finite difference schemes and central interpolation schemes, $|\boldsymbol{v}'| = 0$ is unavoidable. This limits the isotropy of the evaluation in the high wavenumber regime. Comparing the two-dimensional spectral behavior, the collocated schemes and staggered schemes are still nearly identical. As the formal order of accuracy increases, the isotropy successively improves, and the sixth-order compact schemes similarly show the best performance among all listed schemes. A consistent observation can also be obtained by comparing the error of the advective directions in Fig. 2.6. Along the x- and y-directions, the advection degenerates to a one-dimensional problem. The numerical schemes along the advection do not affect the advective direction, and the numerical schemes in the orthogonal direction make no contribution to the results. Along the domain-diagonal direction, the errors of the numerical schemes in the x- and y-directions are canceled. Therefore, for both cases, there is no error in resolving the advective direction. However, other than the axial and domain-diagonal directions, the numerical error in the advective velocity direction occurs as imbalanced errors in the evaluation of the projected advective speeds.

The spectral dissipation can be investigated from the modified spectral diffusivity, ν'. For the one-dimensional advection, the relative values of ν' are shown in Fig. 2.7. The exact differentiation should preserve ν for all resolved wavenumbers. Compared to Fig. 2.4, the effects of the modified wavenumber reduction are worse in the diffusion term, since two derivative operations are applied. The collocated schemes do not resolve the Nyquist wavenumber damping mechanism, which adversely affects the numerical stability in nonlinear problems. In contrast, the staggered schemes have a much enhanced high-wavenumber damping performance, which will make nonlinear systems more robust. This property is also supported by the amplitude of the leading-order truncation error which is derived in A.1 and provided in Tab. A.1 for each of the schemes. By comparison, the staggered differential schemes significantly improve the solution accuracy by reducing the amplitude

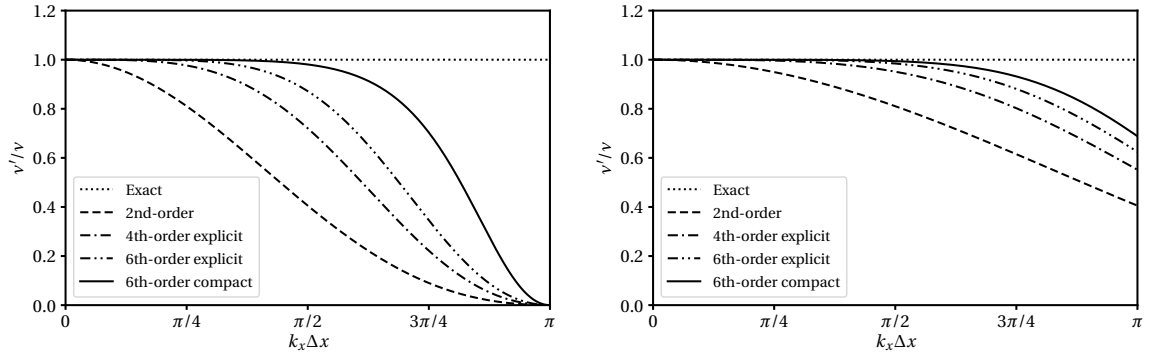

Figure 2.7: Profiles of the modified spectral diffusivities in one-dimensional computations: (a) collocated difference schemes; (b) staggered difference schemes. As $k_x\Delta x \to 0$, the plots show asymptotic behavior.

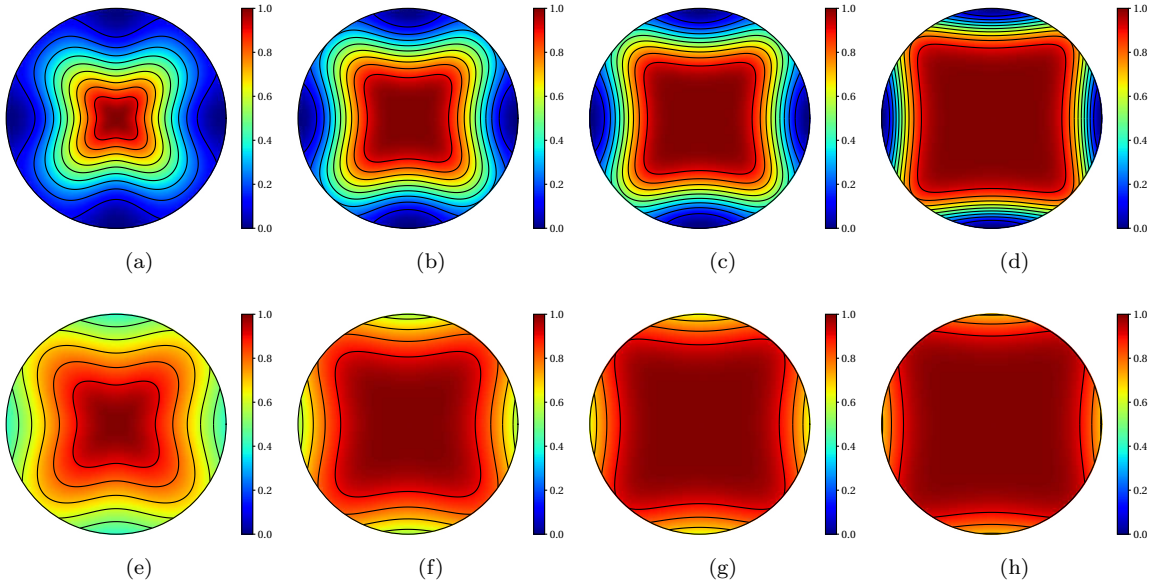

Figure 2.8: Relative modified spectral diffusivities $\nu'(\boldsymbol{k})/\nu$ shown in the $|k|\delta$–φ polar coordinate system: (a) collocated second-order difference; (b) collocated fourth-order explicit difference; (c) collocated sixth-order explicit difference; (d) collocated sixth-order compact difference; (e) staggered second-order difference; (f) staggered fourth-order explicit difference; (g) staggered sixth-order explicit difference; (h) staggered sixth-order compact difference. The isocurves are generated based on a linear scale. As $k \to 0$, the contours show asymptotic behavior.

of the leading-order truncation error in the calculation of the viscous term. The anisotropy is shown in Fig. 2.8. As φ varies, the collocated second-order scheme only shows isotropic behavior at low

wavenumbers. The collocated sixth-order schemes have a much improved isotropy compared to the second-order schemes. Nevertheless, the most significant improvement is observed by using staggered schemes. An alternative way to improve the performance of the diffusion term in damping high-wavenumber modes is to use second derivative operators [89, 107]. However, this treatment is at the cost of sacrificing the conservation form. The approach can be derived based on the product rule of calculus, $\nabla \cdot [\nu \nabla \phi] = \nabla \nu \cdot \nabla \phi + \nu \nabla^2 \phi$, where the calculation of $\nabla^2 \phi$ is based on second partial derivative operators.

2.3 Computational framework

In this section, the computational framework is fully described. The framework requires midpoint interpolation and collocated and staggered central schemes for the evaluation of first derivatives. It is compatible with schemes of an arbitrary order of accuracy. In particular, the proposed framework is favorable to applications of high-order compact schemes.

2.3.1 Governing equations

The compressible Navier-Stokes equations, including conservation of mass, momentum, and total energy, are formulated as

$$\frac{\partial \rho}{\partial t} + \frac{\partial}{\partial x_j} \left(\rho u_j \right) = 0 \tag{2.23}$$

$$\frac{\partial \rho u_i}{\partial t} + \frac{\partial}{\partial x_j} \left(\rho u_i u_j + p \delta_{ij} \right) = \frac{\partial \sigma_{ij}}{\partial x_j} \tag{2.24}$$

$$\frac{\partial \rho e}{\partial t} + \frac{\partial}{\partial x_j} \left(\rho h u_j \right) = \frac{\partial}{\partial x_j} \left(u_i \sigma_{ij} - q_j \right) \tag{2.25}$$

where the expressions are given in index notation [41] with an independent spatial dimension denoted by each free index and a summation over all spatial dimensions implied by each pair of repeated indices. In the equations, ρ is the density; u_i is the velocity vector; p is the pressure; δ_{ij} is the Kronecker delta characterizing an identity tensor; σ_{ij} is the viscous stress tensor; e is the specific total energy; h is the specific total enthalpy; and q_j is the heat flux vector. The governing equations are given in conservation form. The fluxes on the left-hand side of each equation are known as the inviscid fluxes, and the fluxes on the right-hand side are the viscous fluxes. If all the viscous fluxes are dropped, the governing equations will degenerate to an Euler system. σ_{ij} and q_j are formulated based on the transport properties of the fluids. For a Newtonian fluid, the viscous stress tensor is calculated as

$$\sigma_{ij} = 2\mu S_{ij} + \left(\beta - \frac{2}{3}\mu \right) \frac{\partial u_k}{\partial x_k} \delta_{ij} \tag{2.26}$$

where μ and β are the dynamic shear viscosity and bulk viscosity respectively, and S_{ij} is the strain rate tensor, defined as

$$S_{ij} = \frac{1}{2}\left(\frac{\partial u_i}{\partial x_j} + \frac{\partial u_j}{\partial x_i}\right) \tag{2.27}$$

The heat flux vector, q_j, is modeled by the Fourier's law of heat conduction:

$$q_j = -\kappa \frac{\partial T}{\partial x_j} \tag{2.28}$$

where κ is the thermal conductivity, and T is the temperature. The specific total energy, e, is defined as

$$e = e_{\text{th}} + \frac{1}{2} u_j u_j \tag{2.29}$$

where e_{th} is the specific internal energy. The specific total enthalpy, h, is defined as

$$h = e + p/\rho \tag{2.30}$$

The internal energy, e_{th}, and the pressure, p, are calculated based on an equation of state (EOS). For a pure substance, they can be expressed as functions of ρ and T in general. For a calorically perfect gas, they can be calculated as

$$p = \rho R T \tag{2.31}$$

and

$$e_{\text{th}} = \frac{RT}{\gamma - 1} \tag{2.32}$$

where R is the specific gas constant, and γ is the ratio of specific heats. The system is finally closed by giving the expressions of all the transport properties, μ, β, and κ. For LES or DNS with shock-capturing schemes active at a separated scale, these transport properties may also contain modeled components [144, 167, 109, 76]. The detailed description of the LES formulation used in this work is provided in A.2.

2.3.2 Numerical discretization on uniform Cartesian mesh

Consider a uniform Cartesian mesh generated in three-dimensional space. The computational mesh contains collocated grid points and edge-staggered grid points as shown in Fig. 2.9. During time advancement, all conservative variables evolve only at the collocated grid points, and all fluxes are assembled at the corresponding edge-staggered grid points. The divergence operations are performed by staggered central difference methods using input values at the edge-staggered grid points and generating the results at the collocated grid points. The schematic of the time advancement step is shown in Fig. 2.10.

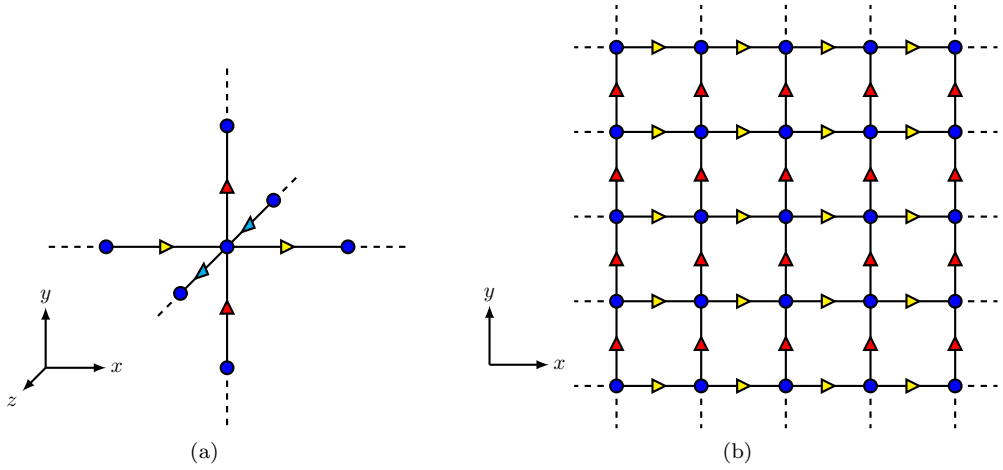

Figure 2.9: Uniform Cartesian mesh: (a) detailed view of the three-dimensional structure; (b) projected view in the x–y plane. The blue circles indicate the collocated grid points, and yellow, red and cyan triangles mark the edge-staggered grid points in the x-, y- and z-directions respectively.

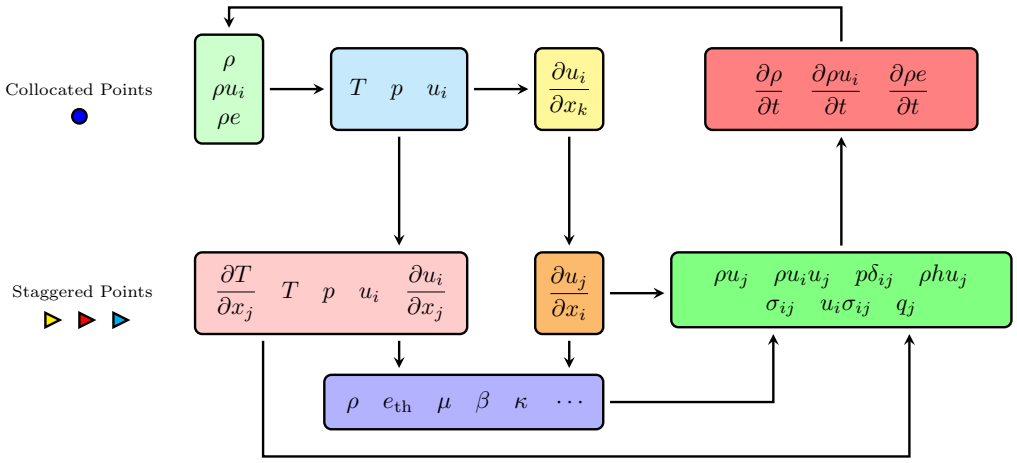

Figure 2.10: Schematics of time advancement step.

The inviscid fluxes are assembled using the primitive variables, u_i, T and p, that are first calculated from the conservative variables at the collocated grid points and then interpolated to the staggered grid points. The choice of the thermodynamic variables used for interpolation provides flexibility in numerically imposing the boundary conditions in a simulation. Using the interpolated p and T, all other required thermodynamic quantities are recalculated at the staggered grid points based on the EOS. According to the spectral behavior of the interpolation operator, shown in Fig. 2.3, all interpolated variables have damped high-wavenumber modes. As the nonlinear fluxes are assembled, aliasing interactions among high-wavenumber modes in the operands are reduced. The quadratic nonlinear interaction, as an example, is investigated in the following context and shown in

Fig. 2.11. Assuming $Q(x) = u(x)v(x)$ in one-dimensional space, the discrete Fourier representation of the direct numerical product can be written as

$$\sum_{n=-N/2}^{N/2-1} \widehat{Q}_n e^{ikx_j} = \sum_{|l+m|\leq N/2} \widehat{u}_l \widehat{v}_m e^{i(\alpha_1+\alpha_2)x_j} + \sum_{|l+m|>N/2} \widehat{u}_l \widehat{v}_m e^{i(\alpha_1+\alpha_2)x_j} \tag{2.33}$$

where $\alpha_1(l) = 2\pi l/L$ and $\alpha_2(m) = 2\pi m/L$ are the wavenumbers for $l, m \in \{n \in \mathbb{Z} \mid -N/2 \leq n < N/2\}$. The first term on the right-hand side of Eq. (2.33) represents the resolved interactions, and the second term on the right-hand side represents the aliased interactions. For resolved interactions, $n = l + m$ and $k = \alpha_1 + \alpha_2$, while for the aliased interactions, $n = l + m \pm N$ for the negative and positive wavenumber modes respectively, and correspondingly, $k = \alpha_1 + \alpha_2 \pm 2\pi$. Combined with the schematic shown in Fig. 2.11a, each location in the two-dimensional plane represents a quadratic interaction between the modes corresponding to wavenumbers α_1 and α_2. Among all quadratic interactions within the dashed-line box, the regions of aliased interactions are marked in red. The aliased interactions will fold back to the resolved modes colored by yellow. Considering the transfer functions, the numerical product of the interpolated factors can be expressed as

$$\sum_{n=-N/2}^{N/2-1} \widehat{Q}_n^F e^{ikx_j} = \sum_{|l+m|\leq N/2} T_{lm} \widehat{u}_l \widehat{v}_m e^{i(\alpha_1+\alpha_2)x_j} + \sum_{|l+m|>N/2} T_{lm} \widehat{u}_l \widehat{v}_m e^{i(\alpha_1+\alpha_2)x_j} \tag{2.34}$$

where $\widehat{Q}_n^F$ is the discrete Fourier transfer of the numerical product, and $T_{lm} = T(\alpha_1 \Delta x) T(\alpha_2 \Delta x)$ can be interpreted as the joint transfer function. Although the magnitude of the aliasing error depends on the factors, the amount of reduction can be quantified by the profile of T_{lm}. For the sixth-order compact interpolation, the profile of the joint transfer function is shown in Fig. 2.11b. As a reference, the "2/3-rule," which identifies the necessary filtered modes to eliminate the aliasing error in a quadratic interaction [115], is shown in Fig. 2.11c. With the interpolation of the primitive variables, although the aliasing error cannot be perfectly eliminated, the aliased interactions are largely reduced to improve the robustness. Additionally, in the compressible Navier-Stokes system, the inviscid fluxes involve cubic and quartic (in the formulation for a curvilinear coordinate system) interactions. For products involving more than two factors, the schematics are similar but need to be shown using a hyperplane in a higher-dimensional space.

Besides the primitive variables, the velocity and temperature gradients are needed for the viscous fluxes. In order to maximize the performance of high wavenumber dissipation, the gradient component aligned with the flux direction and the divergence operation are evaluated by the staggered difference schemes. For the Navier-Stokes equations, the diffusion term in Eq. (2.24) can be rearranged as

$$\frac{\partial \sigma_{ij}}{\partial x_j} = \frac{\partial}{\partial x_j}\left(\mu \frac{\partial u_i}{\partial x_j}\right) + \frac{\partial}{\partial x_j}\left[\mu \frac{\partial u_j}{\partial x_i} + \left(\beta - \frac{2}{3}\mu\right)\frac{\partial u_k}{\partial x_k}\delta_{ij}\right] \tag{2.35}$$

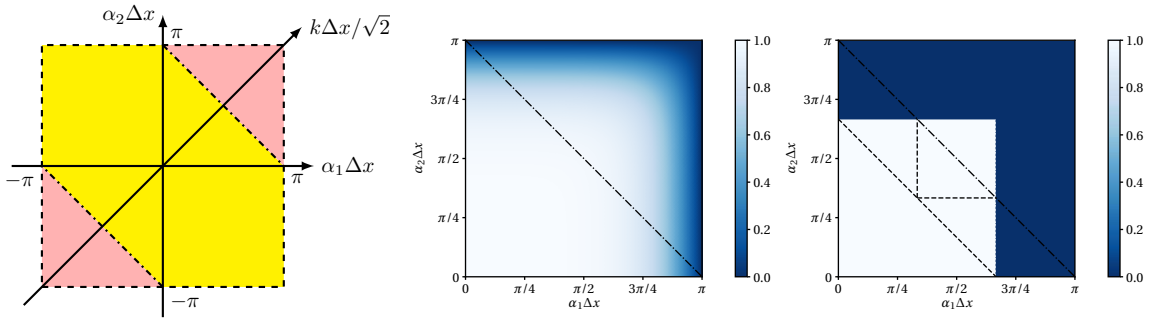

(a) (b) (c)

Figure 2.11: Quadratic interaction between two fields: (a) schematics; (b) fields are interpolated using the compact sixth-order central scheme. The regions beyond the dash-dotted lines characterize the aliased interactions; (c) fields are preprocessed by a spectrally sharp low-pass filter with cut-off wavenumber at $2\pi/3$. The color maps in (b) and (c) represent the joint transfer functions for the quadratic interactions.

where the numerical operator, ∂_{x_j}, uses the staggered central difference scheme, and ∂_{x_i}, for $i \neq j$, is conducted via the collocated central difference scheme in a direction orthogonal to the flux component and interpolated to the staggered grid locations. Numerically, for $\mu > 0$, the first term on the right-hand side of Eq. (2.35) imposes the dominant dissipation. Based on the analysis shown in Fig. 2.2b and Fig. 2.7b, the spectral dissipation can be well represented by the staggered central difference schemes especially in the high-wavenumber regime. The Nyquist wavenumber features caused by the dispersion error and aliased interactions can be effectively dampened following the diffusion mechanism in the governing equations. Similarly, the viscous flux in Eq. (2.25) can be rearranged as

$$\frac{\partial}{\partial x_j}\left[u_i\sigma_{ij} - q_j\right] = \frac{\partial}{\partial x_j}\left(\mu u_i \frac{\partial u_i}{\partial x_j} + \kappa\frac{\partial T}{\partial x_j}\right) + \frac{\partial}{\partial x_j}\left[\mu u_i \frac{\partial u_j}{\partial x_i} + \left(\beta - \frac{2}{3}\mu\right)\frac{\partial u_k}{\partial x_k}u_j\right] \tag{2.36}$$

where the term $\mu u_i u_{i,j}$ can be interpreted as an alternative evaluation of $\mu(u_i u_i/2)_{,j}$. The advantage of the staggered formulation can be observed from the first term on the right-hand side of Eq. (2.36). Additionally, the remaining terms, particularly the ones associated with the bulk viscosity, β, in Eq. (2.35) and Eq. (2.36) partially benefit from the high-wavenumber spectral behavior of the staggered central difference schemes.

2.3.3 Formulations on curvilinear meshes

The numerical differential operations on a curvilinear mesh are conducted based on an invertible mapping taking the coordinates on the curvilinear mesh to coordinates on a uniform Cartesian mesh. In this work, the mapping is assumed to be time-independent. The space where the curvilinear mesh is defined is known as the physical domain or actual domain, while the space where the

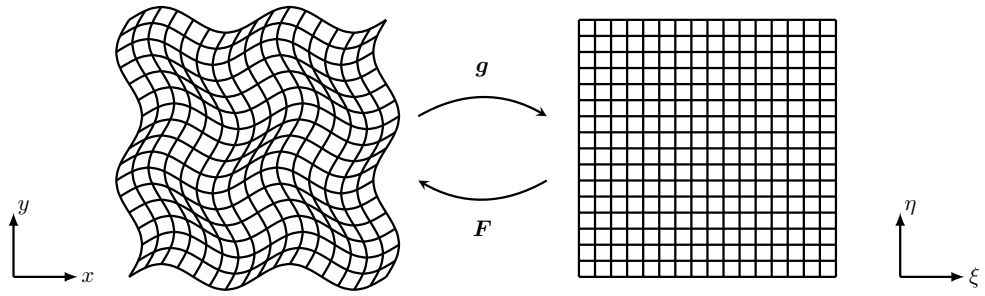

Figure 2.12: Invertible mapping between a curvilinear mesh in the physical domain (left) and a uniform Cartesian mesh in a reference domain (right).

Cartesian mesh is established is known as the reference domain or computational domain. In a three-dimensional physical domain, the orthonormal basis is defined using $\hat{\boldsymbol{e}}_x$, $\hat{\boldsymbol{e}}_y$ and $\hat{\boldsymbol{e}}_z$, and the coordinates can be expressed as $\boldsymbol{x} = x\hat{\boldsymbol{e}}_x + y\hat{\boldsymbol{e}}_y + z\hat{\boldsymbol{e}}_z$. Correspondingly, in the reference domain, the orthonormal basis is defined as $\hat{\boldsymbol{e}}_\xi$, $\hat{\boldsymbol{e}}_\eta$ and $\hat{\boldsymbol{e}}_\zeta$, and the coordinates can be expressed as $\boldsymbol{\xi} = \xi\hat{\boldsymbol{e}}_\xi + \eta\hat{\boldsymbol{e}}_\eta + \zeta\hat{\boldsymbol{e}}_\zeta$. During the solution process, the governing equations formulated in the physical domain are first mapped to the reference domain so that the numerical differential operations can be applied. Then, the evaluated results are mapped back to the physical domain. The mapping of the differential operations between the paired physical and reference domains are established by metric tensors that are defined as follows.

$$F_{iA} = \frac{\partial x_i}{\partial \xi_A} \qquad \text{and} \qquad g_{Ai} = \frac{\partial \xi_A}{\partial x_i} \tag{2.37, 2.38}$$

where the uppercase subscript represents the dimension in the reference domain, and the lowercase subscript represents the dimension in the physical domain [66]. It can be seen from the definitions that both F_{iA} and g_{Ai} are "two-leg" tensors. g_{Ai} maps the differential operation from the physical domain to the reference domain, $d\xi_A = g_{Ai}dx_i$, and F_{iA} maps the differential operation from the reference to the physical domain, $dx_i = F_{iA}d\xi_A$. A schematic is shown in Fig. 2.12. The Jacobian of the metrics, J, is defined as the determinant of the metric tensor $\boldsymbol{F}$.

$$J = \det(\boldsymbol{F}) \tag{2.39}$$

which characterizes the volume mapping from the reference domain to the physical domain, $dxdydz = Jd\xi d\eta d\zeta$. Since the mapping is invertible, the identity $\boldsymbol{F} = \boldsymbol{g}^{-1}$ holds. In addition, for a valid computational mesh, the condition $J > 0$ must be satisfied.

Consider the following weak scalar conservation law formulated in the physical domain.

$$\frac{\partial \phi}{\partial t} + \frac{\partial G_j}{\partial x_j} = \omega \tag{2.40}$$

where ϕ is a scalar conservative variable; G_j is the physical flux; and ω is the source / sink. The mapped flux divergence in the reference domain is

$$J\frac{\partial G_j}{\partial x_j} = \frac{\partial G_j F^*_{jA}}{\partial \xi_A} \tag{2.41}$$

where $\boldsymbol{F}^* = J\boldsymbol{F}^{-\mathrm{T}}$ is the cofactor tensor of $\boldsymbol{F}$. Therefore, an equivalent formulation of Eq. (2.40) in the reference domain is

$$J\frac{\partial \phi}{\partial t} + \frac{\partial \widehat{G}_A}{\partial \xi_A} = J\omega \tag{2.42}$$

where $\widehat{G}_A$ is known as the contravariant flux, defined as

$$\widehat{G}_A = G_j \widetilde{g}^{\mathrm{T}}_{jA} \tag{2.43}$$

The notation $\widetilde{(\cdot)} = J(\cdot)$ in Eq. (2.43) is introduced for shorthand such that $\widetilde{g}^{\mathrm{T}}_{jA} = Jg^{\mathrm{T}}_{jA}$. Also, in accordance with the definitions, the identity $\boldsymbol{F}^* = \widetilde{\boldsymbol{g}}^{\mathrm{T}}$ holds. Analogously, the compressible Navier-Stokes equations, Eq. (2.23), Eq. (2.24) and Eq. (2.25), can be reformulated as follows.

$$J\frac{\partial \rho}{\partial t} + \frac{\partial}{\partial \xi_A}\left(\rho \widehat{U}_A\right) = 0 \tag{2.44}$$

$$J\frac{\partial \rho u_i}{\partial t} + \frac{\partial}{\partial \xi_A}\left(\rho u_i \widehat{U}_A + p\widetilde{g}^{\mathrm{T}}_{iA}\right) = \frac{\partial}{\partial \xi_A}\left(\sigma_{ij}\widetilde{g}^{\mathrm{T}}_{jA}\right) \tag{2.45}$$

$$J\frac{\partial \rho e}{\partial t} + \frac{\partial}{\partial \xi_A}\left(\rho h \widehat{U}_A\right) = \frac{\partial}{\partial \xi_A}\left[\left(u_i\sigma_{ij} - q_j\right)\widetilde{g}^{\mathrm{T}}_{jA}\right] \tag{2.46}$$

where $\widehat{U}_A$ is known as the contravariant velocity defined as

$$\widehat{U}_A = u_i \widetilde{g}^{\mathrm{T}}_{iA} \tag{2.47}$$

The numerical evaluation of the contravariant fluxes follows an approach similar to that used for the uniform Cartesian mesh described in Sec. 2.3.2. The primitive variables, u_i, p and T, are interpolated from the collocated grid points to the staggered grid points to assemble the inviscid contravariant fluxes that appear on the left-hand sides of Eq. (2.44), Eq. (2.45) and Eq. (2.46). The transfer function of the interpolation schemes still contributes to the robustness by reducing high-wavenumber oscillations before any nonlinear interactions. The viscous contravariant fluxes that appear on the right-hand sides of Eq. (2.44), Eq. (2.45), and Eq. (2.46) are assembled based on the interpolated primitive variables and gradient fields with respect to the physical coordinate system that are evaluated using chain rule, $\partial_{x_j} = \left(\partial_{\xi_B}\right) g_{Bj}$ or $\partial_{x_j} = g^{\mathrm{T}}_{jB}\partial_{\xi_B}$. The divergence operations in the reference domain are conducted using the staggered difference schemes. The gradient components in the reference domain aligned with the contravariant flux direction are also evaluated using the

staggered difference schemes. As a result, substituting the expressions of σ_{ij} and q_j, the viscous contravariant fluxes in Eq. (2.45) and Eq. (2.46) are evaluated as follows.

$$\frac{\partial}{\partial \xi_A}\left(\sigma_{ij}\widetilde{g}^{\mathrm{T}}_{jA}\right) = \frac{\partial}{\partial \xi_A}\left(\mu \frac{\partial u_i}{\partial \xi_B} g_{Bj}\widetilde{g}^{\mathrm{T}}_{jA}\right) + \frac{\partial}{\partial \xi_A}\left[\mu g^{\mathrm{T}}_{iB}\frac{\partial u_j}{\partial \xi_B}\widetilde{g}^{\mathrm{T}}_{jA} + \left(\beta - \frac{2}{3}\mu\right)\frac{\partial u_k}{\partial \xi_B} g_{Bk}\widetilde{g}^{\mathrm{T}}_{iA}\right] \tag{2.48}$$

$$\begin{aligned} &\frac{\partial}{\partial \xi_A}\left[\left(u_i\sigma_{ij} - q_j\right)\widetilde{g}^{\mathrm{T}}_{jA}\right] \\ &= \frac{\partial}{\partial \xi_A}\left[\left(\mu u_i \frac{\partial u_i}{\partial \xi_B} + \kappa \frac{\partial T}{\partial \xi_B}\right) g_{Bj}\widetilde{g}^{\mathrm{T}}_{jA}\right] + \frac{\partial}{\partial \xi_A}\left[\mu u_i g^{\mathrm{T}}_{iB}\frac{\partial u_j}{\partial \xi_B}\widetilde{g}^{\mathrm{T}}_{jA} + \left(\beta - \frac{2}{3}\mu\right)\frac{\partial u_k}{\partial \xi_B} g_{Bk} u_i \widetilde{g}^{\mathrm{T}}_{iA}\right] \end{aligned} \tag{2.49}$$

For a valid mapping, $g_{Bj}\widetilde{g}^{\mathrm{T}}_{jA}$ is symmetric and positive-definite in the reference domain. Using the staggered central difference schemes for ∂_{ξ_A}, the dissipation of high-wavenumber oscillations in the reference domain can still be effectively resolved. The differential operator, ∂_{ξ_B}, for $B \neq A$, is evaluated using the collocated central difference scheme and then interpolated to the staggered grid points.

2.3.4 Generation of metrics

The metric tensor used to assemble the contravariant fluxes is $\widetilde{\boldsymbol{g}}$. Analytically, it can be calculated by inverting $\boldsymbol{F}$.

$$\widetilde{g}^{\mathrm{T}}_{iA} = \left(\frac{1}{2}\varepsilon_{ijk}\varepsilon_{ABC}\right)\frac{\partial x_j}{\partial \xi_B}\frac{\partial x_k}{\partial \xi_C} \tag{2.50}$$

where ε_{ijk} and ε_{ABC} are Levi-Civita permutation tensors in the physical and reference domains respectively. However, Eq. (2.50) cannot be directly used to generate metrics for a numerical solver as noted in [156]. Consider a homogeneous steady state solution to Eq. (2.40), where $\omega = 0$ and both ϕ and G_j are constant in space and time. In the reference domain, Eq. (2.42), combined with Eq. (2.41), reduces to the following constraint.

$$\frac{\partial \widetilde{g}^{\mathrm{T}}_{iA}}{\partial \xi_A} = 0 \tag{2.51}$$

Eq. (2.51) is known as the GCL for a stationary curvilinear mesh [156]. In this work, the GCL is further discussed from an alternative perspective.

On one hand, the GCL indicates a consistency between the numerical divergence operator and the generation of the discrete metric tensor as described in many works [156, 165, 111]. On the other hand, it also reveals numerical enforcement of a compatibility condition of the metrics. The metric tensor $\boldsymbol{F}$ can be interpreted as a type of "deformation gradient" of the physical coordinates with respect to the reference coordinates, i.e., $\boldsymbol{F}^{\mathrm{T}} = \nabla_{\boldsymbol{\xi}}\boldsymbol{x}^{\mathrm{T}}$, where the gradient operator with respect to the reference coordinates is defined as $\nabla_{\boldsymbol{\xi}} = \partial_{\xi_A}$. As an identity, $\boldsymbol{F}^{\mathrm{T}}$ is "curl-free" on the reference

domain, i.e., $\nabla_{\boldsymbol{\xi}} \times \boldsymbol{F}^{\mathrm{T}} = \mathbf{0}$. This is known as compatibility of the metric tensor. Taking a divergence operation with respect to the reference coordinates on both sides of Eq. (2.50), the following equation can be obtained.

$$\frac{\partial \widetilde{g}_{iA}^{\mathrm{T}}}{\partial \xi_A} = \frac{1}{2}\varepsilon_{ijk}\left[\frac{\partial x_k}{\partial \xi_C}\left(\varepsilon_{ABC}\frac{\partial}{\partial \xi_A}\frac{\partial x_j}{\partial \xi_B}\right) + \frac{\partial x_j}{\partial \xi_B}\left(\varepsilon_{ABC}\frac{\partial}{\partial \xi_A}\frac{\partial x_k}{\partial \xi_C}\right)\right] \tag{2.52}$$

where the expression in the brackets on the right-hand side yields $\boldsymbol{F}\left(\nabla_{\boldsymbol{\xi}} \times \boldsymbol{F}^{\mathrm{T}}\right) - \left(\nabla_{\boldsymbol{\xi}} \times \boldsymbol{F}^{\mathrm{T}}\right)^{\mathrm{T}} \boldsymbol{F}^{\mathrm{T}}$. The right-hand side of Eq. (2.52) is identically zero due to compatibility if all differential operations are exact. However, for numerically-approximated derivative operations, the left-hand side and right-hand side of Eq. (2.52) are not discretely equivalent. The "curl-free" condition of $\boldsymbol{F}^{\mathrm{T}}$ is weakly imposed in $\widetilde{\boldsymbol{g}}^{\mathrm{T}}$, which relies on numerical consistency and is achieved by grid convergence. This is due to the nonlinearity in evaluating $\widetilde{\boldsymbol{g}}^{\mathrm{T}}$ from $\boldsymbol{F}$. The product rule of calculus may not hold discretely to enforce a numerically equivalent form of the right-hand side in Eq. (2.52). As a result, a non-zero residual may be generated from the truncation errors of the numerical schemes. Such a residual is known as the GCL error and often contributes to numerical inaccuracy and instability in simulations of physical conservation laws [165, 164].

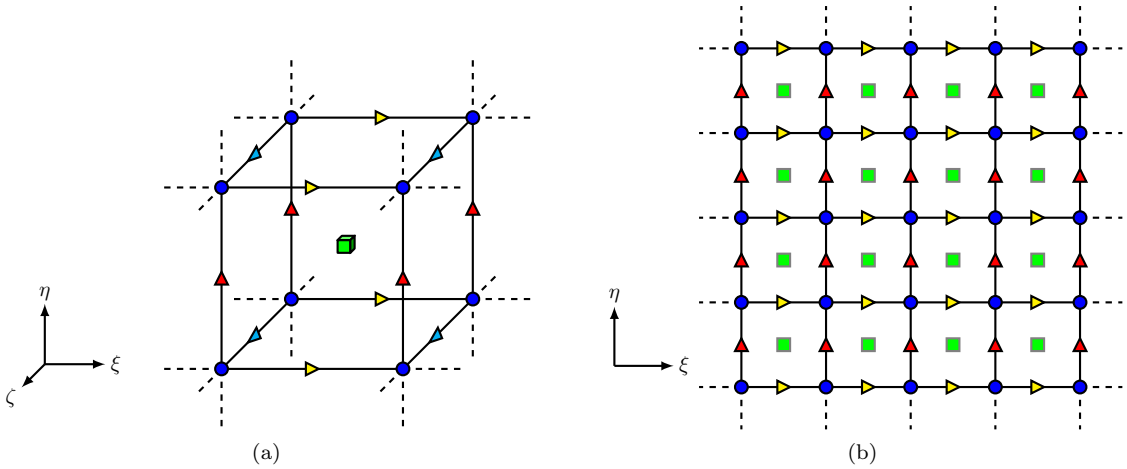

Figure 2.13: Schematics of generation of GCL metrics: (a) detailed isometric view of the three-dimensional structure; (b) projected view on the $\xi - \eta$ plane where fully staggered locations do not belong to the collocated and edge-staggered plane. The mesh is shown in the reference domain. The collocated, edge-staggered and fully staggered points are marked by circle, triangle and square (cube) symbols, respectively.

For numerically-generated metrics, the commonly used approaches are equivalent to strongly imposing the compatibility condition in Eq. (2.50). In order to show this, append two terms that are analytically equal to zero, $x_j \varepsilon_{ABC} F_{kC,B}$ and $x_k \varepsilon_{ABC} F_{jB,C}$, to the right-hand side of Eq. (2.50),

so that the expression of $\widetilde{g}_{iA}^{\mathrm{T}}$ becomes compatibility-aware.

$$\widetilde{g}_{iA}^{\mathrm{T}} = \left(\frac{1}{2}\varepsilon_{ijk}\varepsilon_{ABC}\right)\left[\frac{\partial x_j}{\partial \xi_B}\frac{\partial x_k}{\partial \xi_C} + w x_j \frac{\partial}{\partial \xi_B}\frac{\partial x_k}{\partial \xi_C} + (1-w) x_k \frac{\partial}{\partial \xi_C}\frac{\partial x_j}{\partial \xi_B}\right] \tag{2.53}$$

where w is a weighting factor. Eq. (2.53) can be further analytically manipulated into the so-called conservation form [156].

$$\widetilde{g}_{iA}^{\mathrm{T}} = \left(\frac{1}{2}\varepsilon_{ijk}\varepsilon_{ABC}\right)\left[w\frac{\partial}{\partial \xi_B}\left(x_j\frac{\partial x_k}{\partial \xi_C}\right) + (1-w)\frac{\partial}{\partial \xi_C}\left(x_k\frac{\partial x_j}{\partial \xi_B}\right)\right] \tag{2.54}$$

The effect of the weighting factor w is discussed in detail in Ref. [1]. For further discussion, rewrite Eq. (2.54) as

$$\widetilde{g}_{iA}^{\mathrm{T}} = \left(\frac{1}{2}\varepsilon_{ijk}\varepsilon_{ABC}\right)\left[w\frac{\partial}{\partial \xi_B}\left(x_j F_{kC}\right) - (1-w)\frac{\partial}{\partial \xi_B}\left(x_k F_{jC}\right)\right] \tag{2.55}$$

Comparing Eq. (2.55) with Eq. (2.51), the GCL error can be expressed as

$$\frac{\partial \widetilde{g}_{iA}^{\mathrm{T}}}{\partial \xi_A} = \left(\frac{1}{2}\varepsilon_{ijk}\varepsilon_{ABC}\right)\left[w\frac{\partial^2}{\partial \xi_A \partial \xi_B}\left(x_j F_{kC}\right) - (1-w)\frac{\partial^2}{\partial \xi_A \partial \xi_B}\left(x_k F_{jC}\right)\right] \tag{2.56}$$

The GCL constraint, derived by imposing compatibility, is satisfied by fully relying on the commutativity of the differential operator used for divergence evaluation in the computational framework, ∂_{ξ_A}, and in the numerical calculation of $\widetilde{\boldsymbol{g}}^{\mathrm{T}}$ from $\boldsymbol{F}$, ∂_{ξ_B}. Accordingly, once $\boldsymbol{x}\otimes\boldsymbol{F}$ is assembled, the GCL requires the remaining differential operations to calculate $\widetilde{\boldsymbol{g}}^{\mathrm{T}}$ to be consistent and commutable. However, the GCL constraint does not put any restriction on the calculation of $\boldsymbol{F}$. This implies that $\boldsymbol{F}$ can be either numerically evaluated in different ways or analytically provided. Similarly, prior to calculations of $\boldsymbol{x}\otimes\boldsymbol{F}$, there is no GCL constraint for the evaluation of $\boldsymbol{x}$ either if its components are needed at an abstract location. In practice, as an example, $\boldsymbol{x}\otimes\boldsymbol{F}$ is evaluated at collocated grid points and then interpolated to the edge-staggered locations in Ref. [111], while in this work, $\boldsymbol{F}$ and $\boldsymbol{x}\otimes\boldsymbol{F}$ are evaluated from an interpolated $\boldsymbol{x}$ using staggered derivative schemes. Both approaches have demonstrated numerically zero GCL errors. Therefore, the key step in enforcing the GCL described by Eq. (2.55) should be interpreted as a GCL-consistent inversion of the metric tensor $\boldsymbol{F}$.

In this work, the metric tensor is fully calculated by numerical differentiation for all cases following Eq. (2.54) with $w = 0.5$. All numerical differential operations are conducted by the edge-to-node staggered finite difference methods. Assuming that the physical coordinates are initially provided at the collocated grid points during mesh generation, all coordinates are first interpolated along all three directions to a fully staggered location. In the reference domain, the fully staggered location is at the geometric center of the cube constructed by the neighboring collocated points as shown in Fig. 2.13. Starting from the fully staggered locations, all components in the metric tensor $\boldsymbol{F}$ are numerically evaluated at the corresponding face-staggered location. Then, the corresponding components of $\boldsymbol{x}\otimes\boldsymbol{F}$ are assembled at the face-staggered locations. Eventually, after the second

differential operation, the GCL-consistent metrics are obtained at each edge-staggered location for the assembly of contravariant inviscid fluxes. At these locations, other components of $\widetilde{\boldsymbol{g}}^{\mathrm{T}}$ that are not involved in the GCL constraint are calculated via interpolations. For a periodic domain, specific details of metric evaluations using staggered compact finite difference and midpoint interpolation schemes are given in A.3.

2.3.5 Shock-capturing methods

In simulations of flows where shock waves are present, the shock waves are often treated as under-resolved structures. For high-resolution simulations, high-order shock-capturing schemes are commonly applied [76, 141, 157]. These shock-capturing schemes impose sufficient numerical dissipation at shock locations so that the shock profiles are artificially thickened and well-captured discretely by the computational framework without causing numerical instability or strong spurious oscillations. The computational framework described in previous sections is compatible with a wide variety of shock-capturing techniques. In this work, two common methods – the localized artificial diffusivity (LAD) method and the weighted essentially non-oscillatory (WENO) interpolation scheme combined with a projected approximate Riemann solver – are investigated.

For weak and moderate eddy shocklets in compressible turbulent flows, the LAD approach shows a decent performance. The LAD approach is known to be less dissipative for turbulent flow simulations when used with numerical operators that have high-spectral-resolution properties. For shock-capturing, only artificial bulk viscosity and artificial thermal conductivity are needed. The LAD model detects a shock based on local high-order derivatives. The detailed formulation is described in Ref. [76]. LAD can be easily applied to a computational system combined with diffusion fluxes. It does not require characteristic decomposition or a Riemann solver. Instead, according to Ref. [76], a low-pass filter is required to maintain numerical stability. However, in this computational framework, due to the robustness resulting from dealiasing effects and high-wavenumber viscous dissipation enhancement, the solution filtering, claimed to be necessary in previous applications of LAD models, can be avoided in capturing weak shocks. Furthermore, without solution filtering, the numerical dissipation, due to the spatial discretization, exerted in the computational system can be easily quantified.

WENO-based nonlinear interpolation schemes divide a full stencil into several candidate sub-stencils. Each candidate sub-stencil interpolates the input field individually using a linear scheme whose order of convergence is supported by the width of the sub-stencil. The final interpolated results are determined via a convexly-weighted superposition of all results obtained from candidate sub-stencils. The weights are comprehensively determined by a set of smoothness indicators calculated on each candidate sub-stencil. In a smooth region, the weights tend to make the superposed coefficients converge to a high-order linear interpolation scheme. In a shock region, the weights impose the use of interpolations from locally smooth candidate sub-stencils only. Correspondingly, the formal order

of convergence will be lower.

For better solution behavior, the nonlinear interpolation scheme is commonly applied in conjunction with an approximate Riemann solver [157]. A Riemann solver assumes a discontinuity at the flux assembly location and takes two states of conservative variables on both sides of the discontinuity to evaluate regularized fluxes as the Riemann problem develops in time. For a hyperbolic conservation system, Riemann fluxes can be calculated as $\boldsymbol{\mathcal{F}}_{\text{Riemann}}(\boldsymbol{U}_L, \boldsymbol{U}_R)$, where $\boldsymbol{\mathcal{F}}_{\text{Riemann}}$ is the set of numerical fluxes evaluated by the Riemann solver, $\boldsymbol{U}$ is the set of conservative variables, and the subscripts "L" and "R" denote the "left" and "right" states respectively. In an actual simulation, each edge is assumed to formulate a projected local Riemann problem. $\boldsymbol{U}_L$ and $\boldsymbol{U}_R$ are obtained from the interpolated characteristic variables.

Even with nominally high-order methods, fully using nonlinear interpolation schemes may still result in overly dissipative solution profiles at small scales in simulations of turbulent flows; this phenomenon is shown in Sec. 2.4.4. Therefore, to conduct an LES or DNS at a comparable physical resolution, the computational mesh used for a simulation that fully relies on nonlinear interpolation schemes needs to be much finer than the mesh used for a simulation based on non-dissipative numerical methods. Nevertheless, shock-capturing schemes must be active at shock locations. To address this issue, a hybrid approach can be applied [74]. Conceptually, the hybridization is controlled by a physics-based shock sensor. Ideally, the shock-capturing schemes are active and localized at the shock structures, and only non-dissipative schemes are used in shock-free regions. Accordingly, small-scale dynamics are fully governed by physical dissipation or physics-based SGS model dissipation, and this significantly enhances the simulation resolution.

The computational framework introduced in this study supports a variety of blending strategies. Among all feasible strategies, binary blending of primitive variables (ρ, $\boldsymbol{u}$, T) is used in this work. Based on the compatibility constraint for approximate Riemann solvers, if $\boldsymbol{U}_L = \boldsymbol{U}_R$, then the Riemann solver does not introduce extra numerical dissipation. As a result, when both $\boldsymbol{U}_L$ and $\boldsymbol{U}_R$ are set to be variables interpolated by central schemes, $\boldsymbol{\mathcal{F}}_{\text{Riemann}}(\boldsymbol{U}_L, \boldsymbol{U}_R)$ is identical to directly assembled central fluxes. Details of the shock-capturing schemes are included in A.5.

2.4 Demonstrative numerical performance

In this section, demonstrative simulations are provided to investigate the numerical performance of the computational framework. The demonstrations are primarily selected to examine the capability of the framework to preserve large-scale flow structures, resolve turbulent structures at small scales, and support existing models for LES and shock capturing.

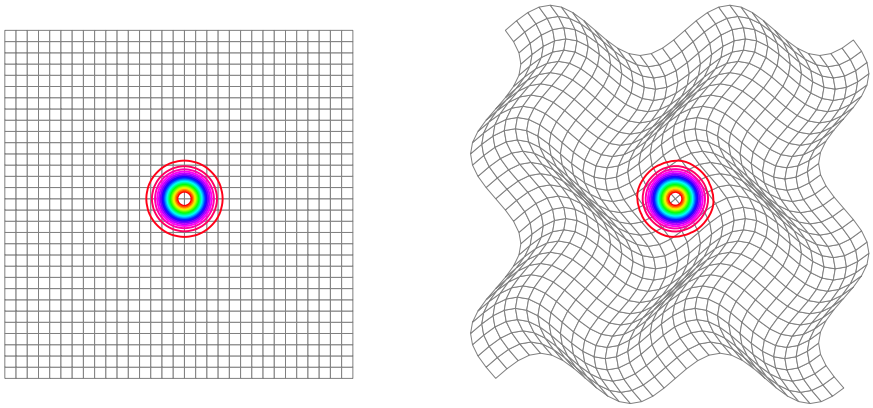

(a) (b)

Figure 2.14: Initial pressure distributions: (a) Cartesian mesh; (b) curvilinear mesh. The contours represent the pressure distributions for $p \in [0.55, 0.71]$.

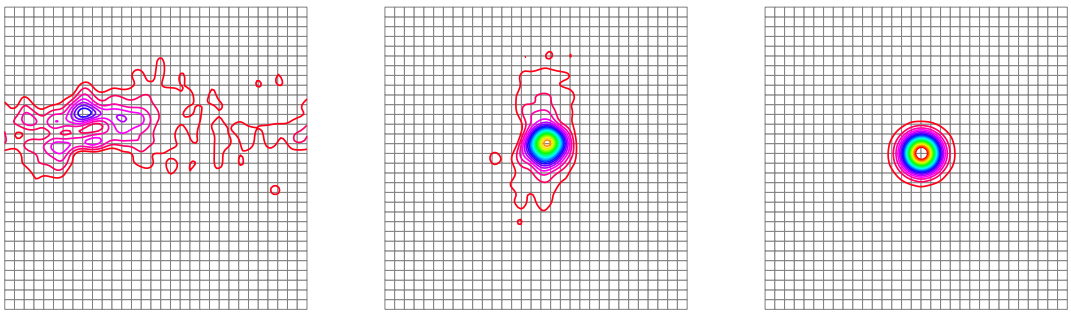

(a) (b) (c)

Figure 2.15: Pressure distributions on a Cartesian mesh after one advection period: (a) second-order schemes; (b) fourth-order schemes; (c) compact sixth-order schemes. The contours represent the pressure distributions for $p \in [0.55, 0.71]$.

2.4.1 Advection of a homentropic swirl

A uniform background flow is prescribed along the x-direction at a Mach number of 0.5 on a two-dimensional periodic domain, $(x, y) \in [-6, 6)^2$. A swirling flow field is superposed as a homoentropic perturbation. The flow is inviscid with no thermal diffusion. Assuming the perturbation amplitude is sufficiently small compared to the freestream, the swirl flow feature will advect following the freestream at a constant velocity. Considering the periodic boundaries, after a period, the initial flow profile should be asymptotically recovered. The initial homoentropic perturbation profiles,

denoted with a "δ" in front of each variable, are given as

$$\begin{cases} \delta \boldsymbol{u} = \epsilon r e^{\alpha(1-r^2)} \hat{\boldsymbol{e}}_l(\theta) \\ \delta T = -\epsilon^2 \frac{\gamma-1}{4\alpha\gamma} e^{2\alpha(1-r^2)} \end{cases} \tag{2.57}$$

where $r^2 = x^2 + y^2$; θ is the polar angle about $(x, y) = (0, 0)$; $\hat{\boldsymbol{e}}_l$ is a clock-wise tangential unit vector, $\hat{\boldsymbol{e}}_l(\theta) = \hat{\boldsymbol{e}}_x \sin\theta - \hat{\boldsymbol{e}}_y \cos\theta$; $\epsilon = 0.3$ characterizes the perturbation amplitude; and $\alpha = 1.2$ characterizes the spatial localization of the swirl flow. The value of α used in this configuration allows the Gaussian profile to achieve spatial decay of $\mathcal{O}(10^{-17}) \sim \mathcal{O}(10^{-19})$ from the domain center to the closest "boundary" point. With these ranges of spatial decay, the perturbation near the domain "boundary" can be treated as numerically zero compared to the perturbation amplitude near the center of the computational domain. Consequently, the non-smoothness caused by the periodic extension of a Gaussian profile can be neglected. The fluid is a calorically perfect gas. The ratio of specific heats is $\gamma = 1.4$, and the specific gas constant is $R = 1$. The speed of sound and density in the freestream state are used for normalization. Therefore, the overall velocity field is $\boldsymbol{u} = 0.5\hat{\boldsymbol{e}}_x + \delta\boldsymbol{u}$, and the overall temperature field is $T = (\gamma R)^{-1} + \delta T$. The perturbation is homoentropic, so p/ρ^γ remains constant over the entire domain [75, 111, 165].

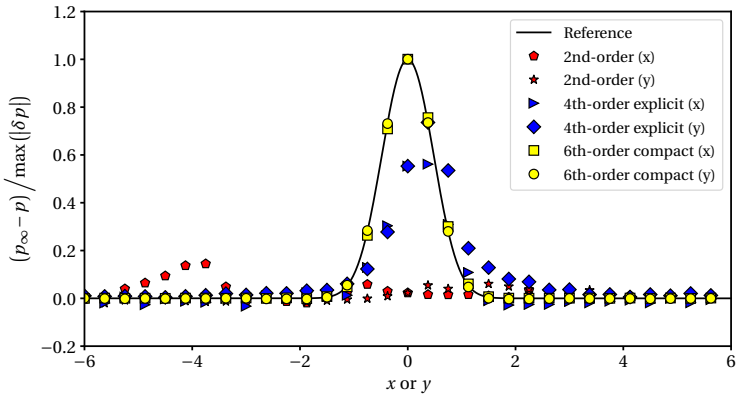

Figure 2.16: Centerline pressure profiles after one advection period using different sets of spatial discretization schemes, where p_∞ is the freestream pressure, and δp is the pressure perturbation. p_∞, δp and the reference profile are analytically calculated from the initial condition.

The simulation is set up on both a Cartesian and a curvilinear mesh with size 32×32 as shown in Fig. 2.14. The curvilinear mesh is generated via a two-dimensional perturbation on the Cartesian mesh. The coordinate mapping is

$$\begin{cases} x = L\left[\xi/N_\xi - 1/2 - A\sin(4\pi\eta/N_\eta)\right] \\ y = L\left[\eta/N_\eta - 1/2 + A\sin(4\pi\xi/N_\xi)\right] \end{cases} \tag{2.58}$$

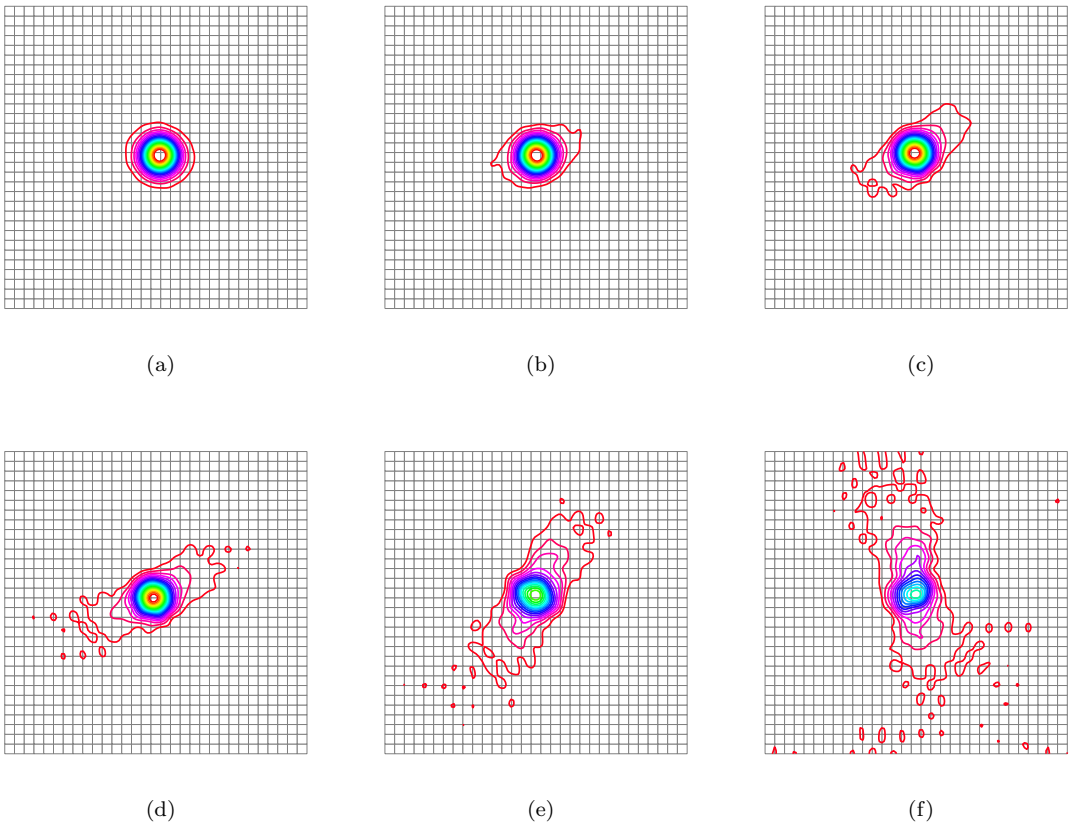

Figure 2.17: Pressure distribution on Cartesian mesh using 6th-order compact schemes after (a) 5 advection periods; (b) 8 advection periods; (c) 11 advection periods; (d) 12 advection periods; (e) 14 advection periods; and (f) 15 advection periods.

where $L = 12$ is the unperturbed domain length, and $A = 0.07$ characterizes the mesh waviness. The mesh spacing in the reference domain is unity in both directions. The interpolation and differentiation with respect to the coordinates that use compact schemes to calculate GCL-consistent metrics on a periodic domain are illustrated in A.3. Time advancement is carried out using the third-order strong-stability-preserving Runge-Kutta (SSP-RK3) method [142] with a constant Courant–Friedrichs–Lewy (CFL) number of 0.4. Spatial computations are conducted using the same framework as previously described with second-order explicit, fourth-order explicit, and sixth-order compact central schemes respectively. All three sets of numerical schemes are non-dissipative.

The simulation results using different spatial discretization schemes on the Cartesian mesh are shown in Fig. 2.15. The contours represent the pressure profile for $p \in [0.55, 0.71]$. For visualization purposes, the simulation results are upsampled using the cubic spline method during post-processing.

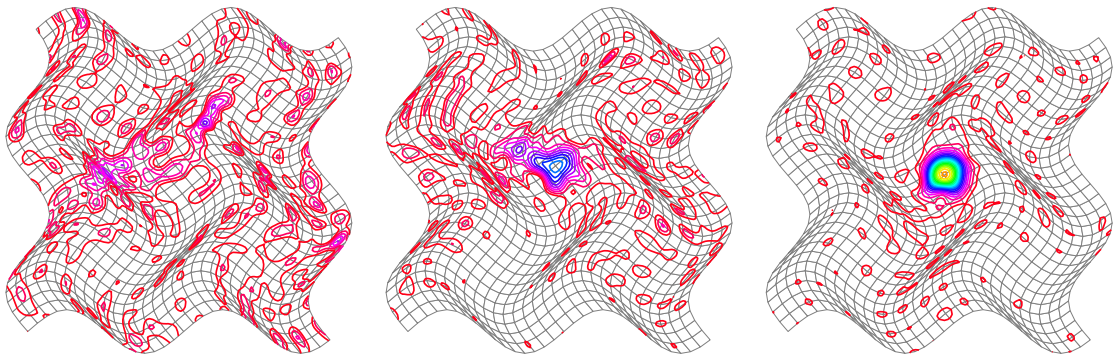

(a) (b) (c)

Figure 2.18: Pressure distributions on a curvilinear mesh after one advection period: (a) second-order schemes; (b) fourth-order schemes; (c) sixth-order compact schemes.

Compared with the reference profile given in Fig. 2.14a, after one advection period, the flow structures in the second-order simulation are completely distorted (Fig. 2.15a); significant numerical errors can be observed in the fourth-order simulations, but the basic flow structures are preserved (Fig. 2.15b); and almost no error is visible from the contours of the simulation using the sixth-order compact schemes (Fig. 2.15c). The centerline pressure profiles for the three simulation cases are shown in Fig. 2.16. As seen from the mesh generation, Eq. (2.58) for $A = 0$, the centerlines in both directions are aligned with a row or column of collocated grid points while using even N_ξ and N_η. Therefore, the data points in Fig. 2.16 represent the nodal values directly computed in the simulations. The reference profile is analytically calculated from the initial conditions, and the profile is normalized by the maximum pressure perturbation in the initial condition. According to the centerline profiles after one advection period, the sixth-order simulation best preserves the center location, profile shape, and the peak value. As a further investigation of the performance of the sixth-order compact schemes, the simulation is continued up to 15 advection periods. Some visualizations at selected numbers of advection periods are shown in Fig. 2.17. As the simulation time progresses, the numerical error accumulates and behaves as nonlinear dispersion. With this simulation setup, the computational accuracy can be well preserved up to 11 advection periods. Beyond that, the numerical error begins to spread out, and the flow structures are more contaminated.

The simulation results on the curvilinear mesh are shown in Fig. 2.18. The results are obtained after one advection period, and Fig. 2.14b should be used for comparison. As shown in Eq. (2.44) – Eq. (2.46), the mesh waviness creates extra nonlinearity in the computational system which makes the simulations more challenging. As shown in Fig. 2.18a, the second-order simulation completely destroys the flow features, and the numerical error is especially localized where the mesh is largely skewed. The flow features in the fourth-order simulation (Fig. 2.18b) are also significantly distorted,

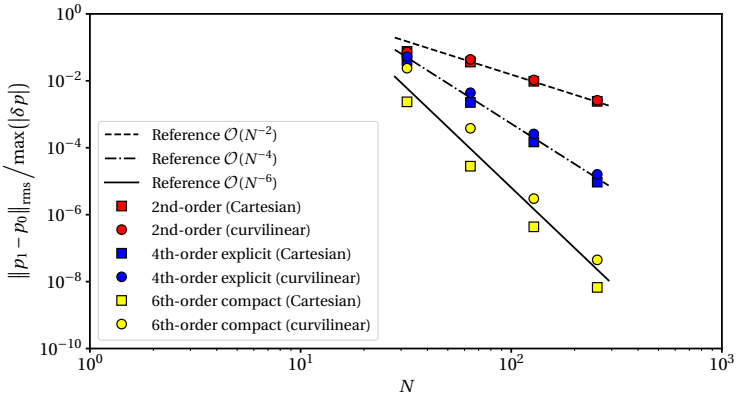

Figure 2.19: Grid convergence measurements of the homentropic swirl advection simulations using different sets of numerical schemes. N represents the number of grid points in each dimension, and the numerical error is indicated by the root-mean-square pressure difference between the initial condition and one advection period and is normalized by the maximum initial pressure perturbation.

but a small number of the original features can still be identified from the resulting field. The compact sixth-order simulation (Fig. 2.18c) preserves majority of the flow features and gives the best result among the three simulations although the numerical error is highly contaminated.

The grid convergence for all sets of simulations shown in this section is measured. In order to reduce the numerical error caused by the time advancement scheme, the CFL number is set to 0.05. For all cases, the solution profiles at one advection period are used to evaluate the numerical error. The numerical error is quantified by the root-mean-square pressure difference between the final state and initial condition that is analytically set. The numerical error is further scaled by the maximum perturbation pressure in the initial condition. The results are shown in Fig. 2.19 where N is the number of grid points in each dimension. Compared to the reference curves in Fig. 2.19, all simulations achieve the expected formal orders of convergence on both a uniform Cartesian mesh and a curvilinear wavy mesh. Additionally, the visualizations of solution convergence with grid refinement are shown in Fig. 2.20 and Fig. 2.21 for simulations on uniform Cartesian meshes and curvilinear wavy meshes respectively.

2.4.2 Forced isotropic turbulence

This problem is configured on a three-dimensional periodic domain, $(x, y, z) \in [0, 2\pi)^3$, with a set up similar to the one described in Ref. [72]. An isotropic turbulent flow is energized by a low-wavenumber solenoidal term, ρf_i, added to the right-hand side of Eq. (2.24). Eq. (2.25) remains unmodified, which implies the existence of an internal energy sink, Λ, that locally and instantaneously balances the forcing work, $\Lambda + \rho f_j u_j = 0$. The forcing, f_i, is updated via a solenoidally

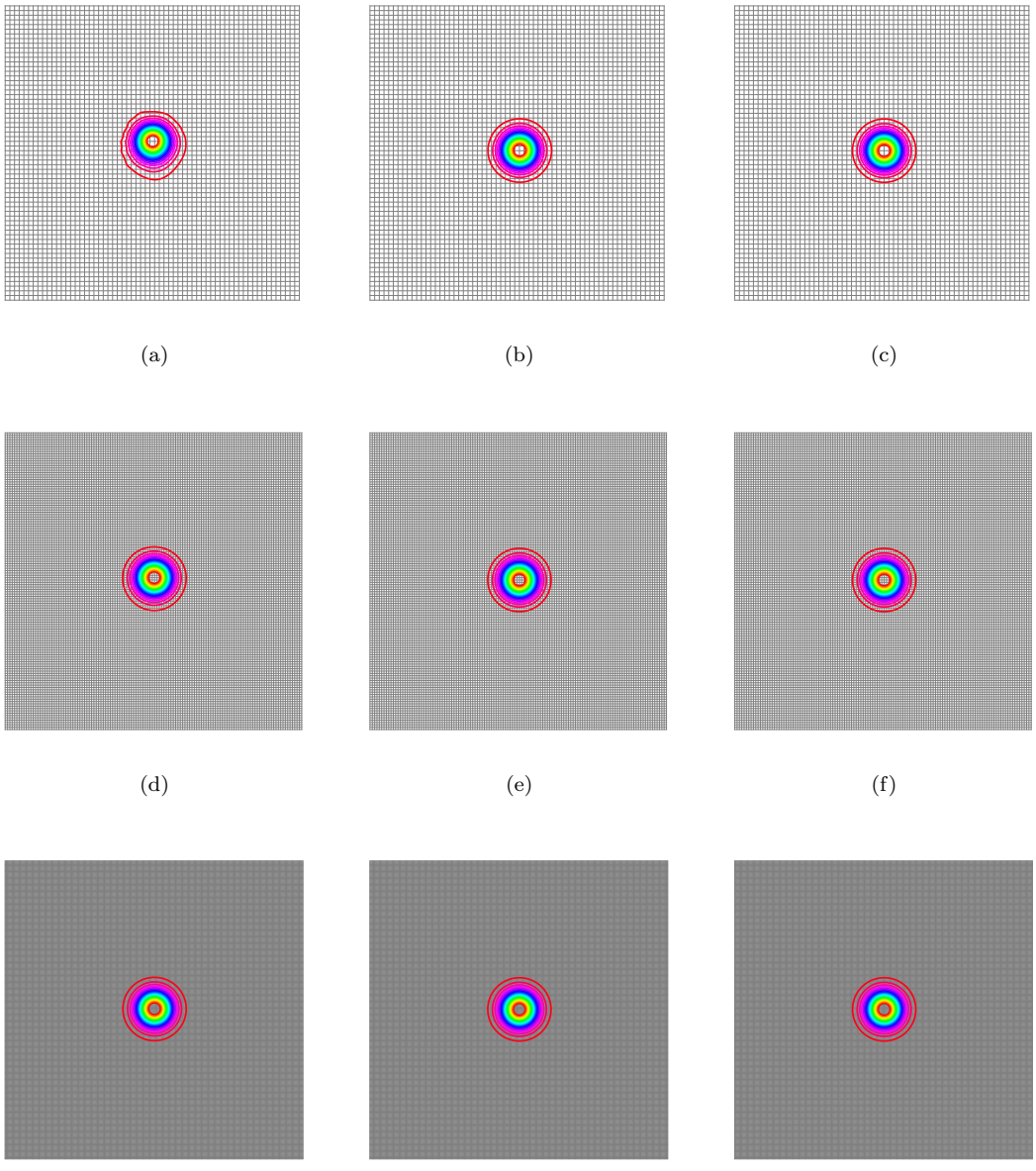

Figure 2.20: Visualization of convergence of pressure on uniform Cartesian meshes. The sub-figures in the first row ((a), (b), and (c)) are computed on a 64^2 mesh; the sub-figures in the second row ((d), (e), and (f)) are computed on a 128^2 mesh; and the sub-figures in the third row ((g), (h), and (i)) are computed on a 256^2 mesh. The sub-figures in the first column ((a), (d), and (g)) are computed using 2nd-order schemes; the sub-figures in the second column ((b), (e), and (h)) are computed using 4th-order schemes; and the sub-figures in the third column ((c), (f), and (i)) are computed using 6th-order compact schemes.

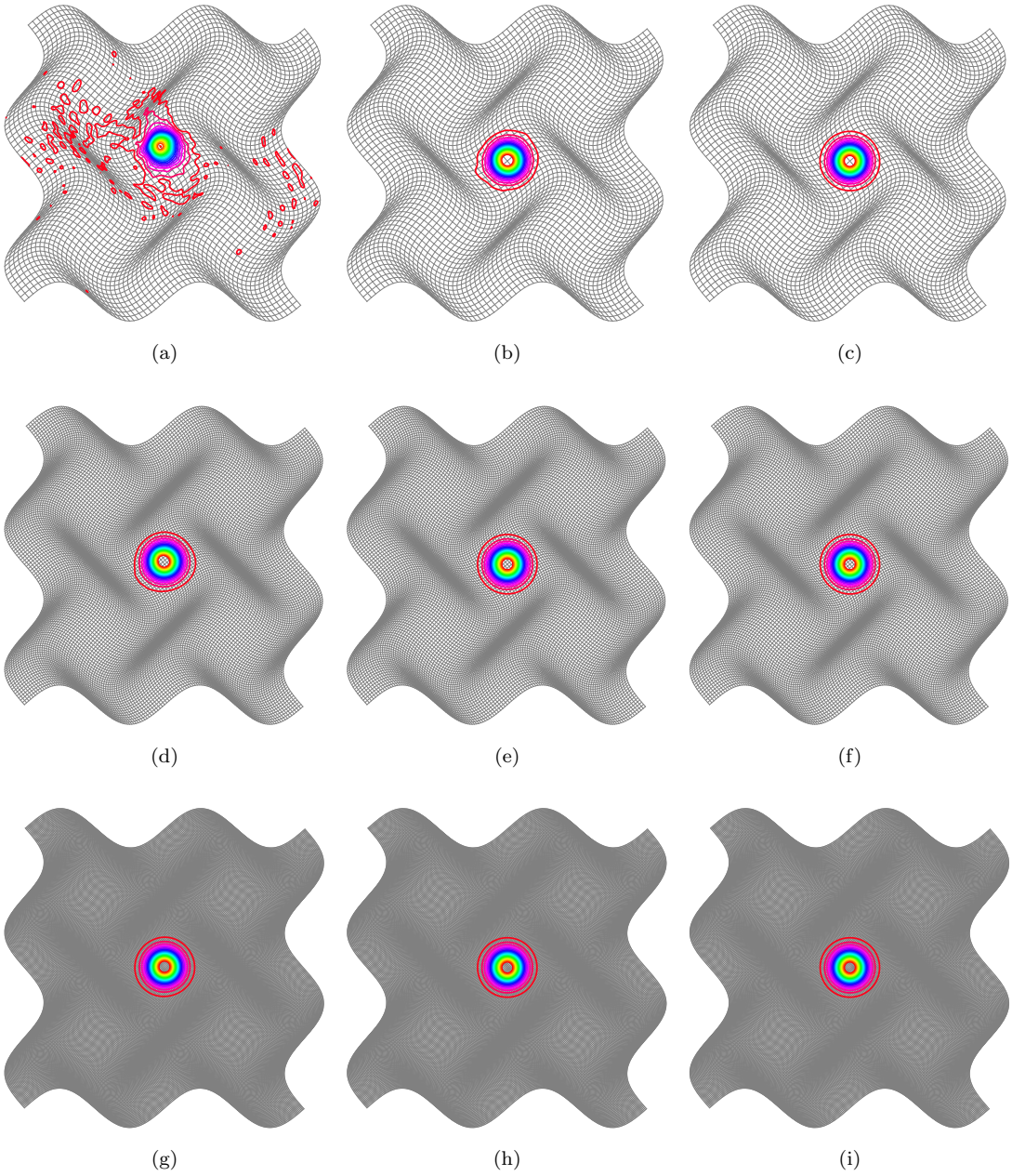

Figure 2.21: Visualization of convergence of pressure on curvilinear meshes. The sub-figures in the first row ((a), (b), and (c)) are computed on a 64^2 mesh; the sub-figures in the second row ((d), (e), and (f)) are computed on a 128^2 mesh; and the sub-figures in the third row ((g), (h), and (i)) are computed on a 256^2 mesh. The sub-figures in the first column ((a), (d), and (g)) are computed using 2nd-order schemes; the sub-figures in the second column ((b), (e), and (h)) are computed using 4th-order schemes; and the sub-figures in the third column ((c), (f), and (i)) are computed using 6th-order compact schemes.

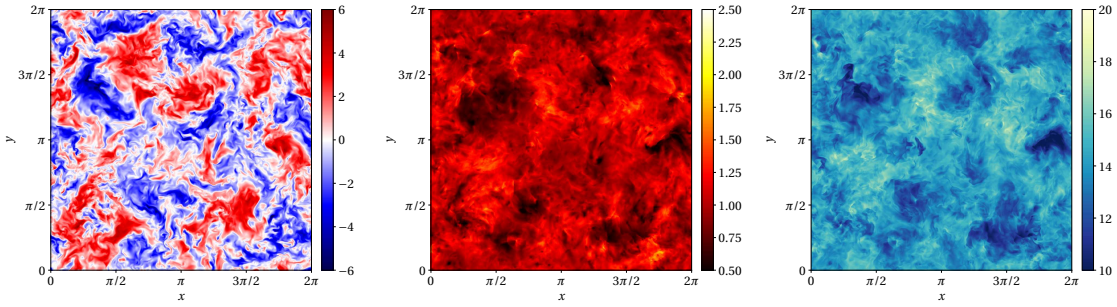

(a) (b) (c)

Figure 2.22: Visualization of flow fields: (a) z-velocity; (b) density; (c) pressure.

projected stochastic process [42] as expressed in Eq. (2.59),

$$f_i = \sum_{k_L \leq k \leq k_H} \mathcal{P}_{ij}^{\perp} \widehat{b}_j(k_m, t) e^{i k_m x_m} \tag{2.59}$$

where $k_L = 3$ and $k_H = 5$ are the cut-off wavenumbers defining a forcing band; $k = \sqrt{k_m k_m}$ is the magnitude of the wavenumber vector; $\mathcal{P}_{ij}^{\perp} = \delta_{ij} - k_i k_j / k^2$ is a solenoidal projector; and $\widehat{b}_j \in \mathbb{C}^3$ for each mode is updated using six independent Uhlenbeck-Ornstein random processes. The fluid is a calorically perfect gas with $\gamma = 1.4$. The dynamic viscosity is calculated based on a power law, $\mu = \mu_{\text{ref}}(T/T_{\text{ref}})^{0.5}$, where the subscript "ref" represents a reference state. The thermal conductivity is calculated based on the Prandtl number, $\text{Pr} = c_p \mu / \kappa$, where $c_p = \gamma R/(\gamma - 1)$ is the specific heat at a constant pressure. In this simulation, the Prandtl number remains constant at $\text{Pr} = 0.72$. The fluid is assumed to have no physical bulk viscosity.

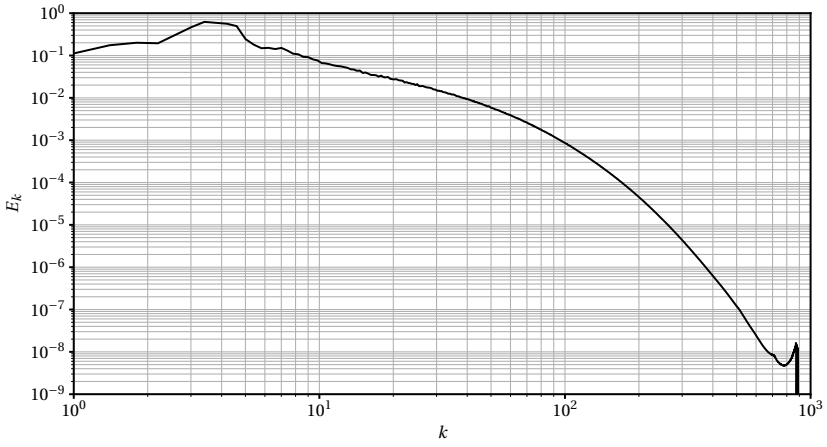

Figure 2.23: Velocity energy spectrum.

The computational mesh size is $1024 \times 1024 \times 1024$. The simulation is conducted using sixth-order compact schemes with the artificial bulk viscosity, β^*, and artificial thermal conductivity, κ^*, added to the physical bulk viscosity and thermal conductivity respectively for eddy shocklet capturing. The formulations of the β^* and κ^* are described in Ref. [76]. However, in this simulation, no solution filtering is applied. The time advancement is calculated using the standard fourth-order Runge-Kutta (RK4) method with CFL = 0.5. The simulation data over a period of seven eddy turnover times is used in post-processing after the flow has reached a statistically stationary state.

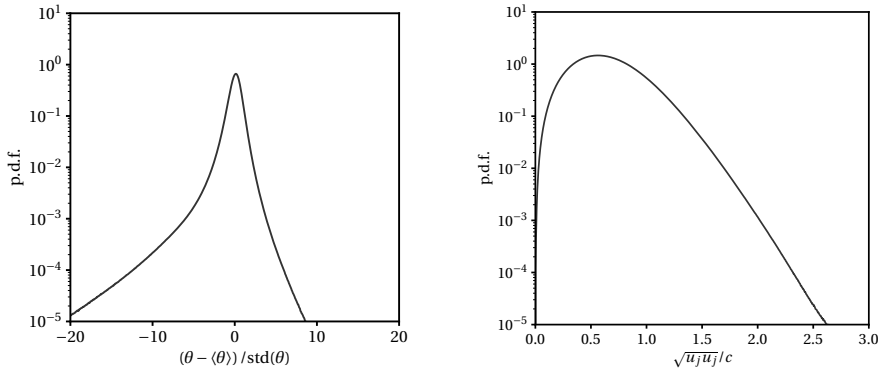

(a) (b)

Figure 2.24: Normalized probability density functions of (a) velocity dilatation and (b) local Mach number.

The visualizations of the instantaneous flow fields are shown in Fig. 2.22. The stationary isotropic turbulence is resolved in the DNS regime with $k_{\max}\eta \approx 3.2$ where $k_{\max}$ is the maximum wavenumber supported by the computational mesh, and η is known as the Kolmogorov length scale. In this case, η is calculated as $\eta = (\langle\mu\rangle^3 \langle\epsilon\rangle^{-1} \langle\rho\rangle^{-2})^{1/4}$, where the angle bracket $\langle\cdot\rangle$ denotes a volume average, and ϵ is the dissipation rate, $\epsilon = 2\mu S_{ij}S_{ij} + (\beta^* - 2\mu/3)S_{kk}^2$. The velocity energy spectrum is provided in Fig. 2.23 where E_k is defined as $E_k = \widehat{u}_j \widehat{u}_j^*/2$ in continuous Fourier space for an infinite domain. Using the discrete Fourier transform on a finite periodic domain, E_k is evaluated as $E_k = 4\pi k^2 \left\langle \widehat{u}_j \widehat{u}_j^*/2 \right\rangle_k$, where the operator $\langle(\cdot)\rangle_k$ indicates the average within a sampling bin centered at k. The distributions of velocity dilatation, $\theta = u_{j,j}$, and local Mach number, $\sqrt{u_j u_j}/c$, are shown in Fig. 2.24 where the function "std(·)" returns the standard deviation. The two-point correlations of each velocity component are also provided in Fig. 2.25 to improve confidence in the computational results, where $R_{ii} = \langle u_i(\boldsymbol{x}) u_i(\boldsymbol{x} + \boldsymbol{r})\rangle$ calculated using the discrete Fourier transform. Here, the subscript indices in the expression for R_{ii} do not follow the summation convention.

According to the post-processing, the demonstrative simulation has $\mathrm{Re}_\lambda \approx 162$ and $M_t \approx 0.7$, where Re_λ is the characteristic Reynolds number based on the Taylor microscale, λ, and M_t is known as the turbulent Mach number. For isotropic turbulence, Re_λ and M_t are calculated as $\mathrm{Re}_\lambda = u_{\mathrm{rms}}\lambda/\langle\nu\rangle$ and $M_t = \sqrt{\langle u_j u_j\rangle}/\langle c\rangle$ respectively, where u_{rms} and λ are calculated as $u_{\mathrm{rms}} =$

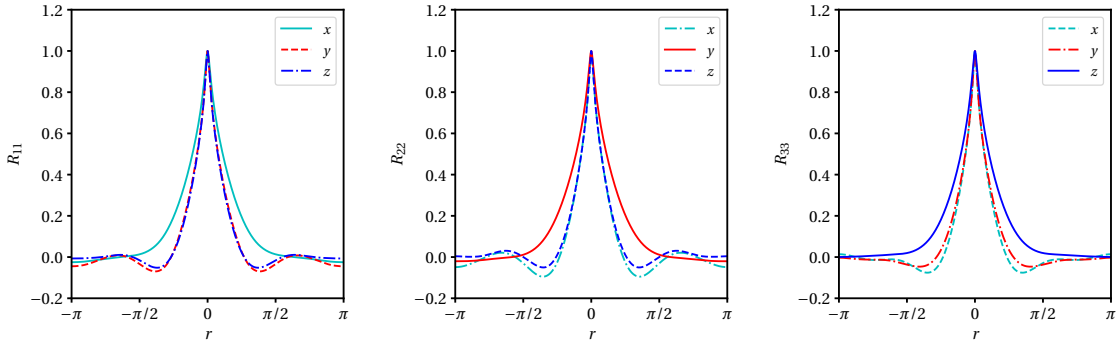

(a) (b) (c)

Figure 2.25: Velocity two-point correlation.

$\sqrt{\langle u_j u_j \rangle / 3}$ and $\lambda = \sqrt{\langle u^2 \rangle / \langle (\partial u / \partial x)^2 \rangle}$ respectively.

The value of M_t measured from this simulation indicates that the turbulence is highly compressible [88]. Figure 2.26 shows the visualization of the shocklet distribution and the relative profiles of β^* and κ^*. The shocklets are visualized using a modified Ducros sensor, defined as $-\theta|\theta| / \left[\theta^2 + \omega_j \omega_j + 10^{-32}\right]$, where $\theta = u_{j,j}$ is the velocity dilatation, and $\omega_i = \varepsilon_{ijk} u_{k,j}$ is the vorticity. With this sensor, a shock is identified since the sensor value is close to $+1$. Compared with Fig. 2.26a, the instantaneous spatial distributions of β^* and κ^* are highly localized at the eddy shocklet structures, as shown in Fig. 2.26c and Fig. 2.26b respectively, to provide sufficient numerical dissipation. With the present framework, the solution filtering, which was deemed necessary by previous works, is no longer required.

2.4.3 Two-dimensional implosion problem

This test problem is used to demonstrate the compatibility of the computational framework with nonlinear shock-capturing schemes and approximate Riemann solvers. The problem is introduced in Ref. [92], and a modified version is used in this demonstration. The problem is configured on a two-dimensional periodic domain for $(x, y) \in [-0.3, 0.3)^2$ and computed on a uniform Cartesian mesh and a curvilinear wavy mesh respectively. Both simulations are conducted using a 512×512 mesh size. The curvilinear mesh generation follows the same analytical mapping used in Sec. 2.4.1 and is described in Eq. (2.58) with $L = 0.6$ and $A = 0.05$. The initial conditions contain two homogeneous sub-regions as shown in Fig. 2.27. "Region 1" is the inner sub-region, and "region 2" is the outer sub-region. The border between the two sub-regions forms a diamond-shaped box with the four corners located at $(\pm 0.15, 0)$ and $(0, \pm 0.15)$. The flow is initially at rest, and the inner sub-region has a lower density and pressure than the outer sub-region. The changes across the sub-region boundary are sharp. The mathematical expressions of the initial density and pressure

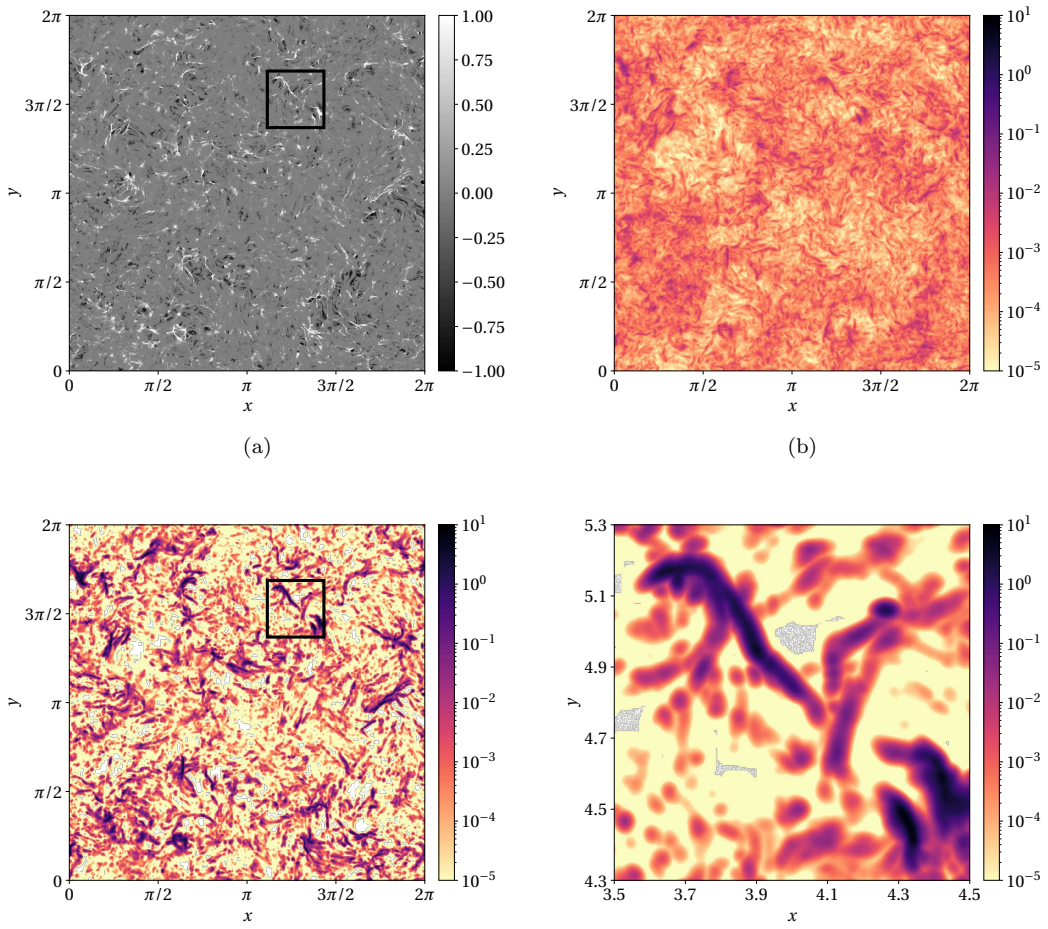

Figure 2.26: Visualization of eddy shocklets and artificial diffusivities: (a) eddy shocklets visualized by the modified Ducros sensor $-\theta|\theta|/\left[\theta^2+\omega_j\omega_j+10^{-32}\right]$; (b) distribution of $\kappa^*\mathrm{Pr}/(c_p\mu_{\mathrm{ref}})$; (c) distribution of $\beta^*/\mu_{\mathrm{ref}}$; and (d) a zoomed-in view of β/μ_{ref} corresponding to the boxed region in (a) and (c). In this simulation, $T_{\mathrm{ref}} \approx \langle T \rangle$ and $\mu_{\mathrm{ref}} \approx \langle \mu \rangle$.

are specified in Eq. (2.60):

$$[\rho, p] = \begin{cases} [0.125, 0.140] & |x| + |y| < 0.15 \\ [1.000, 1.000] & |x| + |y| \geq 0.15 \end{cases} \tag{2.60}$$

The fluid is a calorically perfect gas with $\gamma = 1.4$. The simulation is conducted without including any physical viscosity and thermal conductivity, so the Euler system is solved. In this simulation, all primitive variables at the edge-staggered points are obtained by the eight-point adaptive targeted

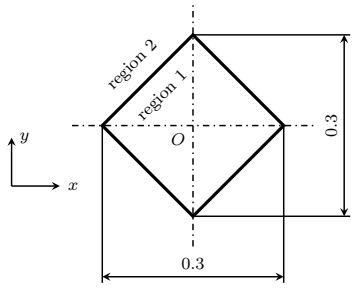

Figure 2.27: Schematic of initial condition of the two-dimensional implosion problem.

essentially non-oscillatory (TENO8-A) interpolation scheme, which is modified from the reconstruction scheme designed for the finite volume framework [48]. The Riemann flux is calculated using the Rusanov method [132]. The time advancement is conducted using SSP-RK3 method with CFL = 0.4.

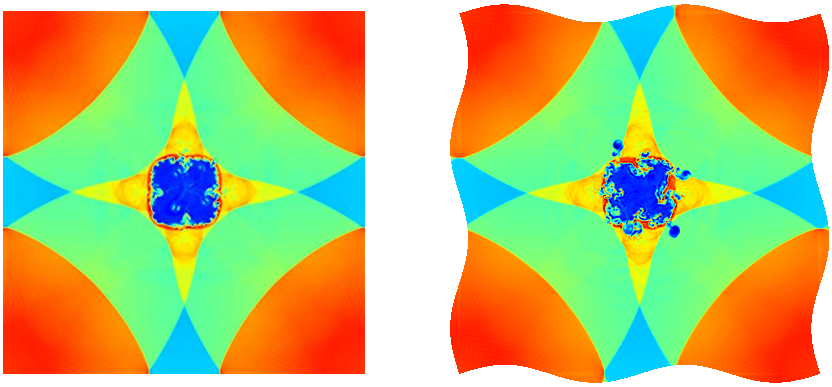

(a) (b)

Figure 2.28: Density distributions of the two-dimensional implosion problem at $t = 0.6$ computed on a (a) uniform Cartesian mesh and (b) curvilinear wavy mesh.

The density profiles of the two simulations at the final calculation time $t = 0.6$ are shown in Fig. 2.28. Comparing the solution profiles on the uniform Cartesian mesh and the curvilinear wavy mesh in Fig. 2.28a and Fig. 2.28b respectively, the large-scale wave patterns are identical. There is no significant numerical issue corresponding to the mesh deformation and periodic domain extension on the curvilinear mesh. The flow instability pattern in the central region is highly sensitive to the perturbations. In these two simulations, the difference in the numerical perturbations is primarily caused by capturing the oblique waves with different mesh deformations. This demonstration only shows a specific combination of the shock-capturing scheme and approximate Riemann solver. Different combinations of shock-capturing schemes and approximate Riemann solvers are also compatible with this computational framework.

2.4.4 LES of decaying isotropic turbulence

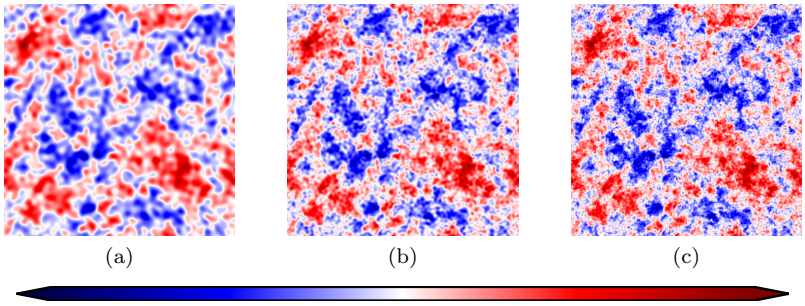

Figure 2.29: Visualizations of z-velocity fields in the x-y plane with the initial conditions: (a) mesh resolution of 64^3; (b) mesh resolution of 128^3; and (c) mesh resolution of 256^3. For the purpose of visualization, the coarse grid fields are upsampled to a fine grid via zero-padding in Fourier space. The scale of the color maps are the same for the three different cases. The color map scale is symmetric about 0.

This test problem is designed to investigate the performance of the simulation framework used in LES or other eddy-resolving simulations of turbulent flows at very high Reynolds numbers. In an LES or other eddy-resolving simulation of turbulence, when the Kolmogorov length scale is significantly smaller than the computational grid size, physical viscous dissipation may be negligible compared to the model dissipation or numerical dissipation. A high-resolution LES or high-quality eddy-resolving simulation of a turbulent flow should keep the artificial dissipation length scale sufficiently small and near the grid size in order to preserve the resolvable turbulent flow structures across a wide range of length scales. In this test problem, the flow is assumed to be inviscid ($\mathrm{Re}_\lambda \to \infty$). This can be alternatively interpreted as the viscous dissipation occurs at a vanishingly small length scale ($k_{\max}\eta \to 0$). The definitions of λ and η are consistent with those defined in Sec. 2.4.2, and $k_{\max}$ is the Nyquist wavenumber supported by the computational mesh. Therefore, no physical dissipation exists in the computational system. The simulations are configured as LES using different central schemes with an explicit SGS model and compared with eddy-resolving simulations using high-order shock-capturing schemes in combination with an approximate Riemann solver without the explicit SGS model.

The initial velocity field is solenoidal and randomly sampled in the Fourier space based on the von Kármán spectrum [166]. The expression of the von Kármán velocity spectrum is given in Eq. (2.61).

$$E_k = \frac{(A/k_s)\,(k/k_s)^4}{\left[1 + (k/k_s)^2\right]^{17/6}} \tag{2.61}$$

where given the most energetic wavenumber, k_e, k_s is calculated as $k_s = k_e\sqrt{5/12}$. In this configuration, $k_e = 3$ is used. A is an amplitude factor. The detail of the velocity generation approach for

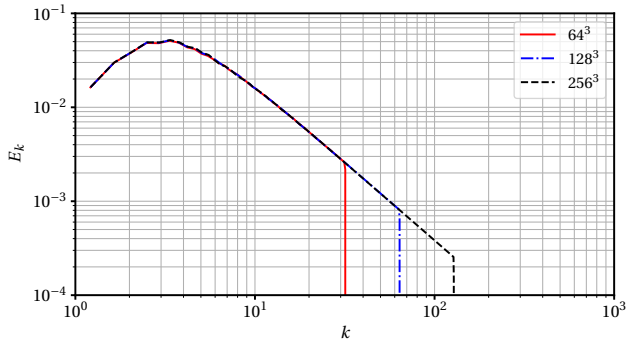

Figure 2.30: Initial velocity energy spectra of the simulations at different grid resolutions.

isotropic turbulence with a given energy spectrum is illustrated in Ref. [74]. Following this approach, the velocity is first generated on a 256^3 mesh. Then, a three-dimensional spectrally-sharp low-pass filter is applied to only keep the non-trivial modes within a spherical region for $k < 128$ in Fourier space. After filtering, the field of each velocity component is consistently re-scaled to numerically match $\langle u_j u_j \rangle = 1$. Using this velocity field as the reference, the velocity fields are further filtered using the three-dimensional spectrally-sharp low-pass filter to keep the non-trivial modes within smaller spherical regions for $k < 64$ and $k < 32$. These filtered fields are eventually downsampled to a 128^3 mesh and a 64^3 mesh respectively. As a consequence, three sets of initial velocity fields are obtained with three different grid resolutions. The cut-off wavenumbers of the low-pass filters are equal to the Nyquist wavenumbers in each dimension instead of the maximum wavenumber that can be resolved using the three-dimensional meshes. This use of spherical spectrally-sharp filtering, as opposed to Cartesian spectrally-sharp filtering, allows for maintaining good statistical isotropy in the initial conditions at every coarser grid level. Additionally, since all the velocity fields are obtained via filtering and downsampling from the same velocity profile generated on a 256^3 mesh, the discrete initial velocity fields used as the initial conditions represent the same asymptotically smooth velocity field resolved at different levels of resolution. The initial z-component velocity profiles are visualized in Fig. 2.29, and the initial velocity energy spectra are shown in Fig. 2.30. The calculation of the velocity energy spectra in this section follows the same method described in Sec. 2.4.2. The initial dimensionless density field is uniform and set to be unity as a reference. The initial dimensionless pressure is also uniform and equal to 3.5. This configuration leads to an initial turbulent Mach number of $M_t \approx 0.45$.

The LES are conducted using the 6th-order compact schemes, 4th-order explicit schemes, and 2nd-order explicit schemes respectively with the Vreman SGS model [167] in the momentum equation and a constant turbulent Prandtl number, Pr_t, model in the energy equation. For a calorically perfect gas, Pr_t is defined as $\mathrm{Pr}_t = c_p \mu_{\mathrm{SGS}} / \kappa_{\mathrm{SGS}}$, where μ_{SGS} and κ_{SGS} are the SGS eddy viscosity and thermal conductivity respectively. The Vreman SGS model requires a constant coefficient,

C_{SGS}, which is defined in A.2. In this demonstrative problem, C_{SGS} is 0.044, 0.05 and 0.07 for the simulations using the 6th-order compact schemes, 4th-order explicit schemes, and 2nd-order explicit schemes respectively and is calibrated to obtain the correct turbulent kinetic energy decay rate. The turbulent Prandtl number is 0.7 for all simulations in this sub-section. Additional eddy-resolving simulations are conducted respectively using the TENO8-A and the five-point weighted essentially non-oscillatory (WENO5-JS) interpolation schemes [73] which are modified from their reconstruction forms designed for the finite volume framework. The simulations using the dissipative shock capturing schemes (TENO8-A and WENO5-JS) do not include any explicit SGS model. The time advancement for all simulations is conducted using the SSP-RK3 method with CFL = 0.4. The stop time for all simulations is $t = 10$, which is when the turbulent kinetic energy decays by more than a factor of 15 compared to the initial condition. At the final stage, the turbulent Mach number is $M_t \approx 0.1$.

The velocity fields of all simulations are visualized in Fig. 2.31. The color map scales for all sub-figures in Fig. 2.31 are identical. The computational results are interpolated using the sinc modes [140] during post-processing for visualization purposes only. The velocity energy spectra for all the simulations are shown in Fig. 2.32. As shown by this comparison, the LES using central numerical schemes with explicit SGS model shows much higher spectral resolution than the two simulations conducted using dissipative schemes without SGS models. The SGS model dissipation starts to become dominant approximately beyond the wavenumber of $k_{\mathrm{max}}/2$. In contrast, the selected high-order (corresponding to the optimal weights [73, 48]) shock-capturing schemes impose numerical dissipation starting at a much lower wavenumber. As a result, from the flow visualizations shown in Fig. 2.31, small-scale flow features are not well resolved using shock-capturing schemes compared to the simulations using central schemes with the SGS model. In Fig. 2.32, the energy spectra of all simulations using central schemes with the explicit SGS model clearly show the inertial sub-range where the turbulent kinetic energy cascades follow the $k^{-5/3}$ law. In contrast, the energy spectra of simulations using implicit numerical dissipation without the SGS model do not show the power-law energy cascade. This indicates that the dissipation implicitly imposed by the numerical scheme is noticeably inconsistent with the scale similarity of the turbulent cascade compared to the dissipation imposed by an explicit SGS model.

The LES results based on the central schemes do not show an observable difference in the velocity fields. Compared to the simulations using 6th-order compact schemes, the simulations using 4th-order and 2nd-order schemes do not show visible deterioration. As a further investigation of the small-scale-resolving quality of simulations obtained with the three central schemes, a three-dimensional bandpass filter is applied to only keep the non-trivial model within a spherical shell for $k \in [16, 32)$ in Fourier space. The bandpass-filtered velocity fields of all the simulations on the 64^3 mesh are shown in Fig. 2.33 (from Fig. 2.33a to Fig. 2.33e), and the bandpass-filtered velocity obtained from the LES on the 256^3 mesh using the 6th-order compact schemes is also provided in

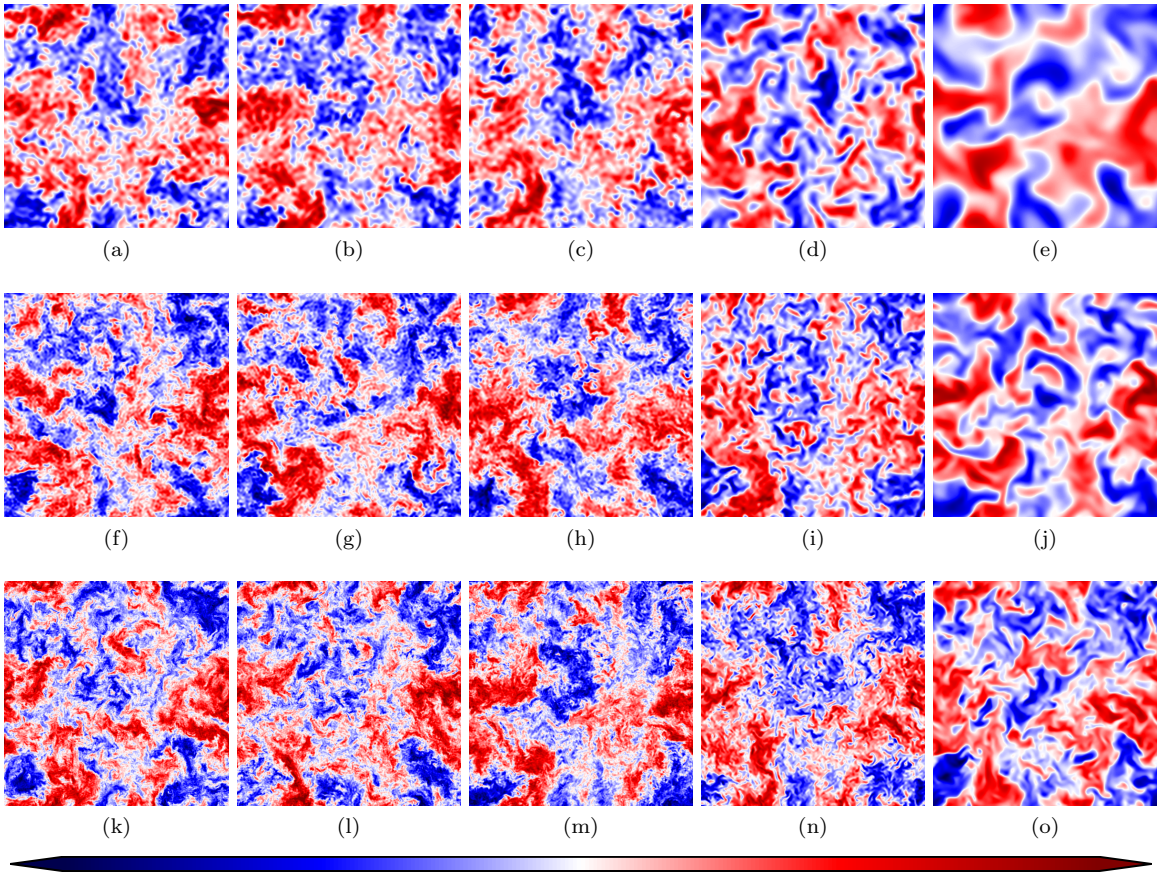

Figure 2.31: Visualizations of the final ($t = 10$) z-component velocity fields in the x-y plane. The sub-figures in the first row ((a), (b), (c), (d), and (e)) are obtained from a 64^3 mesh; the sub-figures in the second row ((f), (g), (h), (i), and (j)) are obtained from a 128^3 mesh; and the sub-figures in the third row ((k), (l), (m), (n), and (o)) are obtained from a 256^3 mesh. The sub-figures in the first column ((a), (f), and (k)) are computed using the 6th-order compact schemes; the sub-figures in the second column ((b), (g), and (l)) are computed using the 4th-order explicit schemes; the sub-figures in the third column ((c), (h), and (m)) are computed using the 2nd-order explicit schemes; the sub-figures in the fourth column ((d), (i), and (n)) are computed using the TENO8-A interpolation schemes in combination with the 6th-order compact finite difference schemes as the divergence operator; and the sub-figures in the fifth column ((e), (j), and (o)) are computed using the WENO5-JS interpolation schemes in combination with the staggered 6th-order compact finite difference schemes as the divergence operator. The data, for visualization, has been upsampled in Fourier space by zero-padding during post-processing. The scales of color maps are same for all sub-figures, and the color scale is symmetric about 0.

Fig. 2.33f for reference. All sub-figures in Fig. 2.33 are shown with same scale of the color map. The simulations based on the shock capturing schemes (Fig. 2.33d and Fig. 2.33e) have lower feature intensities in the visualized wavenumber regime, and the sizes of the visualized features are larger

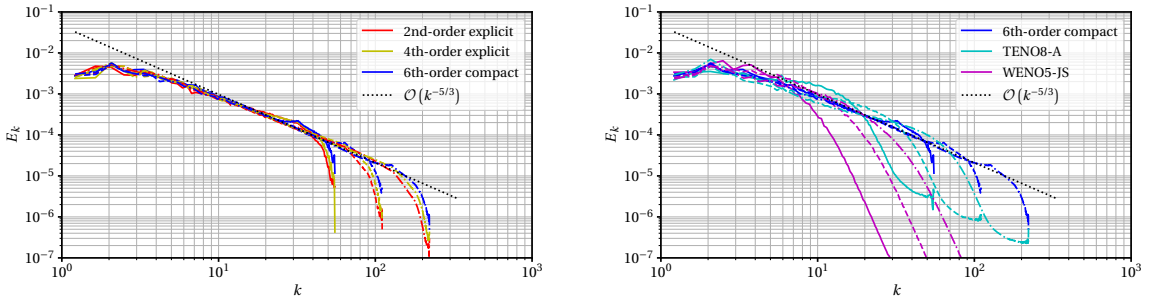

(a) (b)

Figure 2.32: Velocity energy spectra at the final simulation step ($t = 10$): (a) central schemes with Vreman SGS model; (b) nonlinear shock capturing schemes with approximate Riemann solver where the divergence operation is computed by the staggered 6th-order compact finite difference schemes. The spectra obtained from the 64^3 mesh are plotted using solid curves, the spectra obtained from the 128^3 mesh are plotted using dashed curves, and the spectra obtained from the 256^3 mesh are plotted using dot-dashed curves.

than those of the bandpass-filtered LES results and the reference field (Fig. 2.33f). However, the bandpass-filtered LES solutions (Fig. 2.33a, Fig. 2.33b, and Fig. 2.33c) are equally optimal compared to the reference profile in Fig. 2.33f. These observations are consistent with the results presented in Ref. [103].

A reasonable explanation of this observation is that the total error is not dominated by the dispersion error of the numerical schemes. As opposed to the problem of the homoentropic swirl advection illustrated in Sec. 2.4.1, the isotropic turbulence solution shows highly nonlinear behavior although both solutions are obtained by solving fully nonlinear systems. The linear solution behavior in the swirl advection problem (cf. Sec. 2.4.1) indicates that the net contributions of all the nonlinear interactions in the system are purely canceled. In contrast, the nonlinear interactions in the isotropic turbulence produce higher-wavenumber features consistent with the turbulent energy cascade. In LES, the higher-wavenumber flow features are eventually dissipated by the SGS model near the grid-size scale. When a solution has strong linear behavior, although obtained from a nonlinear system, the dispersion error will significantly affect the computational quality in terms of the flow structure preservation. On the other hand, the evolution of the LES solution of the isotropic turbulence is dominated by the nonlinear interactions of the lower-wavenumber modes, and the higher-wavenumber modes can also intrinsically tolerate more randomness. Therefore, the solution quality evaluated from the velocity energy spectra shown in Fig. 2.32a and the flow visualizations of the LES solutions in Fig. 2.31 and Fig. 2.33 essentially illustrate the aliasing error produced by the nonlinear interactions among the low-wavenumber modes. Referring to the discussion in Sec. 2.2, the numerical error of the three sets of central schemes are not as significant in the low-wavenumber

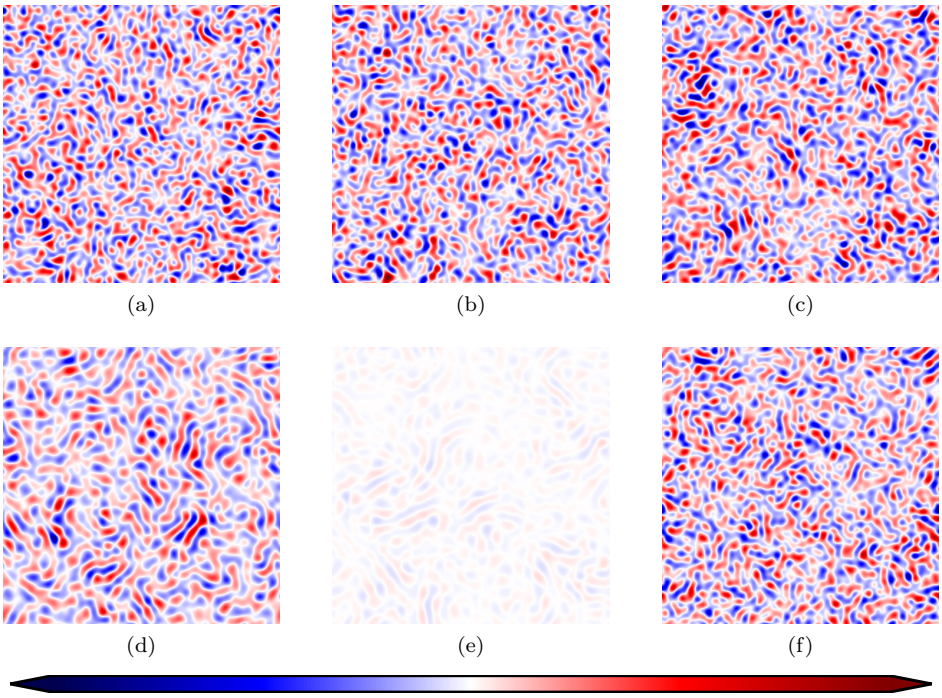

Figure 2.33: Visualizations of bandpass-filtered z-component velocity fields on an x-y plane: (a) 6th-order compact schemes; (b) 4th-order explicit schemes; (c) 2nd-order explicit schemes; (d) TENO8-A interpolation schemes in combination with the staggered 6th-order compact finite difference schemes for the divergence operation; and (e) WENO5-JS interpolation schemes in combination with the staggered 6th-order compact finite difference schemes for the divergence operation. The sub-figures from (a) to (e) are computed from a 64^3 mesh. (f) is used for reference which is computed using the 6th-order compact schemes from a 256^3 mesh. The velocity profiles shown in all the sub-figures are sampled within a spherical shell for $k \in [16, 32)$ in Fourier space. For visualization only, the data has been upsampled in Fourier space by zero-padding. The color map scale of all the sub-figures are identical and symmetric about 0.

regime as they are in the high-wavenumber regime. Additionally, the transfer functions of the interpolation schemes of the lower-order schemes are even more favorable to dealiasing in the nonlinear fluxes assembly by more aggressively reducing high-wavenumber mode amplitudes. Consequently, for LES of decaying isotropic turbulence, the 2nd-order explicit schemes, 4th-order explicit schemes, and 6th-order compact schemes present equally high-quality solutions in the velocity fields.

Besides the velocity field, the pressure field is also investigated. The configuration of the initial condition generates significant transients in the flow, and they remain as acoustic waves in this inviscid (asymptotically high-Reynolds-number) turbulence as it decays at the resolved scale. At the final stage ($t = 10$), the visualizations of the pressure field from all simulations are shown in Fig. 2.34 with same color map scale. For each scheme, more detailed wave structures are resolved as the grid resolution increases. Comparing different schemes, higher-order schemes provide sharper and

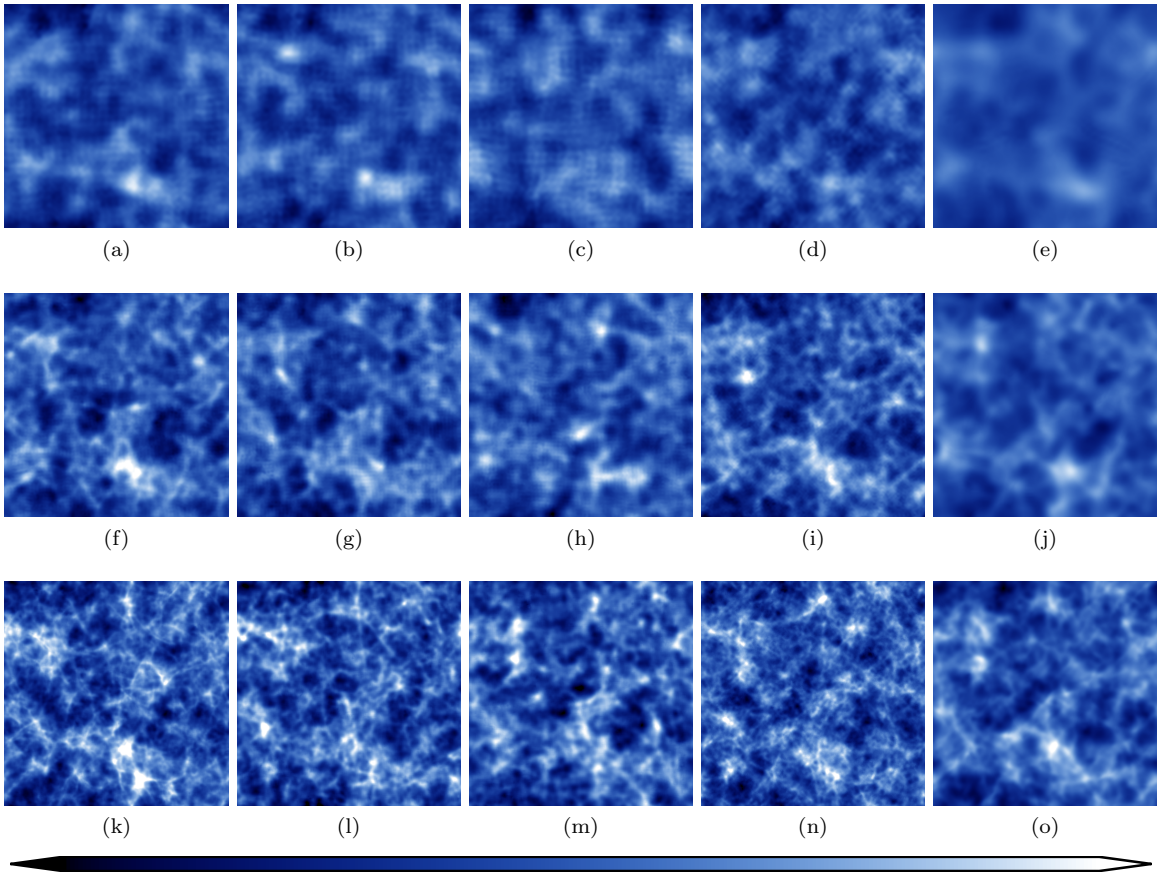

Figure 2.34: Visualizations of the final ($t = 10$) pressure fields in the x-y plane. The color map scales are same for all sub-figures. See caption in Fig. 2.31 for details of each sub-figure.

clearer coherent wave structures at the same grid resolution, and they show more rapid enhancement in resolving detailed wave features associated with grid refinement. Unlike the velocity field, the simulations with the TENO8-A scheme and without an explicit SGS model provide significantly improved spectral performance in resolving transient pressure waves. To quantify the numerical performance, the pressure field is decomposed as follows.

$$p = p^{\mathrm{sol}} + p^{\mathrm{dil}} + \langle p \rangle \tag{2.62}$$

where p^{sol} and p^{dil} are the solenoidal and dilatational components respectively, and $\langle p \rangle$ is the mean component. For the low-Mach number regime, the solenoidal pressure is estimated by solving the Poisson equation [72].

$$-\frac{\partial^2 p^{\mathrm{sol}}}{\partial x_j \partial x_j} \approx \langle \rho \rangle \frac{\partial u_i^{\mathrm{sol}}}{\partial x_j} \frac{\partial u_j^{\mathrm{sol}}}{\partial x_i} \tag{2.63}$$

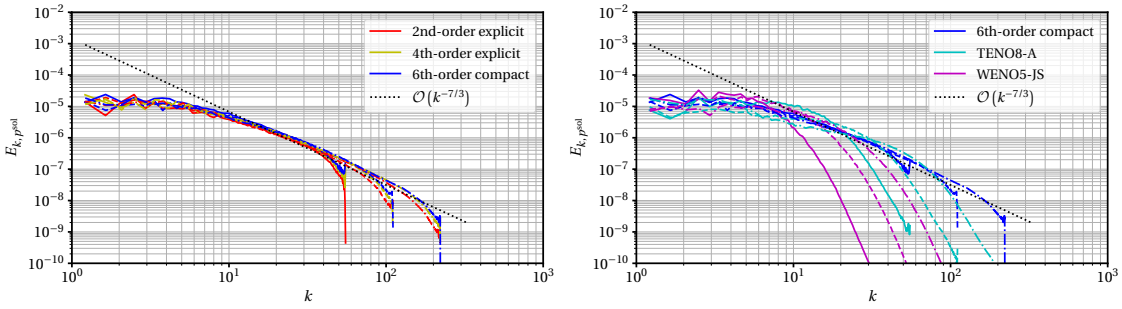

(a) (b)

Figure 2.35: Energy spectra of solenoidal pressure at final step ($t = 10$): (a) central schemes with Vreman SGS model and (b) nonlinear shock-capturing schemes with an approximate Riemann solver where the divergence operation is computed by the staggered 6th-order compact finite difference schemes. The line styles are same as those used in Fig. 2.32.

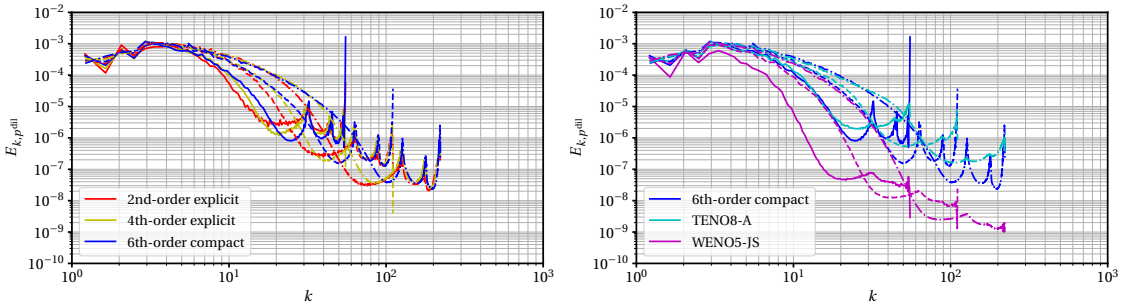

(a) (b)

Figure 2.36: Energy spectra of dilatational pressure at the final step ($t = 10$): (a) central schemes with the Vreman SGS model and (b) nonlinear shock-capturing schemes with an approximated Riemann solver where the divergence operation is computed by the staggered 6th-order compact finite difference schemes. The line styles are same as those used in Fig. 2.32.

where u_i^{sol} is the solenoidal component of the velocity field. In this work, the solenoidal projection is conducted in Fourier space using $\widehat{u}_i(k_m)$, the three-dimensional discrete Fourier transform of u_i with respect to each wavenumber vector k_m.

$$u_i^{\text{sol}} = \sum_{k_m \neq 0} \mathcal{P}_{ij}^{\perp} \widehat{u}_j(k_m) e^{ik_m x_m} \tag{2.64}$$

where $\mathcal{P}_{ij}^{\perp}$ is the solenoidal projector defined in Sec. 2.4.2. With the solenoidal pressure solved, the dilatational pressure is calculated from Eq. (2.62). The energy spectra of the solenoidal and dilatational pressure from all simulations are shown in Fig. 2.35 and Fig. 2.36 respectively. At a

low turbulent Mach number, the solenoidal pressure is a reflection of the velocity field. Similar trends are observed by comparing the energy spectra of the velocity in Fig. 2.32 and solenoidal pressure in Fig. 2.36. The solenoidal pressure spectra of all the simulations using central schemes with an explicit SGS model exhibit clear inertial sub-ranges up to near-Nyquist wavenumbers, and at the same grid resolution, no large differences are observed as shown in Fig. 2.35a. The spectra of solenoidal pressure obtained from shock-capturing-scheme-based simulations indicate overly dissipative velocity fields and do not clearly resolve the turbulent cascade features, as shown in Fig. 2.35b, due to the inconsistent numerical dissipation behavior between the nonlinear numerical dissipation and physically expected SGS dissipation. On the other hand, the dilatational pressure energy spectra, shown in Fig. 2.36, convey different evaluation perspectives compared to the velocity and solenoidal pressure spectra. Since the transient acoustic waves have relatively sharp wave fronts and are strongly coherent at large scales, the simulation results are sensitive to the dispersion error and the spectral resolution. Comparing the simulations conducted with central schemes, in Fig. 2.36a, simulations using higher-order schemes resolve more acoustic energy in the moderate wavenumber regime. In Fig. 2.36b, the simulations conducted with the TENO8-A scheme resolve even more transient acoustic energy compared to the simulations using sixth-order compact schemes that primarily benefit from higher-order convergence in the moderate wavenumber regime.

2.4.5 LES of flow over a cylinder

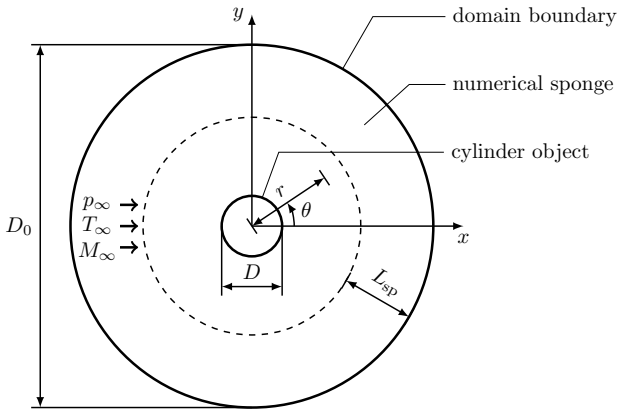

Figure 2.37: Schematic of configuration of LES of flow over a cylinder. The configuration is homogeneous in the z-direction (not shown in the schematic).

This set of problems is selected to demonstrate the numerical performance in applications of LES using curvilinear meshes. The problems are defined in a three-dimensional domain where the z-direction is periodic with length L_z. The schematic of the problem configuration in the x-y cross-section is shown in Fig. 2.37. The cylinder object with a diameter D is placed at the origin, and the wall of the cylinder defines the inner boundary of the physical domain. The outer boundary of

the domain is concentric with the cylinder object, and its diameter is D_0. The freestream in the far-field is imposed and preserved by a numerical sponge layer [96]. The thickness of the sponge layer is denoted as L_{sp}. For a quality setup, $(D_0 - 2L_{\text{sp}})/D \gg 1$ must be satisfied. The freestream flow is aligned with the x-direction and specified by the pressure (p_∞), temperature (T_∞), and Mach number (M_∞). M_∞ is defined as the ratio of the flow speed to the speed of sound at the freestream conditions. For a calorically perfect gas, expressed in terms of the specified quantities, the freestream speed is $u_\infty = M_\infty\sqrt{\gamma R T_\infty}$. The characteristic Reynolds number is defined as $\text{Re}_D = \rho_\infty u_\infty D/\mu_\infty$, where ρ_∞ is the freestream density calculated by the EOS of a calorically perfect gas. In this set of problems, the specific gas constant and the ratio of specific heats are $R = 1$ and $\gamma = 1.4$ respectively. The local dynamic viscosity is evaluated as $\breve{\mu} = \mu_\infty \left(T/T_\infty\right)^{0.76}$. The Prandtl number is assumed to be constant at $\text{Pr} = 0.7$. The definition of Pr is the same as that in Sec. 2.4.2 which is used to determine the local physical thermal conductivity. The Vreman SGS model [167] is applied with $C_{\text{SGS}} = 0.06$, and a constant turbulent Prandtl number, $\text{Pr}_t = 1$, is used for all the simulations in this sub-section, where the definition of Pr_t is the same as that used in Sec. 2.4.4. The compact numerical schemes along the non-periodic dimension where physical boundary conditions are imposed are discussed in A.4, and the detailed SGS treatment is provided in A.2.

Label	M_∞	Re_D	Mesh Size	L_z/D	D_0/D	L_{sp}/D	CFL	ϕ^*_{T}	ϕ^*_{A}
Case I	0.25	3900	$256 \times 128 \times 128$	2π	200	50	0.98	-	-
Case II	0.25	3900	$512 \times 256 \times 128$	2π	200	50	0.98	-	-
Case III	0.25	3900	$512 \times 512 \times 128$	2π	200	50	0.98	-	-
Case IV	0.80	1.66×10^5	$512 \times 512 \times 128$	2π	200	60	0.60	0.45	0.05
Case V	0.80	1.66×10^5	$768 \times 768 \times 128$	2π	200	60	0.60	0.38	0.07
Case VI	0.80	1.66×10^5	$1024 \times 1024 \times 384$	2π	200	60	0.60	0.35	0.05
Case VII	0.80	1.66×10^5	$1024 \times 1024 \times 384$	2π	200	60	0.60	0.35	0

Table 2.2: Specifications of simulations in Sec. 2.4.5: Cases I, II and III use central fluxes only; Cases IV, V, VI, and VII use central-Riemann hybrid fluxes, where a sharp switching, indicated by the threshold values of a turbulence-based shock sensor, ϕ^*_{T}, and an acoustics-based shock sensor, ϕ^*_{A}, is applied.

A nearly incompressible flow and a transonic flow are simulated as demonstrations. The freestream Mach numbers for the two flow conditions are $M_\infty = 0.25$ and $M_\infty = 0.8$ respectively. The Reynolds numbers are $\text{Re}_D = 3900$ and $\text{Re}_D = 1.66 \times 10^5$ respectively for the low-Mach flow and transonic flow respectively. Both flow conditions have been investigated in prior studies [84, 113, 106]. For the low-Mach flow condition, the simulation only uses central fluxes, and for the transonic flow condition, the simulation uses hybrid central-Riemann fluxes. The central fluxes are calculated using the sixth-order compact schemes, and the Riemann fluxes are assembled in Rusanov form [132] with the WENO5-JS interpolation scheme [73]. The hybridization is sharply switched, so the fluxes are either fully central or Riemann-type. The switching is indicated by two shock sensors evaluated based on the turbulent and acoustic flow features respectively. The values

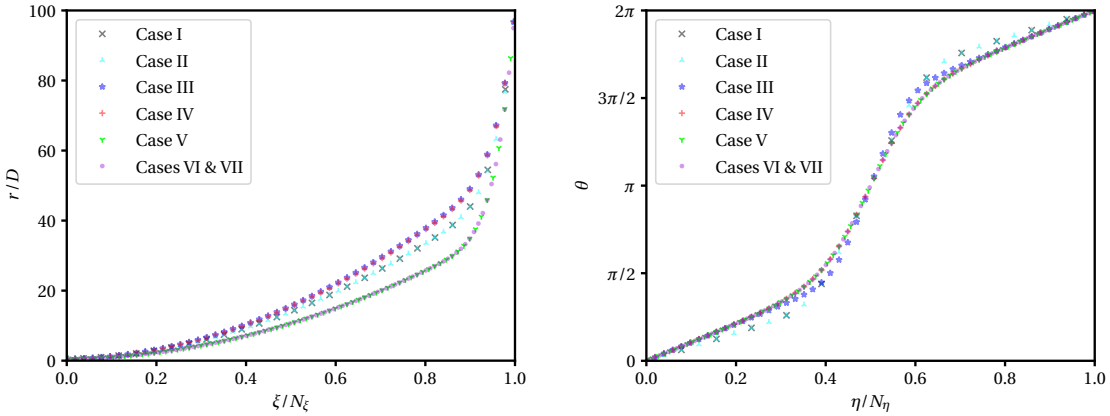

(a) (b)

Figure 2.38: Curvilinear mesh mapping in the x-y plane: (a) mapping of the radial coordinate; (b) mapping of the azimuthal coordinate. Symbols shown in the sub-figures are plotted every ten grid points.

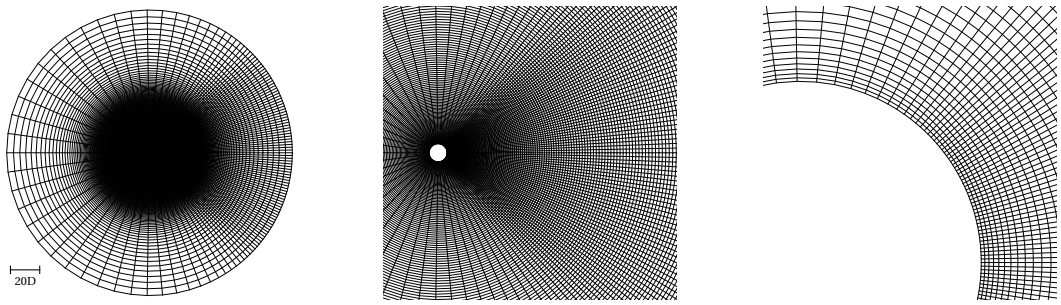

(a) (b) (c)

Figure 2.39: Visualization of the computational mesh in an x-y cross-section used for Case I: (a) full view; (b) detailed view in the wake region; (c) detailed view in the near-wall region. The mesh spacing in z-direction is uniform.

of the turbulence-based shock sensor and the acoustics-based shock sensor are denoted as ϕ_{T} and ϕ_{A} respectively. In this work, the range of the sensor values are $\phi_{\mathrm{T}} \in (-1, 1)$ and $\phi_{\mathrm{A}} \in (-1, 1)$ where a higher value indicates a stronger local compression. The Riemann flux will be used if both sensor values are greater than their threshold values, $\phi_{\mathrm{T}} > \phi_{\mathrm{T}}^*$ and $\phi_{\mathrm{A}} > \phi_{\mathrm{A}}^*$ where the superscript, "$*$", denotes the corresponding threshold value. The shock sensors are evaluated at each edge-staggered location. The details of central-Riemann flux hybridization are discussed in the following context in this section. Three simulations for the low-Mach flow condition (Cases I, II, and III) and three for the transonic flow condition (Cases IV, V, and VI) were conducted to assess grid sensitivity, and one additional simulation under the same transonic flow condition (Case VII) was conducted to further investigate the effects of shock sensors. The detailed setup for each simulation is listed in Tab. 2.2.

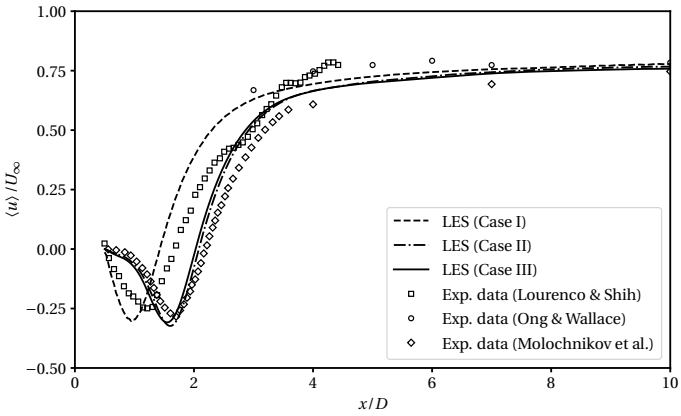

Figure 2.40: Streamwise velocity profiles along the centerline in the cylinder wake in the low-Mach flow: the experimental data are from Lourenco and Shih [93], Ong and Wallace [113], and Molochnikov et al. [105], measured using PIV, HWA, and SIV respectively.

The computational mesh is of the "O-" type with orthogonality preserved in physical space. In order to keep the consistency of the right-hand coordinate system in both the reference domain and the physical domain, the mapping from the reference domain to the physical domain is of the form $\xi \mapsto r$, $\eta \mapsto \theta$, and $\zeta \mapsto z$, where r and θ are the radial distance and the azimuthal angle respectively as marked in Fig. 2.37. The grid spacing is uniform in z-direction. The detailed mapping for each case listed in Tab. 2.2 is plotted in Fig. 2.39. Along the radial direction, the mesh is refined near the cylinder object to resolve the laminar boundary layer and coarsened in the far-field region to save the grid resolution while maintaining a sufficiently large domain. In the azimuthal direction, more grid points are distributed on the wake side to enhance the mesh resolution in region of interest. The computational mesh used for Case I is shown in Fig. 2.39 as an illustration. The near-wall mesh pattern shown in Fig. 2.39c implies that the acoustic CFL condition is limited by the wall-normal mesh refinement, and the azimuthal grid refinement does not cause a more restrictive constraint on the time advancement process.

For the low-Mach conditions, the mean streamwise velocity profile along the centerline in the cylinder wake region for each simulation (Cases I, II, and III) is shown in Fig. 2.40, and the simulation results are compared with the experimental data [93, 113, 105]. The experimental data from Lourenco & Shin (1994) [93] are collected using the method of particle image velocimetry (PIV), the data from Ong & Wallace (1996) [113] are measured using hot wire anemometry (HWA), and the data from Molochnikov et al. (2019) [105] are obtained using the smoke image velocimetry (SIV) technique. The operator $\langle(\cdot)\rangle$ in this section denotes the temporal averaging and spatial averaging in the z-direction. Temporal averaging is performed at every time-step once a statistically stationary state devoid of any initial transients has been reached. With successive mesh refinement from Case I to Case III, the streamwise velocity profiles asymptotically converge. In the near wake region, $x/D < 3$, the converged profile is closer to the experimental data from Molochnikov et al. (2019) [105]. It is also argued by Kravchenko & Moin (2000) [84] that an early transition in the shear layers possibly occurs in the measurement conducted by Lourenco & Shin (1994) [93].

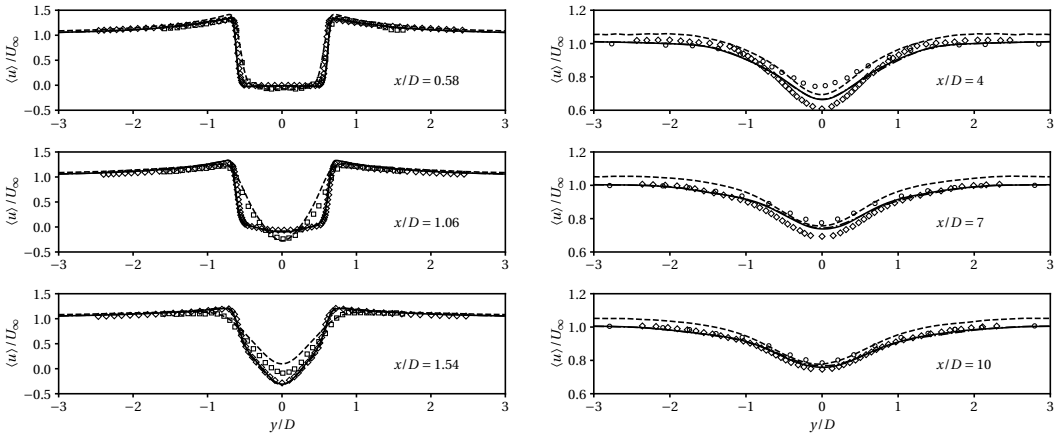

Figure 2.41: Streamwise velocity profiles at different locations in the cylinder wake in the low-Mach flow: (a) velocity profiles at near-wake locations; (b) velocity profiles at far-wake locations. The symbols of the experimental data points are identical to those in Fig. 2.40.

The averaged streamwise velocity profiles along the transverse direction at different locations in the cylinder wake are shown in Fig. 2.41. In the near-wake region, as shown in Fig. 2.41a, the velocity profiles from all three cases well match the experimental measurements at $x/D = 0.58$. However, at $x/D = 1.06$ and $x/D = 1.54$, the experimental data from Lourenco & Shih (1994) [93] and Molochnikov et al. (2019) [105] have obvious discrepancies. The LES results from the coarsest mesh (Case I) most closely match the measured profiles in Lourenco & Shih (1994) [93], and the results from the refined meshes (Cases II and III) converge to the measured profiles in Molochnikov et al. (2019) [105]. In the far-wake region, as shown in Fig. 2.41b, the discrepancy between the two experimental measurements reduces as x/D increases, and the converged LES results agree well

with the experimental data.

The profiles of velocity variance related to the streamwise and transverse velocity components along the transverse direction at different cylinder wake locations are shown in Fig. 2.42. The LES results are compared with the experimental measurements. Defining the fluctuating component $u_i' = u_i - \langle u_i \rangle$, the velocity variance is calculated as $\langle u_i' u_j' \rangle = \langle u_i u_j \rangle - \langle u_i \rangle \langle u_j \rangle$ assuming fully-converged statistics. For all three variances, $\langle u'u' \rangle$, $\langle u'v' \rangle$, and $\langle v'v' \rangle$, the converged simulation data qualitatively agree with the experimental data. For the autovariances, $\langle u'u' \rangle$ and $\langle v'v' \rangle$, the simulation on the coarsest mesh gives an overestimation. The converged LES profiles still slightly overestimate the experimental data at $x/D = 4$, but the profiles match well at other wake locations. For the covariance, $\langle u'v' \rangle$, a slight discrepancy between the LES and experimental data can be observed at $x/D = 4$, but all three LES profiles agree well with the experimental measurements at $x/D = 7$ and $x/D = 10$.

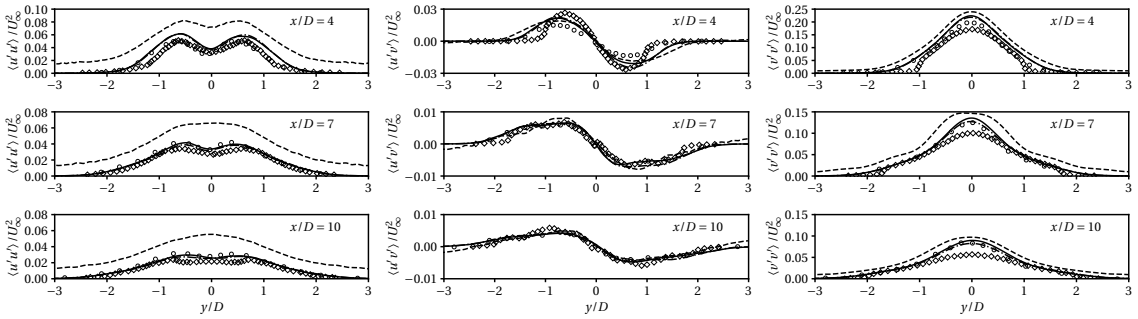

Figure 2.42: Velocity variance profiles at different cylinder wake locations in the low-Mach flow: (a) $\langle u'u' \rangle$ profiles; (b) $\langle u'v' \rangle$ profiles; (c) $\langle v'v' \rangle$ profiles. The symbols of the experimental data points are identical to those in Fig. 2.40.

The simulations with the transonic freestream conditions, used as a demonstration, involve comprehensive use of the capabilities developed in this framework including the curvilinear mesh with periodic and non-periodic boundary conditions, SGS models, and central-Riemann flux-hybridization. Representative flow visualizations from Case VI are shown in Fig. 2.43. Fig. 2.43a shows the numerical Schlieren imaging at a cross-section in z-direction. The numerical Schlieren imaging primarily reveals the turbulent wake flow structures associated with vortex shedding, a spatially and temporally growing Kevin-Helmholtz instability at the edge of the near-wake region leading to transition to turbulence, and shock waves. The flow contains two strong normal shocks interacting with the edge of turbulent wake and two weak oblique shocks attached to the laminar boundary layer at the cylinder surface as observed from prior experimental and numerical studies [162, 97]. In addition, the simulation also captures the eddy shocklets in the near wake region as well as the periodic formation of normal shocks between the neighbouring shedding vortices caused by the counter-rotating

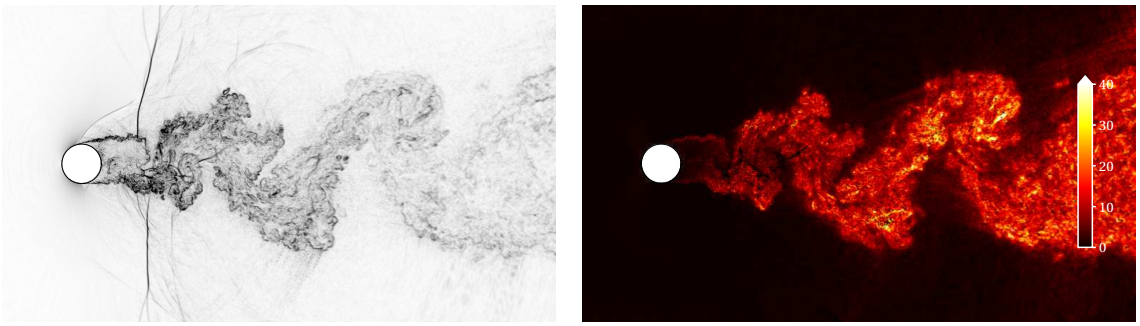

(a) (b)

Figure 2.43: Visualizations of the LES of transonic flow over a cylinder (Case VI) at the same physical time: (a) numerical Schlieren imaging, $|\nabla\rho|$; (b) ratio of the SGS viscosity to the physically computable viscosity, $\mu_{\mathrm{SGS}}/\check{\mu}$ (cf. A.2).

flow motion. The ratio of the SGS viscosity to the physically computable viscosity is visualized in Fig. 2.43b. Using an SGS viscosity model, this ratio of the viscosities also indicates the ratio of the dissipation imposed by the SGS model to the resolved viscous dissipation in the LES. As shown in Fig. 2.43b, in comparison with the numerical Schlieren imaging, the SGS viscosity rapidly vanishes away from the turbulent flow structures. Near the cylinder wall, the SGS viscosity is nearly zero, and the near-wall flow is well-resolved. Farther away from the cylinder, SGS dissipation becomes dominant in resolving the turbulent structures mainly because of the mesh coarsening. For the shock-turbulence interactions, to avoid the overly dissipative numerical behavior due to the activation of the shock-capturing treatment as well as the SGS model [6], the SGS model is enforced to be zero locally where the shock-capturing scheme is active.

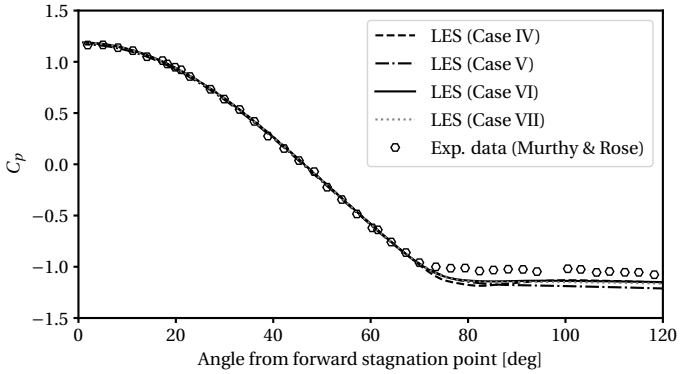

Figure 2.44: Profile of the pressure coefficient, $C_p = (p - p_\infty) \,/\, \left(\rho U_\infty^2/2\right)$, on the cylinder surface in the transonic flow. The experimental data are from Murthy and Rose [106] and measured at the static surface pressure ports through a scanning valve device.

The pressure coefficient profiles at the cylinder surface for the simulations of the transonic

freestream condition (Cases IV, V, VI, and VII) are shown in Fig. 2.44. The simulation results are compared with the experimental data [106] which are collected at the surface pressure ports placed near the midspan locations through a scanning valve device. All four LES profiles show quantitative agreement in the region where the angle from the forward stagnation point is less than 70°. Additionally, the boundary layer separation points indicated by the pressure coefficient profiles consistently match between the LES and experimental data. Some discrepancies exist in the back pressure between the LES results and the experimental measurements, and the simulation results with mesh refinement in the near-wake region (Cases V and VI) show a non-monotonic convergence in the back pressure calculation compared to that of the coarsest mesh (Case IV). The use of the acoustics-based shock sensor is insensitive to the calculation of the mean pressure coefficient for Cases VI and VII.

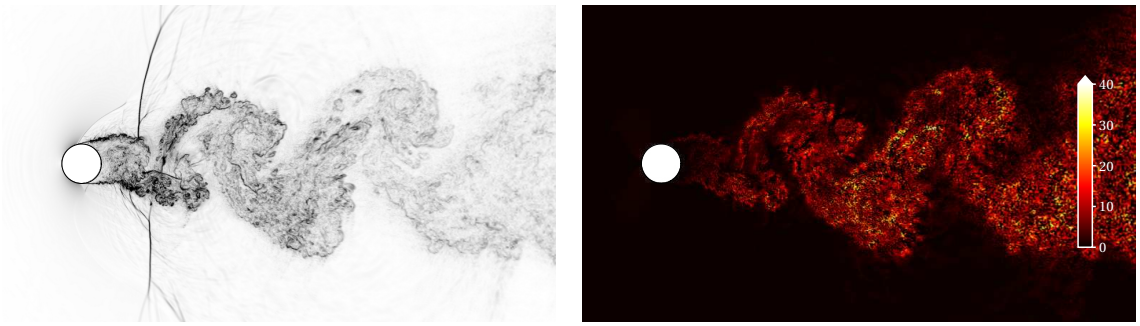

(a) (b)

Figure 2.45: Visualizations of the LES of transonic flow over a cylinder (Case VII) at the same physical time: (a) numerical Schlieren imaging, $|\nabla\rho|$; (b) ratio of the SGS viscosity to the physically computable viscosity, $\mu_{\mathrm{SGS}}/\check{\mu}$ (cf. A.2).

The hybridization of central and Riemann fluxes is jointly controlled by a turbulence-based shock sensor and an acoustics-based shock sensor. The Riemann fluxes will be selected only when both shock sensor values are greater than their corresponding threshold values as listed in Tab. 2.2. In this work, the modified Ducros sensor (cf. Sec. 2.4.2) is used as the turbulence-based shock sensor, ϕ_{T}.

$$\phi_{\mathrm{T}} = \frac{-\theta|\theta|}{\theta^2 + \omega_j\omega_j + \epsilon^2} \tag{2.65}$$

where θ is the velocity dilatation, ω_j is the vorticity vector, and $\epsilon = 10^{-16}$ is applied for numerical regularization. The acoustics-based shock sensor is given as

$$\phi_{\mathrm{A}} = -\tanh\left(2\theta\Delta/c\right) \tag{2.66}$$

where c is the local speed of sound, and Δ is a characteristic length scale representing the local grid size. In this work, $\Delta = \sqrt[3]{J}$ is used where J is the Jacobian of the metric tensor (cf. Sec. 2.3.3) defined

in Eq. (2.39). The modified Ducros sensor in Eq. (2.65) detects the shock based on the velocity dilatation strength relative to the enstrophy. This sensor is particularly sensitive to the turbulent flow structures and will deactivate the use of Riemann fluxes in the turbulent region. However, when the enstrophy is relatively low as in the laminar flow region or the edge of the turbulent flow region, the modified Ducros sensor is less sensitive due to the lack of reference enstrophy and may mis-identify weak compression waves as shocks. The acoustics-based sensor will then play a dominant role in such regions. In the definition of the acoustics-based sensor, in Eq. (2.66), the dimensionless quantity, $\theta\Delta/c$, represents a "grid Mach number." For a strong compression wave, including a shock wave, the grid Mach number quantifies the difficulty in numerically resolving the wave with the resolution supported by the computational mesh. According to the acoustics-based sensor, if a compression wave is too strong to be well-resolved by the computational mesh, the shock-capturing method should be enabled. The combination of the turbulence-based and acoustics-based shock sensors will more effectively suppress the unnecessary utilization of the shock-capturing method to avoid overly dissipative simulation results.

The simulation results from Cases VI and VII are used to compare the effects of the flux hybridization. The simulation of Case VII uses a flow state computed with Case VI as its initial conditions where all transients are flushed out of the domain of interest. The simulation results are visualized in Fig. 2.45 after approximately another 33 convective time units, i.e., $tU_\infty/D \approx 33$. The visualizations in Fig. 2.43, for Case VI, and Fig. 2.45, for Case VII, are at the same physical time for comparison. The large-scale flow structures in the two cases are identical. Setting the acoustics-based shock sensor threshold to $\phi^*_{\mathrm{A}} = 0$ (Case VII) yields the strategy described in Ref. [76], where the activation of a shock-capturing method is fully controlled by the modified Ducros sensor in the compression region. In contrast, $\phi^*_{\mathrm{A}} > 0$ (Case VI) additionally enforces the central flux to be applied if the compression motion is relatively weak in both turbulent and laminar regions. Comparing the visualizations shown in Fig. 2.43 and Fig. 2.45, more small-scale wave structures in the laminar flow regions can be resolved in Case VI where $\phi^*_{\mathrm{A}} > 0$. Furthermore, the relative SGS viscosity in the turbulent wake region is larger in Case VI compared to that in Case VII.

The behavior of the shock sensors and flux hybridization status for Cases VI and VII are visualized in Fig. 2.46. The turbulence-based shock sensor in both cases is capable of identifying the shock structures and can effectively suppress the use of Riemann fluxes in the turbulent wake region. However, near the forward stagnation point where the flow is laminar and shock-free, the turbulence-based shock sensor mis-identifies the shock structure in both cases due to the small vorticity magnitude compared to the compression motion characterized by negative dilatation. In addition, in the wake region at the edges of the turbulent shedding vortices and the region farther away, the acoustic waves are also mis-identified as shocks by the turbulence-based shock sensor. The acoustics-based sensor in both cases highlights the shock structures and successfully recognizes the weak compression near the forward stagnation point and the acoustic waves that can be well-resolved

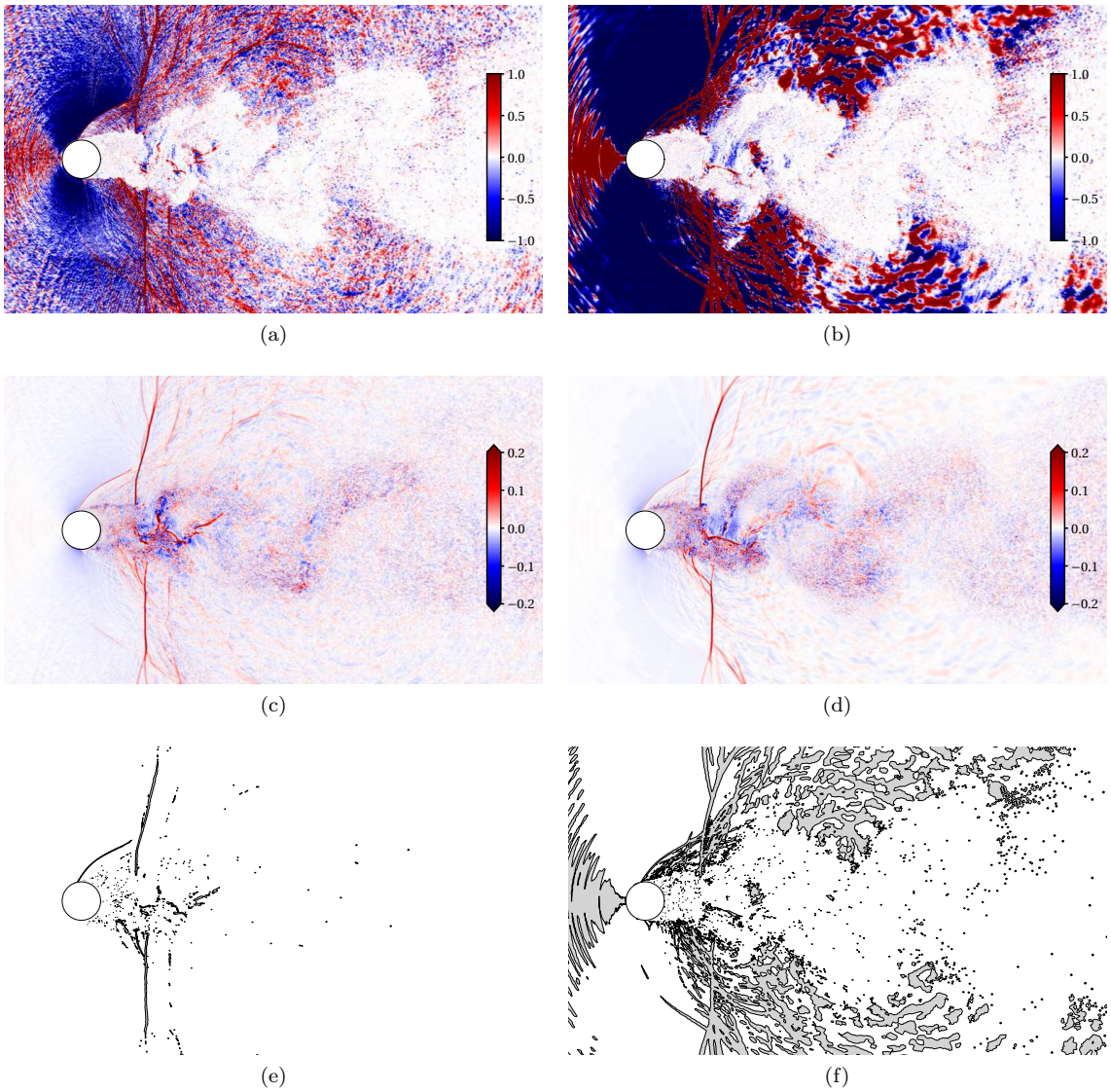

Figure 2.46: Visualizations of shock sensors and central-Riemann flux hybridization in LES of transonic flow over a cylinder in Cases VI and VII: (a) and (b) are visualizations of the turbulence-based shock sensor values; (c) and (d) are visualizations of the acoustics-based shock sensor values; and in (e) and (f), the Riemann fluxes are used in the dark regions, and the central fluxes are used in the bright regions. The sub-figures in the left column, (a), (c), and (e), are from Case VI, and the sub-figures in the right column, (b), (d), and (f), are from Case VII. The simulations of Cases VI and VII start from the same initial conditions, and the visualizations are at the same computational time.

with the local mesh resolution. The simulation of Case VI benefits from the acoustics-based sensor while the simulation of Case VII only uses the acoustics-based sensor to distinguish compression motion from expansion motion. In the comparison shown in Fig. 2.46e and Fig. 2.46f, the use of Riemann fluxes in Case VI is highly localized to the shock structures, and the shock-capturing method is effectively deactivated elsewhere. In contrast, in Case VII, the shock-capturing method is unnecessarily enabled in the non-turbulent flow region although it is successfully suppressed in the turbulent flow structures.

2.5 Conclusions

A high-order compact finite difference based computational framework is proposed for simulations of compressible turbulent flows. This framework uses collocated and staggered first derivative schemes as well as the mid-point interpolation scheme. During the solution process, all conservative variables are only stored at the collocated nodal points, and the fluxes are assembled at the edge-staggered locations using the interpolated primitive variables. Fourier analysis indicates that robustness is gained by reducing the aliased interactions during the assembly of the non-linear advective fluxes at edge-staggered points. Additional robustness results from staggered evaluation of viscous fluxes that leads to enhanced accuracy in resolving the viscous-type dissipation at small scales especially near and at the Nyquist wavenumber. Eddy-resolving simulations, such as DNS and LES, can therefore maintain numerical stability without additional numerical filtering of the solution. This attribute is particularly pertinent to computations on curvilinear meshes where spatial variations of the metric terms add to further aliasing. A GCL-consistent metric generation process is also developed as part of the framework. For flows containing shocks, the flux evaluation is compatible with the application of nonlinear shock-capturing schemes combined with an approximate Riemann solver via state variable blending. The staggered calculation of viscous fluxes is favorable when other shock-regularization schemes, such as localized artificial bulk viscosity and thermal conductivity models, are used, especially in problems where small-scale eddy shocklets are present.

Different aspects of the numerical performance of the scheme are investigated using several demonstrative computations of 2D and 3D canonical flow configurations. The results indicate that high-order compact numerical schemes have significantly lower dispersion error and preserve coherent flow structures even on highly skewed curvilinear meshes. The LES of decaying isotropic turbulence shows that the framework is suitable for use with high-order compact schemes and can be favorably combined with lower-order explicit central schemes to resolve decorrelated turbulent structures. The results relying on implicit numerical dissipation are overly dissipative compared to those simulated using explicit SGS models. Comprehensive use of the framework is demonstrated in the set of LES of flow over a cylinder. The robustness and accuracy are justified in both the low-Mach and transonic flow cases. For the transonic flow case, central-Riemann hybrid fluxes are used. The

blending of primitive variables is self-controlled by two physics-based shock sensors. The simulation results show that the turbulent flow structures and acoustic wave structures are preserved by central fluxes with the SGS model only and are not affected by the numerical dissipation added from the shock-capturing scheme and the approximate Riemann fluxes.

Chapter 3

Simulations of Compressible Dense-Gas Flows

Supercritical fluids have a number of thermodynamic and chemical properties which make them attractive for use in environmentally sustainable technologies. However, the dynamics of supercritical and transcritical fluid flows are less well-explored and understood even though the thermodynamic properties of supercritical fluids have been studied comprehensively. Studying the behavior of such fluid flows through high-quality computational investigations could provide crucial insights into designing and controlling flow systems operating under supercritical and transcritical conditions. An accurate and robust computational framework is a prerequisite to conducting high-quality computational investigations. This work extends a high-resolution computational framework for calorically-perfect-gas flows (cf. Ch. 2) by including real-gas thermodynamic and transport models. The computational approach achieves robustness by reducing the aliasing error and improving the spectral resolution of the viscous fluxes at high wavenumbers. No non-conservative correction or filtering is needed to maintain robustness for shock-free flows if physical or physics-based model dissipation is included. The framework is also compatible with applications of shock capturing schemes and approximated Riemann solvers and supports simulations on curvilinear meshes.

The study illustrated in this chapter is published in Ref. [145].

3.1 Introduction

Supercritical fluids have recently drawn increasing attention in many industrial applications [18, 79]. As an example, supercritical CO_2 power cycles offer key advantages in energy conversion due to their compactness, high thermal efficiency, and longer life cycles due to corrosion resistance. They can operate with a variety of heat sources, including sustainable sources, such as geothermal

power, concentrated solar power and high temperature fuel cells, nuclear reactors, and traditional fossil fuels [2]. A pure fluid reaches the supercritical state when both its pressure and temperature are above the critical point. Transitioning between subcritical and supercritical states, the fluid undergoes a pseudo phase change where the thermodynamic and transport properties, e.g., density, viscosity, thermal conductivity, vary significantly within a narrow range of temperature and pressure. Unlike ideal gases, a fluid near the critical point exhibits complex thermodynamic behavior. The pressure-volume-temperature (p-v-T) relation is highly nonlinear. Additionally, the specific internal energy is dependent on both temperature and density (or specific volume) and accounts for the effects of intermolecular interactions. Due to the complexities introduced by the behavior of thermodynamic and transport properties, numerical solutions of flows in this regime require special consideration. In many cases, when a flow of a transcritical or supercritical fluid is turbulent, the significant variations in thermodynamic and transport properties of the fluid are highly coupled with the fluid motions which further increases the complexity of the turbulence dynamics.

Numerical computations have been utilized to investigate the flows of dense gases. However, for the fully compressible system, abrupt changes in thermodynamic properties, especially density, associated with a small range of temperature and pressure variation may cause severe and spurious oscillations [62, 77]. There are two common methods used to address this problem in the simulations. The first approach is to rely on extra numerical dissipation, especially around the pseudo-phase change regions [62, 36], and the second approach is to introduce a total energy correction [137] or replace the energy equation by the pressure evolution equation [77]. Both of these modifications, in general, achieve numerical robustness at the cost of sacrificing simulation accuracy to some degree. Excessive numerical dissipation tends to damp the physically growing high wavenumber features. If numerical dissipation is applied as a dominant mechanism in the computational approach, the local simulation results should be considered as physically under-resolved solutions. Careful assessment of fine-scale features is required to establish the physical quality of the simulated results.

In simulations of transcritical flows, the abrupt density changes are determined by the equation of state (EOS) and are caused by physical temperature and pressure fluctuations in the flow. During the pseudo-phase change from the subcritical state to the supercritical state, or vice versa, the density change associated with pressure and temperature is still smooth. Therefore, in a shock-free flow, there is no discontinuity in the flow during the pseudo-phase change. The simulation quality thus primarily depends on the tolerance of the simulation framework to dispersion and aliasing errors without excessive numerical dissipation. From this point of view, the pressure-based solver [77] can effectively reduce the spurious oscillations in the simulation results. However, this robustness may be at a cost of breaking the discrete conservation. For a fully compressible system that involves shock waves, additional treatment may be needed under specific flow conditions.

This work proposes a unified simulation framework for simulations of transcritical fluid flows that is an extension of the one proposed in Ch. 2. The conservative formulation of the computational

systems for ideal gas flows is preserved. Additionally, the spatial discretization is based on compact finite difference schemes and compact interpolations to achieve both high-order grid convergence and highly improved spectral resolution [146]. The thermodynamic and transport properties are calculated using physics-based models that resolve the abrupt changes in properties during pseudo phase changes. In this chapter, the mathematical formulation of the problem and the associated physical closure models are described in Sec. 3.2, the numerical solution methods are summarized in Sec. 3.3, and some demonstrative computational results for simulations of a compressible planar shear layer and turbulent boundary layer are presented and discussed in Sec. 3.4.

3.2 Physical and mathematical formulations

3.2.1 Governing equations

The simulation solves the compressible Navier-Stokes equations, including conservation of mass, momentum, and total energy, given as

$$\frac{\partial \rho}{\partial t} + \frac{\partial \rho u_j}{\partial x_j} = 0 \tag{3.1}$$

$$\frac{\partial \rho u_i}{\partial t} + \frac{\partial}{\partial x_j}\left(\rho u_i u_j + p\delta_{ij}\right) = \frac{\partial \sigma_{ij}}{\partial x_j} \tag{3.2}$$

$$\frac{\partial \rho e_{\text{tot}}}{\partial t} + \frac{\partial}{\partial x_j}\left[\left(\rho e_{\text{tot}} + p\right) u_j\right] = \frac{\partial}{\partial x_j}\left(u_i \sigma_{ij} - q_j\right) \tag{3.3}$$

where index notation is applied, ρ is the density, u_i is the velocity vector, p is the pressure, δ_{ij} is the identity tensor, σ_{ij} is the viscous stress tensor, and e_{tot} is the specific total energy which includes the specific internal energy, e, and the specific kinetic energy, $e_{\text{tot}} = e + u_j u_j/2$. The bulk viscosity of the fluid is not considered, and thus, the viscous stress tensor, σ_{ij}, is calculated as

$$\sigma_{ij} = 2\mu\left(S_{ij} - S_{kk}\delta_{ij}/3\right) \tag{3.4}$$

where μ is the dynamic viscosity of the fluid, S_{ij} is the rate-of-strain tensor, defined as $S_{ij} = (u_{i,j} + u_{j,i})/2$, and δ_{ij} is the identity tensor. The heat flux, q_j, is calculated using Fourier's law as

$$q_j = -\lambda \frac{\partial T}{\partial x_j} \tag{3.5}$$

where λ is the thermal conductivity.

For a dense gas, the EOS includes the p-v-T relation, i.e., $p = p(T, \rho)$, and the formulation of the internal energy is determined by both temperature and density, or $e = e(T, \rho)$. The transport properties are calculated using both temperature and pressure. The formulation and non-dimensionalization of the EOS and transport models are discussed in the following sub-sections, and

more detailed derivations are provided in Appendix B.

3.2.2 Thermodynamic models

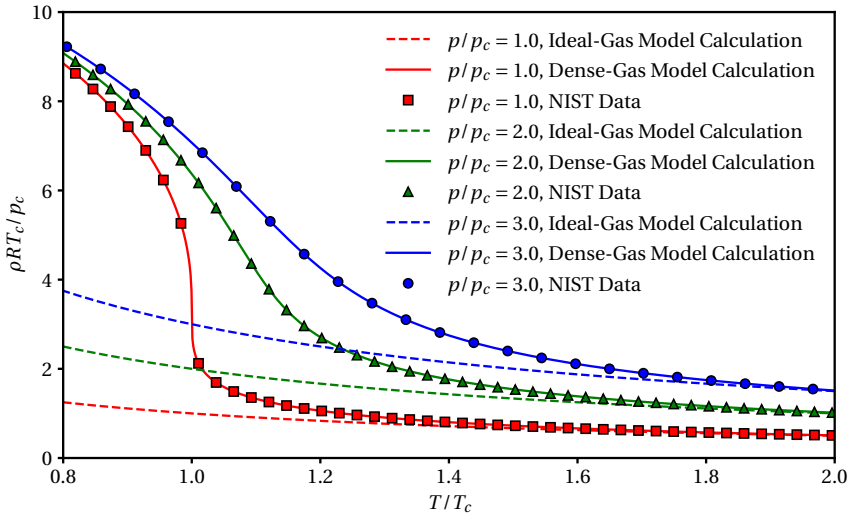

Figure 3.1: p-v-T relation calculated from the Peng-Robinson EOS.

For a pure gas near its critical condition, the Peng-Robinson EOS [119] is used for the p-v-T relation. The mathematical expression is provided as follows:

$$p = \frac{RT}{v-b} - \frac{a\alpha(T_r)}{v^2 + 2vb - b^2} \tag{3.6}$$

where p is the pressure, T is the temperature, R is the specific gas constant, and a and b are model constants defined as

$$a = 0.45723553\frac{R^2T_c^2}{p_c} \qquad \text{and} \qquad b = 0.07779607\frac{RT_c}{p_c} \tag{3.7, 3.8}$$

where T_c and p_c are the critical temperature and pressure respectively. T_r in Eq. (3.6) is the reduced temperature, which is dimensionless, defined as $T_r = T/T_c$. The expression of $\alpha(T_r)$ in Eq. (3.6) is given as

$$\alpha(T_r) = \left[1 + \kappa\left(1 - \sqrt{T_r}\right)\right]^2 \tag{3.9}$$

where κ is a quadratic fitting of the acentric factor ω and is given as

$$\kappa = 0.37464 + 1.54226\omega - 0.26992\omega^2 \tag{3.10}$$

For CO_2, $\omega \approx 0.239$. Eq. (3.6) implies a non-dimensionalization using p_c, T_c and R, where p_c and T_c

provide a pressure and temperature scale respectively. The density scale is defined as $\rho_0 = p_c/(RT_c)$. Furthermore, drawing a parallel to kinematic motion, a velocity scale is derived as $U_0 = \sqrt{RT_c}$. As a side note, ρ_0 and U_0 are results from dimensional analysis that may not be equal to the density or speed of sound at the critical condition. The dimensionless form of Eq. (3.6) can be written as

$$p_r = \frac{T_r}{v^* - b^*} - \frac{a^* \alpha(T_r)}{v^{*2} + 2v^* b^* - b^{*2}} \tag{3.11}$$

where $p_r = p/p_c$ is known as the reduced pressure. The superscript "$*$" denotes the non-dimensionalized quantity, and the parameters a^*, b^*, and v^* are given as:

$$a^* = 0.45723553 \qquad b^* = 0.07779607 \qquad v^* = \rho_0 v \tag{3.12, 3.13, 3.14}$$

The p-v-T behavior is plotted in Fig. 3.1. The model parameters are set for CO_2. For reference, the results obtained from the Peng-Robinson EOS are compared with data from the National Institute of Standards and Technology (NIST) Web Book [91]. As shown in Fig. 3.1, the pseudo phase change behavior is well-captured by the model p-v-T relation near the critical temperature at supercritical pressures.

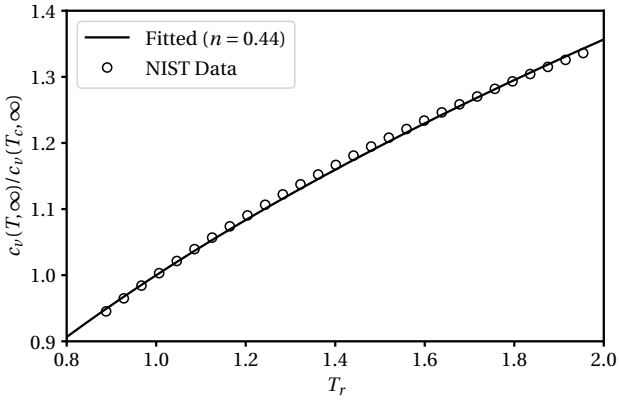

Figure 3.2: Fitted isochoric specific heat for CO_2 in the ideal-gas limit. The reference state is chosen to be at the critical temperature in the ideal gas limit, and the model calculation results are compared against the values obtained from the NIST database [91].

The internal energy can be calculated using the following equation:

$$e = e_{\text{ref}} + \int_{T_{\text{ref}}}^{T} c_v(T, v_{\text{ref}}) dT + \int_{v_{\text{ref}}}^{v} \left[T \left(\frac{\partial p}{\partial T} \right)_v - p \right] dv \tag{3.15}$$

where c_v is the specific heat at constant volume, and the subscript "ref" indicates a reference state. Eq. (B.17) indicates a two-step integration along an isochoric path followed by an isothermal path. On the right-hand side of Eq. (B.17), the second integral can be evaluated by the p-v-T relation from

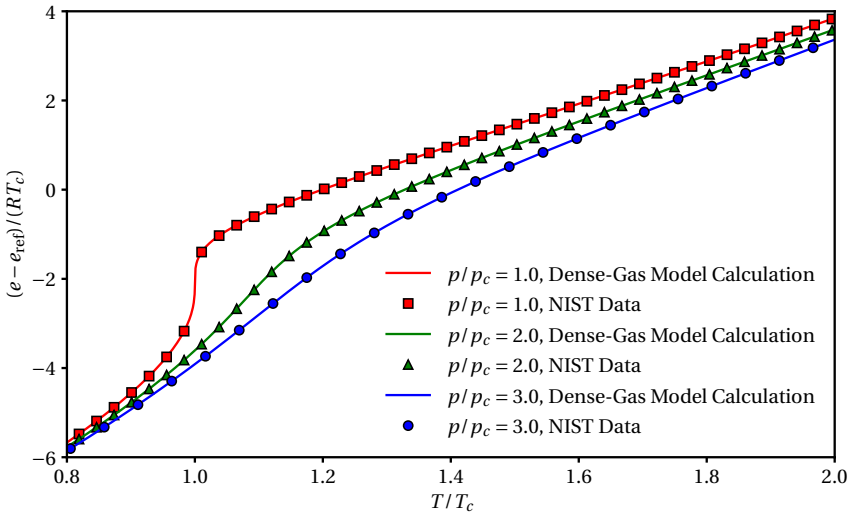

Figure 3.3: Evaluation of the specific internal energy calculation for CO_2: the reference state is chosen to be at the critical temperature in the ideal gas limit, and the model calculation results are compared against the values obtained from the NIST database [91].

Eq. (3.6). The first integral, however, requires an additional model for the temperature dependent c_v at a reference specific volume. Taking $v_{\mathrm{ref}} \to \infty$, the reference state is in the ideal gas regime. For certain gases, $c_v(T, \infty)$ can be evaluated based on the following power law for simplicity:

$$c_v(T, \infty) = c_v(T_{\mathrm{ref}}, \infty) \left(\frac{T}{T_{\mathrm{ref}}} \right)^n \tag{3.16}$$

Using CO_2 as an example, the accuracy of the calculation of the internal energy using Eq. (3.15) is shown in Fig. 3.3, and the results are compared with data from the NIST database [91].

3.2.3 Transport models

The calculations of a fluid's viscosity and thermal conductivity in the transcritical and supercritical regimes are based on the approach proposed in Chung et al. (1988) [25]. The model accounts for the effects of both temperature and pressure. The original version of the model, particularly for the calculation of thermal conductivity, is formulated in a dimensional form for engineering applications. Its utilization requires that quantities be provided in particular physical units. In this work, all the dimensional parameters in the model formulation have been consistently scaled so that the model can be directly used for both dimensional and dimensionless computations.

According to the model from Chung et al. (1988), the dynamic shear viscosity of a pure gas is evaluated as

$$\frac{\mu}{\mu_c} = \frac{\mu^*}{\mu_c^*} \tag{3.17}$$

where μ_c is the dynamic shear viscosity at the critical condition defined as $\mu_c = \mu(T_c, p_c)$. μ^* is a dimensionless function of temperature and density, and μ_c^* is μ^* evaluated at the critical condition, or $\mu_c^* = \mu^*(T_c, \rho_c)$. The calculation of μ^* requires a p-v-T relation, and to maintain consistency, the Peng-Robinson model as described in Sec. 3.2.2 is used. The expression for μ^* calculated using the Peng-Robinson model is given as

$$\mu^* = \frac{\sqrt{T^*}}{\Omega_v(T^*)} F_c \left(\frac{1}{G_2(\rho^*)} + E_6 \rho^* \right) + \eta^{**}(T^*, \rho^*) \tag{3.18}$$

where the dimensionless temperature T^* is calculated as $T^* = 1.2593 T_r$, and the dimensionless density is evaluated as $\rho^* = \rho v_c / 6$ with v_c representing the specific volume at the critical condition. The parameters involved in Eq. (3.18) are determined from the properties of the gas molecules and detailed in Ref. [25] and Ref. [125]. The whole calculation process is also documented in Appendix B.3.1.

The thermal conductivity, λ, based on the methods from Chung et al. (1988), can be calculated as

$$\frac{\lambda}{R\mu_c} = 3.75256 \mu_r^{\ominus} \Psi(T_r, p_r) \left(\frac{1}{G_2} + E_6 \rho^* \right) + q^* E_7 G_2 {\rho^*}^2 \sqrt{T_r} \tag{3.19}$$

where $\mu_r^{\ominus} = \mu^{\ominus}/\mu_c$ is the relative low-pressure dynamic shear viscosity, and the superscript "$\ominus$" denotes that the quantity is evaluated at the same temperature but in the low-pressure regime. The detailed calculations of the model parameters are provided in Ref. [25] and Ref. [125]. The left-hand side of Eq. (3.19) implies that the thermal conductivity is consistently scaled by $R\mu_c$, and all calculations necessary to compute the right-hand side of Eq. (3.19) can be conducted using the non-dimensionalized quantities. The calculations using the original transport models from Chung et al. are dimensional. The complete instructions for non-dimensional calculations including the determinations of the model parameters are documented in Appendix B.3.2.

3.3 Summary of numerical schemes

All numerical schemes used for collocated-to-edge interpolation and derivative operations are sixth-order compact schemes [89, 107] as described in Sec. 2.3. The high-order formulation will provide rapid grid convergence. Moreover, compared to explicit schemes, the compact scheme has significantly improved spectral resolution especially in the high wavenumber regime. However, for high-order and high-resolution schemes, numerical stability becomes a major concern [107].

The spatial discretization used in this work is based on the framework proposed by Song et al. [146] which is also illustrated in Ch. 2. During the solution process, all conservative variables evolve at the collocated grid points while the fluxes are assembled at the edge-staggered points in each direction respectively. A minimum set of primitive variables, calculated from the conservative variables, are interpolated from the collocated grid points to assemble the inviscid fluxes at the

staggered grid points. For the viscous fluxes, the gradient components which are aligned with the flux direction are calculated using staggered first derivative schemes, and the components that are not aligned with fluxes directions are first calculated using collocated differential schemes and then interpolated from the collocated grid points to the corresponding edge-staggered points. Eventually, the divergence operators are evaluated using staggered first derivative schemes in each direction, and the results are taken back from the edge-staggered grid points to the collocated grid points. The discretization has been proven to work on both uniform Cartesian meshes and curvilinear wavy meshes.

The discretization method significantly contributes to reducing the aliasing error in the nonlinear inviscid fluxes and resolving the viscous dissipation in the high-wavenumber region including a non-trivial response of viscous dissipation at the Nyquist wavenumber. A more quantitative analysis and mathematical proofs are provided in Ch. 2. In simulations of flows in the transcritical regime, the pseudo phase change of the fluid amplifies the aliasing error originating from the calculation of temperature and pressure. The small spurious oscillations in the pressure and temperature fields may lead to noticeable fluctuations in the mass flux that cause numerical errors to grow. The proposed simulation framework addresses this issue by providing sufficient dealiasing during the assembly of the nonlinear fluxes. Additionally, the high spectral resolution of the compact schemes used in the simulation framework significantly reduces the dispersion error. Furthermore, the non-trivial response of the viscous dissipation at the Nyquist wavenumber damps the grid-to-grid oscillations, making the computational system more stable. The solution filtering operations, claimed to be necessary in many compact-scheme-based frameworks, can be avoided.

In addition, for flows under transcritical conditions, the pseudo phase change behavior is physically regular per the EOS model on the macro scale. Therefore, the rapid density change associated with a relatively small temperature fluctuation during the pseudo phase change should be a numerically well-resolved feature in a direct numerical simulation (DNS). This requires the numerical framework to have high spectral resolution and low numerical dispersion to resolve the solution profile with a large local gradient and curvature.

For highly compressible flows, shocks may develop. In the proposed simulation framework, all the fluxes are assembled at the edge-staggered grid points. The solution approach is naturally compatible with the non-linear shock-capturing scheme combined with an approximate Riemann solver. As a result, a hybrid central-Riemann flux is assembled. The approximate Riemann solver and characteristic decomposition for a real-gas are detailed in Appendix A.5.3. In simulations of compressible turbulent flows containing shocks, it is desirable that the numerical dissipation be highly localized to the shock structures to artificially capture the under-resolved features. In the shock-free region, the turbulent flow behavior should only rely on the physical or physics-based model dissipation.

In this work, the flux blending is controlled by a physics-based shock sensor that is modified

from the Ducros sensor. The mathematical formulation of the modified Ducros sensor, ϕ, is given in the following equation:

$$\phi = \frac{-|\theta|\,\theta}{\theta^2 + \boldsymbol{\omega}\cdot\boldsymbol{\omega} + \varepsilon^2} \tag{3.20}$$

Here, $\theta = \nabla\cdot\boldsymbol{u}$ is the velocity dilatation, $\boldsymbol{\omega} = \nabla\times\boldsymbol{u}$ is the vorticity vector, and $\varepsilon = 1\times10^{-16}$ is used for round-off regularization. According to the equation, in a non-uniform flow, $\phi < 0$ indicates local expansion, and $\phi > 0$ indicates local compression. During simulation, a threshold sensor value, ϕ_{TH}, is specified. If $\phi > \phi_{\mathrm{TH}}$, Riemann fluxes will be used. Otherwise, only central fluxes will be used.

3.4 Demonstrative computations

Results from idealized unit test problems are not shown in this paper. Instead, results from high-resolution, three-dimensional turbulent flow simulations in two illustrative problems are shown. These problems are intended as a numerical demonstration of the success of the proposed method in simulating realistic turbulent flows.

3.4.1 Planar shear layer

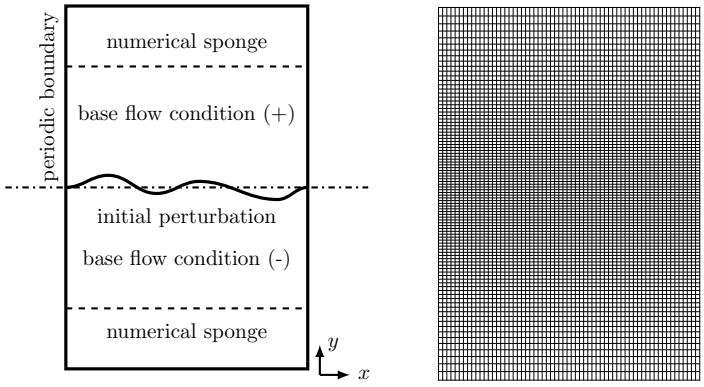

Figure 3.4: Simulation configuration of compressible planar shear layer: (a) configuration of computational domain; (b) computational mesh. The computational domain is periodic in the z-direction, and the computational mesh is uniform in x and z.

The basic configuration of the compressible shear layer simulation is shown in Fig. 3.4. The computational domain size is $L_x\times L_y\times L_z = 12\pi\times20\times6\pi$, and the mesh size is $N_x\times N_y\times N_z = 1024\times512\times512$. The computational domain is periodic in the $x-$ and $z-$ directions, and the computational mesh is uniform along these two dimensions. The computational mesh is stretched in the y-direction to use a majority of the grid points to resolve the growth of the shear layer. Near

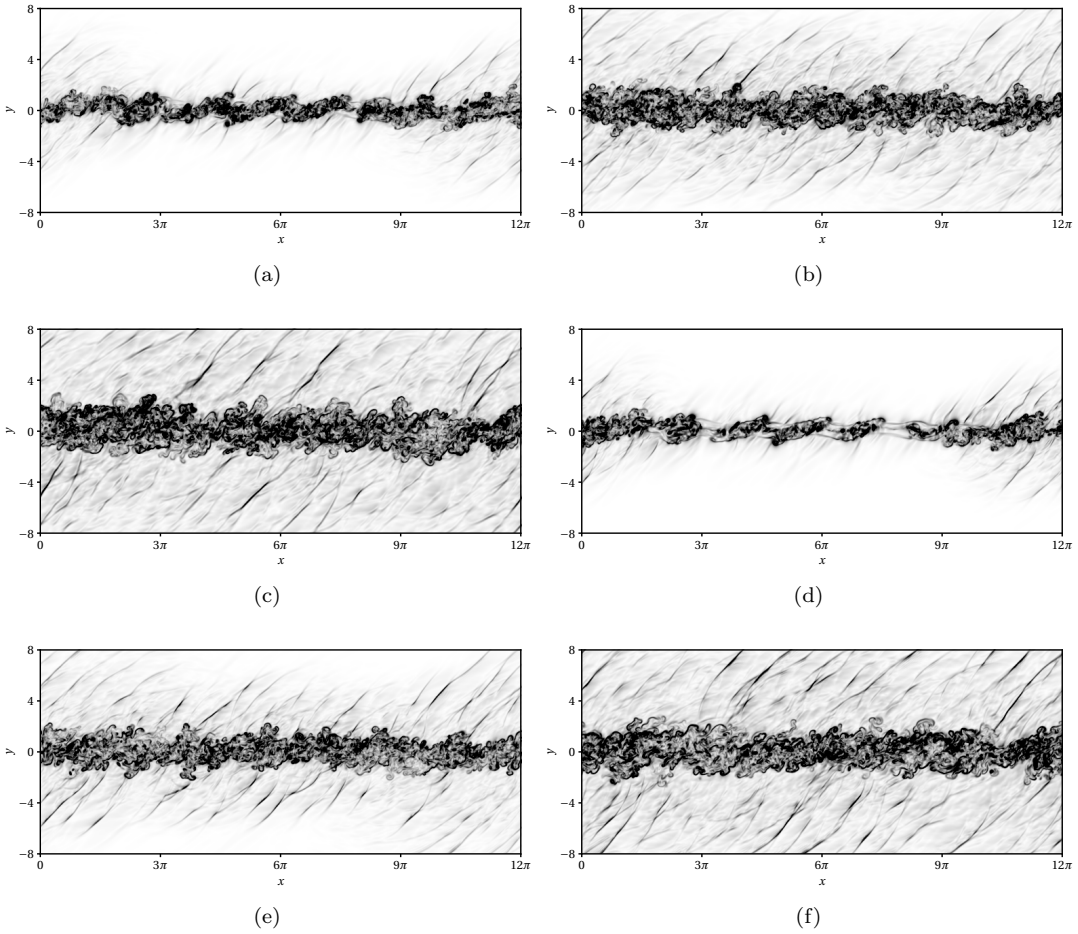

Figure 3.5: Numerical Schlieren imaging of the planar shear layers: (a), (b), and (c) are the visualizations of the supercritial CO_2 flow at the normalized time, τ, at values of 500, 600, and 700 respectively; (d), (e), and (f) are the visualizations of the calorically perfect gas at the same corresponding normalized times.

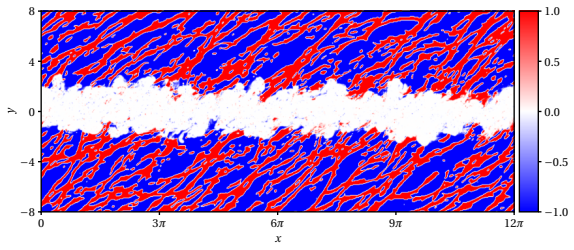

Figure 3.6: Visualization of the modified Ducros sensor in the dense gas shear layer at $\tau = 700$. The modified Ducros sensor is defined in Eq. (3.20). The flow is at the same state as shown in Fig. 3.5c.

the upper and lower domain boundaries in the y-direction, numerical sponge layers are applied to enforce the far-field flow conditions on each side. The base flow velocity is parallel to the x-direction with variation in the y-direction. The initial base flow velocity profile, U_0, is regularized with a finite shear layer thickness using the following hyperbolic tangent profile:

$$U_0(y) = \frac{U_{+\infty} + U_{-\infty}}{2} + \frac{U_{+\infty} - U_{-\infty}}{2} \tanh\left(C_\delta \frac{y}{\delta_0}\right) \tag{3.21}$$

where $U_{+\infty}$ and $U_{-\infty}$ are constants representing the far-field velocities on the upper and lower sides of the domain respectively. The dimensionless constant C_δ is a scaling factor that defines the characteristic velocity based on the shear layer thickness δ_0. In this simulation, $C_\delta = 2\tanh^{-1}(0.99)$, and δ_0 represents the shear layer thickness such that the edge velocity matches 99% of the far-field velocity. The momentum thickness, δ^{**}, for an instantaneous velocity profile is defined as

$$\delta^{**} = \frac{1}{\rho_{-\infty} U_{-\infty}^2} \int_{-\infty}^{0} \overline{\rho}\widetilde{u}\,(U_{-\infty} - \widetilde{u})\,dy + \frac{1}{\rho_{+\infty} U_{+\infty}^2} \int_{0}^{+\infty} \overline{\rho}\widetilde{u}\,(U_{+\infty} - \widetilde{u})\,dy \tag{3.22}$$

where $\rho_{-\infty}$ and $\rho_{+\infty}$ are the far-field densities in the lower and upper sides of the domain respectively. The operator $\overline{(\cdot)}$ denotes Reynolds averaging within the x-z plane at each y location, and the operator $\widetilde{(\cdot)}$ denotes Favre averaging, such that $\widetilde{(\cdot)} = \overline{\rho(\cdot)}/\overline{\rho}$. The convective Mach number M_c is defined as

$$M_c = \frac{|U_{+\infty} - U_{-\infty}|}{c_{+\infty} + c_{-\infty}} \tag{3.23}$$

where $c_{+\infty}$ and $c_{-\infty}$ are the far-field speeds of sound on the upper and lower sides of the domain respectively. The Reynolds numbers are defined as

$$\mathrm{Re}_\delta = \rho_0 \frac{|U_{+\infty} - U_{-\infty}|\,\delta}{\mu_0} \qquad \text{and} \qquad \mathrm{Re}_{\delta^{**}} = \rho_0 \frac{|U_{+\infty} - U_{-\infty}|\,\delta^{**}}{\mu_0} \tag{3.24, 3.25}$$

where ρ_0 and μ_0 are the characteristic density and dynamic shear viscosity respectively. In this demonstrative simulation, the initial temperature and pressure are uniform. The initial reduced pressure is $p_{r0} = 1.8$, and the initial reduced temperature is $T_{r0} = 1.4$. Accordingly, ρ_0 and μ_0 in (3.24) and Eq. (3.25) are the initial density and viscosity respectively. Given the symmetry of the problem, the far-field velocities are set as $U_{+\infty} = -U_{-\infty} = U_\infty$ for $U_\infty > 0$. As initial conditions, a wide-band velocity perturbation is prescribed within the shear layer. The simulation is configured with $M_c = 1$. The initial Reynolds numbers are $\mathrm{Re}_\delta \approx 2232$ and $\mathrm{Re}_{\delta^{**}} \approx 243$ respectively. The time advancement is conducted using the third-order strong stability preserving Runge-Kutta method (SSP-RK3) [142] with CFL = 0.6.

As a comparison, a calorically perfect gas flow is also simulated with identical configurations. In the simulation of the calorically perfect gas flow, the dynamic shear viscosity is calculated as $\mu = \mu_0(T_r/T_{r0})^{0.76}$. The thermal conductivity is calculated as $\lambda = c_p\mu/\mathrm{Pr}$, where c_p is the specific

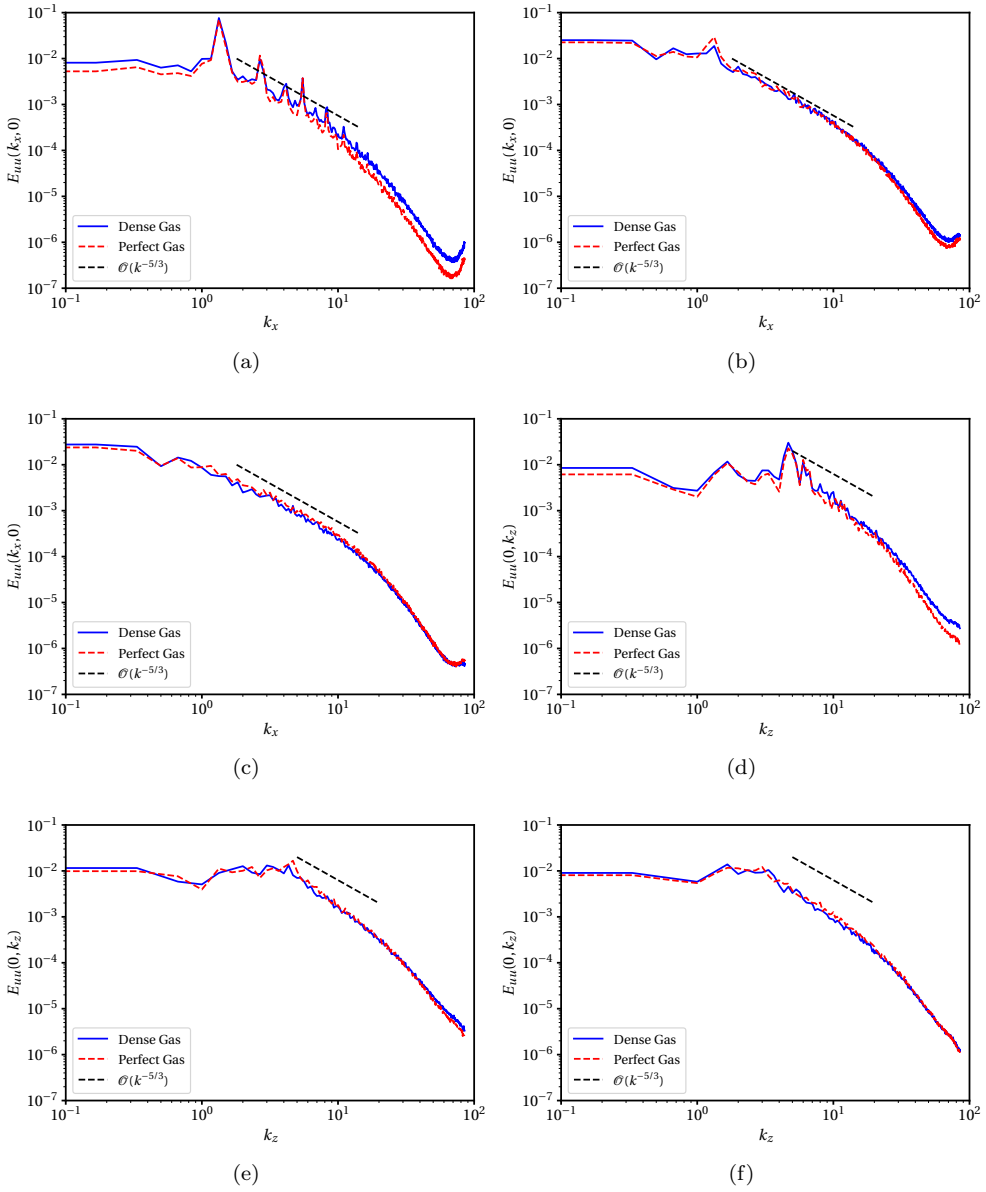

Figure 3.7: One-dimensional streamwise velocity energy spectra at the center plane $y = 0$: (a) and (d): $\tau = 500$; (b) and (e): $\tau = 600$; (c) and (f): $\tau = 700$.

heat at constant pressure evaluated as $c_p = \gamma R/(\gamma - 1)$, and the Prandtl number, Pr is assumed to be constant at $\mathrm{Pr} = 0.7$. The ratio of the specific heats, γ, is a constant, and $\gamma = 1.4$ here.

A convective nondimensional time, τ, is introduced as

$$\tau = tU_\infty/\delta_0^{**} \tag{3.26}$$

Visualizations of the simulation results are shown in Fig. 3.5 using numerical Schlieren imaging, $|\nabla\rho|$, at $\tau = 500$, 600, and 700 respectively. For comparison, the visualizations of the dense gas flow and perfect gas flow are shown at the same normalized convective time. The numerical Schlieren imaging visualizations show that in both simulations, the turbulent shear layer structures generate significant Mach waves and shock waves. In these simulations, the hybrid central-Riemann flux is used as described in Sec. 3.3. The threshold sensor value is set to be $\phi_{\mathrm{TH}} = 0.4$. The Riemann flux is assembled in the Rusanov form [132] with the fifth-order weighted essentially non-oscillatory interpolation scheme (WENO5-JS) [73] for finite difference methods. An instantaneous visualization of the modified Ducros sensor for the dense gas flow at $\tau = 700$ is shown in Fig. 3.6. The visualization corresponds to the flow structures shown in Fig. 3.5c. By comparison, it can be seen that the shock capturing scheme is highly localized to the shock structures, and no artificial dissipation is imposed in the simulation of turbulent flow structures within the shear layer.

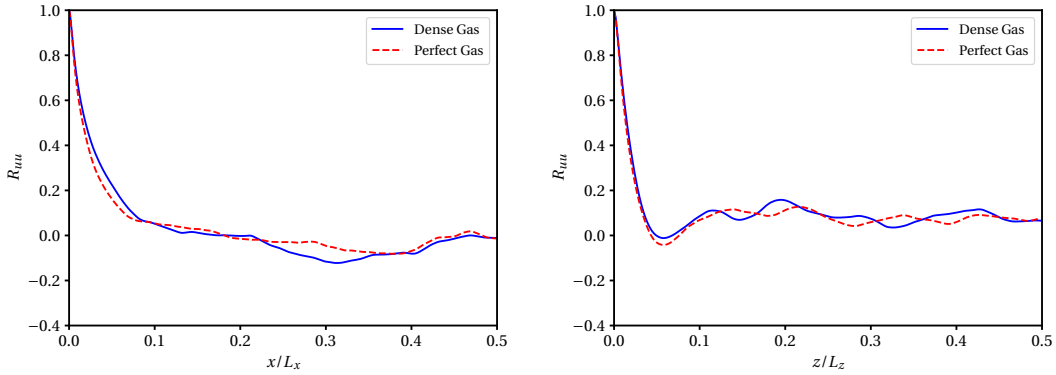

(a) (b)

Figure 3.8: Two-point correlation of the streamwise velocity at the center plane ($y = 0$): (a) the two-point correlation in the x-direction and (b) the two-point correlation in the z-direction.

The one-dimensional streamwise velocity energy spectra along the streamwise (x) and spanwise (z) directions at different times are shown in Fig. 3.7. As the turbulent shear layer grows, approximately one decade of turbulent cascade forms in both the dense gas and perfect gas flows, and there is no significant difference between the energy spectra for the two types of flows. The two-point correlation of the streamwise velocity in the center plane ($y = 0$) at $\tau = 700$ is shown in Fig. 3.8. The results indicate that the turbulent structures have sufficient decorrelation in both streamwise and spanwise directions, and the confinement from the domain periodicity has no noticeable effects on the growth of the turbulent shear layer in both cases.

Lastly, the time histories of several flow profiles are provided in Fig. 3.9 for reference. The fluctuating component corresponding to the Reynolds decomposition is defined as $(\cdot)' = (\cdot) - \overline{(\cdot)}$, and the fluctuating component corresponding to the Favre decomposition is defined as $(\cdot)'' = (\cdot) - \widetilde{(\cdot)}$.

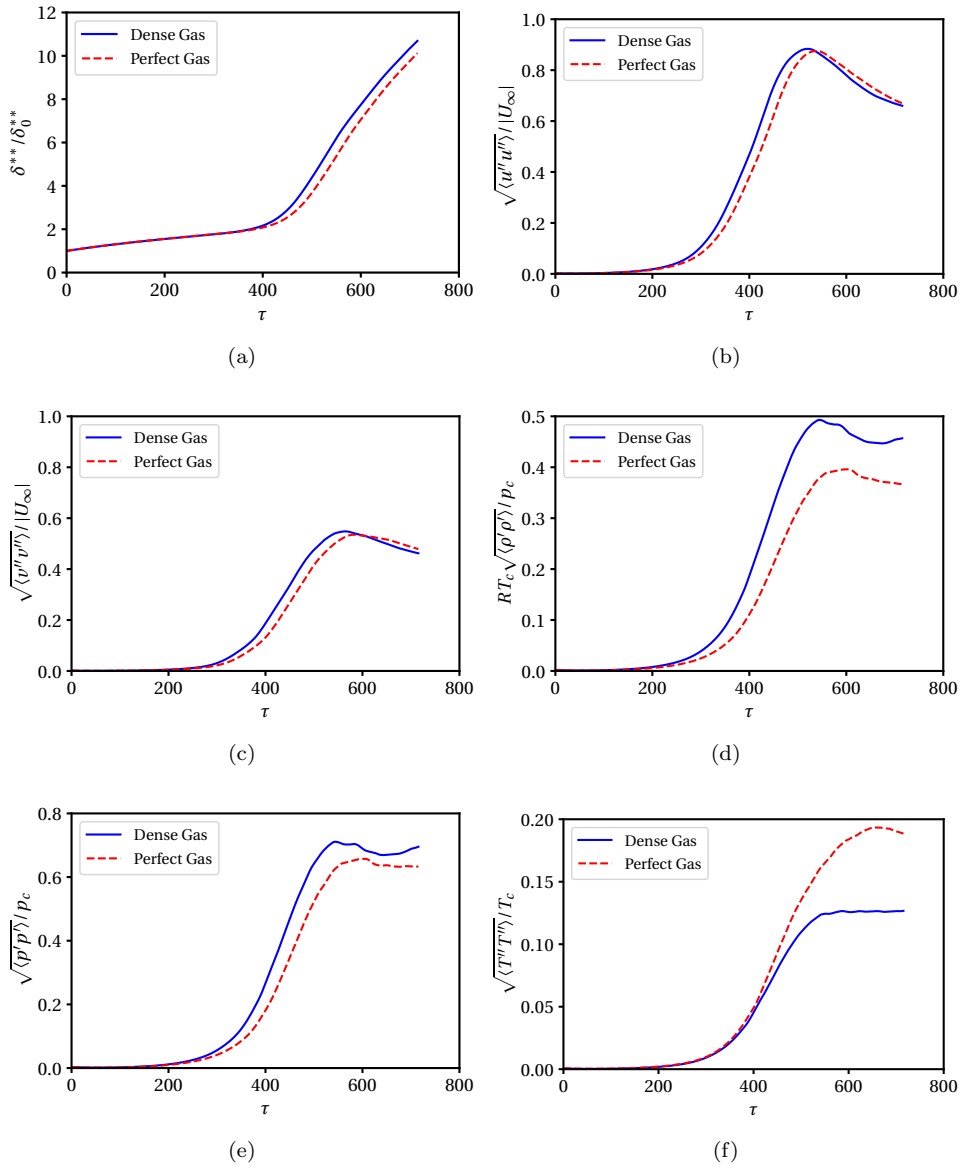

Figure 3.9: Time histories of flow properties in growing planar shear layer: (a) momentum thickness; (b) streamwise velocity fluctuation; (c) transverse velocity fluctuation; (d) density fluctuation; (e) pressure fluctuation; and (f) temperature fluctuation.

The operator "$\langle(\cdot)\rangle$" denotes the domain average defined as

$$\langle(\cdot)\rangle = \frac{1}{\delta^{**}}\int_{-\infty}^{+\infty}\overline{(\cdot)}dy$$

The results show that the turbulent shear layers for the dense gas and perfect gas have similar growth rates measured from momentum thickness and turbulent velocity fluctuations. More noticeable differences are present in the profiles of fluctuating thermodynamic quantities. The dense-gas shear layer has a larger fluctuation in density and pressure during the entire history of shear layer growth. However, as the shear layer becomes fully turbulent, the perfect-gas flow shows higher temperature fluctuations. This phenomenon implies that under the flow conditions, the density fluctuations are primarily due to the turbulent dilatational motion. Comparing the EOS of the dense gas and perfect gas near the critical temperature, the dense-gas temperature is significantly less sensitive to the density change. For similar turbulence intensities (Fig. 3.7), the temperature fluctuations of the dense gas are less affected by the turbulent dilatational motion.

3.4.2 Zero-pressure-gradient turbulent boundary layer

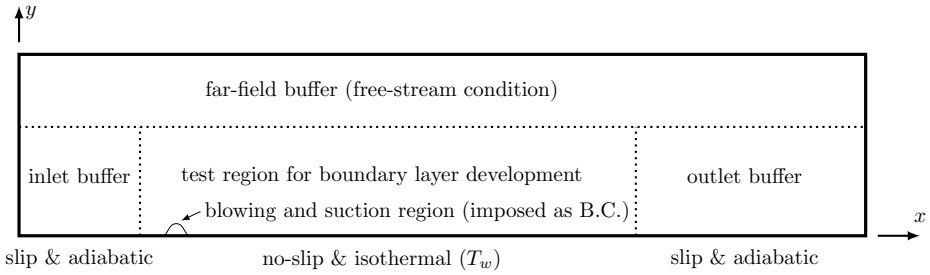

Figure 3.10: Simulation configuration of turbulent boundary layer flow.

The basic simulation configuration is shown in Fig. 3.10. The spanwise direction is homogeneous and periodic (not shown in the schematics). The computational domain in the x-y plane is divided into four sub-regions: the top far-field buffer, inlet buffer, outlet buffer, and test region where the boundary layer develops. The numerical sponge method is applied to the far-field region near the top boundary to preserve the freestream flow conditions including streamwise velocity, zero spanwise velocity, freestream density and temperature. The vertical velocity is not forced by the sponge, and the boundary condition on the top of the domain enforces $\partial v/\partial y = 0$. The inlet buffer also contains a numerical sponge to enforce a prescribed inlet flow profile given as a function of the y-coordinate. The prescribed velocity and temperature profiles are numerically regularized close to the bottom boundary to mimic an infinitesimally thin but numerically resolved boundary layer. The thickness of the numerically regularized inlet boundary layer is denoted as δ_{in}. Beyond the thickness, $y > \delta_{\text{in}}$, the flow is forced to reach freestream condition in the inlet buffer region. The density profile in the inlet buffer is calculated using the Peng-Robinson p-v-T relation to preserve the uniform freestream pressure. The flow in the outlet buffer is damped using the Riemann-flux with the WENO5-JS interpolation scheme, and the homogeneous Neumann boundary condition is applied to the whole flow field at the streamwise boundary. The bottom boundary in the test region is configured as a

no-slip isothermal wall, and the wall temperature is denoted as T_w. The bottom boundary in the inlet and outlet buffer regions are both slip and adiabatic.

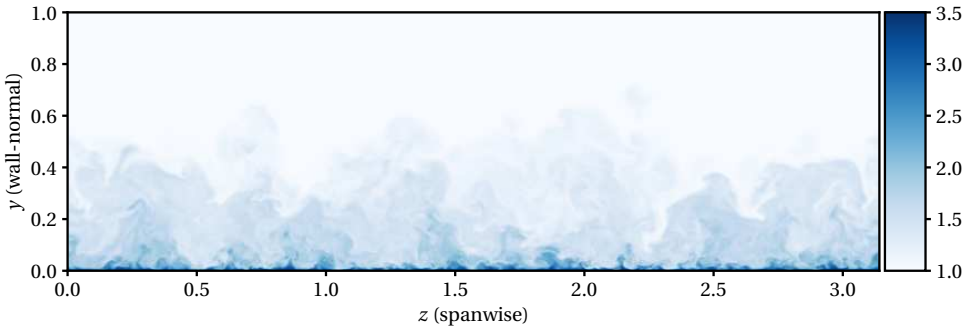

Figure 3.11: Visualization of the density field, ρ/ρ_∞, in the turbulent boundary layer flow in the streamwise cross-section.

In order to trigger a transition to turbulence, a region of blowing and suction is introduced as the boundary condition near the inlet buffer. The blowing and suction region extends across the entire spanwise direction but is narrow and localized in the streamwise direction. The center of the blowing and suction region is denoted as x_b, and the width of the region in the streamwise direction is denoted as Δx_b. Within the blowing and suction region, a locally scaled streamwise coordinate is defined as

$$x_b^* = (x - x_b)/\Delta x_b \tag{3.27}$$

and the wall-normal velocity is prescribed as

$$v_b(x_b^*, z) = W(x_b^*)\left[A_0 \frac{3x_b^* \exp[(1 - 3x_b^*)/2]}{\cos^2(\pi/6)} + \sum_{j=1}^{N_b} A_j \cos(k_j z - \varphi_j)\right] \tag{3.28}$$

where A_0 is the amplitude of the blowing and suction velocity, A_1 through A_{N_b} represent the amplitudes of perturbations in the spanwise direction, and each perturbation is an individual spatial Fourier mode with the wavenumber k_j and phase angle φ_j. In practice, $(A_j/U_\infty) \ll (A_0/U_\infty) \ll 1$ is satisfied for $j \neq 0$ where U_∞ represents the freestream velocity. The blowing and suction boundary condition is constant in time. $W(x_b^*)$ is a mask function, defined as

$$W(x_b^*) = \begin{cases} \cos^2(\pi x_b^*) & |x_b^*| \leq 0.5 \\ 0 & |x_b^*| > 0.5 \end{cases} \tag{3.29}$$

In this work, $A_0/U_\infty = 0.03$ is used, and four spanwise Fourier modes are applied with randomly generated phase angles. The amplitudes of the spanwise perturbations are $A_j/U_\infty = 0.0144/2^j$, and the spanwise wavenumbers are $k_j L_z = 2^{3+j}\pi$ for $j = 1, 2, 3, \text{and}, 4$.

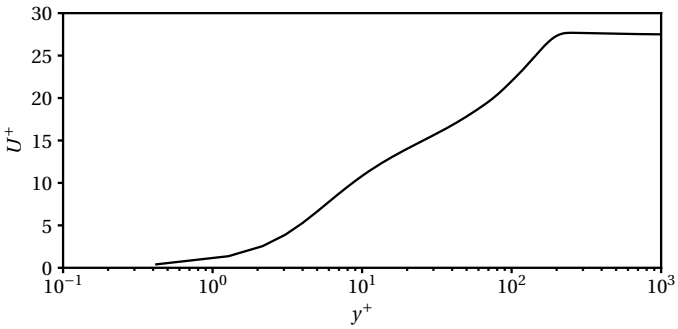

Figure 3.12: Scaled mean streamwise velocity profile in the wall-normal direction.

The computational mesh in the test region is uniform in the x-direction and slightly stretched in the y-direction. The computational mesh in the buffer regions is highly coarsened away from the test region with a large mesh stretch rate in both the x- and y- directions. The computational mesh in the z-direction is uniform in the entire computational domain. The freestream Mach number is $M_\infty = 0.3$, and the freestream reduced temperature and pressure are $T_\infty/T_c = 1.5$ and $p_\infty/p_c = 3$ respectively. The reduced temperature at the isothermal wall is $T_w/T_c = 0.9$. The temperature specification implies that the simulated boundary layer flow develops in the transcritical regime with the pseudo phase change occurring when the Widom line is crossed. The time advancement is conducted using the SSP-RK3 scheme with the adaptive time step limited by CFL = 0.85. The shock capturing scheme is deactivated in the computational domain other than at the outlet buffer region, and no other types of artificial dissipation are imposed within the test region.

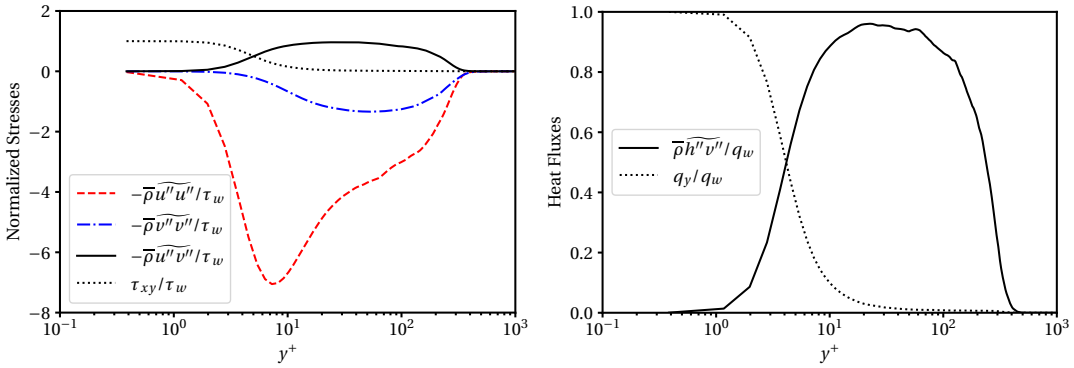

(a) (b)

Figure 3.13: Normalized second-order moments in the transcritical CO_2 turbulent boundary layer flow: (a) components in the Reynolds stress tensor and (b) turbulent heat fluxes.

After reaching a statistically stationary state, the flow conditions at a streamwise stage are

analyzed. The visualization of an instantaneous density field, ρ/ρ_∞, is shown in Fig. 3.11. The visualization qualitatively shows a rapid density change near the wall due to heat transfer. The statistical quantities are averaged in both time and the spanwise direction. The mean streamwise velocity profile is shown in Fig. 3.12, where the y coordinate and u are scaled by the "law of the wall" quantities as $y^+ = yu_\tau/(\mu_w/\rho_w)$ and $u^+ = u/u_\tau$. μ_w is the kinematic viscosity at the wall, and u_τ is calculated as $u_\tau^2 = \tau_w/\rho_w$ where $\tau_w = \mu_w[\partial u/\partial y]_w$. Several components of the Reynolds stress tensor and turbulent heat fluxes are shown in Fig. 3.13. The Reynolds stresses are scaled by the wall shear stress, and the turbulent heat flux along the wall-normal direction is scaled using the heat flux at the wall where $h = e_{\text{th}} + p/\rho$ is the specific enthalpy. The observed behavior indicates that the simulation has achieved a realistic turbulent boundary layer state.

3.5 Conclusions

A high-order compact-finite-difference-based simulation framework has been applied to simulations of compressible dense gas flows near the critical condition. The solution system is fully conservative and closed by the Peng-Robinson p-v-T relation and the Chung et al. (1988) transport models. Owing to the staggered flux assembly using interpolated primitive variables, the computational results for nonlinear problems have a significantly lower aliasing error than those computed using traditional collocated flux assembly. The divergence operations conducted by the edge-to-node staggered difference scheme dramatically improve the accuracy of the viscous fluxes at small scales. Combined with the compact finite difference methods, high-order convergence, high spectral resolution, and robustness can be achieved without non-conservative correction or solution filtering. For highly compressible flow simulations, central-Riemann hybrid fluxes can be used. The flux blending is controlled by a physics-based shock sensor so that the numerical dissipation is highly localized at the shock structures without contaminating the simulation of the turbulent regions. The numerical performance of the simulation framework has been demonstrated in simulations of a compressible supercritical shear layer flow at unity convective Mach number and a zero-pressure-gradient transcritical turbulent boundary layer flow with an isothermal wall. The results of the shear layer simulation are compared with those of a calorically perfect gas flow under the same flow conditions. Different solution behaviors are observed in the thermodynamic quantities associated with the shear layer growth. The boundary layer flow simulation results imply that a rapid change in the fluid properties within a small portion of the turbulent boundary layer occurs due to the pseudo phase change.

Chapter 4

Scalable Parallel Linear Solver for Compact Banded Systems on Heterogeneous Architectures

A scalable algorithm for solving compact banded linear systems on distributed memory architectures is presented. The proposed method factorizes the original system into two levels of memory hierarchies, and solves it using parallel cyclic reduction on both distributed and shared memory. This method has a lower communication footprint across distributed memory partitions compared to conventional algorithms involving data transposes or re-partitioning. The algorithm developed in this work is generalized to cyclic compact banded systems with flexible data decomposition. For cyclic compact banded systems, the method is a direct solver with deterministic operations and communication counts depending on the matrix size, its bandwidth, and the partition strategy. The implementation and runtime configuration details are discussed for performance optimization. Scalability is demonstrated on the linear solver as well as on a representative fluid mechanics application problem, in which the dominant computational cost is solving the cyclic tridiagonal linear systems of compact numerical schemes on a 3D periodic domain. The algorithm is particularly useful for solving the linear systems arising from the application of compact finite difference operators to a wide range of partial differential equation problems, such as, but not limited to, the numerical simulations of compressible turbulent flows, aeroacoustics, elastic-plastic wave propagation, and electromagnetics. It alleviates obstacles to their use on modern high performance computing hardware, where memory and computational power are distributed across nodes with multi-threaded processing units.

The study illustrated in this chapter has been published in Ref. [147].

4.1 Introduction

In the past few decades, the use of graphics processing units (GPUs) in scientific computing has emerged as an attractive option to significantly accelerate various algorithms. The transition of several leadership class computing platforms to such heterogeneous architectures underscores the importance of numerical methods which can take full advantage of the parallel nature of these nodes. The methods for solving certain linear systems presented in this work are well-suited for not only GPUs but also platforms with hybrid memory management and can take advantage of systems with distributed memory combined with multithreading.

In multiscale physics problems, such as simulations of compressible turbulent flows, the resolution of both large and small scales on a discrete grid is essential. Similarly, computational applications involving hydrodynamic instabilities and wave-propagation, such as in aeroacoustics, solid mechanics, and electromagnetics, require numerical discretizations with very low dispersion and dissipation errors. High-order numerical methods have become increasingly attractive in tackling such problems since they provide high solution fidelity at a manageable computational cost [27]. Differentiation using compact finite difference schemes and elliptic solves using spectral methods can be represented discretely as compact banded matrices, and are prime candidates for such multiscale computations due to their increased performance in the high wavenumber regime [89, 57]. The desirable performance of compact schemes for resolving large ranges of scales has been demonstrated in incompressible [85, 143, 54, 161] and compressible [159, 133, 72, 112] turbulent flows, aeroacoustics [10, 175], as well as multiphysics applications with complex physical phenomena [53, 139]. These higher-order finite differences are computed as a linear system with tridiagonal or other compact banded matrices. As derived by Lele (1992) [89], the tridiagonal schemes for collocated first order derivatives, f', at grid point i with spacing $h = x_i - x_{i-1}$ are formulated as

$$\alpha f'_{i-1} + f'_i + \alpha f'_{i+1} = b\frac{f_{i+2} - f_{i-2}}{4h} + a\frac{f_{i+1} - f_{i-1}}{2h} \tag{4.1}$$

Similarly, interpolation between values on collocated and staggered grids can also be formulated as a tridiagonal matrix, where f is the original field and f^I is the interpolated field [107]:

$$\hat{\alpha} f^I_{i-1} + f^I_i + \hat{\alpha} f^I_{i+1} = b\frac{f_{i+3/2} + f_{i-3/2}}{2} + a\frac{f_{i+1/2} + f_{i-1/2}}{2} \tag{4.2}$$

For strong shock-turbulence interaction problems, the compact shock capturing schemes combined with an approximate Riemann solver have been proved to be both robust and less dissipative [176, 150]. For such schemes, block tridiagonal (or wider banded) systems will be formed, and the systems commonly remain well-conditioned as their size grows.

Multiphysics solvers for structured, Eulerian grids in a multidimensional domain may be decomposed as shown in Fig. 4.1, with each processor given access to a single chunk of the global domain.

This decomposition is particularly useful for fixed, structured, Cartesian grids since the grid chunks on each processor can easily be determined from the decomposition layout using simple algebra. This method of grid decomposition facilitates workload distribution and works particularly well for architectures with a distributed memory layout. Operations such as derivatives or interpolation along one dimension involve communication across a single row or column of grid partitioning such as the chunks highlighted in red in Fig. 4.1. As shown by dotted lines in the matrix, sections of the matrix are initially distributed among several processors or nodes; traditional parallel linear solvers of this system commonly assume uniform memory access; and the solving process relies heavily on its communication requirements for data transpose.

This work presents a linear solver for compact banded systems with highly scalable properties. First, a brief review of cyclic reduction (CR) and parallel cyclic reduction (PCR) for banded matrices is given. Sec. 4.2 illustrates the generalized PCR for generic acyclic compact banded systems, which serves as a building block of the proposed algorithm. Sec. 4.3 describes in detail the solution process for tridiagonal matrices of arbitrary size on an arbitrary number of processors followed by an analytical extension of the method for other compact banded matrices. Sec. 4.4 provides additional implementation details to improve performance. In Sec. 4.5, a demonstration is provided of the computational performance of the linear solver and its use in solving the Navier-Stokes equations for the Taylor-Green vortex problem.

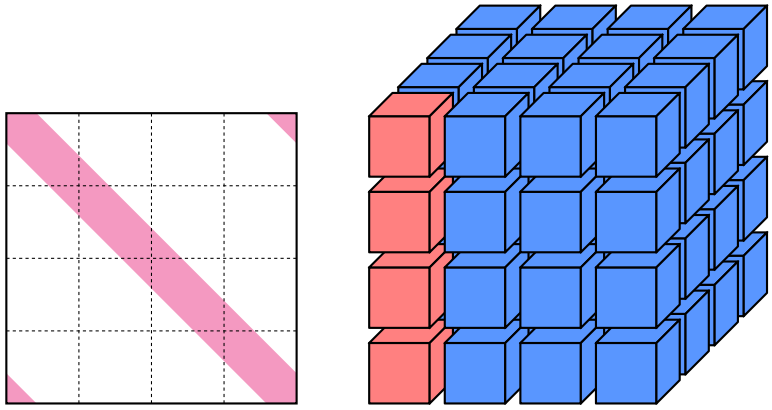

Figure 4.1: Structure of cyclic banded linear system (left) and 3D grid decomposition (right). A pencil of chunks aligned in the solve direction forms a sub-group. Each sub-group constructs an individual linear system as shown on the left. An example sub-group is highlighted in red in the grid decomposition on the right.

CR is a popular direct solve algorithm for structured-matrix linear systems, particularly block tridiagonal linear systems [51]. It recursively reduces a linear system to half-size sub-systems until the size of the sub-system (typically 1×1) makes it affordable to solve. Once the sub-system is solved, the results can propagate backward to the parent system to solve for the remaining unknowns. Hockney (1965) [64] initially derived CR in combination with the fast Fourier transform as an alternative

algorithm for iterative solvers for the Poisson equation. Later, Buzbee et al. (1970) [21] presented a unified formulation and generalization of Hockney's CR and Buneman's (1969) [20] algorithm, which had mathematically equivalent reduction processes but differences in round-off errors and stability. Sweet (1974) [153] and Sweet (1977) [154] further generalized CR from matrices with block sizes of power-of-two to matrices of arbitrary block sizes. Similarly, Swarztrauber (1974) [152] also generalized CR for tridiagonal systems associated with separable elliptic equations. A parallel variant of CR, also known as PCR, was introduced by Hockney and Jesshope (1981) [65]. In the PCR process, the upper and lower off-diagonal elements of both the even and odd indexed rows of a tridiagonal matrix are simultaneously eliminated by the previous and the next rows in one step of reduction. As a consequence, it splits a system into two half-size sub-systems at each step. The communication pattern of an 8×8 non-cyclic tridiagonal system is shown in Fig. 4.2. After enough recursive splitting, all the sub-systems are of effectively trivial size, e.g. 1×1 in the bottom layer of Fig. 4.2, to solve all the unknowns in parallel. This means that PCR solves the linear system in a single forward pass and does not require a backward substitution phase.

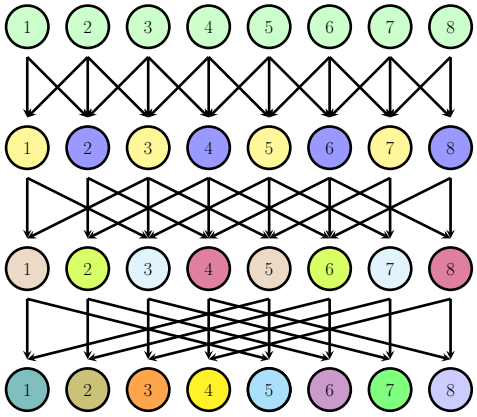

Figure 4.2: Communication pattern of PCR for an 8×8 non-cyclic tridiagonal system. The sub-systems in each step are grouped by the same colors.

Recent works have optimized both CR and PCR for modern parallel computing architectures and have achieved considerable performance improvements for specific applications. For example, a GPU implementation is suggested by Zhang et al. (2010) [183], and the works of Hirshman et al. (2010) [63] and Seal et al. (2013) [138] improve the algorithm for block tridiagonal systems with large dense blocks. Nevertheless, most of the general PCR solvers are implemented for shared memory data access, and few improved algorithms have comprehensively considered data partitioning for distributed memory. The parallel linear solver developed in this chapter to solve the banded system is based on the concepts of CR and PCR, and optimized for grid decomposition on distributed memory as shown in Fig. 4.1. These banded systems are typically (block) tridiagonal or (block) pentadiagonal systems, but the present algorithm can be extended to wider bandwidths.

4.2 Generalized parallel cyclic reduction method

Beyond the tridiagonal system, PCR can be easily generalized to compact banded systems with arbitrary bandwidth. In order to form two sub-systems grouped by even and odd rows, each row in the parent system, after a reduction step, is staggered with a zero entry between any of the two non-zero entries on the diagonal and off-diagonals, as shown in Fig. 4.3. In the generalized PCR approach, the total number of neighboring rows involved in eliminating the entries in row i equals the number of off-diagonal elements. And the resulting row i is the linear combination of row i and the neighboring rows.

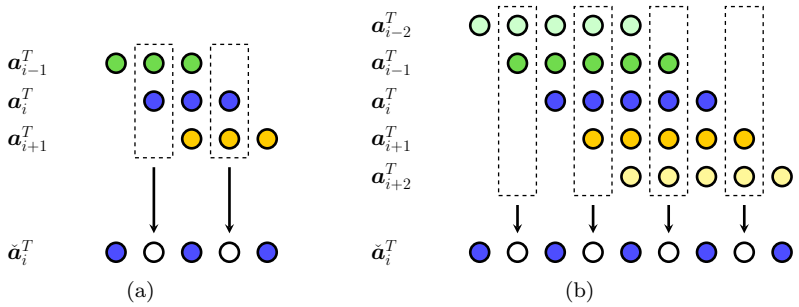

Figure 4.3: Example of one step in generalized PCR: (a) tridiagonal system; (b) penta-diagonal system. The colored circles are non-identically-zero entries and the uncolored circles are identically-zero entries.

Let $\boldsymbol{a}_i^T$ be the i-th row vector in the parent matrix, and the reduction operation to obtain the i-th row vector in the resulted matrix, $\check{\boldsymbol{a}}_i^T$, can be expressed as

$$\check{\boldsymbol{a}}_i^T = \boldsymbol{a}_i^T - \sum_{j=1}^{(w-1)/2} \left(k_{+j} \boldsymbol{a}_{i+j}^T + k_{-j} \boldsymbol{a}_{i-j}^T \right) \tag{4.3}$$

where w is the bandwidth of the compact banded system. During a reduction step, each of the zero staggered entries can be formed with a unique linear combination of the involved neighboring row vectors, as shown by the boxed columns in Fig. 4.3. The coefficients, k_{+j} and k_{-j} can be solved from the linear system described in Eq. (4.4).

$$\begin{bmatrix}
\ddots & \ddots & \ddots & & & & \\
\cdots & a_{i-2,i-3} & a_{i-1,i-3} & \cdots & & & \\
\cdots & a_{i-2,i-1} & a_{i-1,i-1} & a_{i+1,i-1} & \cdots & & \\
 & \cdots & a_{i-1,i+1} & a_{i+1,i+1} & a_{i+2,i+1} & \cdots \\
 & & \cdots & a_{i+1,i+3} & a_{i+2,i+3} & \cdots \\
 & & & \ddots & \ddots & \ddots
\end{bmatrix}
\begin{bmatrix} \vdots \\ k_{-2} \\ k_{-1} \\ k_{+1} \\ k_{+2} \\ \vdots \end{bmatrix}
=
\begin{bmatrix} \vdots \\ a_{i,i-3} \\ a_{i,i-1} \\ a_{i,i+1} \\ a_{i,i+3} \\ \vdots \end{bmatrix} \tag{4.4}$$

Specifically, for a tridiagonal parent system ($w = 3$), k_{+j} and k_{-j} for each row i are governed by a 2×2 diagonal system shown in Eq. (4.5). For a penta-diagonal parent system ($w = 5$), $a_{i,i-3} = a_{i,i+3} = 0$ for each row i, and k_{+j} and k_{-j} are governed by a 4×4 tridiagonal system described in Eq. (4.6).

$$\begin{bmatrix} a_{i-1,i-1} & \\ & a_{i+1,i+1} \end{bmatrix} \begin{bmatrix} k_{-1} \\ k_{+1} \end{bmatrix} = \begin{bmatrix} a_{i,i-1} \\ a_{i,i+1} \end{bmatrix} \tag{4.5}$$

$$\begin{bmatrix} a_{i-2,i-3} & a_{i-1,i-3} & & \\ a_{i-2,i-1} & a_{i-1,i-1} & a_{i+1,i-1} & \\ & a_{i-1,i+1} & a_{i+1,i+1} & a_{i+2,i+1} \\ & & a_{i+1,i+3} & a_{i+2,i+3} \end{bmatrix} \begin{bmatrix} k_{-2} \\ k_{-1} \\ k_{+1} \\ k_{+2} \end{bmatrix} = \begin{bmatrix} 0 \\ a_{i,i-1} \\ a_{i,i+1} \\ 0 \end{bmatrix} \tag{4.6}$$

4.3 Parallel linear solver for compact banded system

This section will introduce the parallel direct solver used for solving compact banded linear systems with the data partitioned on distributed memory. Consistent with the grid decomposition pattern in Fig. 4.1, the compact banded linear system, $\boldsymbol{A}\boldsymbol{x} = \boldsymbol{b}$, is also correspondingly decomposed into a sparse block tridiagonal system [149] shown in Fig. 4.4. The data in $\boldsymbol{x}$ and $\boldsymbol{b}$ are stored in distributed memory. Typically, applications require solving multiple systems with the same $\boldsymbol{A}$ matrix, like in Fig. 4.1. Then, $\boldsymbol{x}$ and $\boldsymbol{b}$ can be a batch of vectors forming an $N \times M$ matrix where M is the number of independent solutions needed. The subscripts in Fig. 4.4 indicate the rank of the aligned grid decomposition. Each rank has access to the data stored in its shared memory, the boundaries of which are indicated by dotted lines. $\widetilde{\boldsymbol{D}}_i$ is an $r \times r$ dense square matrix whose dimension, r, is equal to half the number of off-diagonal bands in the linear system, $(w-1)/2$. For a tridiagonal system ($w = 3$), $\widetilde{\boldsymbol{D}}_i$ is 1×1, and for a penta-diagonal system ($w = 5$), $\widetilde{\boldsymbol{D}}_i$ is 2×2, etc. $\widetilde{\boldsymbol{L}}_i$ and $\widetilde{\boldsymbol{U}}_i$ are short, fat blocks, and $\boldsymbol{L}_i$ and $\boldsymbol{U}_i$ are tall, skinny blocks. $\boldsymbol{D}_i$ is a large, square, non-cyclic, banded block.

According to this grouping strategy, as shown in Fig. 4.4, two equations are formed within each partition.

$$\widetilde{\boldsymbol{L}}_i \boldsymbol{x}_{i-1} + \widetilde{\boldsymbol{D}}_i \widetilde{\boldsymbol{x}}_i + \widetilde{\boldsymbol{U}}_i \boldsymbol{x}_i = \widetilde{\boldsymbol{b}}_i \tag{4.7}$$

$$\boldsymbol{L}_i \widetilde{\boldsymbol{x}}_i + \boldsymbol{D}_i \boldsymbol{x}_i + \boldsymbol{U}_i \widetilde{\boldsymbol{x}}_{i+1} = \boldsymbol{b}_i \tag{4.8}$$

Assuming $\boldsymbol{D}_i$ is invertible – which is true for the linear systems formed from compact schemes – then $\boldsymbol{x}_i$ can be obtained if both $\widetilde{\boldsymbol{x}}_i$ and $\widetilde{\boldsymbol{x}}_{i-1}$ are known.

$$\boldsymbol{x}_i = \boldsymbol{D}_i^{-1} \left[\boldsymbol{b}_i - \boldsymbol{L}_i \widetilde{\boldsymbol{x}}_i - \boldsymbol{U}_i \widetilde{\boldsymbol{x}}_{i+1} \right] \tag{4.9}$$

Following the logic of CR, Eq. (4.9) can be used to eliminate $\boldsymbol{x}_{i-1}$ and $\boldsymbol{x}_i$ in Eq. (4.7), which forms

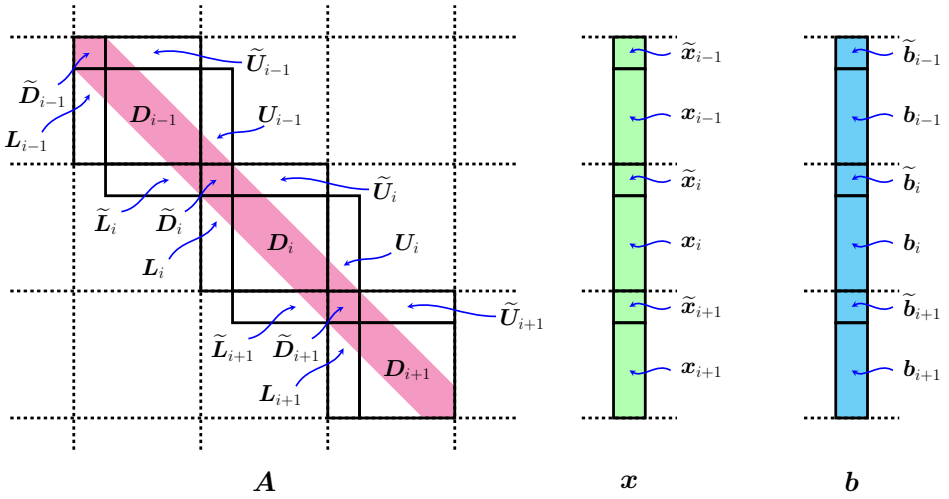

Figure 4.4: Partitioned linear system.

a sub-system, or a reduced system, shown in Eq. (4.10).

$$\widehat{\boldsymbol{L}}_i\widetilde{\boldsymbol{x}}_{i-1} + \widehat{\boldsymbol{D}}_i\widetilde{\boldsymbol{x}}_i + \widehat{\boldsymbol{U}}_i\widetilde{\boldsymbol{x}}_{i+1} = \widehat{\boldsymbol{b}}_i \tag{4.10}$$

where

$$\widehat{\boldsymbol{L}}_i = -\widetilde{\boldsymbol{L}}_i\boldsymbol{D}_{i-1}^{-1}\boldsymbol{L}_{i-1} \tag{4.11}$$

$$\widehat{\boldsymbol{D}}_i = \widetilde{\boldsymbol{D}}_i - \widetilde{\boldsymbol{L}}_i\boldsymbol{D}_{i-1}^{-1}\boldsymbol{U}_{i-1} - \widetilde{\boldsymbol{U}}_i\boldsymbol{D}_i^{-1}\boldsymbol{L}_i \tag{4.12}$$

$$\widehat{\boldsymbol{U}}_i = -\widetilde{\boldsymbol{U}}_i\boldsymbol{D}_i^{-1}\boldsymbol{U}_i \tag{4.13}$$

$$\widehat{\boldsymbol{b}}_i = \widetilde{\boldsymbol{b}}_i - \widetilde{\boldsymbol{L}}_i\boldsymbol{D}_{i-1}^{-1}\boldsymbol{b}_{i-1} - \widetilde{\boldsymbol{U}}_i\boldsymbol{D}_i^{-1}\boldsymbol{b}_i \tag{4.14}$$

Eq. (4.10) can be represented as $\widehat{\boldsymbol{A}}\widetilde{\boldsymbol{x}} = \widehat{\boldsymbol{b}}$, where $\widehat{\boldsymbol{A}}$ is a block tridiagonal system. If $\boldsymbol{A}$ is cyclic, then $\widehat{\boldsymbol{A}}$ is also cyclic. Considering the grid decomposition strategy, each block in $\widetilde{\boldsymbol{x}}_i$ or $\widehat{\boldsymbol{b}}_i$ is stored across distributed memory, and each block can be solved efficiently with PCR. This data storage pattern is favorable to PCR because the blocks can be easily located by the rank of the aligned grid decomposition to conduct the data transfer across the distributed memory. Once the sub-system is solved, all the $\widetilde{\boldsymbol{x}}_i$ are known, and the results can be propagated backward to solve $\boldsymbol{x}_i$ in parallel.

The method can be also interpreted as a block LU-factorization, analogous to the illustration in Gander & Golub (1997) [51]. Introducing a permutation matrix, $\boldsymbol{P}$, the linear system, $\boldsymbol{Ax} = \boldsymbol{b}$, can be modified to $(\boldsymbol{PAP}^T)(\boldsymbol{Px}) = \boldsymbol{Pb}$, where the row and column permutations, $\boldsymbol{PAP}^T$, regroup $\boldsymbol{D}_i$ and $\widetilde{\boldsymbol{D}}_i$ respectively. The resulting pattern is shown in Fig. 4.5b. The $\boldsymbol{D}_i$ blocks remain in the top left region on the diagonal, and the $\widetilde{\boldsymbol{D}}_i$ blocks are moved to the bottom right region also on the diagonal. Correspondingly, the $\widetilde{\boldsymbol{L}}_i$ and $\widetilde{\boldsymbol{U}}_i$ blocks show up in the bottom left region, and the $\boldsymbol{L}_i$ and

$\boldsymbol{U}_i$ blocks are placed in the top right region. The process of obtaining Eq. (4.10) is block Gaussian elimination. As a result, the permuted system becomes a block upper triangular system as shown in Fig. 4.5c, and the sub-system $\widehat{\boldsymbol{A}}$ is formed as the last diagonal block. Additionally, it is clearly shown in Fig. 4.5c that the top left region only contains the diagonal located blocks, $\boldsymbol{D}_i$. All the non-diagonal blocks link $\boldsymbol{D}_i$ with $\widehat{\boldsymbol{A}}$ only, and no coupling is created among different $\boldsymbol{D}_i$ blocks. This reaffirms that once the sub-system, $\widehat{\boldsymbol{A}}\widetilde{x} = \widehat{\boldsymbol{b}}$, is solved, then the remaining sub-system, formed by Eq. (4.8), can be solved in parallel on each data partition.

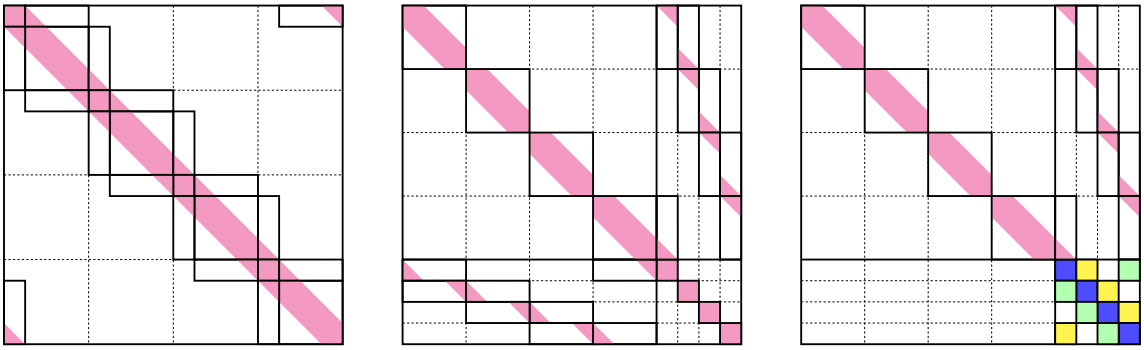

Figure 4.5: Sparsity patterns of the system during permutation and block LU-factorization. (a) is the original matrix $\boldsymbol{A}$; (b) is the permuted matrix $\boldsymbol{PAP}^T$; and (c) is the block upper triangular matrix obtained via the block LU-factorization from $\boldsymbol{PAP}^T$.

The following section discusses the solution methods for the sub-system, $\widehat{\boldsymbol{A}}\widetilde{\boldsymbol{x}} = \widehat{\boldsymbol{b}}$. As aforementioned, $\widehat{\boldsymbol{A}}$ is a block tridiagonal system that may be cyclic depending on the original banded system, $\boldsymbol{A}$. The block size depends on the half bandwidth of $\boldsymbol{A}$, and the dimension of $\widehat{\boldsymbol{A}}$ equals the number of the aligned grid partitions. The "dimension" of $\widehat{\boldsymbol{A}}$ refers to the number of blocks in each row and column of $\widehat{\boldsymbol{A}}$. Each block in $\widetilde{\boldsymbol{x}}$ and $\widehat{\boldsymbol{b}}$ is stored in a unique partition. With non-periodic boundaries, $\widehat{\boldsymbol{A}}$ is acyclic, and the solution methods will follow the block PCR in a fairly straightforward way. With periodic boundaries, $\widehat{\boldsymbol{A}}$ is cyclic, so a non-zero block will show up in the top right and bottom left corners. In this case, if the dimension of $\widehat{\boldsymbol{A}}$ is a power of two, PCR can directly be applied. PCR can still be applied for cyclic $\widehat{\boldsymbol{A}}$ of arbitrary dimension using special treatment. Sweet, in his work [154], suggests such a treatment for cyclic block tridiagonal systems. However, considering the complexity of data storage and data migration, a different treatment is proposed in this paper which requires the dimension of a sub-system of $\widehat{\boldsymbol{A}}$ undergoing a PCR step to be even. If the dimension is odd, a detaching step is needed before the PCR step. During the detaching step, the last row of each sub-system will be used to eliminate the upper and lower off-diagonal blocks of the previous row and the first row of the same sub-system respectively and then detached from the sub-system. For periodicity, the lower diagonal block in the first row is placed in the last column. After this step, the dimension of each sub-system is an even number, which is ready for the next PCR step.

The detached rows will then be addressed and reattached to the sub-system through a backward substitution phase after the rows are solved.

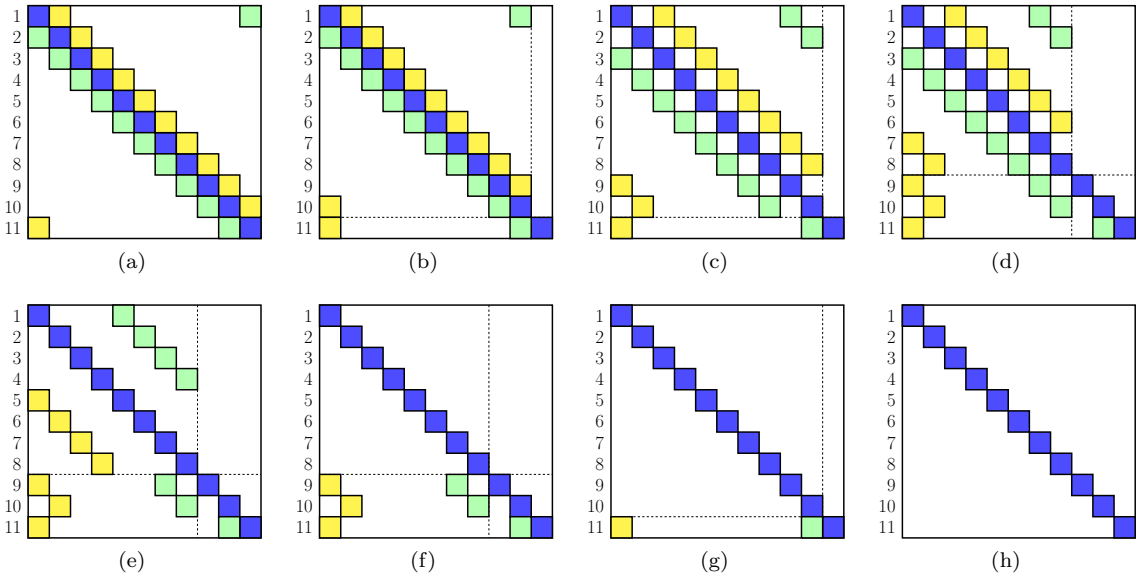

Figure 4.6: Reduction procedure of an 11×11 $\widehat{\boldsymbol{A}}$. From (a) to (b), the row 11 is detached from the sub-system; from (b) to (c), two sub-systems are formed by a PCR step; from (c) to (d), row 9 and row 10 are detached from the sub-systems; from (d) to (f), all the eight unknowns in the sub-systems are solved; from (f) to (g), solutions backward propagate to the first level to solve row 9 and row 10; from (g) to (h), solutions backwards propagate to the root level to solve row 11.

An example is provided by setting $\widehat{\boldsymbol{A}}$ to be a 11×11 cyclic tridiagonal matrix. The sparsity pattern in each step is visualized in Fig. 4.6, and the communication pattern is shown in Fig. 4.7. At the root level, the number of sub-systems is 1, and the dimension is 11. Since the dimension of this subsystem is odd, the last row needs to detach from the sub-system before conducting PCR. The last row can be used to eliminate the upper off-diagonal element of the tenth row and the lower off-diagonal element of the first row, so that a 10×10 sub-system is created and the last row is detached, as shown in Fig. 4.6b. After a PCR step, the 10×10 sub-system is split into two 5×5 sub-systems on the first level, as shown in Fig. 4.6c. Before conducting PCR on the first level, the last row of each of the two sub-systems (row 9 and row 10) needs to be detached. Row 9 is used to eliminate the upper off-diagonal element of row 7 (the second-to-last row of its sub-system on this level) and the lower off-diagonal element of row 1. Row 10 is used to eliminate the upper off-diagonal element of row 8 and the lower diagonal element of row 2 (the first row of its sub-system on this level), so the two sub-systems are reduced to 4×4 from 5×5 as shown in Fig. 4.6d. Starting from this level, the number of rows involved in the remaining PCR steps is eight, which is a power of two. At this point, no further detachment is needed, and all the eight unknowns can be solved by two steps of PCR. Then, the eight solutions are substituted backwards into the two 5×5 sub-systems on

the first level to solve row 9 and row 10. In the final step, the ten solutions propagate backwards to the root level and are substituted into the 11×11 system to solve row 11 so that all the unknowns are solved.

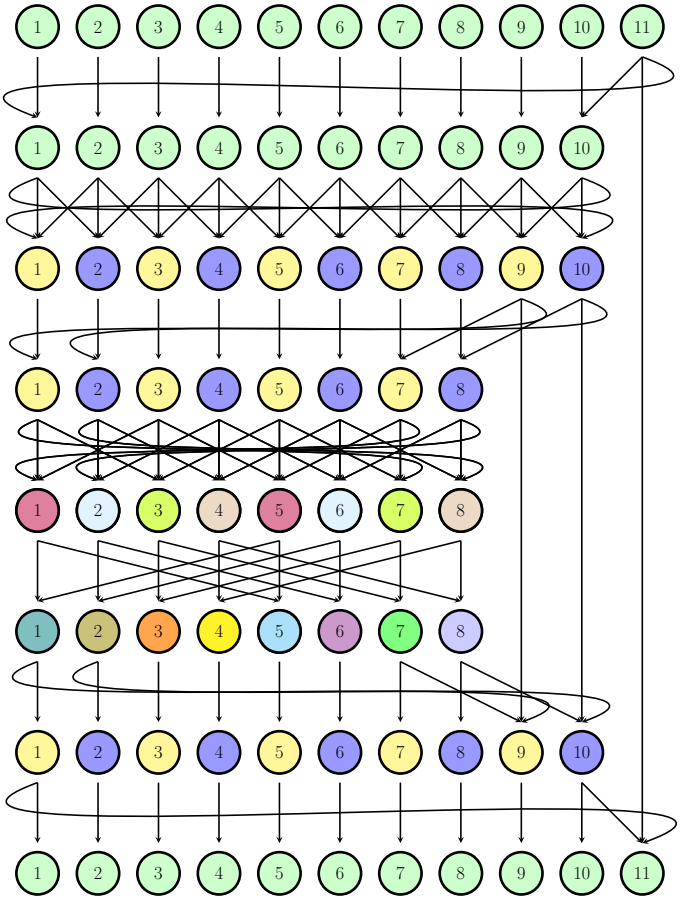

Figure 4.7: Communication pattern of PCR for an 11×11 cyclic tridiagonal system. The subsystems in each step are grouped by the same colors.

4.4 Implementation details

The terms $\boldsymbol{D}_i^{-1}\boldsymbol{L}_i$, $\boldsymbol{D}_i^{-1}\boldsymbol{U}_i$, and $\boldsymbol{D}_i^{-1}\boldsymbol{b}_i$, in Eq. (4.11) – Eq. (4.14), are computed by solving the following linear systems for $\boldsymbol{S}_i$, $\boldsymbol{R}_i$, and $\boldsymbol{y}_i$ respectively.

$$\boldsymbol{D}_i\boldsymbol{S}_i = \boldsymbol{L}_i \tag{4.15}$$

$$\boldsymbol{D}_i\boldsymbol{R}_i = \boldsymbol{U}_i \tag{4.16}$$

$$\boldsymbol{D}_i\boldsymbol{y}_i = \boldsymbol{b}_i \tag{4.17}$$

Based on the proposed approach, $\boldsymbol{D}_i$ is an acyclic, compact banded matrix, and all the data on the right-hand-side and the unknowns to be solved are stored in the same partition. Therefore, generalized PCR can be used to further parallelize these solves. Using generalized PCR to solve $\boldsymbol{S}_i$, $\boldsymbol{R}_i$, and $\boldsymbol{y}_i$, the number of the parallel reduction steps for each system is $\lceil \log_2 N_i \rceil$, where N_i is the dimension of $\boldsymbol{D}_i$. All the operations at this stage are conducted on the shared memory simultaneously on each partition. Substituting $\boldsymbol{S}_i$, $\boldsymbol{R}_i$, and $\boldsymbol{y}_i$ into Eq. (4.11) – Eq. (4.14), the reduced system – Eq. (4.10) – can be practically constructed according to the following equations.

$$\widehat{\boldsymbol{L}}_i = -\widetilde{\boldsymbol{L}}_i \boldsymbol{S}_{i-1} \tag{4.18}$$

$$\widehat{\boldsymbol{D}}_i = \widetilde{\boldsymbol{D}}_i - \widetilde{\boldsymbol{L}}_i \boldsymbol{R}_{i-1} - \widetilde{\boldsymbol{U}}_i \boldsymbol{S}_i \tag{4.19}$$

$$\widehat{\boldsymbol{U}}_i = -\widetilde{\boldsymbol{U}}_i \boldsymbol{R}_i \tag{4.20}$$

$$\widehat{\boldsymbol{b}}_i = \widetilde{\boldsymbol{b}}_i - \widetilde{\boldsymbol{L}}_i \boldsymbol{y}_{i-1} - \widetilde{\boldsymbol{U}}_i \boldsymbol{y}_i \tag{4.21}$$

Following the proposed approach to solve for $\widetilde{\boldsymbol{x}}_i$ and substituting into Eq. (4.9), $\boldsymbol{x}_i$ can be obtained by the following operation.

$$\boldsymbol{x}_i = \boldsymbol{y}_i - \boldsymbol{S}_i \widetilde{\boldsymbol{x}}_i - \boldsymbol{R}_i \widetilde{\boldsymbol{x}}_{i+1} \tag{4.22}$$

A sample implementation is shown in Algorithm 1 where the detaching step, block PCR step, and reattaching step are shown in Algorithms 2, 3, and 4, respectively. The sample code is given in the MPI (message passing interface) style where the rank of partition starts from zero.

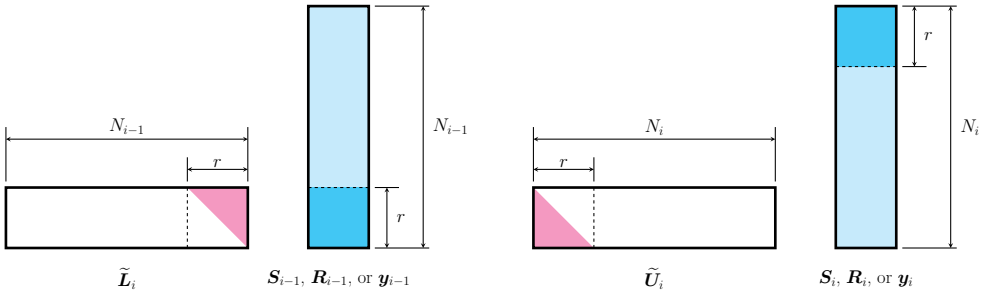

Figure 4.8: Communication and multiplication patterns: (a) $\widetilde{\boldsymbol{L}}_i \boldsymbol{S}_{i-1}$, $\widetilde{\boldsymbol{L}}_i \boldsymbol{R}_{i-1}$, and $\widetilde{\boldsymbol{L}}_i \boldsymbol{y}_{i-1}$; (b) $\widetilde{\boldsymbol{U}}_i \boldsymbol{S}_i$, $\widetilde{\boldsymbol{U}}_i \boldsymbol{R}_i$, and $\widetilde{\boldsymbol{U}}_i \boldsymbol{y}_i$

Throughout the solution process, the terms $\widetilde{\boldsymbol{L}}_i \boldsymbol{S}_{i-1}$, $\widetilde{\boldsymbol{L}}_i \boldsymbol{R}_{i-1}$, and $\widetilde{\boldsymbol{L}}_i \boldsymbol{y}_{i-1}$ require data transfer from partition $i-1$ to i, and the term $\boldsymbol{R}_i \widetilde{\boldsymbol{x}}_{i+1}$ implies the data transfer from partition $i+1$ to i. It is important to emphasize that the sparsity pattern of the matrix $\widetilde{\boldsymbol{L}}_i$ results in only a fraction of the allocated data in $\boldsymbol{y}_{i-1}$, $\boldsymbol{R}_{i-1}$ and $\boldsymbol{S}_{i-1}$ being exchanged across neighboring data partitions as illustrated in Fig. 4.5b and Fig. 4.8a. For the banded matrix $\boldsymbol{A}$ with a bandwidth of $w = 2r+1$, only the last r columns in $\widetilde{\boldsymbol{L}}_i$ are non-trivial. Therefore, only the last r columns in $\boldsymbol{S}_{i-1}$, $\boldsymbol{R}_{i-1}$, and $\boldsymbol{y}_{i-1}$

Algorithm 1: Implementation of in-place solver following the partitioning shown in Figure 4.4. The index i is the rank of partition of the distributed memory sub-group involved in the linear system and is zero-based. The number of distributed memory chunks in the linear system is given by p.

in : $\boldsymbol{D}_i$, $\widetilde{\boldsymbol{L}}_i$, $\widetilde{\boldsymbol{U}}_i$, i, p
in/out: $\boldsymbol{W}_i \leftarrow \widetilde{\boldsymbol{D}}_i$, $\boldsymbol{Y}_i \leftarrow \boldsymbol{L}_i$, $\boldsymbol{Z}_i \leftarrow \boldsymbol{U}_i$, $\boldsymbol{x}_i \leftarrow \boldsymbol{b}_i$, $\widetilde{\boldsymbol{x}}_i \leftarrow \widetilde{\boldsymbol{b}}_i$

/* Factorization */
$\boldsymbol{Y}_i \leftarrow$ generalizedPCR($\boldsymbol{D}_i$, $\boldsymbol{Y}_i$);
$\boldsymbol{Z}_i \leftarrow$ generalizedPCR($\boldsymbol{D}_i$, $\boldsymbol{Z}_i$);
tag $\leftarrow$ sendToPartition(send_buffer $= \{\boldsymbol{Y}_i, \boldsymbol{Z}_i\}$, dest_rank $= (i+1) \mod p$);
$\widehat{\boldsymbol{U}}_i \leftarrow -\widetilde{\boldsymbol{U}}_i \boldsymbol{Z}_i$;
$\{\boldsymbol{Y}_i, \boldsymbol{Z}_i\} \leftarrow$ getFromPartition(tag, src_rank $= (p+i-1) \mod p$);
$\widehat{\boldsymbol{L}}_i \leftarrow -\widetilde{\boldsymbol{L}}_i \boldsymbol{Y}_{i-1}$;
$\boldsymbol{W}_i \leftarrow \boldsymbol{W}_i - \widetilde{\boldsymbol{L}}_i \boldsymbol{Z}_{i-1} - \widetilde{\boldsymbol{U}}_i \boldsymbol{Y}_i$;
/* Solve reduced system */
$\boldsymbol{x}_i \leftarrow$ generalizedPCR($\boldsymbol{D}_i$, $\boldsymbol{x}_i$);
tag $\leftarrow$ sendToPartition(send_buffer $= \boldsymbol{x}_i$, dest_rank $= (i+1) \mod p$);
$\boldsymbol{x}_{i-1} \leftarrow$ getFromPartition(tag, src_rank $= (p+i-1) \mod p$);
$\widetilde{\boldsymbol{x}}_i \leftarrow \widetilde{\boldsymbol{x}}_i - \widetilde{\boldsymbol{L}}_i \boldsymbol{x}_{i-1} - \widetilde{\boldsymbol{U}}_i \boldsymbol{x}_i$;
$s \leftarrow 1$; // stride as well as the number of sub-systems
$n_0 \leftarrow p$; // size of each sub-system in the current PCR step
$n_a \leftarrow p$; // number of attached rows in the PCR step $n_a \equiv s \times n_0$
$\mathcal{S} \leftarrow$ initEmptyStack(); // a stack of boolean
while $n_0 > 1$ **do**
  $\mathcal{S} \leftarrow$ stackPush($n_0 \mod 2 > 0$);
  if $n_0 \mod 2 > 0$ **then**
    $n_0 \leftarrow n_0 - 1$;
    $n_a \leftarrow n_a - s$;
    Detach the last row of each sub-system (See Algorithm 2);
  end
  Block PCR step (See Algorithm 3);
  $s \leftarrow s \times 2$;
  $n_0 \leftarrow n_0/2$;
end
if $i < n_a$ **then**
  $\widetilde{\boldsymbol{x}}_i \leftarrow \boldsymbol{W}_i^{-1} \widetilde{\boldsymbol{x}}_i$;
end
while isNotEmpty($\mathcal{S}$) **do**
  $n_0 \leftarrow n_0 \times 2$;
  $s \leftarrow s/2$;
  if stackPop($\mathcal{S}$) **then**
    Reattach the last row of each sub-system (See Algorithm 4);
    $n_a \leftarrow n_a + s$;
    $n_0 \leftarrow n_0 + 1$;
  end
end
tag $\leftarrow$ sendToPartition(send_buffer $= \widetilde{\boldsymbol{x}}_i$, dest_rank $= (p+i-1) \mod p$);
$\widetilde{\boldsymbol{x}}_{i+1} \leftarrow$ getFromPartition(tag, src_rank $= (i+1) \mod p$);
$\boldsymbol{x}_i \leftarrow \boldsymbol{x}_i - \boldsymbol{Y}_i \widetilde{\boldsymbol{x}}_i - \boldsymbol{Z}_i \widetilde{\boldsymbol{x}}_{i+1}$;

Algorithm 2: Detaching process in Algorithm 1.

if $n_a \leq i < (n_a + s)$ **then**
  tag_a $\leftarrow$ sendToPartition(send_buffer $= \{\widehat{\boldsymbol{L}}_i, \boldsymbol{W}_i, \widehat{\boldsymbol{U}}_i, \widetilde{\boldsymbol{x}}_i\}$, dest_rank $= i - s$);
  tag_b $\leftarrow$ sendToPartition(send_buffer $= \{\widehat{\boldsymbol{L}}_i, \boldsymbol{W}_i, \widehat{\boldsymbol{U}}_i, \widetilde{\boldsymbol{x}}_i\}$, dest_rank $= i - n_a$);
end
if $n_a \leq (i + s) < (n_a + s)$ **then**
  $\{\widehat{\boldsymbol{L}}_{i+s}, \boldsymbol{W}_{i+s}, \widehat{\boldsymbol{U}}_{i+s}, \widetilde{\boldsymbol{x}}_{i+s}\} \leftarrow$ getFromPartition(tag_a, src_rank $= i + s$);
  $\boldsymbol{W}_i \leftarrow \boldsymbol{W}_i - \widehat{\boldsymbol{U}}_i \boldsymbol{W}_{i+s}^{-1} \widehat{\boldsymbol{L}}_{i+s}$;
  $\widetilde{\boldsymbol{x}}_i \leftarrow \widetilde{\boldsymbol{x}}_i - \widehat{\boldsymbol{U}}_i \boldsymbol{W}_{i+s}^{-1} \widetilde{\boldsymbol{x}}_{i+s}$;
  $\widehat{\boldsymbol{U}}_i \leftarrow -\widehat{\boldsymbol{U}}_i \boldsymbol{W}_{i+s}^{-1} \widehat{\boldsymbol{U}}_{i+s}$;
end
if $n_a \leq (i + n_a) < (n_a + s)$ **then**
  $\{\widehat{\boldsymbol{L}}_{i-s}, \boldsymbol{W}_{i-s}, \widehat{\boldsymbol{U}}_{i-s}, \widetilde{\boldsymbol{x}}_{i-s}\} \leftarrow$ getFromPartition(tag_b, src_rank $= i + n_a$);
  $\boldsymbol{W}_i \leftarrow \boldsymbol{W}_i - \widehat{\boldsymbol{L}}_i \boldsymbol{W}_{i-s}^{-1} \widehat{\boldsymbol{U}}_{i-s}$;
  $\widetilde{\boldsymbol{x}}_i \leftarrow \widetilde{\boldsymbol{x}}_i - \widehat{\boldsymbol{L}}_i \boldsymbol{W}_{i-s}^{-1} \widetilde{\boldsymbol{x}}_{i-s}$;
  $\widehat{\boldsymbol{L}}_i \leftarrow -\widehat{\boldsymbol{L}}_i \boldsymbol{W}_{i-s}^{-1} \widehat{\boldsymbol{L}}_{i-s}$;
end

Algorithm 3: Block PCR process in Algorithm 1.

if $i < n_a$ **then**
  tag_a $\leftarrow$ sendToPartition(send_buffer $= \{\widehat{\boldsymbol{L}}_i, \boldsymbol{W}_i, \widehat{\boldsymbol{U}}_i, \widetilde{\boldsymbol{x}}_i\}$, dest_rank $= (n_a + i - s) \mod n_a$);
  tag_b $\leftarrow$ sendToPartition(send_buffer $= \{\widehat{\boldsymbol{L}}_i, \boldsymbol{W}_i, \widehat{\boldsymbol{U}}_i, \widetilde{\boldsymbol{x}}_i\}$, dest_rank $= (i + s) \mod n_a$);
  $\{\widehat{\boldsymbol{L}}_{i+s}, \boldsymbol{W}_{i+s}, \widehat{\boldsymbol{U}}_{i+s}, \widetilde{\boldsymbol{x}}_{i+s}\} \leftarrow$ getFromPartition(tag_a, src_rank $= (i + s) \mod n_a$);
  $\{\widehat{\boldsymbol{L}}_{i-s}, \boldsymbol{W}_{i-s}, \widehat{\boldsymbol{U}}_{i-s}, \widetilde{\boldsymbol{x}}_{i-s}\} \leftarrow$ getFromPartition(tag_b, src_rank $= (n_a + i - s) \mod n_a$);
  $\boldsymbol{W}_i \leftarrow \boldsymbol{W}_i - \widehat{\boldsymbol{U}}_i \boldsymbol{W}_{i+s}^{-1} \widehat{\boldsymbol{L}}_{i+s} - \widehat{\boldsymbol{L}}_i \boldsymbol{W}_{i-s}^{-1} \widehat{\boldsymbol{U}}_{i-s}$;
  $\widetilde{\boldsymbol{x}}_i \leftarrow \widetilde{\boldsymbol{x}}_i - \widehat{\boldsymbol{U}}_i \boldsymbol{W}_{i+s}^{-1} \widetilde{\boldsymbol{x}}_{x+s} - \widehat{\boldsymbol{L}}_i \boldsymbol{W}_{i-s}^{-1} \widetilde{\boldsymbol{x}}_{i-s}$;
  $\widehat{\boldsymbol{L}}_i \leftarrow -\widehat{\boldsymbol{L}}_i \boldsymbol{W}_{i-s}^{-1} \widehat{\boldsymbol{L}}_{i-s}$;
  $\widehat{\boldsymbol{U}}_i \leftarrow -\widehat{\boldsymbol{U}}_i \boldsymbol{W}_{i+s}^{-1} \widehat{\boldsymbol{U}}_{i+s}$;
end

Algorithm 4: Reattaching process in Algorithm 1.

if $n_a \leq (i+s) < (n_a+s)$ **then**
  tag_b $\leftarrow$ sendToPartition(send_buffer $= \widetilde{\boldsymbol{x}}_i$, dest_rank $= i+s$);
end
if $n_a \leq (i+n_a) < (n_a+s)$ **then**
  tag_a $\leftarrow$ sendToPartition(send_buffer $= \widetilde{\boldsymbol{x}}_i$, dest_rank $= i+n_a$);
end
if $n_a \leq i < (n_a+s)$ **then**
  $\widetilde{\boldsymbol{x}}_{i+s} \leftarrow$ getFromPartition(tag_a, src_rank $= i-n_a$);
  $\widetilde{\boldsymbol{x}}_{i-s} \leftarrow$ getFromPartition(tag_b, src_rank $= i-s$);
  $\widetilde{\boldsymbol{x}}_i \leftarrow \widetilde{\boldsymbol{x}}_i - \widehat{\boldsymbol{L}}_i\widetilde{\boldsymbol{x}}_{i-s} - \widehat{\boldsymbol{U}}_i\widetilde{\boldsymbol{x}}_{i+s}$;
  $\widetilde{\boldsymbol{x}}_i \leftarrow \boldsymbol{W}_i^{-1}\widetilde{\boldsymbol{x}}_i$;
end

are needed for communication between neighbors. Similarly, the matrix products involving $\boldsymbol{U}_i$ can be computed very efficiently due to its sparsity pattern as shown in Fig. 4.8b. If the number of rows in each partition is much larger than the system bandwidth ($N_i \gg r$), significant reduction of data size for communication and multiplication can be achieved. The reduced system $\widehat{\boldsymbol{A}}\widetilde{\boldsymbol{x}} = \widehat{\boldsymbol{b}}$ (Eq. (4.10)) is solved on distributed memory, and each parallel reduction step requires data communication between neighboring partitions. If $\boldsymbol{A}$ is acyclic, then $\widehat{\boldsymbol{A}}$ can be solved with classic block PCR, although the proposed algorithm can still be used by setting the cyclic entries to zero, and the number of parallel reduction steps is $\lceil \log_2 p \rceil$, where p is the number of partitions. If $\boldsymbol{A}$ is cyclic, using the proposed algorithm, the number of parallel reduction steps is $\lfloor \log_2 p \rfloor$. In addition, if p is not a power of 2, the number of rows that are involved in the detaching and reattaching throughout the solving process equals $p - 2^{\lfloor \log_2 p \rfloor}$, and the number of parallel detaching and reattaching steps are $\left\{ \sum_{n=0}^{\lfloor \log_2 p \rfloor} \left(\lfloor 2^{-n} p \rfloor \mod 2 \right) \right\} - 1$.

In motivating applications, such as evaluating derivatives using compact finite difference schemes in a multiphysics application, $\boldsymbol{A}\boldsymbol{x} = \boldsymbol{b}$ is frequently solved with varying $\boldsymbol{b}$ but constant $\boldsymbol{A}$. Noticing that the construction of $\widehat{\boldsymbol{L}}_i$, $\widehat{\boldsymbol{D}}_i$, $\widehat{\boldsymbol{U}}_i$, and $\boldsymbol{D}_i$, does not require the right-hand side, $\boldsymbol{b}$, such construction is needed only once, and the original matrix can be pre-factorized. During the pre-factorization, the reduction coefficients on each stage, k_{+j} and k_{-j}, and the information needed to solve $\widehat{\boldsymbol{A}}\widetilde{\boldsymbol{x}} = \widehat{\boldsymbol{b}}$, can be calculated and stored. During the solution process, Eq. (4.17) and Eq. (4.21) are needed to construct the right-hand-side of the reduced system to solve for $\widetilde{\boldsymbol{x}}_i$. Finally, Eq. (4.22) is used to solve for $\boldsymbol{x}_i$.

4.5 Performance

4.5.1 Asymptotic performance analysis

This section describes the asymptotic analysis of compute and communication scaling for the proposed algorithm. As described in Section 4.3 and 4.4, consider the system $\boldsymbol{A}\boldsymbol{x} = \boldsymbol{b}$ where $\boldsymbol{A}$ is an $N \times N$ cyclic compact banded matrix with bandwidth $2r+1$. $\boldsymbol{x}$ and $\boldsymbol{b}$ are $N \times M$ matrices representing M independent solutions and right-hand-side vectors respectively. This system is partitioned across p distributed memory processes, and the local system for process i, $\boldsymbol{D}_i$, is of size $N_i \times N_i$.

The algorithm can be grouped into 4 phases. Phases I and II are the local and coupled forward elimination phases respectively. Phase III is the distributed solve of the reduced system, and phase IV is the concurrent backward substitution phase. Tab. 4.1 shows the asymptotic scaling of the dominant compute and communication costs per process for each phase of the algorithm. The table shows that the explicit p-dependence is only in Phase III which computes the solution of the reduced system. However, depending on the scaling regime and partitioning strategy, other hidden dependencies on p might also be important.

Phase	Equations	Computation cost	Communication cost
I	(4.15) (4.16) (4.17)	$\mathcal{O}\left[N_i \log_2 N_i \max(r, M)\right]$	0
II	(4.18) (4.19) (4.20) (4.21)	$\mathcal{O}\left[r^2 \max(r, M)\right]$	$\mathcal{O}\left[r \max(r, M)\right]$
III	(4.10)	$\mathcal{O}\left[r^2 M \log_2 p\right]$	$\mathcal{O}\left[rM \log_2 p\right]$
IV	(4.22)	$\mathcal{O}\left[N_i r M\right]$	$\mathcal{O}\left[rM\right]$

Table 4.1: Asymptotic scaling of computation and communication of each phase in the solution process.

1D decomposition

Consider a problem with an $N \times N_0 \times N_0$ grid requiring a solution along the first dimension and partitioned using p processes. The matrix bandwidth can also be considered to be much smaller than the batch size, $r \ll M$, and the size of the local system, $r \ll N_i$. Then, $\max(r, M) = M$. The total cost of computation and communication during the solve process in the asymptotic limit is

$$\text{Computation cost} \sim \mathcal{O}\left(MN_i \log_2 N_i + Mr\left[C_1 N_i + C_2 r \log_2 p\right]\right) \tag{4.23}$$

$$\text{Communication cost} \sim \mathcal{O}\left(rM\left[C_3 + \log_2 p\right]\right) \tag{4.24}$$

where C_1, C_2 and C_3 are all $\mathcal{O}(1)$ constants.

For strong scaling, N and $M = N_0^2$ are held constant. From Table 4.1, the total cost of the

algorithm in the strong scaling regime is

$$\text{Computation cost} \sim \mathcal{O}\left(N_0^2 N\left\{\frac{1}{p}\left[C_1 r + \log_2\left(\frac{N}{p}\right)\right] + C_2\frac{r^2}{N}\log_2 p\right\}\right) \tag{4.25}$$

$$\text{Communication cost} \sim \mathcal{O}\left(rN_0^2\left[C_3 + \log_2 p\right]\right) \tag{4.26}$$

For weak scaling, $N_i \approx N/p$, and $M = N_0^2$ remaining constant. The total cost of the algorithm in the weak scaling regime is then given by

$$\text{Computation cost} \sim \mathcal{O}\left(N_0^2 N_i\left[C_1 r + \log_2 N_i\right] + C_2 N_0^2 r^2 \log_2 p\right) \tag{4.27}$$

$$\text{Communication cost} \sim \mathcal{O}\left(rN_0^2\left[C_3 + \log_2 p\right]\right) \tag{4.28}$$

3D decomposition

Consider a three dimensional problem with an $N \times N \times N$ grid partitioned using p processes with $p^{1/3}$ processes per dimension. Then, $N_i \approx N/p^{1/3}$ and $M \approx N_i^2 \approx N^2/p^{2/3}$ are held constant. The matrix bandwidth can also be considered to be much smaller than the batch size, $r \ll M$. As a direct result, $\max(r, M) = M$. From Table 4.1, the total cost of the algorithm in the weak scaling regime is

$$\text{Computation cost} \sim \mathcal{O}\left(N_i^3\left[C_1 r + \log_2 N_i\right] + \frac{1}{3}C_2 N_i^2 r^2 \log_2 p\right) \tag{4.29}$$

$$\text{Communication cost} \sim \mathcal{O}\left(rN_i^2\left[C_3 + \frac{1}{3}\log_2 p\right]\right) \tag{4.30}$$

4.5.2 Measured scaling results

In this section, the performance of the linear solver is demonstrated both in isolation and in the context of a representative fluid mechanics application problem. All tests in this section were performed on the *Summit* supercomputer at the Oak Ridge Leadership Computing Facility (OLCF) at Oak Ridge National Laboratory (ORNL) [163]. Each *Summit* node consists of 6 NVIDIA Tesla V100 GPUs and 2 IBM Power 9 processors. The nodes on the system are connected with the Mellanox EDR 100G Infiniband interconnect arranged in a non-blocking fat tree topology. In the present implementation, all compute operations are conducted on GPUs, while CPUs are dedicated to control and communication tasks. The code for the results in this section was written in C++ using the Kokkos framework [40, 160].

For the linear solver alone, both strong and weak scaling results are presented for solving $\boldsymbol{A}\boldsymbol{x} = \boldsymbol{b}$, where $\boldsymbol{A}$ is a cyclic tridiagonal system with bands given by $\boldsymbol{A} = \mathcal{B}\ [\ 1/3,\ 1,\ 1/3\ ]$. This linear system represents the left hand side of the sixth order compact first derivative scheme on a periodic domain [89]. For all linear solver scaling tests, the linear system is solved 1000 times, and speedup based on the average time is reported. In the strong scaling test, the dimension of $\boldsymbol{A}$ is

8192×8192, and the linear system is solved 256^2 times in parallel, i.e., the dimensions of $\boldsymbol{b}$ and $\boldsymbol{x}$ are 8192×256^2. In the context of compact finite difference schemes, this is equivalent to computing a spatial derivative along a column of 3D Cartesian grid partitions, where the grid dimension is 8192 along the solving direction and 256×256 perpendicular to the solving direction. For example, when solving along the first index, the grid dimension is $8192 \times 256 \times 256$. As the number of GPUs used is increased, the domain is decomposed equally along the solving direction so that each partition has a size of $(8192/p) \times 256 \times 256$. When solving along other directions, the dimensions are permuted correspondingly. Some small differences in performance among the directions are expected because of memory striding. In this implementation, the right-memory layout is used where the third index maps to contiguous memory. The strong scaling speedup, S_s, is defined as

$$S_s(p) = \frac{T_1}{T_p} \tag{4.31}$$

where T_p is the wall time when using p GPUs. The strong scaling results for each index direction are shown in Fig. 4.9.

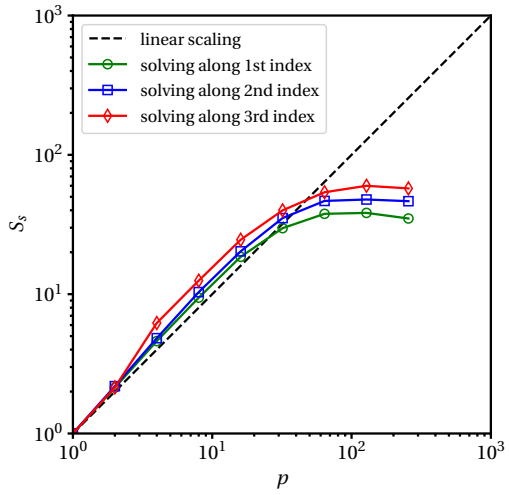

Figure 4.9: Measured strong scaling of the linear solver for each of the coordinate indices. The curve for each index is normalized by its own single-GPU time, so all speedups start at unity.

The strong scaling plot shows speedup from $p = 1$ to $p = 64$. Beyond $p = 64$, the speedup plateaus. This is because in the strong scaling regime, the leading order compute cost decreases linearly with p while the communication cost increases as $\log_2 p$ as described in Section 4.5.1. The speedup between $p = 2$ and $p = 4$ is super-linear and it is suspected that this is mainly due to GPU cache benefits as the problem size per GPU keeps getting smaller. There is another effect that contributes to this super linear scaling that stems from Eq. (4.25). As p increases, the computation cost initially decreases as $p^{-1} \log_2 p$ contributing to the super-linear scaling behavior. This is only

valid in the compute-dominant limit of low p and large N, particularly when $r^2/N \ll 1$. As p increases, the cost of solving the reduced system increases causing a reduction in scaling efficiency in addition to the increased communication cost. At $p = 32$, approximately where the three curves cross the ideal scaling line, the data chunk on each GPU is $256 \times 256 \times 256$. This is the chunk size used as the basis of the weak scaling tests, which are discussed next.

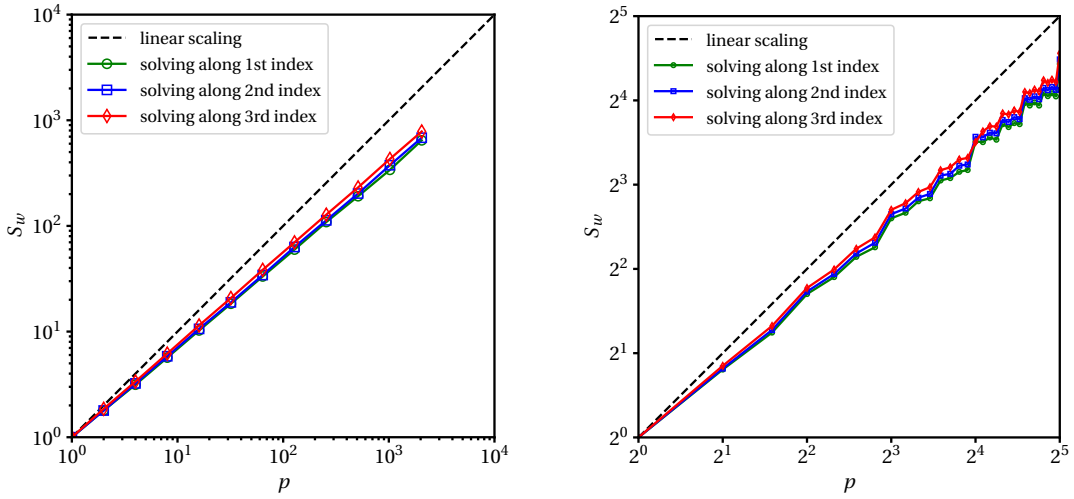

Figure 4.10: Measured weak scaling of the linear solver: (a) number of GPUs increasing in powers of 2; (b) number of GPUs increasing linearly. Data is stored on the left memory layout where the 3rd index is the fast looping index.

The weak scaling performance is shown for solving $\boldsymbol{Ax} = \boldsymbol{b}$, with the same matrix $\boldsymbol{A}$ as in the strong scaling test. The computational domain is partitioned along the solve direction into cubic sub-domains of size $N_0 \times N_0 \times N_0$, so $\boldsymbol{A}$ is $pN_0 \times pN_0$, and it is solved N_0^2 times in parallel. For all the weak scaling tests, $N_0 = 256$ is chosen, so that each GPU operates on a chunk of data that is 256^3. The weak scaling results for the isolated linear system solve are presented in two ways in Fig. 4.10. Here, the weak scaling "speedup", S_w, is reported:

$$S_w(p) = \frac{p \times T_1}{T_p} \tag{4.32}$$

First, in Fig. 4.10a, the number of GPUs used is always a power of 2, from 1 to 2048. As the number of GPUs is increased in the weak scaling test, the dimension of only one coordinate direction is increased at a time, and all three directions are tested. The grid sizes for the series of tests for the first index, for example, are $256 \times 256 \times 256$, $512 \times 256 \times 256$, $1024 \times 256 \times 256$, etc. Second, in Fig. 4.10b, the number of GPUs used increases linearly from 1 to 32 to show the effects of a non-ideal problem decomposition on performance. Also, the differences in scaling among the index

directions are very small, meaning that in a large-scale 3D problem, no one direction will dominate the computational cost. These results show that the scaling of the linear solver is reasonably good up to a very large number of GPUs. For context, the last data point comes from running on 2048 GPUs on *Summit*, or about 8% of the entire machine. This test exercises one coordinate direction at a time on a column of the domain decomposition, comparable to the highlighted partitions in Fig. 4.1, in order to predict the performance in a realistic computation application. Accordingly, the last data point represents the intended 3D equal size domain decomposition used by the linear solver in a production-size simulation which uses 2048^3 GPUs.

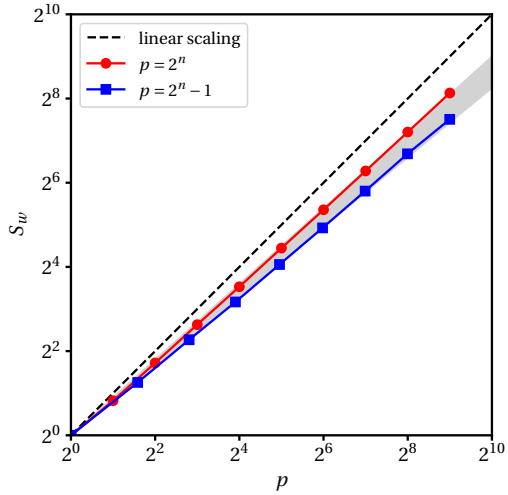

Figure 4.11: Measured weak scaling of the linear solver using best-case (2^n) and worst-case ($2^n - 1$) numbers of GPUs, solving along the 1st index.

These results also show that while the solver scales best when using a number of GPUs equal to a power of 2, its performance is degraded using odd or even prime numbers of GPUs. This occurs because additional work in the form of detach-reattach steps is required when not using power of 2 number of GPUs. The worst case scenario in terms of additional work required is to use a number of GPUs equal to $2^n - 1$. This choice requires $p - 1$ stages of PCR and $p - 1$ stages of detach-reattach operations. An additional series of weak scaling results is presented in Fig. 4.11, which compares the weak scaling performance of using 2^n vs. $2^n - 1$ GPUs. Only the 1st index direction is shown since the results are qualitatively the same for all directions. Depending on the specific machine and application size, it may not always be practical to use a number of GPUs that is a power of 2. As a result, it is expected that the practical weak scaling behavior of this algorithm lies in the range between the curves in Fig. 4.11. Both curves are demonstrated to be linear over the range tested. This is expected based on how the number of PCR steps and attach-reattach operations scales with the number of processes. Since the lines have different slopes, this means that the relative benefit of using the ideal number of GPUs becomes greater as the problem size is increased.

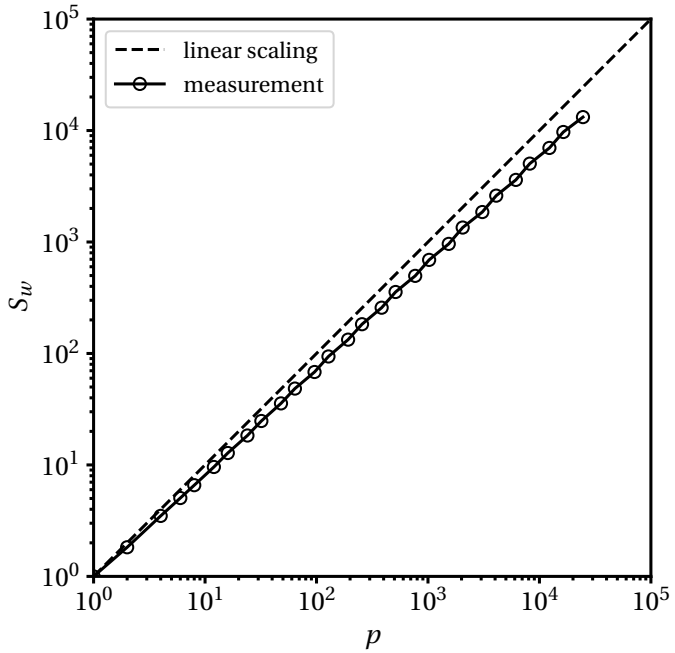

Figure 4.12: Measured weak scaling (256^3 grid point per GPU) of a Navier-Stokes solver on the Taylor-Green vortex problem using compact finite difference and interpolation methods. Data is reported using both 4×2^n and 6×2^n GPUs per node on *Summit*.

Finally, weak scaling is demonstrated on a fluid mechanics application – the direct numerical simulation of a Taylor-Green vortex problem at a Reynolds number of 1600 and Mach number of 0.08 [19] – by using a compressible Navier-Stokes direct numerical simulation solver. The simulations were conducted using the sixth-order staggered compact finite difference schemes and compact interpolators for spatial discretization [107]. The details of the problem description and numerical formulation are illustrated in Appendix C. For each weak scaling test, a constant time step determined by stability requirements was used, and wall time data was collected for 100 time steps. The computational cost is dominated by calculating derivatives and interpolations in the Navier-Stokes equations, which involves solving linear systems similar to the one above. The solution at a representative time is visualized in Fig. C.1. This test is useful because its domain and domain decomposition are much more realistic than the isolated linear solver test, and because it involves approximately an equal number of linear solves along all three coordinate indices. Finally, it tests whether the linear solver performance enables good scaling on a practical problem. Like the first linear solver test, scaling is reported in powers of 2, but quantities of GPUs of 6×2^n were also tested. This second series corresponds to full utilization of *Summit* nodes, which have 6 GPUs each. The weak scaling results, including both setups, are shown in Fig. 4.12, which demonstrates excellent scaling up to 24576 GPUs, or 89% of the nodes on *Summit*.

The reason that Taylor-Green vortex problem scales better than the linear solver test is due to the 3D domain decomposition. The linear solver weak scaling tested an extreme scenario with a 1D domain decomposition. This would only be appropriate for a domain with one dimension much longer than the other two. Such an aspect ratio is not typical for simulations of turbulent flows.

4.6 Conclusions

In this work, a direct linear solver for compact banded systems is presented and demonstrated to have scalable performance on a petascale GPU platform. The algorithm is applicable for a wide variety of high performance computing platforms with heterogeneous computing capabilities. The sparsity patterns that result in the factorized matrix blocks are leveraged in the overall algorithm to avoid large data transfers across the distributed memory partitions and to reduce the floating point operational cost of matrix-matrix multiplications. As such, the proposed algorithm has significant advantages over conventional strategies that involve "all-to-all" communication patterns. These advantages thereby enable the proposed algorithm to be suitable for distributed heterogeneous computing environments requiring programming paradigms such as "MPI+X," and to reduce the strong performance dependence on the underlying network topology. The weak scalability is shown on a canonical 3D periodic Navier-Stokes problem using compact finite difference and interpolation schemes involving cyclic banded tridiagonal linear systems. The algorithm works on a flexible number of distributed memory partitions and optimal performance is recovered when the number of ranks is a power of two. This work is directly beneficial to large-scale computations of a wide range of partial differential equation problems using compact numerical schemes such as those in fluid mechanics, solid mechanics, and electromagnetics.

Chapter 5

Compressibility Effects in Compressible Isotropic Turbulence

In this chapter, compressibility effects are studied using direct numerical simulations of solenoidally forced compressible isotropic turbulence. The turbulent Mach numbers, M_t, range from 0.2 to 0.7, and the Taylor-microscale Reynolds numbers, Re_λ, are approximately 170. For each case, data over approximately 10 eddy-turnover times at statistically stationary states are collected for analysis. The effects of compressibility are investigated from the statistics of the fluctuating thermodynamic and kinematic quantities. The solenoidal and dilatational motions are studied based on the Helmholtz decomposition of the velocity field. The budget equations of the decomposed velocity variance are analytically derived from the Navier-Stokes system. According to the budget equations, the simulation data indicates a balance between solenoidal forcing work and solenoidal dissipation at low M_t. As M_t increases, specific terms develop a bias in their statistical distribution and thus represent the net transfer or exchange of energy characterized by variance.

5.1 Introduction

Compressible turbulence is prevalent and plays a significant role in many industrial applications involving high-speed flows as well as in many natural astrophysical and terrestrial phenomena. Fundamental understanding of compressible turbulence dynamics is crucial yet still quite limited. In the formulation of compressible flows, the propagation of acoustic waves is resolved at a finite speed. Due to the acoustic wave propagation and non-radiative local flow motion, local compression and expansion occur and are associated with density and pressure changes. This has been referred to as the compressibility of the flow [90]. An obvious consequence of compressibility is that the flow velocity field does not maintain a divergence-free state, which leads to local compression and

expansion and enables bidirectional transfer between kinetic energy and internal energy. In compressible turbulence, the strength of the compressibility is characterized by the turbulent Mach number, M_t, which is defined as the ratio of the turbulent velocity fluctuations to the mean speed of sound. M_t can be defined in different ways, and the definition used in this work is consistent with $M_t = \sqrt{\langle \boldsymbol{u}'' \cdot \boldsymbol{u}'' \rangle} / \langle c \rangle$, where the pair of angle braces, $\langle (\cdot) \rangle$, denotes a spatial average; $\boldsymbol{u}''$ is the fluctuating velocity with respect to the Favre average [45], $\boldsymbol{u}'' = \boldsymbol{u} - \langle \rho \boldsymbol{u} \rangle / \langle \rho \rangle$ where $\boldsymbol{u}$ is the flow velocity field and ρ is the density field; and c is the speed of sound. As $M_t \to 0$, compressibility effects asymptotically vanish, and the flow behavior degenerates to incompressible turbulence. Kovásznay (1953) [81] conducted a perturbation analysis at vanishing M_t and identified three distinct modes – the vorticity mode, sound-wave mode, and entropy mode – from the linearized Navier-Stokes equations, commonly known as the Kovásznay decomposition. Adding on to the leading order of the Kovásznay decomposition, Chu & Kovásznay (1958) [24] carry the quadratic terms and conduct a weakly nonlinear analysis to investigate the bilateral interactions among the three modes, which serves as a second-order correction to the linearized solution. The inclusion of the quadratic terms improves the accuracy on an extended range of M_t, but as a prerequisite of the perturbation analysis, Kovásznay decomposition is valid only for $M_t \ll 1$. At large M_t, the linear theory and weakly nonlinear analysis no longer hold due to strong nonlinear interactions among different modes. These nonlinear interactions dominate the dynamics of compressibility, creating more complex flow behavior such as eddy shocklets [88, 168] and change of scaling in M_t [72].

A more generic approach to examining the compressibility effects is to study the decomposed turbulent motion using the Helmholtz decomposition. For a smooth vector field, $\boldsymbol{v}(\boldsymbol{x})$, the Helmholtz decomposition uniquely identifies three components, $\boldsymbol{v} = \boldsymbol{v}^s + \boldsymbol{v}^d + \langle \boldsymbol{v} \rangle$, where $\boldsymbol{v}^s$ and $\boldsymbol{v}^d$ are the solenoidal and dilatational components respectively, satisfying $\nabla \cdot \boldsymbol{v}^s = 0$ and $\nabla \times \boldsymbol{v}^d = \boldsymbol{0}$, and $\langle \boldsymbol{v} \rangle$ corresponds to the spatially-averaged mean. In Fourier space, the solenoidal and dilatational components are orthogonal with respect to the same wavenumber, $\widehat{\boldsymbol{v}}^s_{\boldsymbol{k}} \cdot \widehat{\boldsymbol{v}}^d_{\boldsymbol{k}} = 0$, where $\boldsymbol{k}$ is the wavenumber vector and $\boldsymbol{v}^{s/d} = \sum_{\boldsymbol{k}} \widehat{\boldsymbol{v}}^{s/d}_{\boldsymbol{k}} e^{i\boldsymbol{k}\cdot\boldsymbol{x}}$. In physical space, the orthogonality leads to the identity $\left\langle \boldsymbol{v}^s \cdot \boldsymbol{v}^d \right\rangle = 0$. For incompressible turbulence, the density is constant and the flow motion is purely solenoidal, while for compressible turbulence, the dilatational motion directly contributes to the density fluctuations, which thereby forms the aforementioned local compression and expansion. Conceptually relating to the Kovásznay decomposition at a low M_t, the solenoidal motion is associated with the vorticity mode, and the dilatational motion contains the sound-wave mode and entropy mode. In the low-M_t limit, Sarkar et al. (1991) [135] argue that the time scales of solenoidal motion and acoustic dilatational motion differ, and the ratio of the two time scales is $\mathcal{O}(M_t)$. Accordingly, the dilatational velocity and pressure fluctuations are estimated based on a justified acoustic quasi-equilibrium assumption with respect to the solenoidal motion. Additionally, Ristorcelli (1997) [128] proposes a pseudo-sound theory based on the assumptions of statistical homogeneity and normality where two relevant length scales – an inner length scale associated with the turbulence field and an

outer length scale associated with radiative acoustic waves generated from turbulent solenoidal motion – were recognized in a homogeneous low-M_t turbulent flow, and the ratio of the two length scales is $\mathcal{O}(M_t)$. The pressure fluctuations associated with local solenoidal motion within the inner length scale, known as the pseudo-sound, are the dominant component in the overall pressure fluctuations. Accordingly, the compressibility effects are calculated from a one-way coupling of the solenoidal motion. The pseudo-sound theory also provides a single-point moment closure model to calculate the pressure dilatation, $\langle p'\theta' \rangle$ and variance of velocity dilatation, $\langle \theta'\theta' \rangle$ where p is the pressure, θ is the velocity dilatation, and $(\cdot)' = (\cdot) - \langle (\cdot) \rangle$ denotes the fluctuating component of a given quantity. For isotropic turbulence at a high Reynolds number, two-point moment closure models, such as the direct interaction approximation (DIA) and eddy-damped quasi-normal Markovian (EDQNM), are proposed by Kraichnan (1959) [82] and Orszag (1970) [114] respectively, where the spectral damping mechanism due to the viscosity and the leading-order energy transfer mechanism are modeled. Furthermore, Bertoglio et al. (2001) [7] extend the DIA and EDQNM models for weakly compressible isotropic turbulence, but the model is applied to a relatively wide range of M_t [134]. Moreover, the compressibility effects on turbulent statistics and flow structures were also investigated based on direct numerical simulations (DNS) of forced compressible isotropic turbulence at variable Reynolds numbers and turbulent Mach numbers [171, 170, 37, 72, 169, 172, 38].

For quantitative study of the decomposed motions in compressible turbulence beyond the low-M_t regime, an important question encountered in applying the Helmholtz decomposition is which vector field, representing the flow motion, should be decomposed. The answer is not as obvious as it seems to be because any choice will create consequential difficulty in the analysis. Towards the incompressible limit, all kinematic vector fields, such as velocity and momentum, are mathematically equivalent. Considering density fluctuations, some inconsistency is unavoidable due to triadic mode interactions. The orthogonality only holds for vector fields that directly result from the Helmholtz decomposition. The decomposed momentum and the decomposed velocity are no longer mathematically equivalent. The momentum associated with the solenoidal velocity permits non-zero dilatational components, and vice versa. Additionally, the decomposed motion strength, characterized by the mean turbulent kinetic energy may introduce a cross term to close the budget, $\langle K \rangle = \langle K^s \rangle + \langle K^d \rangle + \langle K^{sd} \rangle$, where $K = \rho \boldsymbol{u} \cdot \boldsymbol{u}/2$ is the kinetic energy; K^s and K^d are the solenoidal and dilatational fields respectively calculated from the decomposed motion vectors; and K^{sd} is the cross-contribution to the overall kinetic energy. As an example, if the velocity field $\boldsymbol{u}$ undergoes the Helmholtz decomposition, $\boldsymbol{u} = \boldsymbol{u}^s + \boldsymbol{u}^d$ assuming $\langle \boldsymbol{u} \rangle = \boldsymbol{0}$, then the corresponding decomposed kinetic energy terms are $\langle K^s \rangle = \langle \rho \boldsymbol{u}^s \cdot \boldsymbol{u}^s \rangle /2$, $\langle K^d \rangle = \langle \rho \boldsymbol{u}^d \cdot \boldsymbol{u}^d \rangle /2$, and $\langle K^{sd} \rangle = \langle \rho \boldsymbol{u}^s \cdot \boldsymbol{u}^d \rangle$. From the expressions, the density ρ serves as a nonuniform weighting function such that $\langle K^{sd} \rangle$ is not guaranteed to be zero or positive-definite, which is undesirable for analysis. One way to avoid the cross term is to properly select the vector field to characterize the flow motion. Kida & Orszag (1990) [78] defined a state vector $\boldsymbol{w} = \sqrt{\rho}\boldsymbol{u}$ for the Helmholtz decomposition, $\boldsymbol{w} = \boldsymbol{w}^s + \boldsymbol{w}^d + \langle \boldsymbol{w} \rangle$. Correspondingly, assuming

$\langle \boldsymbol{w} \rangle = \boldsymbol{0}$, the expression of K becomes $K = \boldsymbol{w} \cdot \boldsymbol{w}/2$, so that $\langle K \rangle = \langle K^s_{\boldsymbol{w}} \rangle + \langle K^d_{\boldsymbol{w}} \rangle$ and $\langle K^{sd}_{\boldsymbol{w}} \rangle = 0$ are enforced with $K^s_{\boldsymbol{w}} = \boldsymbol{w}^s \cdot \boldsymbol{w}^s/2$, $K^d_{\boldsymbol{w}} = \boldsymbol{w}^d \cdot \boldsymbol{w}^d/2$, and $K^{sd}_{\boldsymbol{w}} = \boldsymbol{w}^s \cdot \boldsymbol{w}^d$. An alternative method is to reinterpret the mean kinetic energy. Following this approach, the mean kinetic energy is not calculated by averaging the local kinetic energy but instead directly calculated using characteristic quantities. For instance, the characteristic mean kinetic energy for velocity decomposition and momentum decomposition can be defined as $K_{\text{avg},\boldsymbol{u}} = \langle \rho \rangle \langle \boldsymbol{u} \cdot \boldsymbol{u} \rangle /2$ and $K_{\text{avg},\rho\boldsymbol{u}} = \frac{1}{2} \langle (\rho \boldsymbol{u}) \cdot (\rho \boldsymbol{u}) \rangle / \langle \rho \rangle$ respectively. This approach may be particularly interesting from the perspective of turbulence modeling [3]. Regarding physical considerations, velocity decomposition is still preferred as the decomposed components directly connect to the vorticity and velocity dilatation fields.

Another challenge encountered in the analysis of compressible turbulence is the fluctuation of transport properties associated with the fluctuation of the thermodynamic state of the fluid. This directly impacts the decomposition of the mean viscous dissipation, $\langle \epsilon \rangle$. It is well-known that the viscous dissipation, ϵ, can be written as $\epsilon = \boldsymbol{\sigma} : \boldsymbol{S}$, where $\boldsymbol{\sigma}$ is the viscous stress tensor and $\boldsymbol{S}$ is the strain rate tensor. Sarkar et al. (1991) derive the decomposition, $\langle \epsilon \rangle = \langle \epsilon^s \rangle + \langle \epsilon^d \rangle$, where ϵ^s and ϵ^d are known as the solenoidal dissipation and dilatational dissipation [135]. The derivation assumes constant viscosity. Following the derivation in Sarkar et al. (1991) and based on the expression for $\boldsymbol{\sigma}$, the expressions for ϵ^s and ϵ^d are $2\mu\Omega^2$ and $(\beta + \frac{4}{3}\mu)\theta^2$ respectively, where μ and β are the dynamic shear viscosity and bulk viscosity respectively, Ω is the enstrophy, and θ is the velocity dilatation. As shown in the expressions for ϵ^s and ϵ^d, for constant transport properties, the solenoidal dissipation is only due to the solenoidal velocity and dilatational dissipation is only caused by the dilatational velocity. However, considering the fluctuations of μ and β, the overall local dissipation is $\epsilon = 2\mu\Omega^2 + (\beta + \frac{4}{3}\mu)\theta^2 - 4\mu\mathcal{I}_2$, where $\mathcal{I}_2 = \frac{1}{2}\left(\theta^2 - \boldsymbol{S} : \boldsymbol{S} + \Omega^2\right)$ is the second invariant of the velocity gradient tensor. The first two terms in the expression for ϵ are the contributions of solenoidal and dilatational velocity components respectively, and the third term, $-4\mu\mathcal{I}_2$, corresponds to the cross-contribution. The positivity of the cross-contribution is not guaranteed although ϵ is positive definite. For modeling purposes, the cross-contribution is usually ignored, as is also commented on by Sarkar et al. (1991) [135], who suggest that the two-component decomposition is asymptotically exact for turbulence with a high Reynolds number.

This work focuses on the compressibility effects and energy exchange between solenoidal and dilatational motions in statistically stationary compressible isotropic turbulence. The investigation is based on a set of DNS of solenoidally forced isotropic turbulence for $0.2 \leq M_t \leq 0.7$. The configurations of the DNS are detailed in Sec. 5.2. The turbulence statistical quantities are provided in Sec. 5.3 where the effects of M_t are discussed. The energy exchange between solenoidal and dilatational motions is investigated based on the analytically derived decomposed velocity variance budget equations in Sec. 5.4.

5.2 Configurations of direct numerical simulations

A set of DNS of solenoidally forced compressible isotropic turbulence were conducted for the numerical investigation. The DNS solves the compressible Navier-Stokes equations including conservation of mass, momentum and total energy, shown as follows,

$$\frac{\partial \rho}{\partial t} + \frac{\partial \rho u_j}{\partial x_j} = 0 \tag{5.1}$$

$$\frac{\partial \rho u_i}{\partial t} + \frac{\partial}{\partial x_j}\left(\rho u_i u_j + p\delta_{ij} - \sigma_{ij}\right) = \rho f_i \tag{5.2}$$

$$\frac{\partial \rho e}{\partial t} + \frac{\partial}{\partial x_j}\left(\rho e u_j + p u_j - u_i \sigma_{ij} + q_j\right) = 0 \tag{5.3}$$

where ρ is density, u_i is the velocity vector, p is pressure, δ_{ij} is the identity tensor, σ_{ij} is the viscous stress tensor, f_i is the external forcing, e is specific total energy, and q_j is conductive heat flux. The fluid is assumed to be a calorically perfect gas satisfying the following equation of state.

$$p = \rho R T \tag{5.4}$$

where R is the specific gas constant and T is temperature. For a calorically perfect gas, the ratio of specific heats, γ, is constant. In this work, $\gamma = 1.4$ and $R = 1$ are used. Consistently, e is the specific total energy at a constant volume.

$$e = \frac{RT}{\gamma - 1} + \frac{1}{2} u_j u_j \tag{5.5}$$

The constitutive formulation of the viscous stress tensor is

$$\sigma_{ij} = 2\mu S_{ij} + \left(\beta^* - \frac{2}{3}\mu\right)\theta\delta_{ij} \tag{5.6}$$

where $S_{ij} = \frac{1}{2}\left(u_{i,j} + u_{j,i}\right)$ is the overall strain rate tensor, and β^* represents an artificial bulk viscosity [76]. The dynamic shear viscosity is temperature-dependent and modeled using the power-law

$$\frac{\mu}{\mu_{\text{ref}}} = \left(\frac{T}{T_{\text{ref}}}\right)^{\alpha} \tag{5.7}$$

where μ_{ref} and T_{ref} are the dynamic shear viscosity and temperature at a reference state, and the exponent α is a dimensionless parameter. The heat flux represents the heat diffusion formulated with Fourier's law

$$q_j = -(\kappa + \kappa^*)\frac{\partial T}{\partial x_j} \tag{5.8}$$

where κ is the molecular thermal conductivity of the fluid, and κ^* is an artificial thermal conductivity [76]. The molecular thermal conductivity is calculated assuming constant Prandtl number,

Pr.

$$\kappa = \frac{\gamma R \mu}{\mathrm{Pr}(\gamma - 1)} \tag{5.9}$$

In this work, $\alpha = 0.5$ and $\mathrm{Pr} = 0.72$ are selected in accordance with Jagannathan & Donzis (2016) [72]. The artificial properties β^* and κ^* belong to the set of localized artificial diffusivities (LAD) formulated in Kawai et al. (2010) [76] for shock capturing at high M_t. The LAD terms are highly localized to the occurrence of strong eddy shocklets for numerical stability and zero elsewhere. Unlike the simulation framework in Kawai et al. (2010) [76], the DNS conducted in this work do not have any numerical filter on simulation results [146]. Using LAD without filtering, all artificial dissipation introduced in the computations is quantifiable.

The numerical operations in the computations are based on a set of six-order compact finite difference methods and compact interpolations [89, 107]. The simulations with and without the LAD model are conducted without solution filtering due to the intrinsic dealiasing and enhanced spectral resolution in the simulation framework [146]. The computational domain is a cubic box with 3D periodic conditions, $x_i \in [0, 2\pi)^3$, and the computational mesh size is 1024^3. The time integration uses the standard fourth-order Runge-Kutta scheme with an adaptive time step determined by Courant–Friedrichs–Lewy (CFL) number. In this work, CFL = 0.6 is used for all simulations.

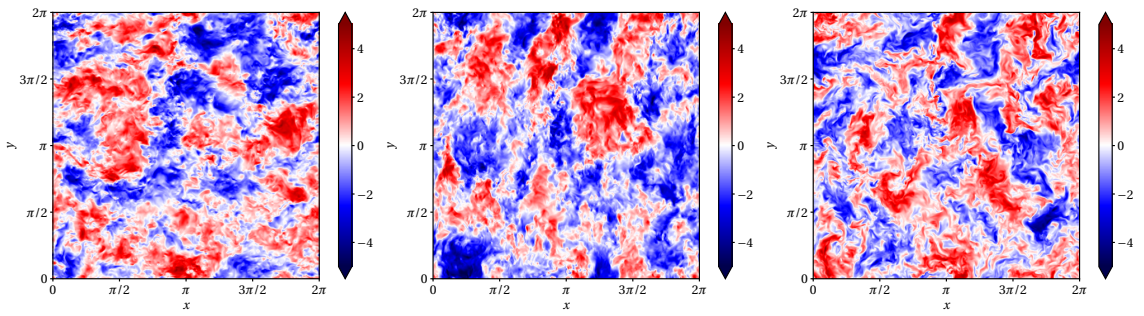

(a) (b) (c)

Figure 5.1: Visualization of an instantaneous velocity field, $\boldsymbol{u} = u\hat{\boldsymbol{e}}_x + v\hat{\boldsymbol{e}}_y + w\hat{\boldsymbol{e}}_z$, in x-y plane at $M_t \approx 0.7$: (a) u/u_{rms}, (b) v/u_{rms}, and (c) w/u_{rms}.

The external forcing f_i is purely solenoidal, $f_{i,i} = 0$, and contains two components, $f_i = f_i^s + \langle f_i \rangle$, where $\langle f_i^s \rangle = 0$ and $\langle f_i \rangle = -\langle \rho f_i^s \rangle / \langle \rho \rangle$. Therefore, $\langle f_i \rangle$ is transient but homogeneous in space, which serves as a correction to numerically enforce $\langle \rho f_i \rangle / \langle \rho \rangle = 0$. As a result, the forcing strategy does not impose net momentum to the flow system, and $\langle \rho u_i \rangle = 0$ is numerically preserved in the computational domain. f_i^s is a low wavenumber banded stochastic forcing generated in Fourier space following the algorithm proposed in Ref. [42]. The Fourier representation of the solenoidal forcing f_i^s is

$$f_i^s = \sum_{k_L \le k \le k_H} \mathcal{P}_{ij}^{\perp} \widehat{b}_j(k_m, t) e^{ik_m x_m} \tag{5.10}$$

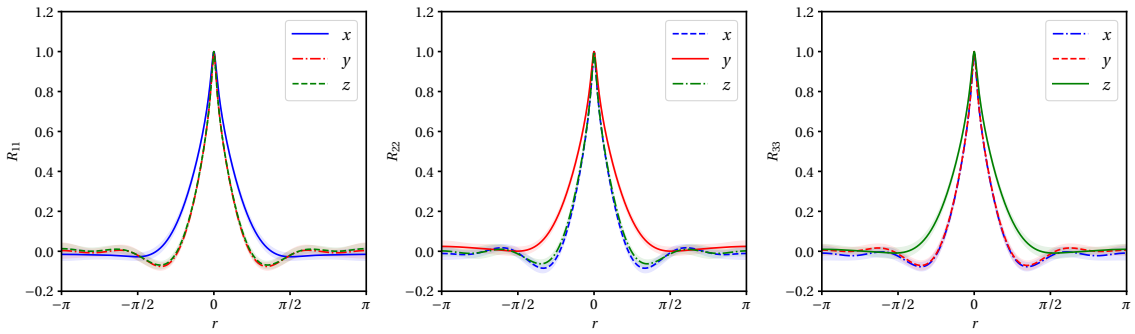

Figure 5.2: Ensemble-averaged velocity two-point correlation at $M_t \approx 0.7$: (a) R_{11}, (b) R_{22}, and (c) R_{33}. The shaded area represents the fluctuation amplitude characterized by the radius of standard deviation in the ensemble averaging.

where $k = \sqrt{k_m k_m}$ is the modulus of the wavenumber vector; k_L and k_H are the cut-off wavenumbers at the low end and high end of the forcing respectively; each Fourier mode, $\widehat{b}_j(k_m, t)$, is generated using six independent, integrated Uhlenbeck-Ornstein random processes, and $\mathcal{P}^{\perp}_{ij} = \delta_{ij} - k_i k_j / k^2$ is a spectral solenoidal projector. In this work, the cut-off wavenumbers are chosen to be $k_L = 3$ and $k_H = 5$ to achieve sufficient spatial decorrelation across the computational domain while maintaining the natural development of turbulence dynamics at intermediate and small scales. The large-scale decorrelation is expected to accelerate the convergence of turbulence statistics. The decorrelation time scale of the Uhlenbeck-Ornstein random process is approximately 0.1 eddy-turnover times, where the time scale of a unity eddy-turnover time, t_e, is defined as $t_e = \langle K \rangle \,/\, \langle \epsilon \rangle$ with ensemble averaging. With the external forcing added to Eq. (5.2), the form of Eq. (5.3) implies a nonuniform sink of internal energy, $-\rho f_j u_j$, where the negative sign indicates that the internal energy is removed from the flow system. Therefore, the work due to the forcing is locally balanced with the sink of the internal energy, and the total energy of the flow system, $\langle \rho e \rangle$, is conservative.

Case	Re_λ	M_t	LAD	$k_{x,\max}\eta$	λ/η	l_e/λ	$\lvert\langle u \rangle\rvert \,/\, \langle u_j u_j \rangle^{1/2}$
M02	173	0.20	none	1.65	25.90	2.18	7.33×10^{-5}
M03	172	0.30	none	1.67	25.80	2.14	6.81×10^{-5}
M04	172	0.40	β^* & κ^*	1.66	25.81	2.14	2.21×10^{-5}
M05	171	0.50	β^* & κ^*	1.68	25.73	2.15	2.09×10^{-4}
M06	171	0.61	β^* & κ^*	1.65	25.90	2.21	7.66×10^{-4}
M07	166	0.70	β^* & κ^*	1.68	25.80	2.16	5.19×10^{-4}

Table 5.1: Configuration details of DNS of solenoidally forced compressible isotropic turbulence.

The numerical investigations in this work use six DNS for comparison at different turbulent Mach numbers. For each case, the simulation data are collected at a constant sampling rate approximately

every 0.055 eddy turnover times, and the total data for analysis span a range of approximately 10 eddy turnover times. The details of each DNS configuration are listed in Tab. 5.1 where all statistics are calculated based on ensemble averaging. The Reynolds number based on the longitudinal Taylor microscale, Re_λ, is approximately 170 for each case. The turbulent Mach number, M_t, ranges from 0.2 to 0.7. l_e is the integral length scale defined as $l_e = \int_0^\infty k^{-1} E_{\boldsymbol{uu}}(k)dk / \int_0^\infty E_{\boldsymbol{uu}}(k)dk$, where $E_{\boldsymbol{uu}}(k)$ is the velocity energy spectrum. For compressible isotropic turbulence, Re_λ and M_t are defined as

$$\mathrm{Re}_\lambda = \frac{u_{\mathrm{rms}}\lambda}{\langle \mu/\rho \rangle} \qquad \text{and} \qquad M_t = \frac{\sqrt{\langle u_j u_j \rangle}}{\langle c \rangle} \tag{5.11, 5.12}$$

where for a calorically perfect gas, $c = \sqrt{\gamma p/\rho}$; for isotropic turbulence, λ and u_{rms} are defined as

$$\lambda = \frac{1}{3}\left(\lambda_x + \lambda_y + \lambda_y\right) \qquad \text{and} \qquad u_{\mathrm{rms}} = \sqrt{\frac{\langle u_j u_j \rangle}{3}} \tag{5.13, 5.14}$$

where

$$\lambda_x = \sqrt{\frac{\langle u^2 \rangle}{\langle (\partial u/\partial x)^2 \rangle}} \qquad \lambda_y = \sqrt{\frac{\langle v^2 \rangle}{\langle (\partial v/\partial y)^2 \rangle}} \qquad \lambda_z = \sqrt{\frac{\langle w^2 \rangle}{\langle (\partial w/\partial z)^2 \rangle}} \tag{5.15, 5.16, 5.17}$$

Re_λ is adjusted by varying μ_{ref}. The variation of M_t is achieved by adjusting the mean speed of sound while preserving the mean density. The Kolmogorov length scale, η, is also tracked. The Kolmogorov length scale identifies the length scale in a turbulent flow where viscous dissipation is dominant, which was originally derived by Kolmogorov (1941) based on dimensional analysis for incompressible turbulent flows [80]. For compressible turbulence, the extended definition of the Kolmogorov length scale, $\eta = (\langle \mu \rangle^3 \langle \epsilon \rangle^{-1} \langle \rho \rangle^{-2})^{1/4}$, is used [72]. The grid resolution satisfies $k_{x,\max}\eta \approx 1.6$ measured from the results. Due to the large-scale decorrelation, the mean velocity is sufficiently small. The averaged x-component of velocity for each case is reported in Tab. 5.1. As a demonstration, the visualizations of the velocity field in an x-y plane are shown in Fig. 5.1, and the two-point correlations of all three components of the velocity field are shown in Fig. 5.2 in all three directions. The spatial two-point correlation of the velocity field is defined as $R_{ii} = \langle u_i(\boldsymbol{x}) u_i(\boldsymbol{x}+\boldsymbol{r}) \rangle \,/\, \langle u_i(\boldsymbol{x}) u_i(\boldsymbol{x}) \rangle$ where the subscript indices in this definition do not imply summation. The LAD model, including the artificial bulk viscosity, β^*, and artificial thermal conductivity, κ^*, is only used in the cases when $M_t \geq 0.4$ for shock capturing. The visualization of β^* is shown in Fig. 5.3 in comparison with the structure of eddy shocklets detected by the modified Ducros sensor, $-\theta|\theta|/(\theta^2 + 2\Omega^2 + \varepsilon^2)$, where $\varepsilon = 10^{-16}$ for numerical regularization. The modified Ducros sensor varies on the interval $(-1, 1)$ for infinitesimal ε, where the shocklets are identified when the local sensor value is close to 1. The artificial bulk viscosity is scaled by the local physical dynamic shear viscosity, β^*/μ, and the visualization in Fig. 5.3b is shown on a logarithmic color scale. The visualizations in Fig. 5.3 demonstrate that the artificial dissipation for shock capturing is highly localized at the shocklet

structures.

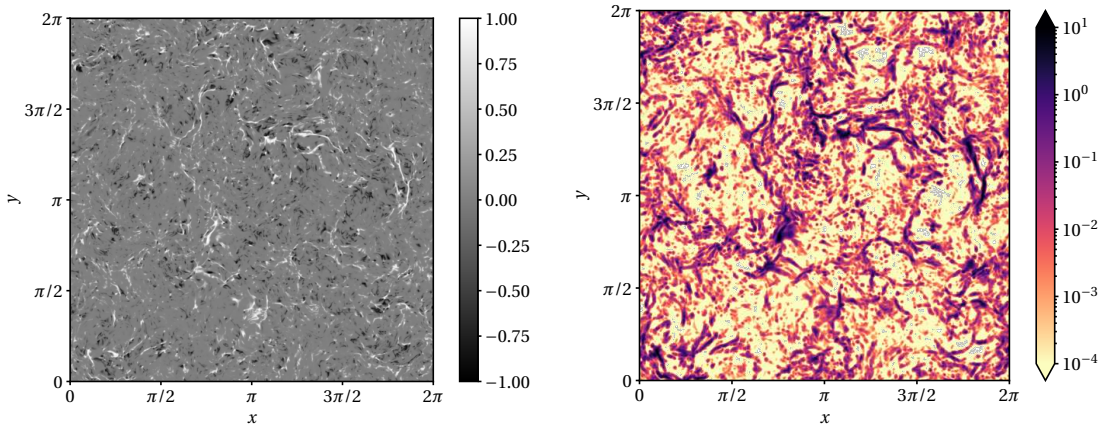

(a) (b)

Figure 5.3: Visualizations of (a) modified Ducros sensor, $-\theta|\theta|/(\theta^2 + 2\Omega^2 + \varepsilon^2)$ and (b) relative artificial bulk viscosity, β^*/μ in the x-y plane at $M_t \approx 0.7$.

5.3 Statistical quantities

The Helmholtz decomposition on the velocity vector field, $\boldsymbol{u} - \langle \boldsymbol{u} \rangle = \boldsymbol{u}^s + \boldsymbol{u}^d$, is calculated as

$$\boldsymbol{u}^d = \nabla \phi \qquad \text{and} \qquad \boldsymbol{u}^s = \boldsymbol{u} - \langle \boldsymbol{u} \rangle - \nabla \phi \tag{5.18, 5.19}$$

where the scalar potential, ϕ, is calculated by solving a Poisson equation.

$$\nabla^2 \phi = \nabla \cdot \boldsymbol{u} \tag{5.20}$$

In a three-dimensional periodic domain $\boldsymbol{x} \in [0, 2\pi)^3$, the Poisson equation is solved in Fourier space

$$-k^2 \widehat{\phi}(\boldsymbol{k}) = i\boldsymbol{k} \cdot \widehat{\boldsymbol{u}}(\boldsymbol{k}) \tag{5.21}$$

where the operator $\widehat{(\cdot)}$ denotes the Fourier transform which is defined as $(\cdot) = \sum_{\boldsymbol{k}} \widehat{(\cdot)}(\boldsymbol{k}) \exp(i\boldsymbol{k} \cdot \boldsymbol{x})$, and $i = \sqrt{-1}$ is an imaginary unit associated with the Fourier transform. The energy spectrum, $E_{\boldsymbol{vv}}(k)$, with respect to an arbitrary vector field $\boldsymbol{v}$ is calculated as

$$E_{\boldsymbol{vv}}(k) = \left(\frac{L}{2\pi}\right)^3 \int_{\boldsymbol{k}_s} \frac{1}{2} \widehat{\boldsymbol{v}}(\boldsymbol{k}_s) \cdot \widehat{\boldsymbol{v}}^*(\boldsymbol{k}_s) \delta\left(|\boldsymbol{k}_s| - k\right) d\boldsymbol{k}_s \tag{5.22}$$

where $L = 2\pi$ is the one-dimensional domain period, "$(\cdot)^*$" denotes the complex conjugate, and δ is a dimensional Dirac delta function with units of "$1/k$." In practice, the $E_{\boldsymbol{vv}}(k)$ is calculated based on sampling within a thin spherical shell in Fourier space.

$$E_{\boldsymbol{vv}}(k) = \frac{4\pi k^2}{N_s(k;\Delta k)} \left(\frac{L}{2\pi}\right)^3 \sum_{||\boldsymbol{k}_s|-k| \leq \Delta k/2} \widehat{\boldsymbol{v}}(\boldsymbol{k}_s) \cdot \widehat{\boldsymbol{v}}^*(\boldsymbol{k}_s)/2$$

where Δk is the thickness of the spherical wavenumber shell for sampling, and $N_s(k;\Delta k)$ is the number of total samples within the wavenumber shell of wavenumber volume $4\pi k^2 \Delta k$. The energy spectrum of a scalar quantity can be calculated with a consistent approach.

The compensated energy spectra of the overall and decomposed velocity fields are shown in Fig. 5.4. The velocity energy spectra are scaled by $k^{-5/3} \left(\langle \epsilon \rangle / \langle \rho \rangle\right)^{2/3}$ according to the Kolmogorov hypothesis [80], and the wavenumber is normalized by the Kolmogorov length scale, η. Comparing the three velocity energy spectra, the solenoidal velocity fluctuations are dominant in the overall velocity fluctuation for $0.2 \leq M_t \leq 0.7$. The solenoidal velocity spectra are not sensitive to M_t. The bumps for all cases at $0.01 < k\eta < 0.02$ are due to the solenoidal forcing where the solenoidal velocity is mostly energetic. A clear inertial subrange associated with the energy cascade over a decade of wavenumbers can be observed for each case, and the energy cascade follows the "$-5/3$" law [80]. Additionally, the viscous subrange for more than 1.2 decades is resolved for each case. The energy spectra of the dilatational velocity component is largely sensitive to M_t. With the increase of M_t, a larger range of the energy cascade is formed. At $M_t \approx 0.7$, the range of the energy cascade shown from the energy spectrum of dilatational velocity is comparable to the inertial subrange shown from the solenoidal velocity spectrum. When $M_t \geq 0.3$, $E_{\boldsymbol{u}^d\boldsymbol{u}^d}(k)$ decays at a slightly smaller rate than $k^{-5/3}$ at large scales. These observations are consistent with the theoretical prediction from the compressible EDQNM model [7]. Furthermore, at $M_t \approx 0.2$, the profile of $E_{\boldsymbol{u}^d\boldsymbol{u}^d}$ is qualitatively similar to the schematic sketch of the energy spectrum of the dilatational velocity in the nonlinear equilibrium state in Sagaut & Cambon (2008) [134], where the sketch is claimed to be created according to the analytical model provided by Fauchet & Bertoglio (1999) [44].

The energy spectra of the vorticity, $\boldsymbol{\omega} = \nabla \times \boldsymbol{u}$, and velocity dilatation, $\theta = \nabla \cdot \boldsymbol{u}$, are shown in Fig. 5.5. Consistently with the observation from the energy spectra of solenoidal and dilatational velocities, the vorticity energy spectra collapse for all M_t. In the inertial subrange, a power-law is observed, and the log-scale slope is slightly larger than $k^{1/3}$. The energy spectra of the velocity dilatation at $M_t \approx 0.3$ is mostly excited in the low-wavenumber regime, and the spectral energy decays rapidly when $k\eta > 0.1$. With increasing M_t, a wider range of wavenumbers is excited. Additionally, at $M_t \approx 0.3$, $E_{\theta\theta}(k)$ does not show a uniform power-law decay in the high-wavenumber regime. $dE_{\theta\theta}/dk$ has clear non-monotonic behavior in the high-wavenumber decay regime, and the profile of $E_{\theta\theta}$ contains an inflection point. This non-monotonic decay behavior does not exist in the dilatation energy spectra for higher M_t. For the cases of $M_t \approx 0.3$ and $M_t \approx 0.4$, $E_{\theta\theta}(k)$ shows

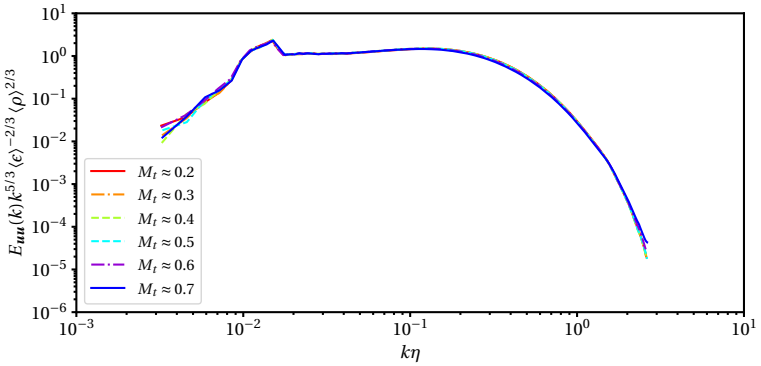

(a)

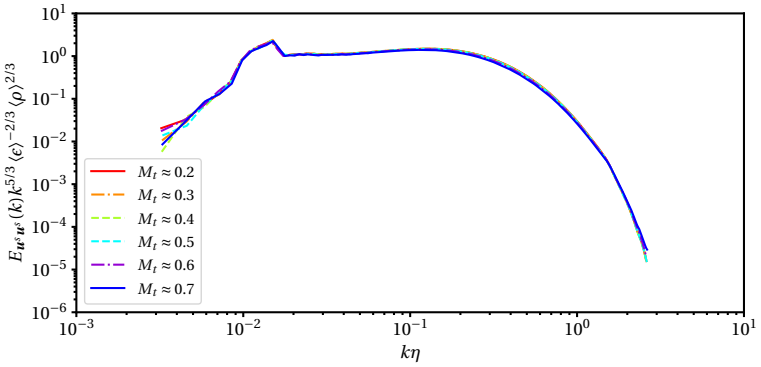

(b)

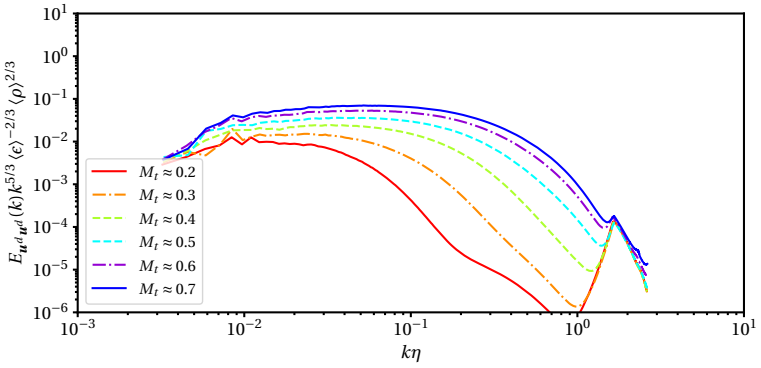

(c)

Figure 5.4: Energy spectra of (a) total velocity, (b) solenoidal velocity, and (c) dilatational velocity.

a power-law decay according to observation. The power-law decay behavior is not resolved for the cases of $M_t > 0.4$ where a larger range of dilatation spectral energy is excited. The visualizations of velocity dilatation at $M_t \approx 0.2$ and $M_t \approx 0.7$ are shown in Fig. 5.6. The values are normalized by their standard deviation. For a three-dimensional periodic domain, $\langle\theta\rangle = 0$ is numerically enforced,

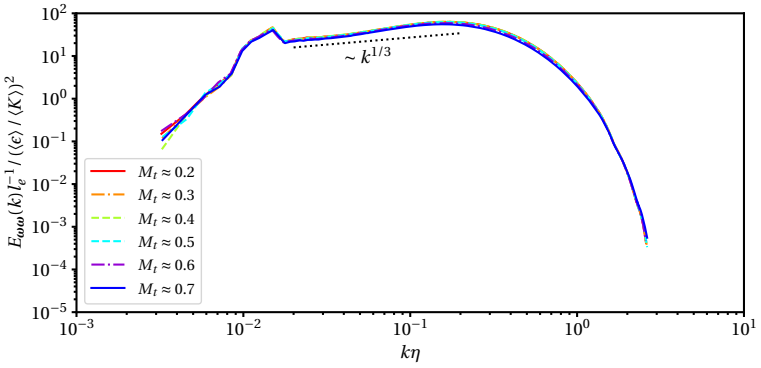

(a)

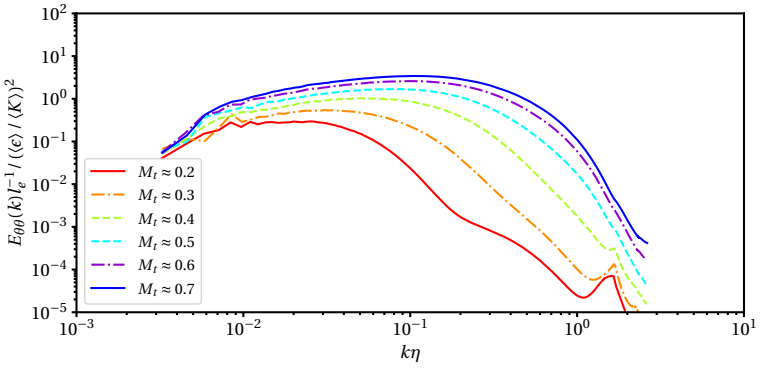

(b)

Figure 5.5: Energy spectra of (a) vorticity and (b) velocity dilatation.

so θ represents the fluctuating component. The structures of velocity dilatation are significantly different between a high-M_t flow and a low-M_t flow. At $M_t \approx 0.2$, the structure of θ, as shown in Fig. 5.6a, appears to have a cloud shape. This is due to the rapid decay of high-wavenumber spectral energy. In contrast, at $M_t \approx 0.7$, the contours of θ, as shown in Fig. 5.6b, contain strong and thin structures at small and intermediate length scales. These structures are highly anisotropic although θ is still homogeneous and isotropic over the whole computational domain due to the large-scale decorrelation. Some of these structures form eddy-shocklets. Combined with the energy spectrum shown in Fig. 5.5b, it is suggested that the formation of these structures is related to the weaker compression motions at larger scales normal to the strong and thin structures. The variance of velocity dilatation as a function of M_t and the probability density functions (PDF) of the normalized velocity dilatation for all cases are shown in Fig. 5.7. In Fig. 5.7a, the trend line, M_t^4, is provided to compare the scaling given by compressible EDQNM [134]. In this work, the eddy-turnover times used for scaling are approximately the same for all cases. The increase of $\langle\theta\theta\rangle$ roughly follows the trend of M_t^4, but discrepancies still exist and become more obvious for $M_t \geq 0.6$.

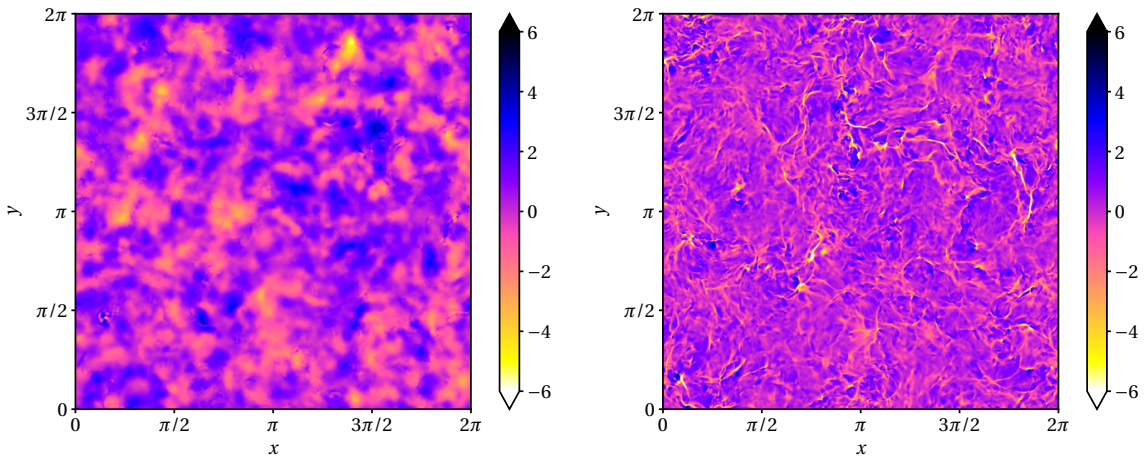

(a) (b)

Figure 5.6: Visualizations of normalized velocity dilatation, $\theta/\mathrm{std}\,(\theta)$, of flows at (a) $M_t \approx 0.2$ and (b) $M_t \approx 0.7$.

At low M_t, the distribution of θ is symmetric. However, the PDF develops negative skewness when $M_t \geq 0.4$, which indicates that the compression motion formed in the flow due to compressibility effects is stronger than the expansion motion measured by θ. This trend in the PDF is consistent with those reported in previous studies [72, 170]. Combined with the visualization in Fig. 5.6b, the skewness of the PDF in the negative branch is due to the formation of local strong and thin compression structures and eddy-shocklets.

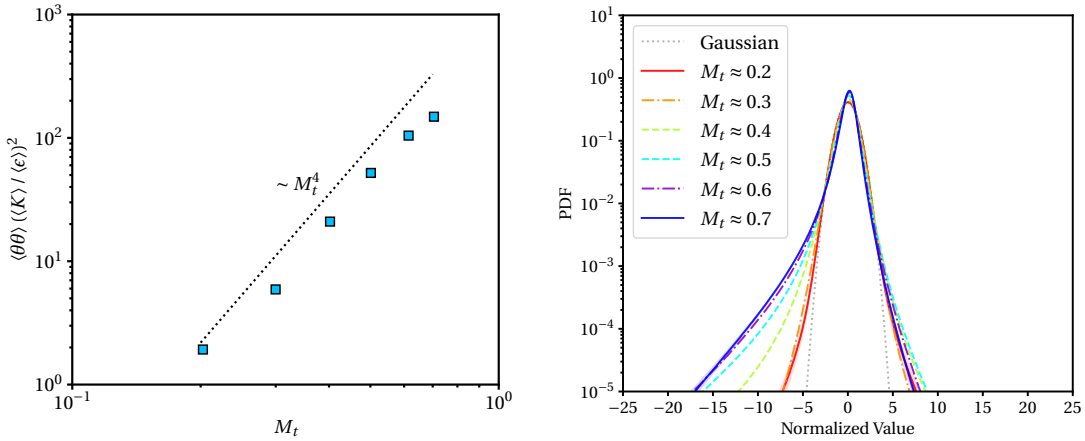

(a) (b)

Figure 5.7: Statistics of velocity dilatation: (a) variance of θ as a function of M_t and (b) PDF of $\theta/\mathrm{std}(\theta)$. The eddy-turnover times are approximately the same for all cases in this work.

The energy spectra of density is shown in Fig. 5.8. The spectra are normalized by the variance of density, $\langle \rho' \rho' \rangle$. At a low M_t, the decay of $E_{\rho'\rho'}$ within the inertial subrange is approximately k^{-2}. At a higher M_t, the scaling changes to $k^{-5/3}$, which is consistent with the corresponding observation in Wang et al. (2019) [172]. The statistics of density at different M_t are shown in Fig. 5.9. For different cases, the variance of density, $\langle \rho' \rho' \rangle$, is plotted as a function of M_t in Fig. 5.9a and an algebraic scaling is observed. For $0.2 \leq M_t \leq 0.7$, the fitting result shows that the density variance is proportional to $M_t^{7/2}$. The PDF of the normalized density fluctuations, $(\rho - \langle \rho \rangle)/\mathrm{std}(\rho)$, for all cases, are shown in Fig. 5.9b. When $M_t \leq 0.4$, the PDF has negative skewness. However, when $M_t \geq 0.5$, the skewness becomes positive and increases with M_t. The density fluctuations can be indirectly visualized using numerical Schlieren imaging, as shown in Fig. 5.10. It can be observed that at a low M_t (Fig. 5.10a), relatively strong fluctuations are localized to the center of vortical flow structures where $\rho' < 0$. However, at a high M_t (Fig. 5.10b), the strong density fluctuations are localized to the compression wave structures where $\rho' > 0$.

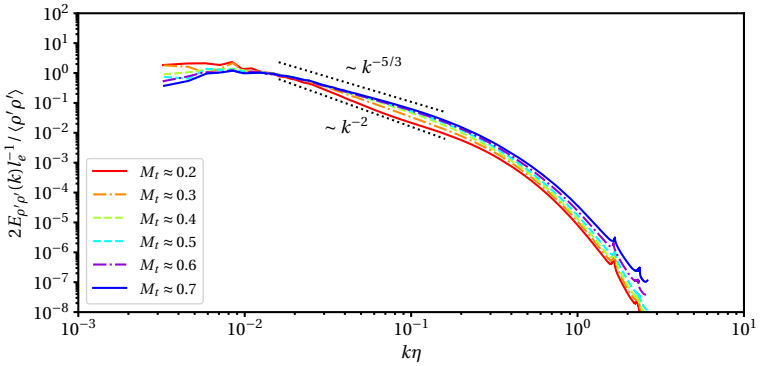

Figure 5.8: Energy spectra of density.

Associated with the velocity decomposition, the pressure field can be decomposed into three components.

$$p = p^s + p^d + \langle p \rangle \tag{5.23}$$

where p^s is known as the solenoidal pressure fluctuation and p^d is known as the dilatational pressure fluctuation. According to Jagannathan & Donzis (2016) [72], the solenoidal pressure fluctuation can be estimated by solving a Poisson equation.

$$-\frac{\partial^2 p^s}{\partial x_j \partial x_j} = \langle \rho \rangle \frac{\partial u_i^s}{\partial x_j} \frac{\partial u_j^s}{\partial x_i} \tag{5.24}$$

and the dilatational pressure fluctuation can then be calculated as $p^d = p - \langle p \rangle - p^s$. In this work, the Poisson equation is solved in Fourier space with the nonlinear term on the right-hand side calculated

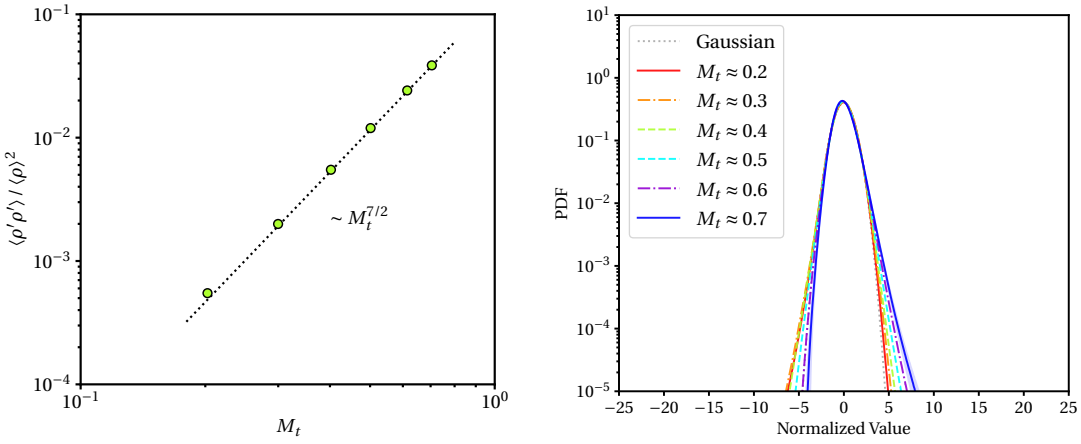

(a) (b)

Figure 5.9: Statistics of density: (a) variance of ρ as a function of M_t and (b) PDF of $(\rho - \langle\rho\rangle)/\text{std}(\rho)$. The mean density $\langle\rho\rangle$ remains the same constant during simulation across all cases.

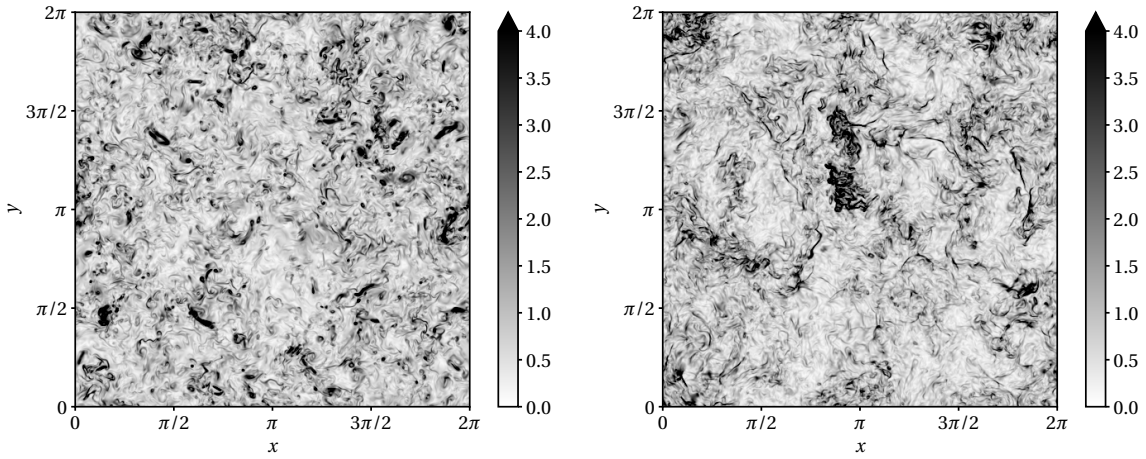

(a) (b)

Figure 5.10: Numerical Schlieren imaging, $|\nabla\rho|\,/\text{std}\,(|\nabla\rho|)$, of flows at (a) $M_t \approx 0.2$ and (b) $M_t \approx 0.7$.

in physical space.

$$k^2 \widehat{p^s} = \langle\rho\rangle \, \widehat{u^s_{i,j} u^s_{j,i}}$$

The energy spectra of p, p^s, and p^d are shown in Fig. 5.11 for all cases. In the energy spectra of the overall pressure field, as shown in Fig. 5.11a, a "$-7/3$" law is observed at $M_t \approx 0.2$ in the inertial subrange. This observation is consistent with the calculation from compressible EDQNM [7, 134]. As M_t increases, the decay of the overall energy spectra changes to a "$-5/3$" law. The $k^{-5/3}$ energy decay is also observed in other DNS of forced compressible isotropic turbulence as reported

in Wang et al. (2019)[172]. The energy spectra of solenoidal pressure fluctuations for all cases (Fig. 5.11b) show a $k^{-5/3}$ decay in the inertial subrange, and the spectra with different M_t show similarity behavior over the entire wavenumber range. The energy spectra of the dilatational pressure fluctuations in Fig. 5.11c show a wider range of excited wavenumbers with increasing M_t. At high wavenumbers, the decay rate in the inertial subrange is close to $k^{-3/2}$ by observation. As predicted by compressible EDQNM, a $k^{-5/3}$ decay will be recovered when M_t is close to 1 [134].

5.4 Decomposed velocity variance budget

Based on the orthogonality of the Helmholtz decomposition, the decomposed velocity variance can be obtained by projection following the identities $\langle u_i^s u_i \rangle = \langle u_i^s u_i^s \rangle$ and $\langle u_i^d u_i \rangle = \langle u_i^d u_i^d \rangle$. The projection is a bilinear spatial operation, and the operation commutes with the time derivative operator, which can be shown in Fourier space. The compressible Navier-Stokes equation, Eq. (5.2), is rearranged in primitive form to obtain the evolution of velocity.

$$\frac{\partial u_i}{\partial t} + u_j \frac{\partial u_i}{\partial x_j} + \frac{1}{\rho} \frac{\partial}{\partial x_j} \left[p\delta_{ij} - \sigma_{ij} \right] = f_i \tag{5.25}$$

The solenoidal and dilatational projections are applied by taking the spatial average of each term in the equation after multiplying by u_i^s and u_i^d respectively. The spatial average of the flux-divergence is zero, which is numerically enforced for the simulations with a 3D periodic domain. As a result, the budget equations of the solenoidal and dilatational velocity variance are obtained in Eq. (5.26) and Eq. (5.27) respectively.

$$\frac{1}{2} \frac{d \left\langle u_j^s u_j^s \right\rangle}{dt} = \left\langle (u_i^s \overline{\sigma}_{ij} - \overline{p} u_j^s) \overline{\rho}_{,j} \right\rangle - \left\langle u_i u_j S_{ij}^d \right\rangle + \langle E \rangle - \left\langle \overline{\sigma}_{ij}^s S_{ij}^s \right\rangle - \left\langle 2\nu S_{ij}^s S_{ij}^d \right\rangle + \left\langle f_j^s u_j^s \right\rangle \tag{5.26}$$

$$\frac{1}{2} \frac{d \left\langle u_j^d u_j^d \right\rangle}{dt} = \left\langle (u_i^d \overline{\sigma}_{ij} - \overline{p} u_j^d) \overline{\rho}_{,j} \right\rangle - \left\langle u_i u_j S_{ij}^s \right\rangle - \langle E \rangle - \left\langle \overline{\sigma}_{ij}^d S_{ij}^d \right\rangle - \left\langle 2\nu S_{ij}^s S_{ij}^d \right\rangle + \left\langle f_j^d u_j^d \right\rangle + \langle \overline{p} \theta \rangle \tag{5.27}$$

where the overbar operator denotes multiplying by ρ^{-1}, $\overline{(\cdot)} = (\cdot)/\rho$; ν is the kinematic shear viscosity, $\nu = \overline{\mu}$; $S_{ij}^s = \frac{1}{2}(u_{i,j}^s + u_{j,i}^s)$ and $S_{ij}^d = \frac{1}{2}(u_{i,j}^d + u_{j,i}^d)$ are the rate of strain tensors of the solenoidal velocity and dilatational velocity respectively; σ_{ij}^s and σ_{ij}^d are the viscous stress tensors associated with the solenoidal and dilatational velocities; f_j^s and f_j^d are the solenoidal and dilatational components of the external forcing; and E serves as the variance exchange term, which has the same expression but different signs in the two budget equations. The expression for the variance exchange term is

$$E = \frac{1}{2} \left(u_j^s u_j^s - u_j^d u_j^d \right) \theta \tag{5.28}$$

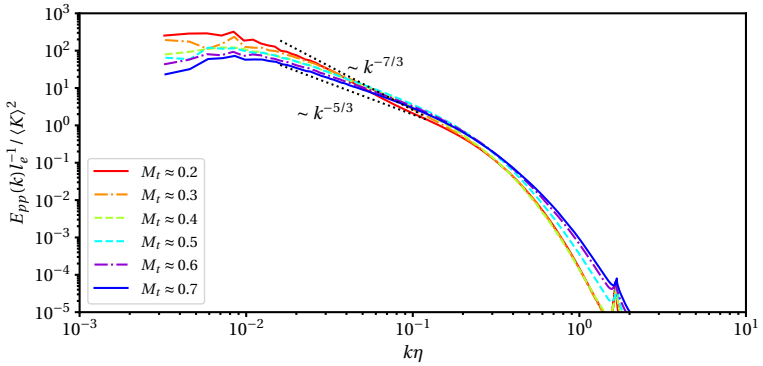

(a)

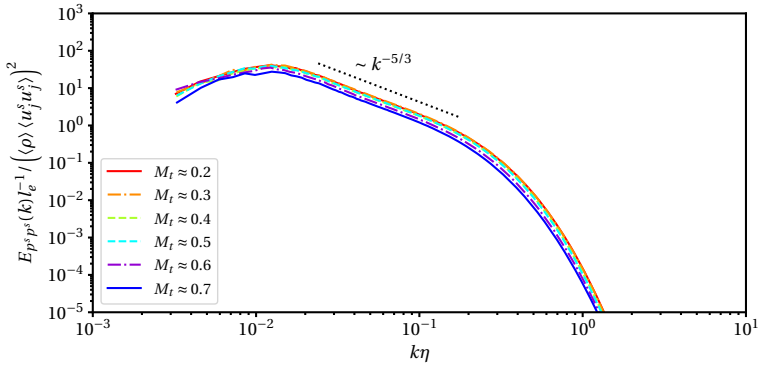

(b)

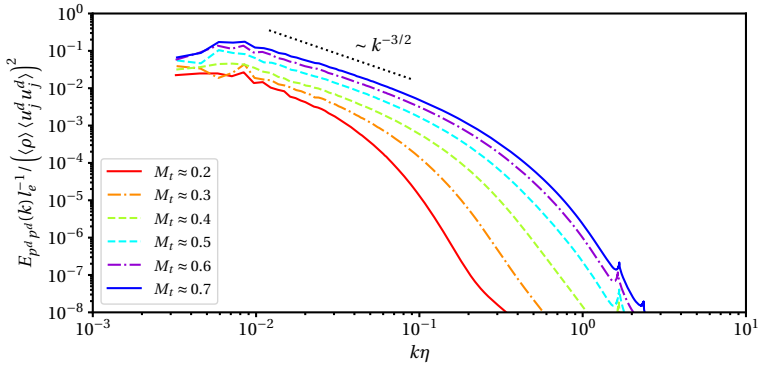

(c)

Figure 5.11: Energy spectra of (a) overall pressure, p, (b) solenoidal pressure fluctuation, p^s, and (c) dilatational pressure fluctuation, p^d.

Based on the expression, the exchange term tends to amplify the stronger decomposed variance while damping the weaker one through local expansion and reduces the discrepancy between the two components of variance through local compression. Following the expression of the viscous stress

tensor σ_{ij} in Eq. (5.6), the decomposed viscous stress tensors σ^s_{ij} and σ^d_{ij} are provided in Eq. (5.29) and Eq. (5.30) respectively.

$$\sigma^s_{ij} = 2\mu S^s_{ij} \qquad \text{and} \qquad \sigma^d_{ij} = 2\mu S^d_{ij} + \left(\beta - \frac{2}{3}\mu\right)\theta\delta_{ij} \tag{5.29, 5.30}$$

The terms on the right-hand sides of Eq. (5.26) and Eq. (5.27) describe the contributing mechanisms to the changes of the decomposed velocity variance. $\left\langle (u^s_i\overline{\sigma}_{ij} - \overline{p}u^s_j)\overline{\rho_{,j}}\right\rangle$ and $\left\langle (u^d_i\overline{\sigma}_{ij} - \overline{p}u^d_j)\overline{\rho_{,j}}\right\rangle$ represent the contributions from the density fluctuations. The factor $\overline{\rho_{,j}}$ characterizes the density non-uniformity, which can be written as

$$\overline{\rho_{,j}} = \frac{\partial}{\partial x_j}\ln(\rho/\langle\rho\rangle) \tag{5.31}$$

$\left\langle u_i u_j S^s_{ij}\right\rangle$ and $\left\langle u_i u_j S^d_{ij}\right\rangle$ can be interpreted as the velocity and solenoidal strain rate alignment, and the velocity and dilatational strain rate alignment respectively. $\left\langle \overline{\sigma}^s_{ij}S^s_{ij}\right\rangle + \left\langle 2\nu S^s_{ij}S^d_{ij}\right\rangle$ and $\left\langle \overline{\sigma}^d_{ij}S^d_{ij}\right\rangle + \left\langle 2\nu S^s_{ij}S^d_{ij}\right\rangle$ are the overall solenoidal and dilatational kinematic dissipation respectively, where $\left\langle 2\nu S^s_{ij}S^d_{ij}\right\rangle$ represents the cross-contributions or the overlap effects. As observed from DNS results, the contribution from $\left\langle 2\nu S^s_{ij}S^d_{ij}\right\rangle$ is negligible compared to $\left\langle \overline{\sigma}^s_{ij}S^s_{ij}\right\rangle$ and $\left\langle \overline{\sigma}^d_{ij}S^d_{ij}\right\rangle$. Based on the expression for σ^s_{ij} and σ^d_{ij} in Eq. (5.29) and Eq. (5.30), the kinematic dissipation satisfies

$$\overline{\sigma}^s_{ij}S^s_{ij} = 2\nu\Omega^2 + 2\nu u^s_{i,j}u^s_{j,i} \tag{5.32}$$

and

$$\overline{\sigma}^d_{ij}S^d_{ij} = \left(\overline{\beta} + \frac{4}{3}\nu\right)\theta^2 + 2\nu\left(\delta_{mp}\delta_{nq} - \delta_{mq}\delta_{np}\right)\left(S^d_{mn}S^d_{pq} - S^d_{mp}S^d_{nq}\right) \tag{5.33}$$

This analysis identifies the similarities and differences between the decomposed velocity variance dissipation and the expressions given by Sarkar et al. (1991) [135]. It is worth noting that the kinematic dissipation terms in Eq. (5.26) and Eq. (5.27) are with regards to the velocity variance instead of the kinetic energy. $\langle\overline{p}\theta\rangle$ is the kinematic pressure dilatation, where $\overline{p} = p/\rho$ is interpreted as the kinematic pressure. $\left\langle f^s_j u^s_j\right\rangle$ and $\left\langle f^d_j u^d_j\right\rangle$ are the specific work associated with the solenoidal and dilatational forcing respectively. For generally forced isotropic turbulence, the Helmholtz decomposition can also be applied to the forcing vector, $f_j = f^s_j + f^d_j + \langle f_j\rangle$, and the biorthogonality, $\left\langle f^s_j u^d_j\right\rangle = \left\langle f^d_j u^s_j\right\rangle = 0$, can be shown in Fourier space. The solenoidal and dilatational modes are always orthogonal with respect to the same wavenumber vector, even between Helmholtz decompositions of different vector fields, since the solenoidal mode is parallel to the wavenumber vector while the dilatational mode is perpendicular to the wavenumber vector. In this work, only solenoidal forcing is applied, so $f^d_j = 0$, and $\langle f_j\rangle = \left\langle \rho f^s_j\right\rangle / \langle\rho\rangle$ to enforce the conservation of mean momentum. Due to large-scale decorrelation, $\langle f_j\rangle \approx 0$.

In this analysis, all terms in the budget equations are normalized by the ensemble average of

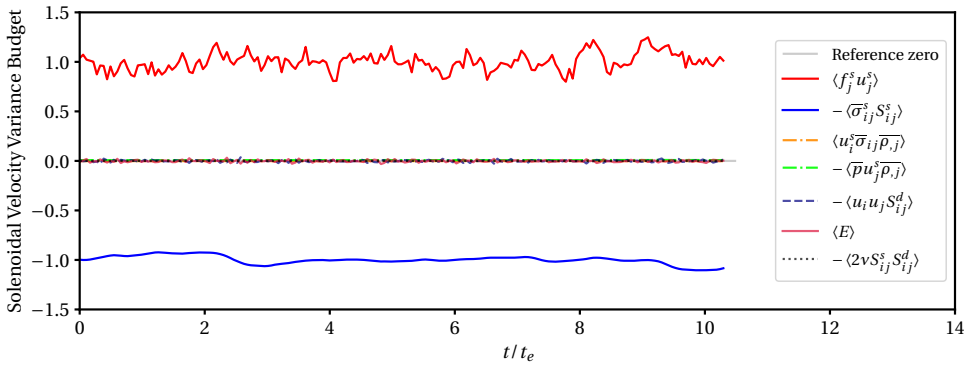

(a)

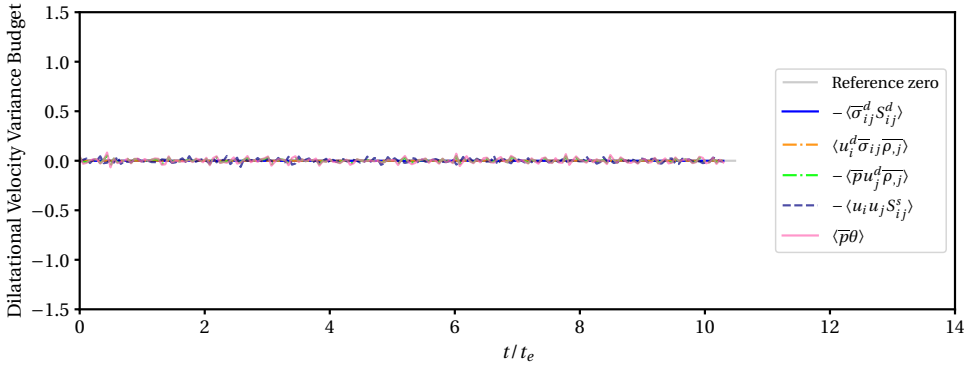

(b)

Figure 5.12: Velocity variance budget at $M_t \approx 0.2$: (a) right-hand side terms in the solenoidal velocity-variance budget and (b) right-hand side terms in the dilatational velocity-variance budget.

the solenoidal velocity variance dissipation, $\langle \overline{\sigma}_{ij}^s S_{ij}^s \rangle$. The time series of the budget terms over approximately 10 eddy-turnover times for $M_t \approx 0.2$ are shown in Fig. 5.12 and Fig. 5.13, where Fig. 5.13 shows zoomed-in views to illustrate small-amplitude contributions from the budget terms. The plots of the time series are signed where positive values indicate amplification contributions, and negative values indicate damping contributions. At $M_t \approx 0.2$, the budget equations primarily show the balance of solenoidal forcing and solenoidal dissipation. The contributions from all other terms are significantly smaller and negligible compared to the two balanced dominant mechanisms. The time series of the budget terms at $M_t \approx 0.7$ are shown in Fig. 5.14 as a zoomed-in view, and contributions from $\langle f_j^s u_j^s \rangle$ and $\langle \overline{\sigma}_{ij}^s S_{ij}^s \rangle$ are outside the scales of the plots. Compared to the low-M_t case, many terms develop clean biased behavior as M_t increases and have net contributions of amplification or damping to the decomposed velocity variance. In the solenoidal budget, both individual terms related to density fluctuations, $\langle u_i^s \overline{\sigma}_{ij} \overline{\rho_{,j}} \rangle$ and $\langle \overline{p} u_j^s \overline{\rho_{,j}} \rangle$, have approximately a 10% contribution to the total budget, and their fluctuations are relatively small compared to other terms.

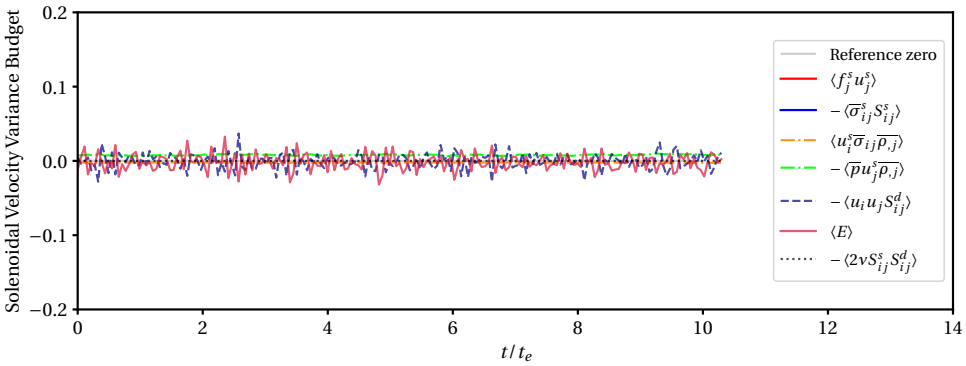

(a)

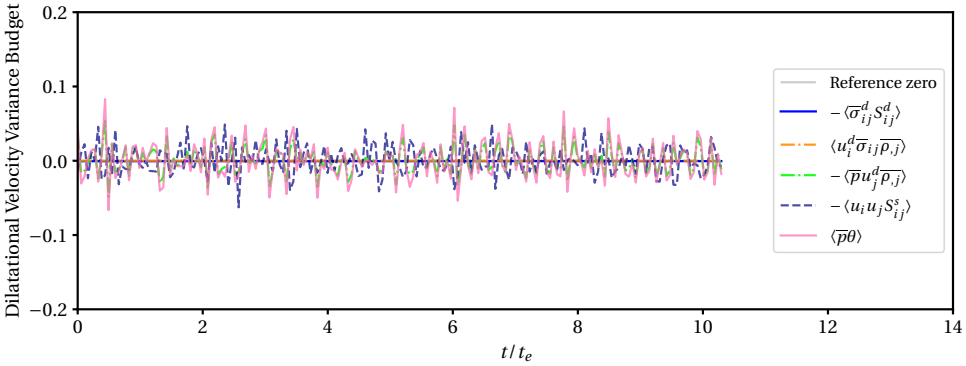

(b)

Figure 5.13: Velocity variance budget at $M_t \approx 0.2$: (a) right-hand side terms in the solenoidal velocity-variance budget and (b) right-hand side terms in the dilatational velocity-variance budget.

However, due to their opposite signs, the contributions from these two terms are largely cancelled. The term related to the alignment of velocity and dilatational strain rate, $\langle u_i u_j S_{ij}^d \rangle$, also has approximately a 10% contribution to the damping of the solenoidal velocity variance, and the amplitude is larger than the terms related to the density fluctuation. This term can be further decomposed into three components, $\langle u_i^s u_j^s S_{ij}^d \rangle$, $\langle u_i^d u_j^d S_{ij}^d \rangle$, and $\langle u_i^s u_j^d S_{ij}^d \rangle$, where the dominant contribution is from $\langle u_i^s u_i^s S_{ij}^d \rangle$. The direct energy exchange term, $\langle E \rangle$, has a net contribution to the transfer from solenoidal motion to dilatational motion. However, the fluctuation of $\langle E \rangle$ is relatively large compared to other terms, and its net contribution is only approximately 3.64%. In the dilatational budget, at $M_t \approx 0.7$, the dilatational dissipation, $\langle \overline{\sigma}_{ij}^d S_{ij}^d \rangle$ has approximately a 10% contribution. Besides the direct energy exchange, $\langle E \rangle$, another major amplification is gained from the alignment of velocity and the solenoidal strain rate, $\langle u_i u_j S_{ij}^s \rangle$. However, this term shows a relatively large fluctuation in time. Among the three further decomposed components, $\langle u_i^s u_j^s S_{ij}^s \rangle$, $\langle u_i^d u_j^d S_{ij}^s \rangle$, and $\langle u_i^s u_j^s S_{ij}^d \rangle$, the amplitude of $\langle u_i^s u_j^s S_{ij}^s \rangle$ is significantly smaller than the other two components by observation.

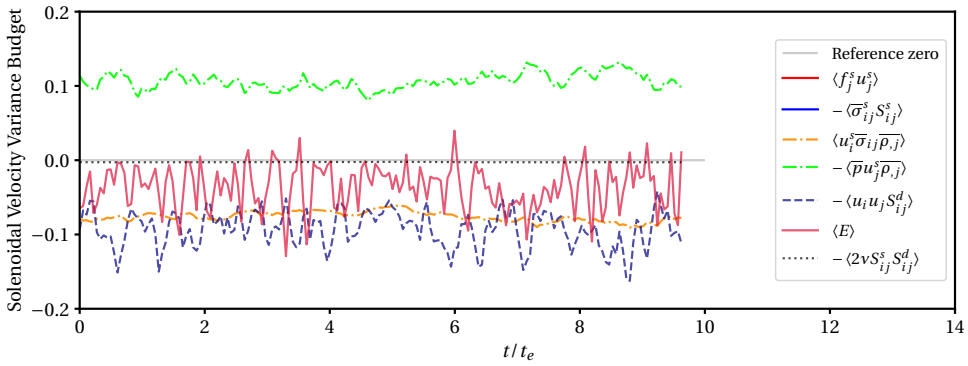

(a)

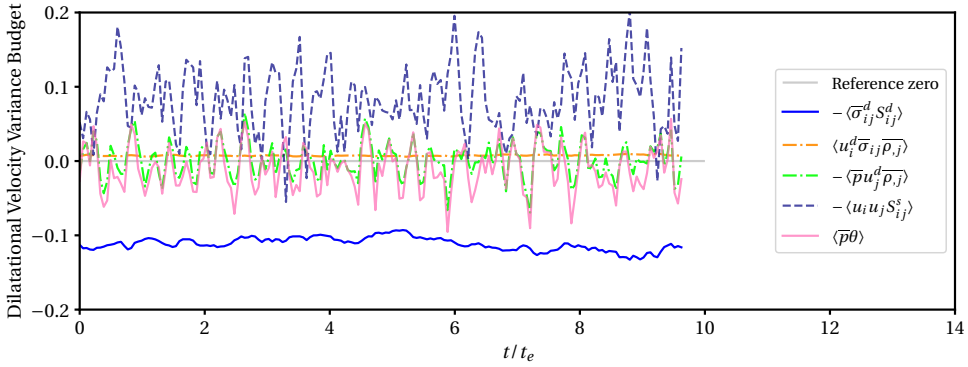

(b)

Figure 5.14: Velocity variance budget at $M_t \approx 0.2$: (a) right-hand side terms in the solenoidal velocity-variance budget and (b) right-hand side terms in the dilatational velocity-variance budget.

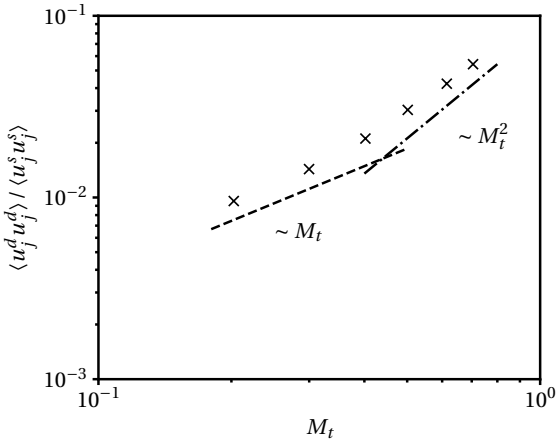

Figure 5.15: Ratio of decomposed velocity variance as a function of M_t.

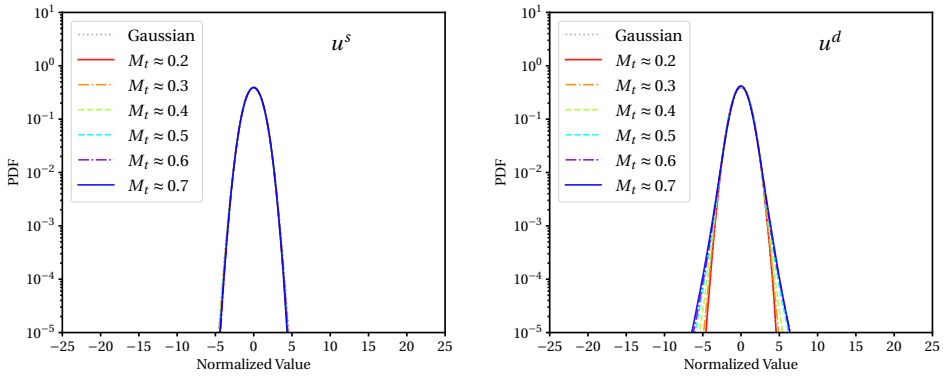

(a) (b)

Figure 5.16: Normalized PDFs of the decomposed velocity in x-direction: (a) solenoidal velocity distribution, $\left(u^s - \langle u^s \rangle\right) / \mathrm{std}\left(u^s\right)$, and (b) dilatational velocity distribution, $\left(u^d - \langle u^d \rangle\right) / \mathrm{std}\left(u^d\right)$.

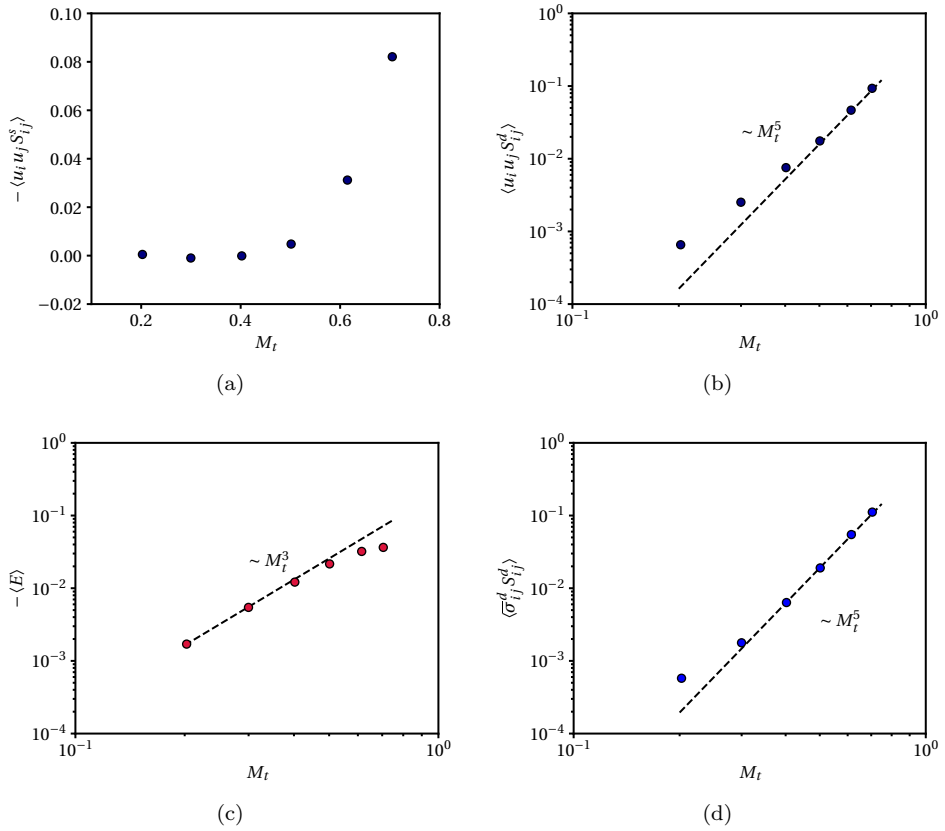

(a) (b)

(c) (d)

Figure 5.17: Selected terms in the decomposed velocity budget equations as functions of M_t: (a) alignment of velocity and solenoidal strain rate, $-\left\langle u_i u_j S^s_{ij} \right\rangle$, (b) alignment of velocity and dilatational strain rate, $\left\langle u_i u_j S^d_{ij} \right\rangle$, (c) exchange $-\langle E \rangle$, and (d) dilatational dissipation $\left\langle \overline{\sigma}^d_{ij} S^d_{ij} \right\rangle$.

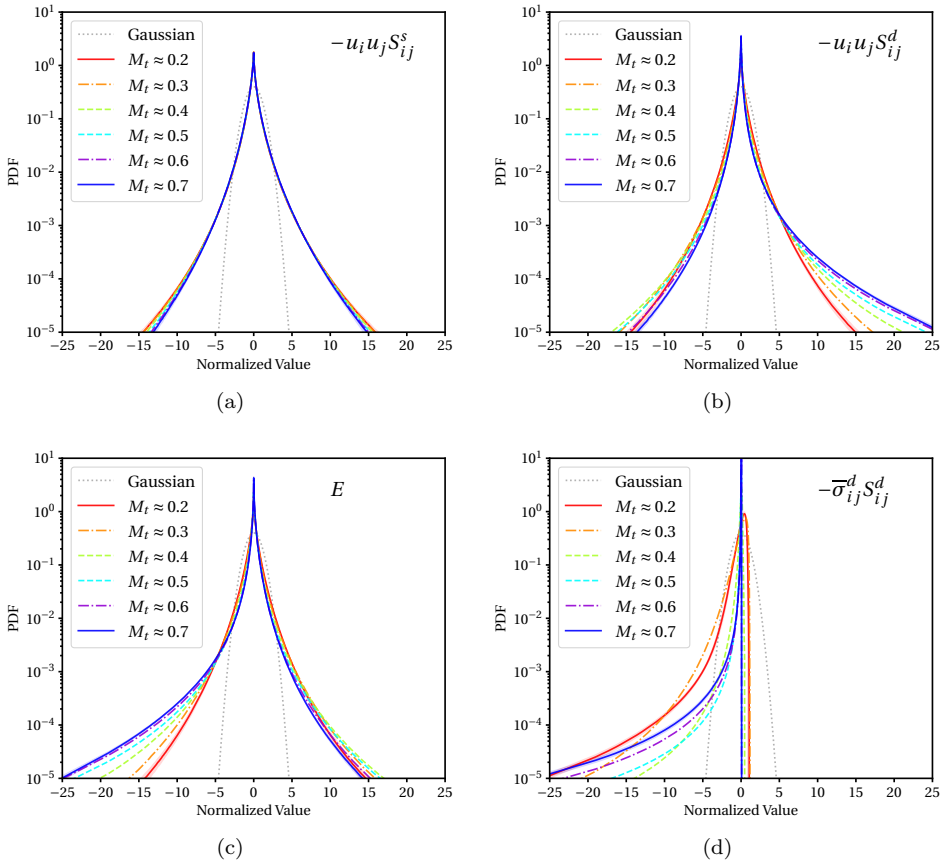

Figure 5.18: Normalized PDFs of selected terms in the decomposed velocity budget equations: (a) alignment of velocity and solenoidal strain rate, $-u_i u_j S^s_{ij}$, (b) alignment of velocity and dilatational strain rate, $-u_i u_j S^d_{ij}$, (c) exchange E, and (d) dilatational dissipation $-\overline{\sigma}^d_{ij} S^d_{ij}$. The normalized values are the fluctuating component scaled by their standard deviations.

The ratio of the decomposed velocity variance, $\langle u^d_j u^d_j \rangle / \langle u^s_j u^s_j \rangle$, as a function of M_t is shown in Fig. 5.15, where the trend lines are plotted for reference only. Within the range of M_t, the ratio of the decomposed velocity variance monotonically increases with M_t as expected, but the trend does not show a uniform scaling of M_t. The normalized PDFs of u^s and u^d (x-components of the decomposed velocities) are shown in Fig. 5.16. The normalized distribution of the solenoidal velocity does not depend on M_t and remains Gaussian for all cases. This behavior is consistent with the observations in Sec. 5.3. The dilatational velocity at low-M_t has a Gaussian distribution. However, as M_t increases, the distribution starts to develop non-Gaussian behavior with heavier tails.

Several terms in the decomposed velocity variance budget equations that make non-negligible contributions at high M_t are shown in Fig. 5.17 as functions of M_t. In order to show the M_t scaling behavior on log-log plots, the sign of each term may not follow the right-hand sides of the budget

equations if a scaling is observed. With M_t increasing approximately from 0.2 to 0.7, the budget term related to the alignment of velocity and solenoidal strain rate, $-\langle u_i u_j S^s_{ij} \rangle$, does not show a monotonic trend (Fig. 5.17a). At $M_t \approx 0.2$ and $M_t \approx 0.3$, the term switches sign. Additionally, the M_t scaling is not obvious as M_t increases. However, as shown in the time series in Fig. 5.13b and Fig. 5.14b, $-\langle u_i u_j S^s_{ij} \rangle$ strongly oscillates in time, and the temporal fluctuation amplitude is comparable to the amplitude of its net contribution. At a high M_t, this term makes a dominant contribution to enhancing dilatational motion and balancing with the dilatational dissipation and other minor mechanisms. The budget term related to the alignment of velocity and dilatational strain rate, $\langle u_i u_j S^d_{ij} \rangle$, shows a scaling of M_t^5 asymptotically in the high-M_t regime (Fig. 5.18b). The direct variance energy exchange, $\langle E \rangle$, shows a scaling of M_t^3 asymptotically towards the low-M_t regime (Fig. 5.17d). For $M_t > 0.5$, the scaling does not hold. The dilatational dissipation term, $\langle \overline{\sigma}^d_{ij} S^d_{ij} \rangle$, asymptotically shows a M_t^5 scaling towards the high-M_t regime when $M_t \geq 0.3$ (Fig. 5.18d). As the value of each budget term is normalized by the solenoidal dissipation, $\langle \overline{\sigma}^s_{ij} S^s_{ij} \rangle$, the scaling shown Fig. 5.18d reveals the scaling of the ratio of the dilatational dissipation to the solenoidal dissipation. In this analysis, $\langle \overline{\sigma}^d_{ij} S^d_{ij} \rangle$ and $\langle \overline{\sigma}^s_{ij} S^s_{ij} \rangle$ represent the dilatational and solenoidal dissipation of the decomposed velocity variance instead of the kinetic energy. Nevertheless, the M_t^5 scaling is consistent with the theoretical prediction of the scaling given by the compressible EDQNM model for $\langle \epsilon^d \rangle / \langle \epsilon^s \rangle$ when $M_t > 0.2$ [134]. This M_t^5 scaling is also consistent with the observation reported in Wang et al. (2017) [169]. In this work, the DNS is conducted without solution filtering as a numerical stabilization mechanism, the dilatational dissipation contains the dissipation from the eddy shocklets quantified by the artificial bulk viscosity.

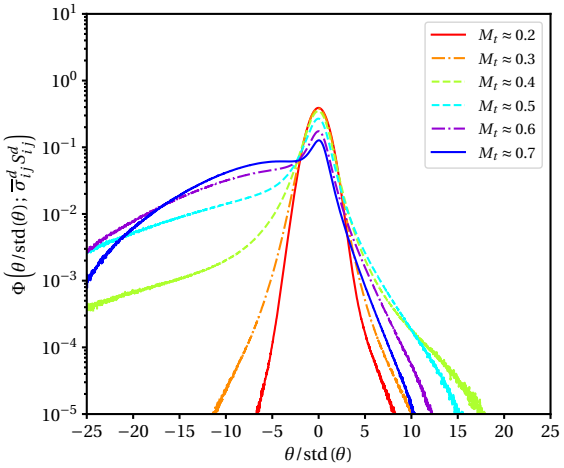

Figure 5.19: Normalized joint statistical density of dilatational dissipation, $\overline{\sigma}^d_{ij} S^d_{ij}$, with respect to the normalized velocity dilatation, $\theta/\mathrm{std}(\theta)$.

The normalized PDFs of the selected terms in the decomposed velocity variance budget equations

are shown in Fig. 5.18 for all cases. The normalized distribution in each plot represents the fluctuating component of the quantity of interest scaled by its standard deviation. The PDFs shown in Fig. 5.18 are obtained by ensemble averaging over approximately 10 eddy-turnover times. As shown in Fig. 5.18, none of the PDFs yield a Gaussian distribution. The profiles of PDFs are all heavy-tailed on both sides, except for the dilatational dissipation, $-\overline{\sigma}^d_{ij}S^d_{ij}$, which is a semi-negative-definite quantity. At low M_t, all PDFs of $-u_iu_jS^s_{ij}$, $-u_iu_jS^d_{ij}$, and E are symmetric. As M_t increases, the PDFs of $-u_iu_jS^d_{ij}$ and E develop obvious skewness, but the normalized PDF of $-u_iu_jS^s_{ij}$ is less sensitive to the variation in M_t.

The normalized joint statistical density of the dilatational dissipation, $\overline{\sigma}^d_{ij}S^d_{ij}$, with respect to the normalized velocity dilatation, $\theta/\mathrm{std}(\theta)$, is shown in Fig. 5.19. The normalized joint statistical density, $\Phi\left(\theta/\mathrm{std}(\theta);\overline{\sigma}^d_{ij}S^d_{ij}\right)$, is defined as

$$\Phi\left(\theta/\mathrm{std}(\theta);\overline{\sigma}^d_{ij}S^d_{ij}\right)=\frac{\displaystyle\int_{X\in\{\overline{\sigma}^d_{ij}S^d_{ij}\}}X\varphi\left(X,\theta/\mathrm{std}(\theta)\right)dX}{\displaystyle\int_{Y\in\{\theta/\mathrm{std}(\theta)\}}\int_{X\in\{\overline{\sigma}^d_{ij}S^d_{ij}\}}X\varphi\left(X,Y\right)dXdY} \tag{5.34}$$

where $\varphi(X,Y)$ represents the joint PDF of the random variables X and Y sampled for $\overline{\sigma}^d_{ij}S^d_{ij}$ and $\theta/\mathrm{std}(\theta)$ respectively. This definition is equivalent to the normalized dilatational-dissipation-weighted PDF of the normalized velocity dilatation. As shown in Fig. 5.19, at $M_t\approx 0.2$, the profile contains minor positive skewness. This indicates that the local expansion motion tends to cause slightly more dilatational dissipation compared to the local compression motion. As discussed in Sec. 5.3, the local expansion regions are localized to the center of small-scale vortical flow structures where density fluctuations tend to be negative, $\rho'<0$, and it is more efficient for the dilatational dissipation to damp the local dilatational velocity fluctuation. At $M_t\approx 0.3$, the profile of Φ is approximately symmetric, which implies that the dilatational velocity variance is approximately equally damped by compression and expansion motions in the domain. When $M_t\geq 0.4$, the profiles of Φ start to develop large negative skewness. At $M_t\approx 0.4$ and $M_t\approx 0.5$, the majority of dilatational dissipation is still due to the weak dilatational motion. However, when $M_t>0.5$, the dilatational dissipation associated with strong compression motions becomes more significant.

5.5 Conclusions

In this work, compressibility effects in compressible isotropic turbulence are studied. The investigation uses a set of DNS of solenoidally forced compressible isotropic turbulence ranging from $M_t\approx 0.2$ to $M_t\approx 0.7$ with $\mathrm{Re}_\lambda\approx 170$ for all cases. The computational mesh size for each case is 1024^3, and the simulations are configured on a 3D periodic domain with mean density and mean momentum numerically preserved. The solenoidal forcing is stochastic and evolves in Fourier space

with wavenumbers in the range $3 \leq k \leq 5$, which provides sufficient large-scale decorrelation while allowing for the development of small-scale turbulent flow structures over a wide range of length scales. For $M_t \geq 0.4$, the localized artificial bulk viscosity and artificial thermal conductivity models are applied for shock capturing. The simulation framework has improved spectral resolution and all simulations do not have solution filtering. Approximately 10 eddy turnover times are used for ensemble averaging of statistical quantities in the analysis. The Helmholtz decomposition is applied to the velocity field. The energy spectra of the overall and decomposed velocity fields, vorticity field, velocity dilatation field, and solenoidal and dilatational pressure fields are provided. The results show that the quantities associated with the solenoidal motions are not sensitive to the change in M_t, but the quantities related to the dilatational motions are quite sensitive to M_t. At a low M_t, the dilatational motion is gentle. The energy spectra associated with the dilatational motion are excited primarily in the low-wavenumber regime. However, as M_t increases, the flow starts to develop strong compression motions and forms thin, locally anisotropic wave-like structures shown by the velocity dilatation field. Some of the strong compression motions form eddy shocklets. This behavior is revealed in the energy spectra where a higher wavenumber regime is excited, and it leads to a negative skewness in the PDF of velocity dilatation when $M_t > 0.3$. The velocity dilatation variance approximately shows a M_t^4 scaling, and the density variance approximately shows a $M_t^{7/2}$ scaling over the range of M_t investigated. The decomposed velocity variances are used as the energy norm to characterize the strength of the decomposed motions. The budget equations of the decomposed velocity variances are analytically derived from the compressible Navier-Stokes equations without a closure model. At a low M_t, the budget equations primarily show the balance between solenoidal forcing and solenoidal dissipation. At a higher M_t, more terms on the right-hand sides of the budget equations are excited and show biased behavior indicating net amplification or damping of the decomposed motions. As M_t increases, the ratio of the dilatational velocity variance to the solenoidal velocity variance monotonically increases, but the ratio does not show a uniform scaling with M_t. However, several terms in the budget equations that have major contributions show a clear M_t scaling within part of the range of M_t used in this work. The PDFs of these terms are non-Gaussian. The normalized PDF of the alignment of velocity and solenoidal strain rate does not show a strong dependence on M_t. The normalized PDFs of the alignment of velocity and dilatational strain rate, $u_i u_j S_{ij}^d$, and the term of exchange, E, develop obvious skewness as M_t increases. The normalized joint statistical density of the dilatational dissipation is calculated, and the results indicate that at $M_t \approx 0.2$ the total dilatational dissipation due to local expansion is slightly greater than that due to the local compression motion. However, when $M_t > 0.3$ the overall dilatational dissipation caused by local compression motions is higher than that caused by the local expansion motions. For $M_t \leq 0.5$, the majority of dilatational dissipation is caused by weak dilatational motions, but the dilatation dissipation caused by strong local compression motion become more significant when $M_t > 0.5$.

Chapter 6

Numerical Study of Transonic Laminar Shock Buffet

The shock buffet phenomenon in a transonic flow over the OALT25 laminar supercritical airfoil is investigated using a wall-resolved large-eddy simulation. The airfoil is configured in a Mach 0.735 freestream with a 4-degree angle-of-attack. The chord-length-based Reynolds number is 1 million. The simulation is conducted using a high-resolution computational framework based on high-order compact finite difference methods and hybrid central-Riemann fluxes combined with nonlinear interpolation schemes for shock-capturing. Data over a range of approximately 267 convective time units are collected and used in the analysis. It is observed that the flow on the suction side remains laminar up to the boundary layer separation point. The flow transitions to turbulence due to the Kelvin-Helmholtz instability after laminar separation, and the main shock is located above the turbulent portion of the boundary layer close to the transitional region. Associated with shock buffet, the signals corresponding to the lift and drag coefficients show two dominant frequencies at Strouhal numbers of approximately 0.1 and 0.55. Further signal processing identifies that the two peak frequencies correspond to shock buffet and turbulent vortex shedding respectively. Spectral proper orthogonal decomposition using different energy norms is applied to further investigate the space-time correlations of the flow system during shock buffet. Five frequencies, including the shock buffet and turbulent vortex shedding frequencies, are identified where the system has low-rank behavior. The evolution of the low-rank mode shapes at the dominant frequencies suggests several feedback mechanisms.

The study illustrated in this chapter is published in Ref. [148].

6.1 Introduction

Shock buffet over an airfoil can create large-amplitude low-frequency fluctuations in its aerodynamic performance and may lead to strong aircraft structural vibrations, which drastically limits the flight envelope [87, 55]. Transonic shock buffet over airfoils has been widely studied both experimentally [123, 124, 71, 99] and numerically [70, 4, 17, 179, 56]. For large-scale airfoils operating under transonic conditions, the chord-length-based Reynolds number is sufficiently high so that the boundary layer becomes fully turbulent close to the leading edge. When shock buffet occurs, the phenomenon is commonly referred to as turbulent buffet. A variety of two-dimensional airfoil geometries, such as OAT15A [71], RA16SC1 [5], NACA 0012 [101], and NACA 64A204 [69], are provided as benchmarks for broad investigations. Numerical investigations based on popular approaches, such as unsteady Reynolds-averaged Navier-Stokes (RANS) simulations [17, 69], wall-modeled large-eddy simulations (LES) [50, 4, 56] , and hybrid RANS / LES [34, 59, 179], have been undertaken for either low-cost parameter studies or high-fidelity analysis of detailed mechanisms. A mechanism for transonic shock buffet over a supercritical airfoil with a fully separated turbulent boundary layer was proposed by Lee (1990) [86] based on signal processing from an experimental measurement. The theory suggests a feedback mechanism in which the pressure disturbance generated from the shock propagates downstream within the separated flow region to the trailing edge and then creates upstream-traveling waves at the trailing edge which further perturbs the shock unsteadiness [86]. In addition, a global instability theory is formulated and justified by Crouch et al. (2007) [32] to predict the onset of turbulent shock buffet. The study analyzes modal linear stability about a steady-state mean flow from a RANS solution [32]. Iwatani et al. (2023) [70] identify two types of mechanisms that contribute to shock buffet using resolvent analysis [155]. The study suggests that the phenomenon of shock buffet is co-contributed to by both periodic pressure disturbances due to the variation of separated flow height near the trailing edge and upstream traveling pressure waves around the shock.

Recently, laminar supercritical airfoils, designed to significantly push the boundary layer transition point further downstream as compared to traditional airfoils, have gained increasing attention motivated by drag reduction for fuel-efficient aircraft design [60]. In transonic flows under buffeting conditions, the shock over a laminar supercritical airfoil is commonly located above the turbulent boundary layer near the transition point. This phenomenon is commonly recognized as laminar shock buffet as opposed to turbulent shock buffet, where the shock is located above a fully turbulent boundary layer. A complete laminar shock buffet system contains shock / laminar boundary layer interactions, unsteadiness of laminar separation, shear-instability-induced flow transitioning to turbulence, turbulent vortex shedding, etc. Several two-dimensional laminar supercritical airfoil geometries with their wind-tunnel experimental data are accessible for public research. These include, but are not limited to, the OALT25 airfoil designed by ONERA [15] and the V2C airfoil designed by Dassault Aviation [124]. High-resolution LES transonic shock buffet over an OALT25 airfoil at

a chord-length-based Reynolds number of 3 million are conducted by Dandois et al. (2018) [33] and the results are validated by the wind-tunnel measurements. Detailed shock and flow structures and signal processing results are reported, and the effects of the Kelvin-Helmholtz instability and the breathing of the separation bubble associated with turbulent vortex shedding are discussed in detail. Zauner et al. (2020) [181] investigate laminar shock buffet at a low Reynolds number. The results show that laminar shock buffet at a relatively low Reynolds number, 0.5 million, contains multiple unsteady shocks, and the primary oscillations of lift may be uncorrelated with the periodic shock motions. Zauner et al. (2023) [180] conduct spectral proper orthogonal decomposition (SPOD) analyses [158] of both OALT25 and V2C airfoils under transonic shock buffet conditions using the LES data. Selected mode shapes are reported. Furthermore, the effects of flow structures and a scaling approach are justified at various Reynolds numbers.

This work focuses on understanding the physical mechanisms that cause transonic laminar shock buffet on a laminar supercritical airfoil. The study uses data generated from a wall-resolved LES of transonic flow over the OALT25 airfoil [15] at a Reynolds number of 1 million. The simulation details are provided in Sec. 6.2. The simulation results and data analysis are shown in Sec. 6.3. Finally, the conclusions are given in Sec. 6.4.

6.2 Simulation setup

6.2.1 Physical formulation

The simulation solves the compressible Navier–Stokes equations using the wall-resolved LES approach, which includes conservation of mass, momentum, and total energy:

$$\frac{\partial \rho}{\partial t} + \frac{\partial \rho u_j}{\partial x_j} = 0, \tag{6.1}$$

$$\frac{\partial \rho u_i}{\partial t} + \frac{\partial}{\partial x_j}\left(\rho u_i u_j + p\delta_{ij}\right) = \frac{\partial \sigma_{ij}}{\partial x_j}, \tag{6.2}$$

$$\frac{\partial \rho e}{\partial t} + \frac{\partial}{\partial x_j}\left[\left(\rho e + p\right) u_j\right] = \frac{\partial}{\partial x_j}\left(u_i \sigma_{ij} + \kappa \frac{\partial T}{\partial x_j}\right). \tag{6.3}$$

The equations are written in index notation, where x_i and t are the spatial coordinate vector and time respectively. ρ is the density, u_i is the velocity vector, p is the pressure, δ_{ij} is the identity tensor, σ_{ij} is the viscous stress tensor, e is the specific total energy, κ is the total thermal conductivity, and T is the temperature. The primitive variables, ρ, u_i, and T are interpreted as filtered quantities supported by the computational grid resolution as compared to the full range of length scales of the turbulent structures. The subgrid-scale (SGS) models are absorbed into the transport properties based on the Boussinesq hypothesis [13]. The fluid is assumed to be calorically perfect with the

ideal gas equation of state:

$$p = \rho RT, \tag{6.4}$$

where R is the specific gas constant. The total energy contains two components, $e = e_{\text{th}} + u_j u_j/2$, where the internal energy and kinetic energy are the first and second terms on the right hand side of the equation. For a calorically perfect gas, the specific internal energy can be calculated as

$$e_{\text{th}} = \frac{RT}{\gamma - 1}, \tag{6.5}$$

where γ is the ratio of specific heats and remains as a constant. The viscous stress tensor is calculated as

$$\sigma_{ij} = 2\mu S_{ij} + \left(\beta - \frac{2}{3}\mu\right) S_{kk}\delta_{ij}, \tag{6.6}$$

where μ is the total dynamic shear viscosity, β is the bulk viscosity, and S_{ij} is the strain rate tensor which is calculated as

$$S_{ij} = \frac{1}{2}\left(\frac{\partial u_i}{\partial x_j} + \frac{\partial u_j}{\partial x_i}\right). \tag{6.7}$$

The total dynamic shear viscosity, μ, includes two components, $\mu = \breve{\mu} + \mu_{\text{SGS}}$, where $\breve{\mu}$ is computed using the power-law relation as a physical model:

$$\breve{\mu} = \mu_{\text{ref}} \left(T/T_{\text{ref}}\right)^{0.76}, \tag{6.8}$$

and μ_{SGS} is calculated based on the Vreman SGS model [167]. The bulk viscosity only includes a physical component, which is set to be directly proportional to the physical dynamic shear viscosity [58]:

$$\beta = 0.67\breve{\mu}. \tag{6.9}$$

No SGS model is applied to the dynamic bulk viscosity in this simulation. The total thermal conductivity also contains the computable physical and SGS components, $\kappa = \breve{\kappa} + \kappa_{\text{SGS}}$. The computable physical component, $\breve{\kappa}$ is calculated based on a constant Prandtl number, Pr:

$$\breve{\kappa} = c_p\breve{\mu}/\text{Pr}, \tag{6.10}$$

where c_p is the specific heat at a constant pressure. For a calorically perfect gas, c_p is calculated as $c_p = \gamma R/(\gamma - 1)$. The SGS component is calculated based on a constant turbulent Prandtl number, Pr_t, as follows.

$$\kappa_{\text{SGS}} = c_p\mu_{\text{SGS}}/\text{Pr}_t. \tag{6.11}$$

In this simulation, the Prandtl numbers are set to $\text{Pr} = 0.7$ and $\text{Pr}_t = 1$.

Transonic flow past the OALT25 supercritical airfoil is investigated in this work. The problem

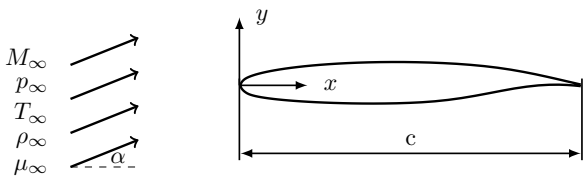

Figure 6.1: Schematics of problem configuration.

configuration is shown in Fig. 6.1. The airfoil is placed so that the chord is aligned with the x-direction, and the chord length is denoted as c. The uniform freestream conditions are specified by the Mach number M_∞ and angle of attack α. The Mach number is defined as $M_\infty = U_\infty/a_\infty$, where U_∞ and a_∞ are the flow speed and the speed of sound in the freestream respectively. With the given thermodynamic values of T_∞ and p_∞, the speed of sound for a calorically perfect gas can be calculated as $a_\infty = \sqrt{\gamma R T_\infty}$. The chord-based Reynolds number is defined as $\mathrm{Re}_c = \rho_\infty U_\infty c/\mu_\infty$, where ρ_∞ and μ_∞ are the density and dynamic shear viscosity in the freestream respectively. The freestream is assumed to be laminar, so $\mu_{\mathrm{SGS}} = 0$ is implied in the far-field.

6.2.2 Numerical methods

The schematic of the computational configuration is shown in Fig. 6.2. The computational domain is circular in the x-y plane. The domain has a radius of $R_{\mathrm{dom}} = 70c$. The far-field flow region is regularized with a numerical sponge using the freestream conditions. The numerical sponge layer starts from $R_{\mathrm{spg}} = 50c$. The simulation uses a hybrid central-Riemann flux with an explicit SGS model in the regions within a radius of R_{LES}, while a pure Riemann flux, calculated using an upwind-biased shock-capturing scheme, is applied beyond the radius R_{LES}. In this work, $R_{\mathrm{LES}} = 1.55c$ is chosen based on the grid resolution as well as the domain of interest.

The simulation is conducted using sixth-order compact finite difference methods [89] arranged in a high-resolution computational framework without numerical filtering [146]. The shock-capturing method is coupled with the compact finite difference method in the convective flux discretization [110, 182, 176, 150]. The shock-capturing method is based on explicit fifth-order interpolation using the nonlinear weights of the weighted essentially non-oscillatory scheme (WENO5-Z) [11] and the Rusanov-type (local Lax-Friedrichs) Riemann flux [132] as a Riemann solver. To localize the numerical dissipation introduced by the shock-capturing scheme, the Riemann flux is hybridized with the central flux controlled by the modified Ducros sensor, ϕ, defined as follows:

$$\phi = \frac{-\theta|\theta| + \varepsilon^2}{\theta^2 + \boldsymbol{\omega}\cdot\boldsymbol{\omega} + \varepsilon^2}, \tag{6.12}$$

where $\theta = \nabla\cdot\boldsymbol{u}$ is the velocity dilatation, $\boldsymbol{\omega} = \nabla\times\boldsymbol{u}$ is the vorticity vector, and ε is a small constant set to $\varepsilon = 1\times10^{-16}$ to avoid division by zero. The simulation in this work uses binary flux blending

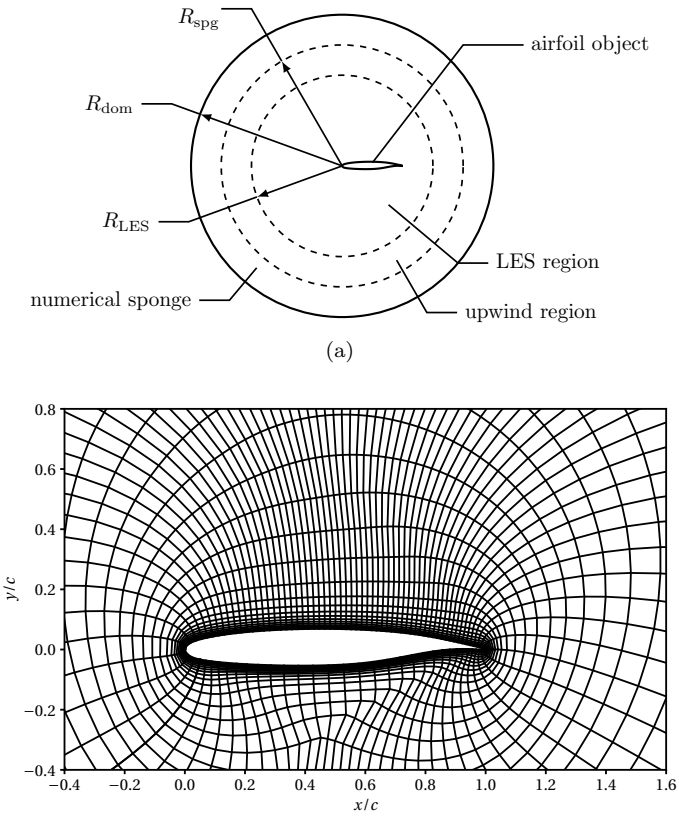

Figure 6.2: Simulation configurations shown in x-y plane: (a) schematics of computational domain setup; and (b) visualization of computational mesh (down-sampled for better visualization) near the airfoil in the x-y plane. The computational domain is periodic and homogeneous in the z-dimension, with uniform computational grid spacing.

with a specified threshold sensor value $\phi_{\mathrm{TH}} = 0.4$. When $\phi > \phi_{\mathrm{TH}}$, the Riemann flux is used; otherwise, only the central flux is used. The time advancement is conducted using the three-stage third-order strong-stability-preserving Runge–Kutta (SSPRK3) method [142] with an adaptive time step controlled by the global Courant–Friedrichs–Lewy (CFL) condition [31]. A CFL number of 0.95 is used for the simulation, and the time step size is mainly limited by the near-wall mesh spacing.

The simulation is deployed on an O-type computational mesh in the x-y plane that is generated by a smooth orthogonal hyperbolic extrusion from the airfoil geometry. To avoid spurious numerical oscillations caused by interactions between any non-smooth geometry components and the high-order numerical schemes on a curvilinear mesh, the trailing edge starting from $x = 0.997c$ on each side of the airfoil is smoothed using a quadratic Bézier curve [43] while maintaining the original chord length. The grid size is stretched along the airfoil wall-normal direction to resolve the boundary

layer flow. Since $\alpha > 0$ for the flow under investigation, the computational grid along the streamwise direction is highly refined on the suction side to capture the shock waves and resolve the Mach waves and turbulent structures at fine scales. The computational domain is periodic in the spanwise z-direction with a span of $W = 0.25c$. The computational grid spacing is uniform in the spanwise direction. The computational mesh size is $420 \times 3072 \times 512$ in the radial, azimuthal, and spanwise directions respectively.

6.2.3 Justification of model and numerical dissipation

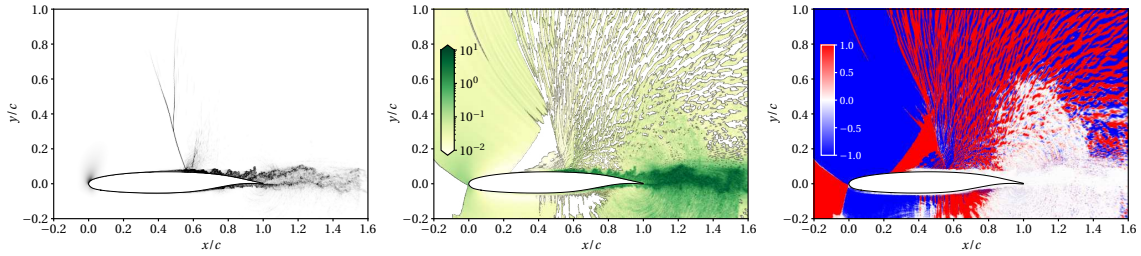

(a) (b) (c)

Figure 6.3: Visualizations of relative model and numerical dissipation imposed in the simulation: (a) numerical Schlieren imaging; (b) ratio of SGS eddy viscosity to the physical viscosity, $\mu_{\text{SGS}}/\check{\mu}$; and (c) modified Ducros sensor, ϕ, shown in Eq. (6.12), where shock-capturing scheme is used when $\phi > 0.4$.

A brief justification of both the SGS and numerical dissipation for shock-capturing is provided by comparing the instantaneous flow fields of the numerical Schlieren imaging, relative SGS eddy viscosity, and modified Ducros sensor, as shown in Fig. 6.3. The relative SGS eddy viscosity is defined as $\mu_{\text{SGS}}/\check{\mu}$, and the modified Ducros sensor is already stated in Eq. (6.12). Based on the comparison shown in Fig. 6.3, the SGS terms are only locally turned on in regions containing the turbulent flow features. In the near-wall region, $\mu_{\text{SGS}}/\check{\mu} \sim \mathcal{O}(1)$, and in the wake region farther away from the airfoil trailing edge, $\mu_{\text{SGS}}/\check{\mu}$ is close to but still lower than 10. The use of Riemann fluxes is highly localized at shocks and strong compression waves, and the numerical dissipation from the shock-capturing scheme is essentially not in effect in the turbulent regions. Additionally, comparing the plots of μ_{SGS} and ϕ, it can be confirmed that the activation of the shock-capturing scheme simultaneously suppresses the SGS model locally to avoid imposing excessive numerical dissipation, which can help capture the shock-turbulence interactions more accurately [6].

6.3 Results and discussions

The analysis illustrated in this section is based on the wall-resolved LES described in Sec. 6.2. In this work, the freestream Mach number of the problem is set as $M_\infty = 0.735$, and the Reynolds number is $\mathrm{Re}_c = 1 \times 10^6$. The angle of attack is chosen to be $\alpha = 4^\circ$ to induce shock buffet. The simulation time is normalized to the convective time unit (CTU) by one flow through time, which is defined as $t_{\mathrm{CTU}} = c/U_\infty$. After the initial transient, the simulation data are collected at a fixed time interval, approximately 0.02174 CTUs. Data, including 12288 snapshots spanning approximately 267 CTUs, are used for post-simulation analysis. In the following context, the visualization-based observations about shock buffet and the related flow structures are described in Sec. 6.3.1. Detailed analysis of signals at selected probe locations is illustrated in Sec. 6.3.2. Finally, the low-rank model analysis based on spectral proper orthogonal decomposition (SPOD) is discussed in Sec. 6.3.3.

6.3.1 Visualizations of shock buffet and related flow structures

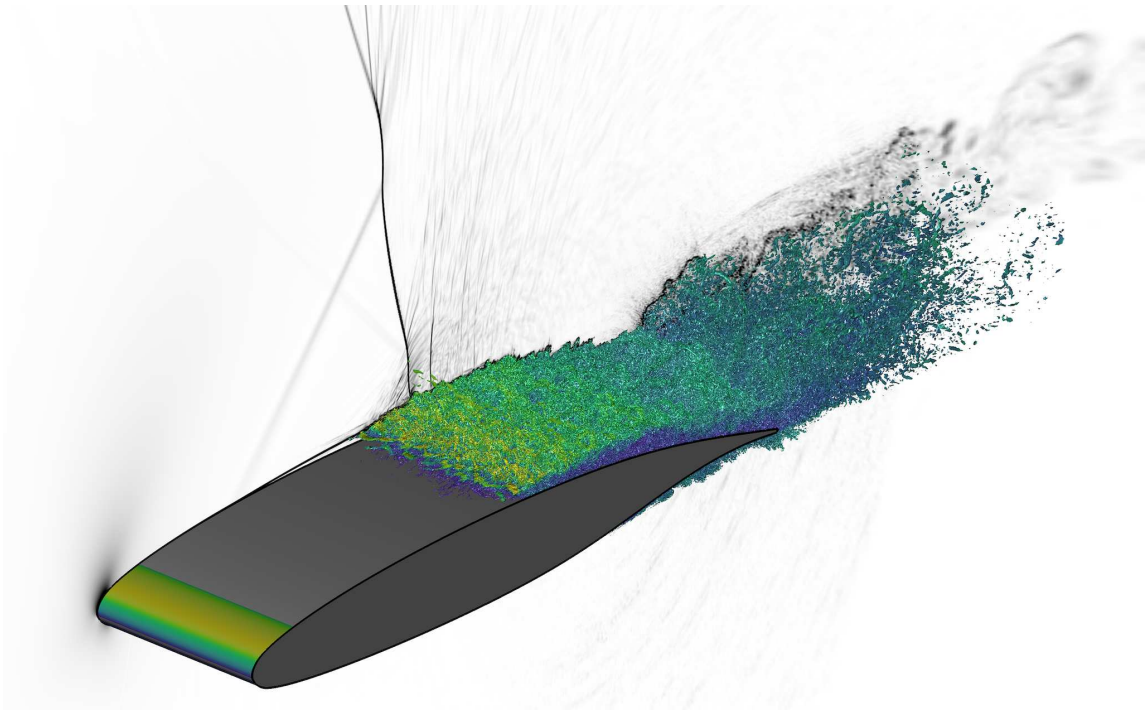

Figure 6.4: Visualization of 3D instantaneous flow fields at approximately 137 CTUs around the gray airfoil geometry, where the cross-sectional view shows numerical Schlieren imaging and the iso-surfaces show the normalized Q-criterion approximately at the value of 2644.4. The iso-surface is colored by the value of the local Mach number.

An instantaneous three-dimensional (3D) flow visualization is shown in Fig. 6.4. The visualization

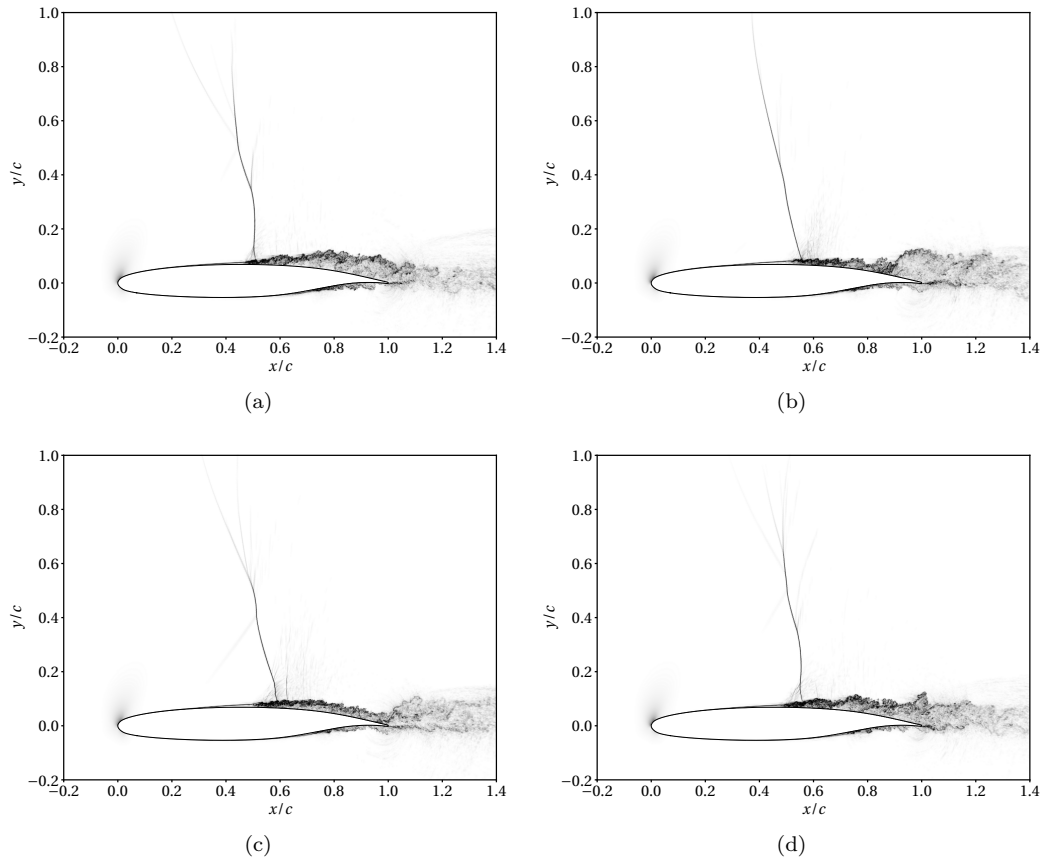

Figure 6.5: Numerical Schlieren imaging of 2D instantaneous flow states: (a) 131.8 CTUs; (b) 134.2 CTUs; (c) 136.6 CTUs; and (d) 139.0 CTUs.

contains cross-sectional numerical Schlieren imaging, indicated by $|\nabla\rho|\,(c/\rho_\infty)$, and iso-surfaces of the normalized Q-criterion at a value of around 2644.4. The concept of Q-criterion is introduced in Hunt et al. (1988) [67]. The definition of the normalized Q-criterion used in this work is

$$Q = \frac{1}{2}\left(\theta^2 + \frac{1}{2}\omega_j\omega_j - S_{ij}S_{ij}\right)\left(\frac{c}{U_\infty}\right)^2.$$

The iso-surfaces are colored by the local Mach number. The visualization indicates that the subsonic freestream flow accelerates to supersonic conditions through an expansion near the leading edge. The flow on the suction side is initially laminar from the leading edge. Then, the boundary layer separates at approximately 30% of the chord length from the leading edge and transitions to turbulence due to the Kelvin-Helmholtz instability. An oblique shock (strong compression wave) / the front-branch of a λ-shock forms in front of the laminar separation points and interacts with the laminar boundary layer. The main shock forms slightly after the boundary layer transitions

to turbulence. A terminating shock behind the main shock is observed in the visualization at this instant in time. This is similar to what is shown in some of the simulation cases of the same airfoil at different Reynolds numbers [180]. The transitional turbulent boundary layer generates strong acoustic waves that propagate into the slightly far-field regions. Turbulent vortex shedding associated with the unsteadiness of the transitional separated boundary layer also occurs. The turbulent structures, visualized by the Q-criterion, suggest sufficient decorrelation in the spanwise periodic and homogeneous computational domain of a quarter of the chord length.

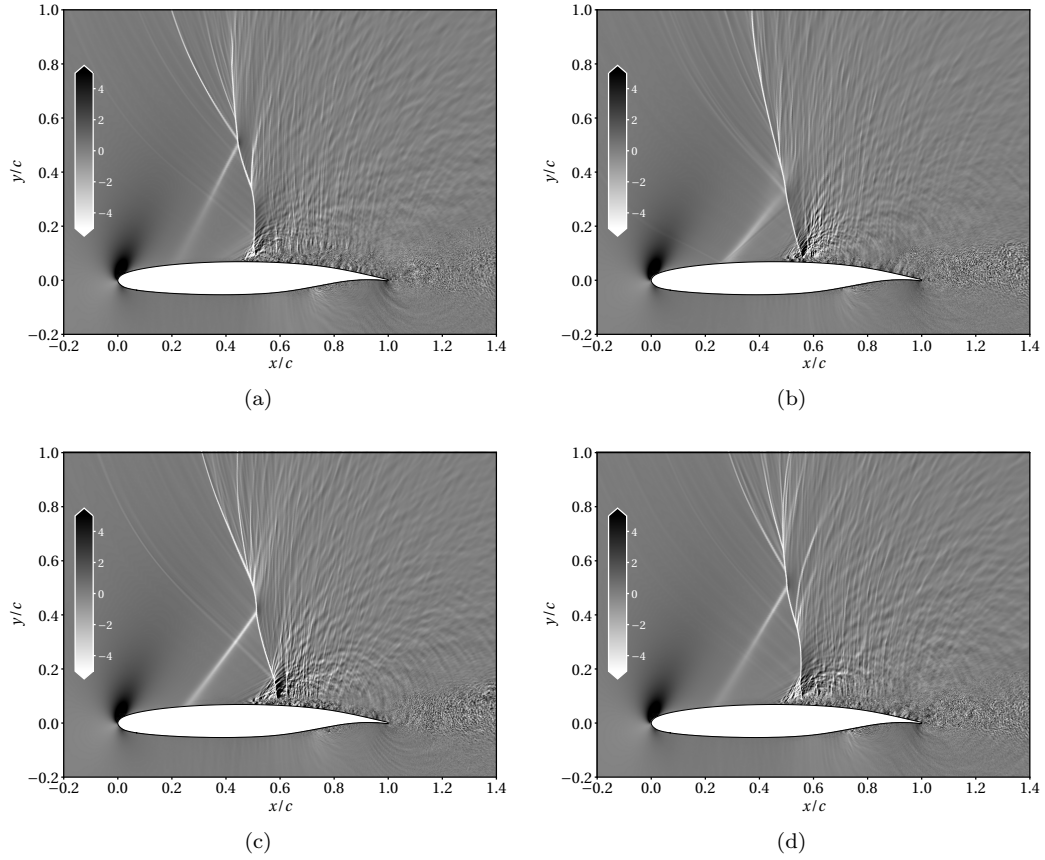

Figure 6.6: Visualizations of velocity dilatation of 2D instantaneous flow states: (a) 131.8 CTUs; (b) 134.2 CTUs; (c) 136.6 CTUs; and (d) 139.0 CTUs.

A set of two-dimensional (2D) visualizations are shown in Fig. 6.5, Fig. 6.6, and Fig. 6.7 at four successive instants in time with an approximately fixed time interval between them. Combined with the 3D visualization, the 2D visualizations show that the up-travelling waves originating from the turbulent boundary layer become steeper along their propagation direction into the slightly far-field regions and form large-scale wave fronts. Some steepened waves merge and form short-lasting shocks. Across the main shock, the flow changes from supersonic to subsonic. Near the back of

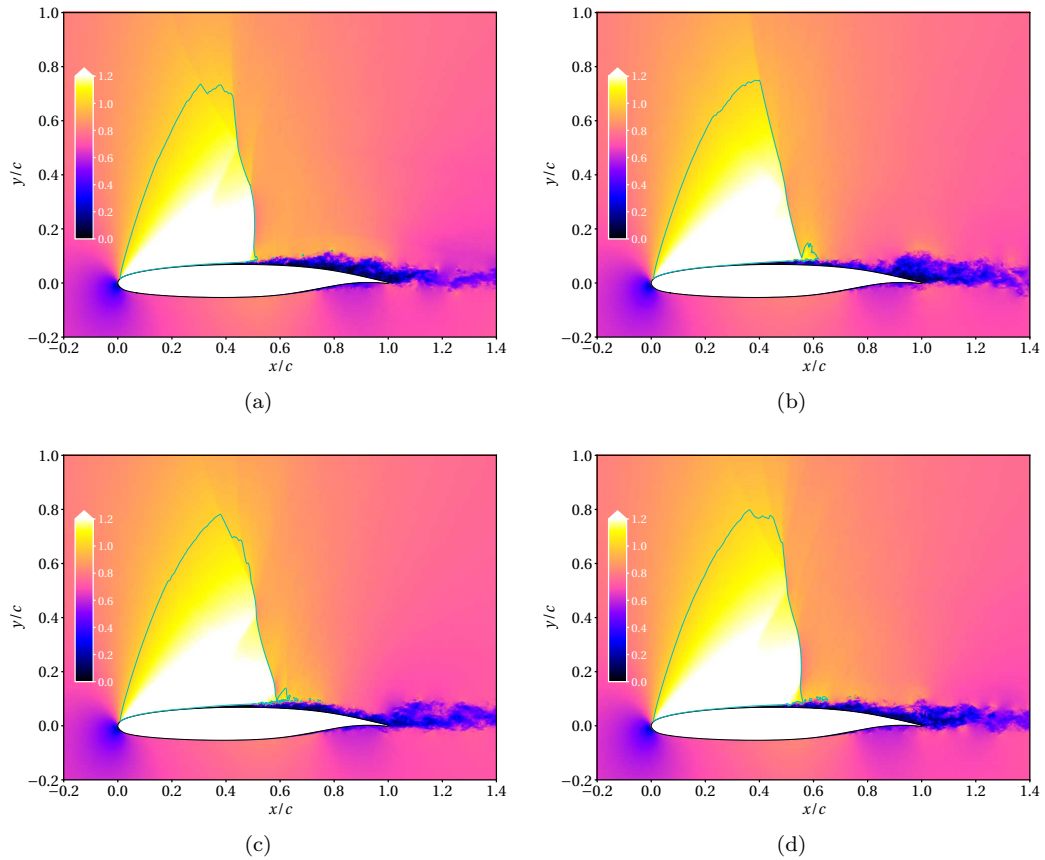

Figure 6.7: Visualizations of Mach number of 2D instantaneous flow states: (a) 131.8 CTUs; (b) 134.2 CTUs; (c) 136.6 CTUs; and (d) 139.0 CTUs.

the main shock foot region, an expansion region periodically forms where the flow re-accelerates to a supersonic state. The re-accelerated flow eventually switches back to subsonic again through a periodically-formed terminating shock that is caused by the steepening of the up-traveling strong acoustic waves in the re-accelerated supersonic flow. Based on observation, the after-shock expansion and terminating shock mostly form behind a retreating shock that moves towards the trailing-edge. While the main shock moves downstream, the expansion wave is strengthened. The terminating shock forms at the end of the expansion region and is pushed farther downstream. When the main shock moves upstream, the expansion wave becomes weaker. The terminating shock also moves forward and eventually merges into the advancing main shock. The upstream-traveling acoustic waves originating from the turbulent wake also steepen while they are propagating upstream and interact with the flow near the main shock region.

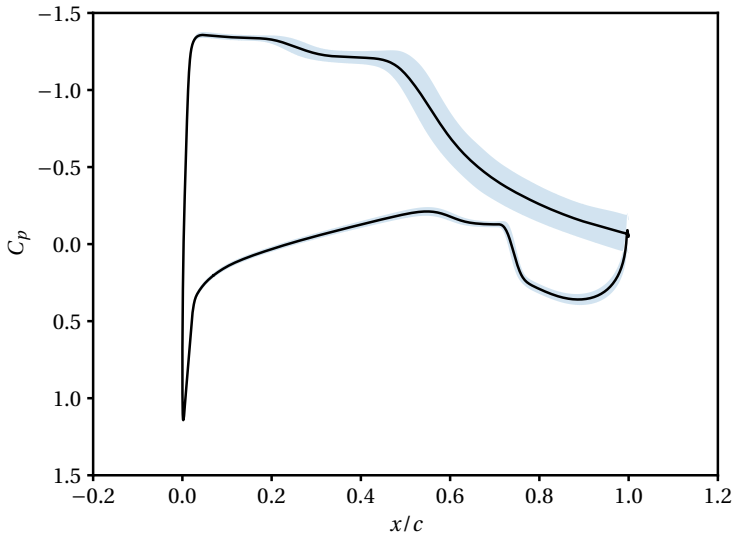

(a)

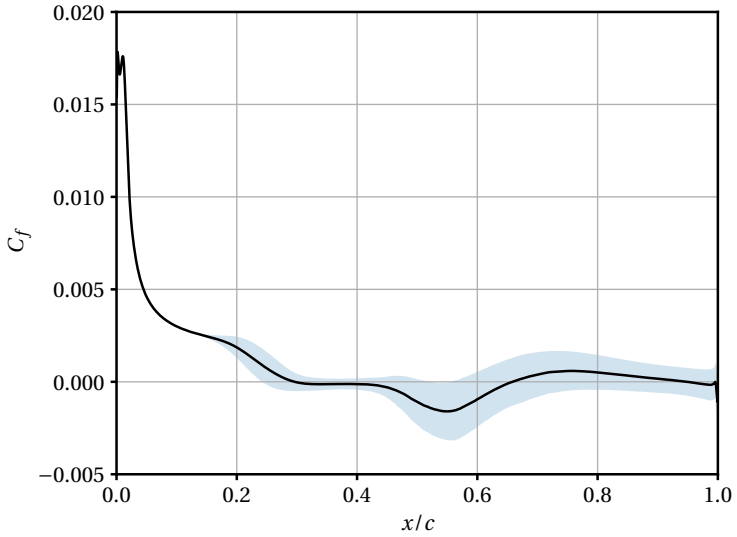

(b)

Figure 6.8: Distributions of mean C_p and C_f , their fluctuations indicated by the symmetric intervals of their temporal standard deviations (marked by the blue shading). The plot of C_f only shows the distribution on the suction side.

6.3.2 Analysis of aerodynamic coefficients and locally probed signals

The pressure coefficient, $C_p = 2(p - p_\infty)/(\rho_\infty U_\infty^2)$, and skin-friction coefficient, $C_f = 2\tau_w/(\rho_\infty U_\infty^2)$, are measured at the airfoil surface, where τ_w is the local wall shear stress. The results are averaged in both the spanwise direction and time. The distribution of C_p and C_f and the magnitudes of

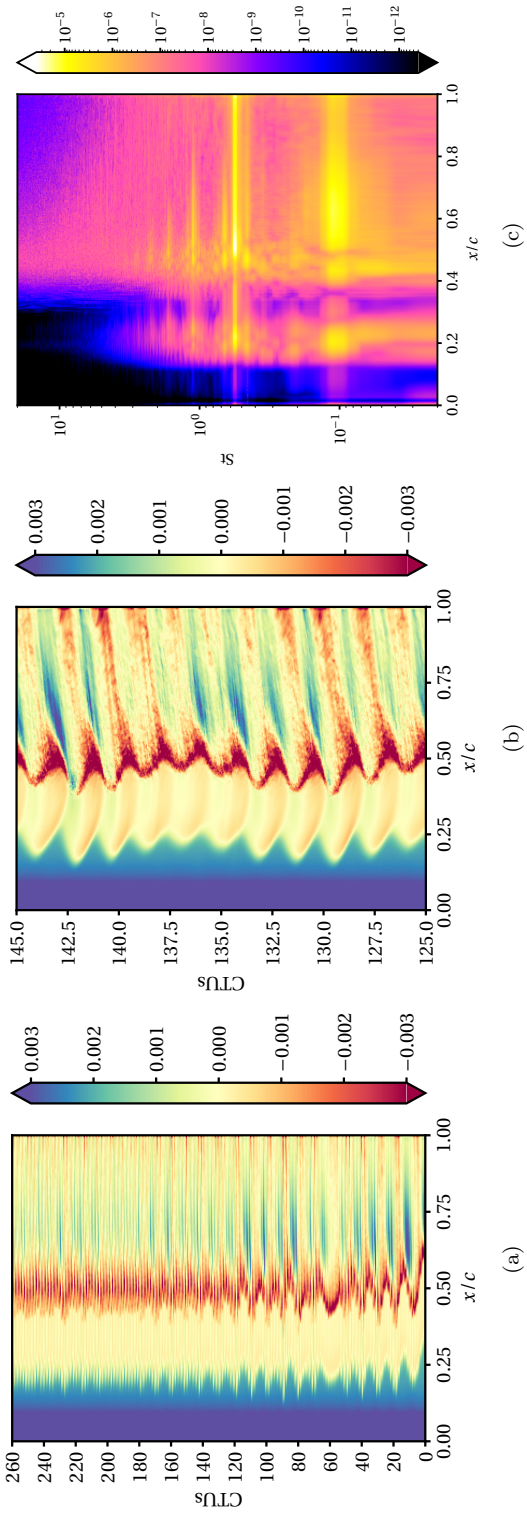

Figure 6.9: Temporal variation of the spanwise averaged C_f on the suction side: (a) x-t diagram over a range of 260 CTUs; (b) zoomed-in x-t diagram over a range of 20 CTUs; (c) spatial distribution of PSD.

their temporal fluctuations, indicated by the symmetric intervals of their standard deviations of the spanwise averaged values, are shown in Fig. 6.8. Combined with the visualizations shown in Sec. 6.3.1, it is seen that in the region where the foot of the oblique shock / compression wave near the laminar separation point ($0.2 < x/c < 0.3$) occurs, large fluctuations in C_p and C_f are observed compared to neighboring regions. The laminar separation point mostly varies in the region of $0.30c$ – $0.42c$. After the flow transitions to turbulence, significant fluctuations in both C_p and C_f are observed due to turbulent vortex shedding.

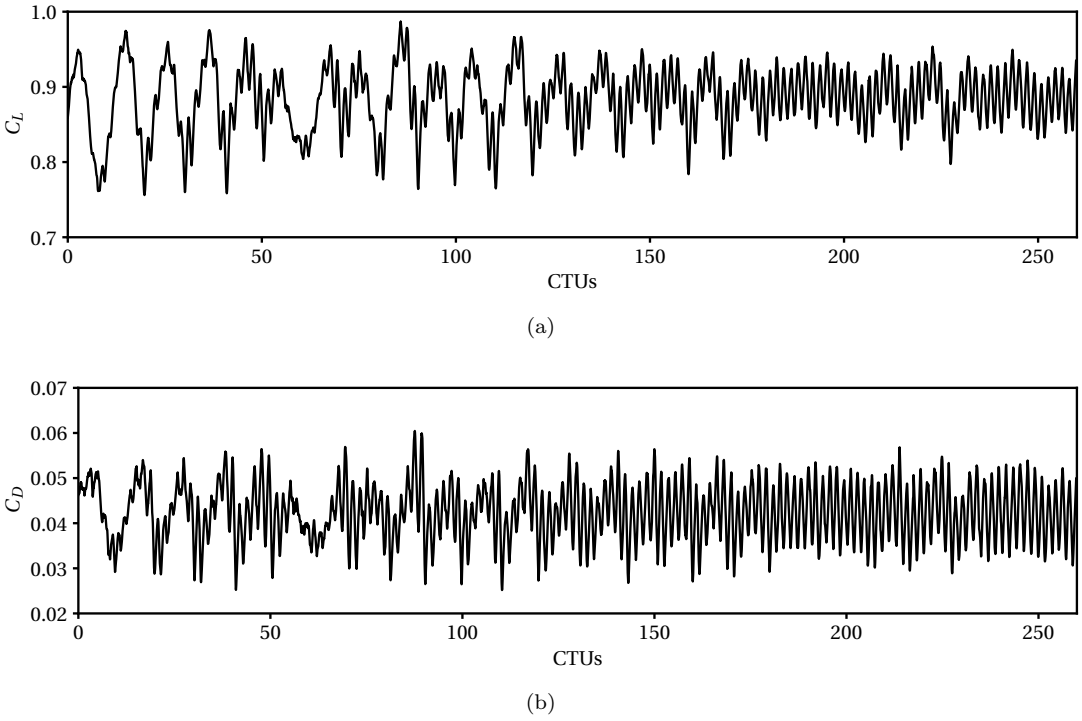

Figure 6.10: Time histories of (a) lift coefficient, C_L, and (b) drag coefficient, C_D.

To further investigate the time history, the x-t diagram of C_f on the suction side and the power spectral density (PSD) are provided in Fig. 6.9. The PSD is generated using the discrete Fourier transform in the time dimension. Welch's method [173] is applied to achieve better convergence of the statistics, and each windowed data segment contains 3072 snapshots and a 75% overlap between each sequential segment. The Hann window is applied to each segment to prevent spectral leakage. In addition, the frequencies in the PSDs are normalized using U_∞/c. Comparing the x-t diagram of C_f shown in Fig. 6.9 with the flow visualizations in Fig. 6.5, the strong negative C_f near $x/c = 0.5$ is caused by the flow separation and transition to turbulence in the separate flow. The oscillations, or periodic growing and detaching, of the separation bubbles are strongly correlated with the vortex shedding. The propagation of shedding vortices is characterized by the interleaved

trajectories of the positive and negative contours of C_f in the x-t diagram in the region where $x/c > 0.6$. The PSD of C_f in Fig. 6.9 indicates that such vortex shedding is at the non-dimensional frequency St ≈ 0.55, where for a given dimensional frequency f, the definition of the non-dimensional frequency, also known as the Strouhal number, is defined as $\mathrm{St} = fc/U_\infty$. Along the x-dimension in the PSD contour, higher fluctuation energy is located at the foot of the oblique shock / compression wave region ($0.2 < x/c < 0.3$) and turbulent flow region ($x/c > 0.6$). In contrast, relatively less fluctuation energy is measured by C_f near the laminar separation point ($x/c \approx 0.3$). Along the frequency dimension, a peak at lower frequency, St ≈ 0.1, is detected beside the shedding frequency at St ≈ 0.55, which is also observed in the x-t diagram in Fig. 6.9a. The corresponding location of the peak at the frequency of St ≈ 0.1 is near $0.5 < x/c < 0.7$ where the main shock, expansion wave, and terminating shock appear.

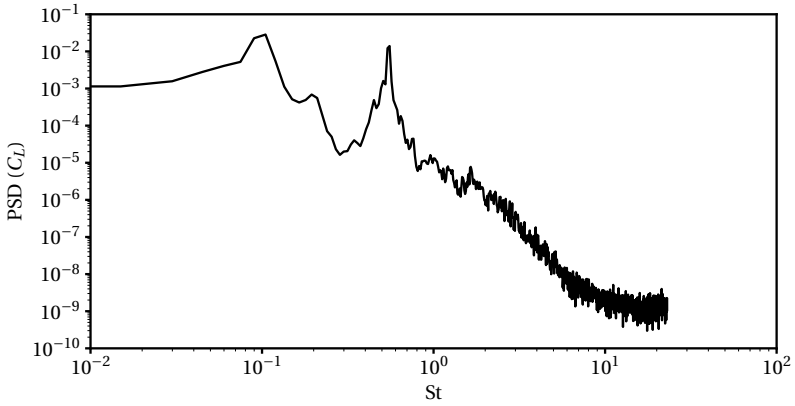

(a)

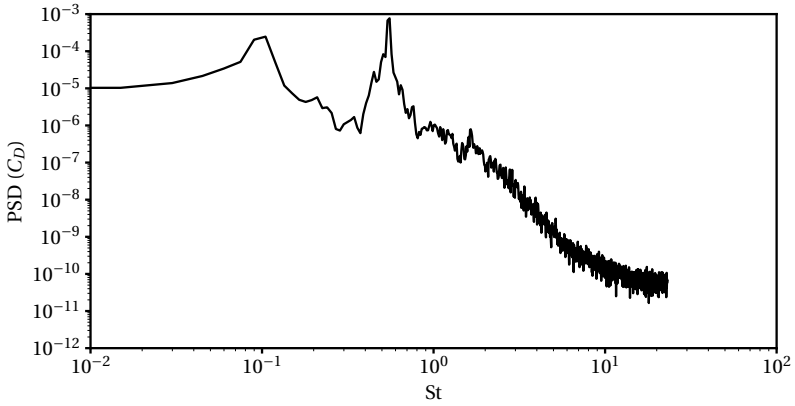

(b)

Figure 6.11: PSD plots of (a) lift coefficient, C_L, and (b) drag coefficient, C_D.

The time series of lift coefficient, C_L, and drag coefficient, C_D, are shown in Fig. 6.10, and their

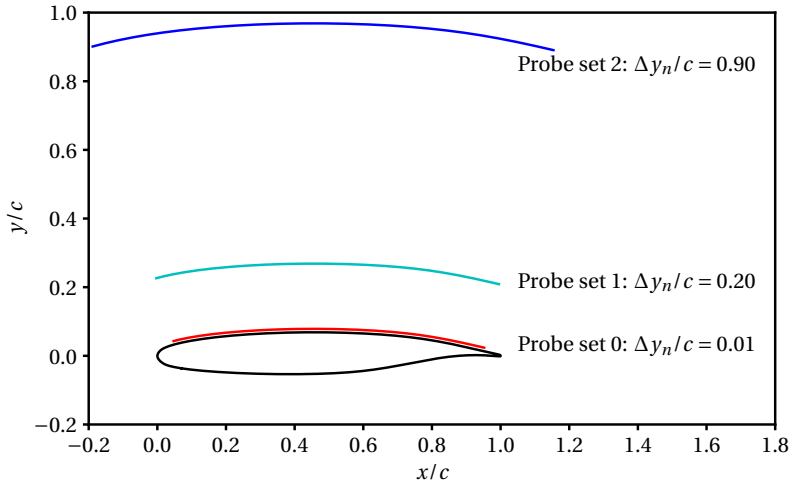

Figure 6.12: Schematic of probing locations relative to the airfoil.

PSDs are shown in Fig. 6.11. The lift and drag coefficients are calculated by integrating the pressure and shear stress over the whole airfoil.

$$C_{L,D} = \frac{1}{A_{\text{airfoil}}} \oint_{\text{airfoil}} \left(C_f \hat{\boldsymbol{t}} - C_p \hat{\boldsymbol{n}}\right) \cdot \hat{\boldsymbol{e}}_{L,D} dA \tag{6.13}$$

where A_{airfoil} is the total area of the airfoil surface, $\hat{\boldsymbol{t}}$ is the unit tangential vector of the airfoil in the x-y plane, $\hat{\boldsymbol{n}}$ is the unit outgoing normal vector of the airfoil geometry, and $\hat{\boldsymbol{e}}_{L,D}$ is the unit reference vector. For the calculation of C_L, $\hat{\boldsymbol{e}}_L = -\hat{\boldsymbol{e}}_x \sin\alpha + \hat{\boldsymbol{e}}_y \cos\alpha$, and for the calculation of C_D, $\hat{\boldsymbol{e}}_D = \hat{\boldsymbol{e}}_x \cos\alpha + \hat{\boldsymbol{e}}_y \sin\alpha$, where $\hat{\boldsymbol{e}}_x$ and $\hat{\boldsymbol{e}}_y$ are the unit vectors in the x and y directions respectively. The oscillations of C_L and C_D, as the integrated aerodynamic coefficients, also contain the two dominant frequencies that are the same as the values measured in the C_f profile on the suction side, where the oscillation at St ≈ 0.55 is identified as caused by the turbulent vortex shedding.

In order to further investigate the Strouhal number at St ≈ 0.1, three line sets of numerical probes are placed at fixed locations to sample the local signals in time. The locations are determined by an normal extrusion of the airfoil surface on the suction side from $x/c = 0.05$ to $x/c = 0.95$. The normal extrusion displacements, Δy_n, are set to $0.01c$, $0.2c$, $0.9c$. At each reference surface in the x-y plane, 512 numerical probes are created. The labeling nomenclature of the numerical probes and their locations are shown in Fig. 6.12. Probe set 0 is used to diagnose the near-wall region, probe set 1 is used to measure the main shock buffet, and probe set 2 is used to sense the flow outside the sonic line.

The pressure and velocity dilatation collected by probe sets 0, 1, and 2 are shown in Fig. 6.13, Fig. 6.14, and Fig. 6.15 respectively as x-t diagrams. Both short-term (range of 20 CTUs) and long-term (range of 260 CTUs) time intervals are plotted. At the location of probe set 0, both

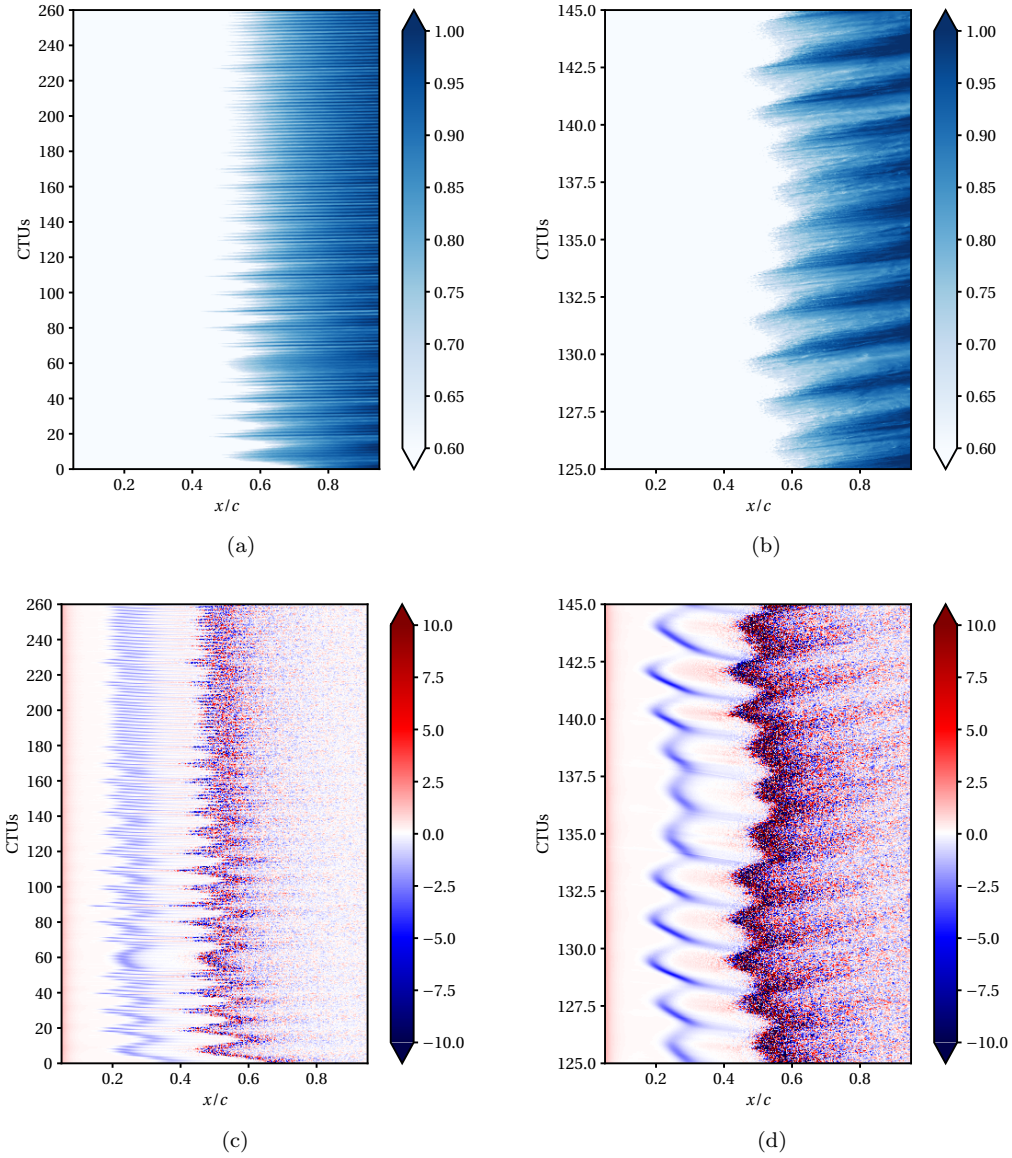

Figure 6.13: x-t diagrams of data collected by probe set 0: (a), (b) pressure (normalized by p_∞); and (c), (d) velocity dilatation (normalized by U_∞/c). (b) and (d) zoom in over a shorter range of time compared to (a) and (c) respectively.

transition and vortex shedding are captured by the pressure and dilatation signals. Moreover, the dilatation x-t diagram also captures the motion of the λ-compression wave / shock in front of the laminar separation point. Its unsteadiness is highly correlated with vortex shedding. Additionally, the lower frequency can be observed in the long-term x-t diagram. It can also be seen that strong fluctuating dilatational motion occurs in the region where the flow transitions to turbulence and

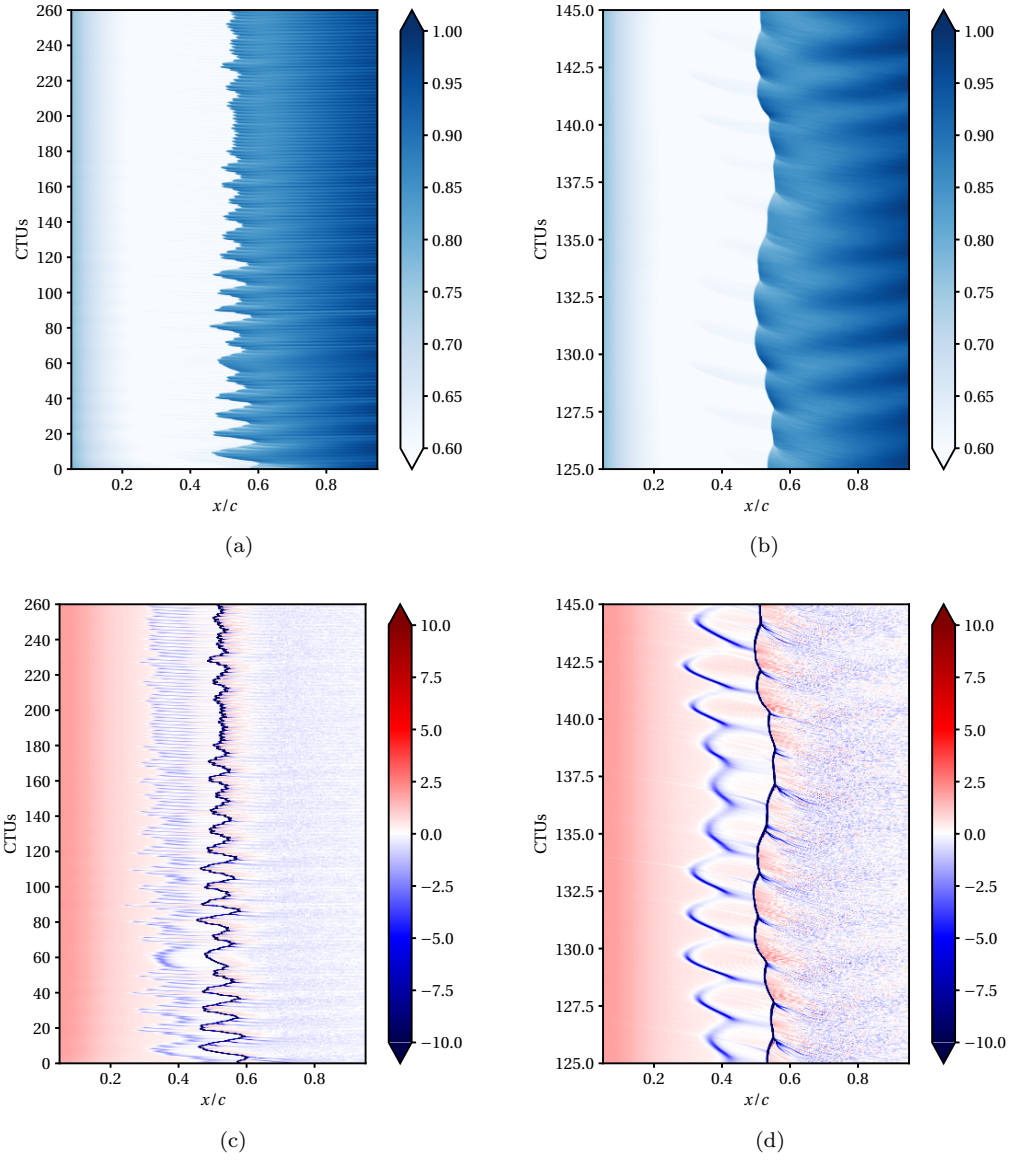

Figure 6.14: x-t diagrams of data collected by the probe set 1: (a), (b) pressure (normalized by p_∞); and (c), (d) velocity dilatation (normalized by U_∞/c). (b) and (d) zoom in over a shorter range of time compared to (a) and (c) respectively.

creates strong acoustic radiation. The location of probe set 2 is set in the freestream region across the main shock location. Both pressure and velocity dilatation signals clearly capture the main shock buffet as shown in Fig. 6.15. It can be seen that the main shock buffet is primarily at a low frequency, but its buffet trajectory is also affected by the vortex shedding frequency. Specifically, from the dilatation x-t diagram in Fig. 6.14, the formation of strong compression waves behind the

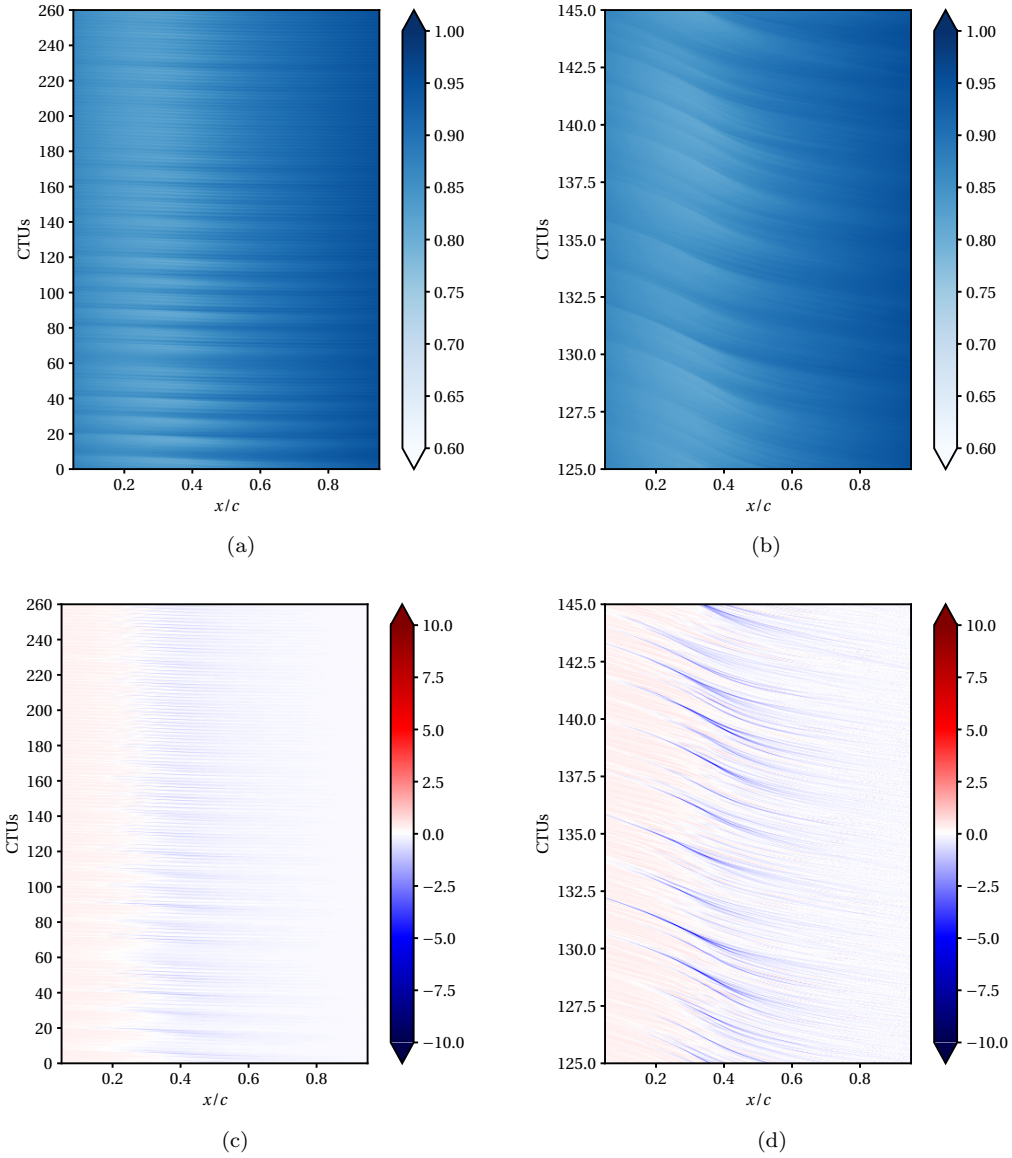

Figure 6.15: x-t diagrams of data collected by the probe set 2: (a), (b) pressure (normalized by p_∞); and (c), (d) velocity dilatation (normalized by U_∞/c). (b) and (d) zoom in over a shorter range of time compared to (a) and (c) respectively.

main shock that partially extend from the terminating shock in the lower region, can be observed, and these waves eventually merge into the main shock. In between, the x-t diagram also captures the periodic expansion waves after the main shock. The signals outside the sonic line collected by probe set 2 shown in Fig. 6.15 are dominated by upstream-traveling waves, and the signal variations contain both higher and lower frequencies as observed from the signals sensed by other sets of probes.

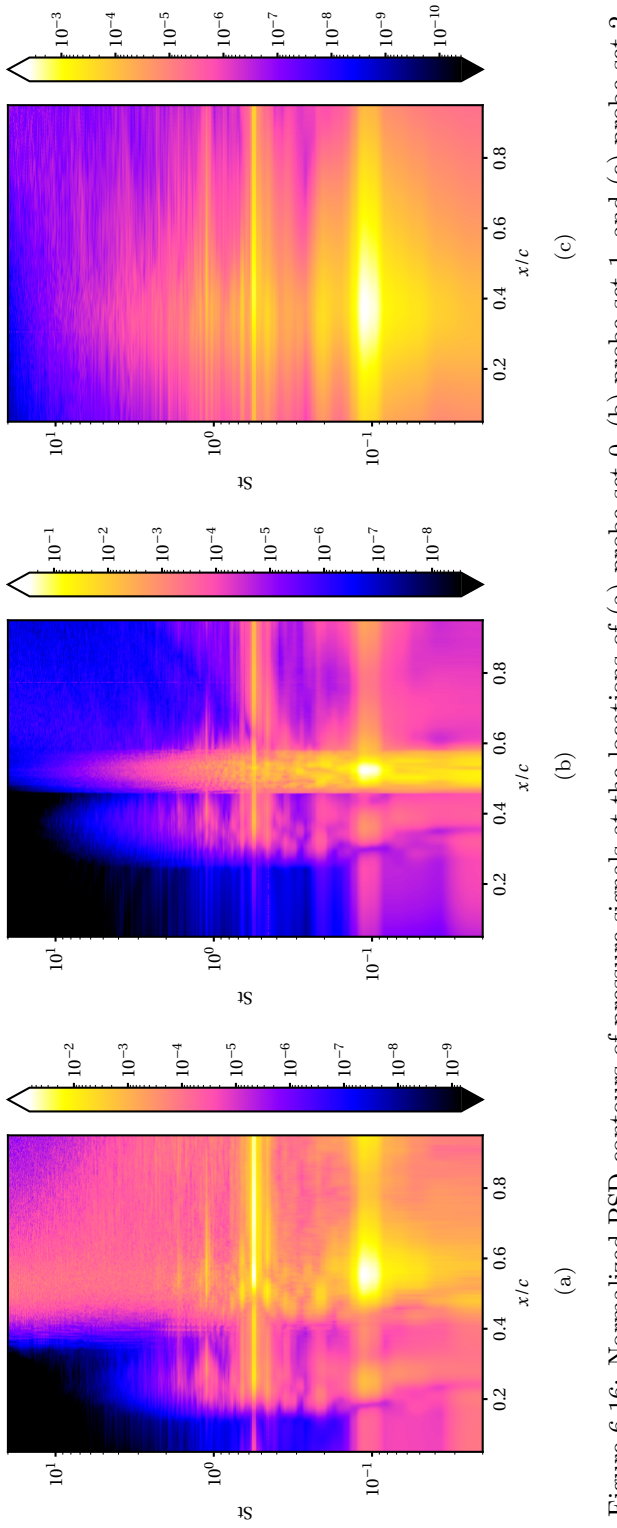

Figure 6.16: Normalized PSD contours of pressure signals at the locations of (a) probe set 0, (b) probe set 1, and (c) probe set 2.

The PSD contours of the pressure signals sampled by all three probe sets are shown in Fig. 6.16. By comparison, it can be seen that the signals at all three locations have the same two dominant frequencies at St ≈ 0.1 and St ≈ 0.55 respectively. Additionally, in Fig. 6.16b, the high spectral energy mostly peaks in the region where $0.5 < x/c < 0.6$ and St ≈ 0.1. This feature confirms that the low-frequency peak at St ≈ 0.1 is the shock buffet Strouhal number. With this, revisiting the PSD of C_f shown in Fig. 6.9, besides the regular turbulent vortex shedding at St ≈ 0.55, the motion of the compression wave / oblique shock, laminar separation points, transition to turbulence, and variation vortex shedding at a longer time range are all correlated with the shock buffet Strouhal number at St ≈ 0.1. It can be also seen that both vortex shedding and shock buffet strongly affect the variations of the integrated aerodynamic coefficients, C_L and C_D.

6.3.3 Low-rank modal analysis

To further investigate the correlation between the shock buffet and other flow structures, a low-rank modal analysis is conducted using SPOD [158, 136]. SPOD is a special form of the proper orthogonal decomposition (POD) method which was introduced as a data-driven approach to the study of fluid mechanics by Lumley (1967) [95]. In this approach, POD modes are extracted by decomposing the two-point spatial correlation matrix arranged in a Fredholm eigenvalue problem [158]. The formulation of the eigenvalue problem defines an inner product with respect to a Hermitian positive-definite matrix serving as the weights. The variance corresponding to the inner product introduces an energy norm. The POD modes are orthogonal corresponding to the inner product and try to generate a set of optimal bases, so that a small subset of the modes can represent the coherence that carries dominant portion of energy in the original data. If most of the energy representing the original data is projected to one or few modes, the data is considered to have low-rank behavior. While POD represents spatial correlations, SPOD analysis can further show space-time correlations using time-resolved data at a stationary state.

An efficient implementation of the SPOD solver for large datasets is described in Towne et al. (2018) [158] and Schmidt et al. (2020) [136]. The discrete eigenvalue problem for SPOD can be denoted as

$$\widehat{\boldsymbol{Q}}\widehat{\boldsymbol{Q}}^H\boldsymbol{W}\widehat{\boldsymbol{\Psi}} = \widehat{\boldsymbol{\Psi}}\boldsymbol{\Lambda} \tag{6.14}$$

where each column in $\widehat{\boldsymbol{Q}}$ contains the discrete Fourier transform in time for one bin of realizations at a specified frequency, $\boldsymbol{W}$ is the weighting matrix which is Hermitian and positive-definite, $\boldsymbol{\Lambda}$ is a diagonal matrix containing the eigenvalues at the given frequency, and the columns of $\widehat{\boldsymbol{\Psi}}$ are the SPOD modes corresponding to the eigenvalues in $\boldsymbol{\Lambda}$. The matrix on the left-hand side of Eq. (6.14), $\widehat{\boldsymbol{Q}}\widehat{\boldsymbol{Q}}^H$, represents a cross-spectral density matrix. An alternative eigenvalue problem can be formulated by left-multiplying Eq. (6.14) by $\widehat{\boldsymbol{Q}}^H\boldsymbol{W}$ and right-multiplying it by $\boldsymbol{\Lambda}^{-1/2}$ on both

sides

$$\widehat{\boldsymbol{Q}}^H \boldsymbol{W} \widehat{\boldsymbol{Q}} \widehat{\boldsymbol{\Theta}} = \widehat{\boldsymbol{\Theta}} \boldsymbol{\Lambda} \tag{6.15}$$

where $\widehat{\boldsymbol{\Theta}}$ is unitary and is defined as

$$\widehat{\boldsymbol{\Theta}} = \widehat{\boldsymbol{Q}}^H \boldsymbol{W} \widehat{\boldsymbol{\Psi}} \boldsymbol{\Lambda}^{-1/2} \tag{6.16}$$

This suggests that $\widehat{\boldsymbol{Q}}^H \boldsymbol{W} \widehat{\boldsymbol{Q}}$ has the same non-zero eigenvalues as $\widehat{\boldsymbol{Q}} \widehat{\boldsymbol{Q}}^H \boldsymbol{W}$. As the number of data points per snapshot becomes much larger than the number of bins, solving the alternative eigenvalue problem shown in Eq. (6.15) can significantly reduce the computational cost. Based on the definition of $\widehat{\boldsymbol{\Theta}}$ and Eq. (6.14), the relation, $\widehat{\boldsymbol{Q}} \widehat{\boldsymbol{\Theta}} = \widehat{\boldsymbol{\Psi}} \boldsymbol{\Lambda}^{1/2}$, can be obtained. Finally, the eigenvectors (SPOD modes), $\widehat{\boldsymbol{\Psi}}$, are calculated as

$$\widehat{\boldsymbol{\Psi}} = \widehat{\boldsymbol{Q}} \widehat{\boldsymbol{\Theta}} \boldsymbol{\Lambda}^{-1/2} \tag{6.17}$$

In this work, an SPOD analysis is conducted with the Chu's disturbance energy norm [23], and two different scalar energy norms, including the pressure, p, and enstrophy, $\rho \omega_j \omega_j / 2$. The expression for the Chu's disturbance energy norm used in this work is

$$E_{\text{Chu}} = \frac{1}{2} \left(\overline{\rho} u_j' u_j' + \overline{a}^2 \overline{\rho}^{-1} \rho'^2 + \overline{\rho} c_v \overline{T}^{-1} T'^2 \right) \tag{6.18}$$

where $\overline{(\cdot)}$ denotes averaging in time and $(\cdot)'$ denotes the fluctuations, calculated as $(\cdot)' = (\cdot) - \overline{(\cdot)}$. For the SPOD analysis using Chu's disturbance energy norm, the time-averaged quantities are absorbed in the weighting matrix. At each data point, the area represented by the local grid point is also contained in $\boldsymbol{W}$. The bin size is set to 3072 with a 75% overlap between each neighboring bin as in the calculations of PSD profiles. The spectra of the largest 10 eigenvalues for each SPOD analysis, λ, are plotted in Fig. 6.17 in the descending order of the energy. The spectra corresponding to the first SPOD mode obtained from all three energy norms resolve five peaks frequencies, $\text{St}_1 \approx 0.105$, $\text{St}_2 \approx 0.195$, $\text{St}_3 \approx 0.554$, $\text{St}_4 \approx 1.093$, and $\text{St}_5 \approx 1.647$, where both the shock buffet frequency and the vortex shedding frequency are included. The five peak frequencies are labeled in Fig. 6.17. At each peak of the first eigenvalue profile, clear low-rank behavior is observed. Among all identified frequencies, St_1 and St_3 are the fundamental frequencies corresponding to shock buffet and vortex shedding. St_2 and St_4 are approximately at the harmonic frequencies corresponding to St_1 and St_3. The value of St_5 suggests a second harmonic mode corresponding to St_3. In the following context, the mode shapes at the two fundamental frequencies of St_1 and St_2 are discussed. The SPOD eigenvalue spectra calculated using the pressure norm and Chu norm still shows high lower-frequency energy below St_1. However, this is limited by the total range of time resolved by the simulation data. In order to further investigate the spectral behavior at lower frequency, much longer simulation is needed to obtain statistically converged spectra.

At the shock buffet frequency, $\text{St}_1 \approx 0.105$, the first SPOD modes of pressure and enstrophy,

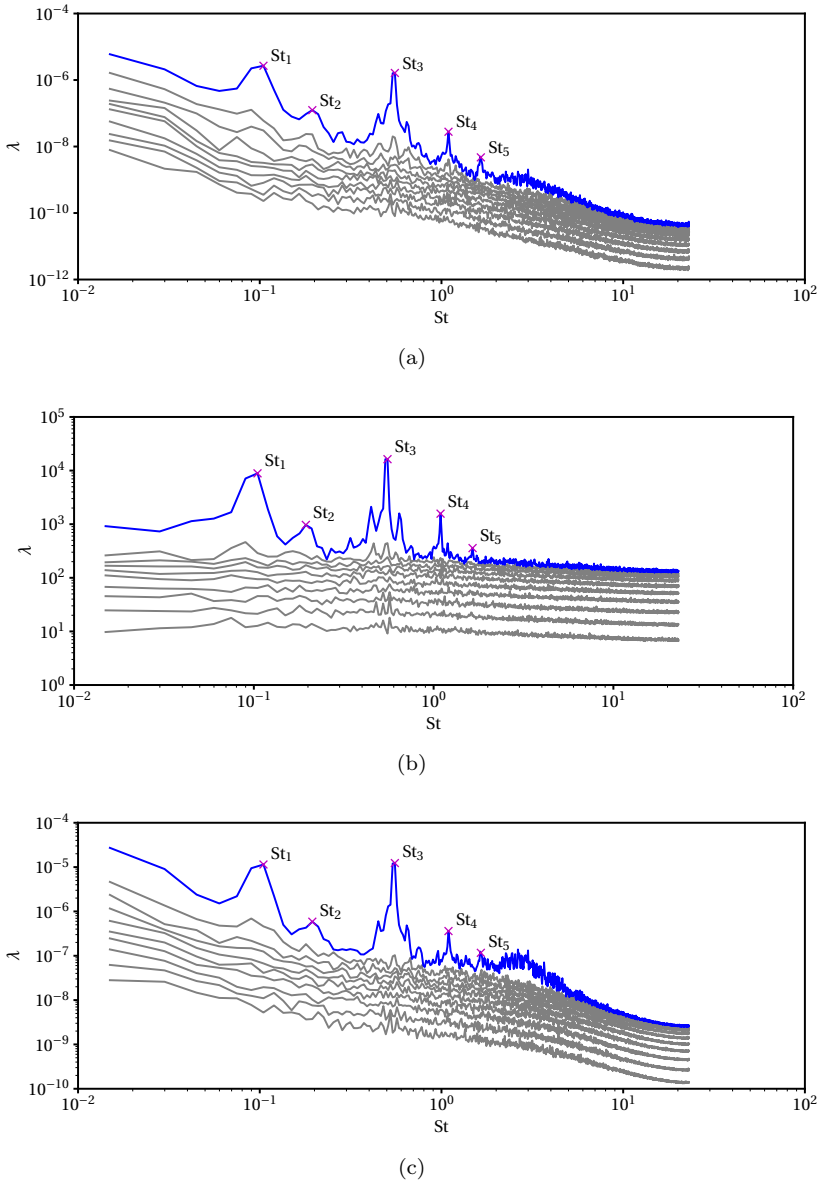

Figure 6.17: Spectra of the largest 10 eigenvalues in the SPOD analysis using (a) pressure norm, p, (b) enstrophy norm, $\rho\omega_j\omega_j/2$, and (c) Chu norm. The marked Strouhal numbers are $\mathrm{St}_1 \approx 0.105$, $\mathrm{St}_2 \approx 0.195$, $\mathrm{St}_3 \approx 0.554$, $\mathrm{St}_4 \approx 1.093$, and $\mathrm{St}_5 \approx 1.647$.

obtained from scalar energy norms, and temperature, obtained from the analysis using Chu's disturbance energy, are shown in Fig. 6.18, Fig. 6.19, and Fig. 6.20 respectively. For each mode, the shapes at different phase angles, φ, are provided to show their evolution. The phase angle is defined as $\varphi = 2\pi\mathrm{St}(tc/U_\infty)$. The evolution of the modal shape is calculated as $\widehat{\Psi}e^{i\varphi}$ for $i = \sqrt{-1}$. The pressure mode directly captures the low-frequency buffet of the main shock although the thin shock

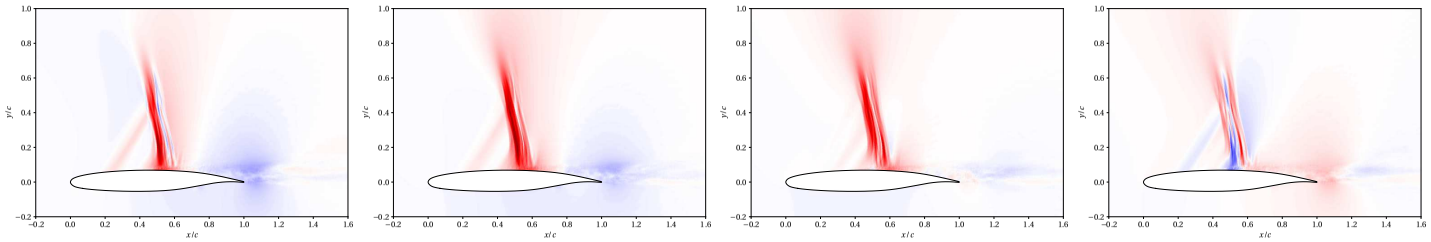

(a) (b) (c) (d)

Figure 6.18: The first SPOD mode of pressure, obtained by the pressure scalar norm, at the shock buffet frequency (St_1): (a) $\varphi = 0$, (b) $\varphi = \pi/4$, (c) $\varphi = \pi/2$, and (d) $\varphi = 3\pi/4$, where $\varphi = 2\pi\mathrm{St}(tc/U_\infty)$ is the phase angle.

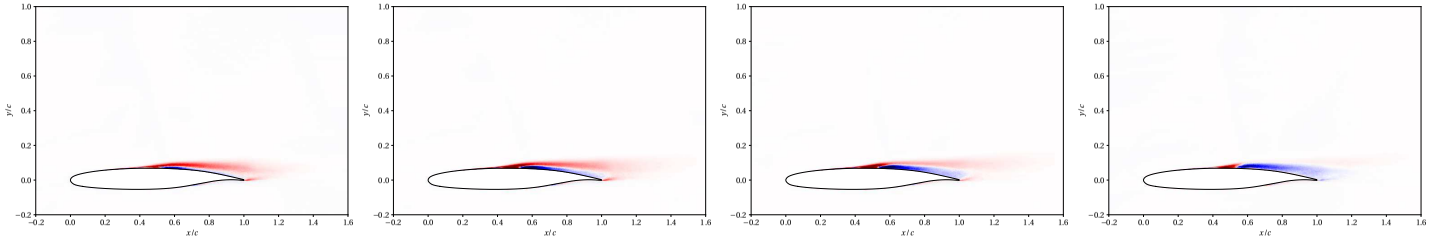

(a) (b) (c) (d)

Figure 6.19: The first SPOD mode of enstrophy, obtained by the enstrophy scalar norm, at the shock buffet frequency (St_1): (a) $\varphi = 0$, (b) $\varphi = \pi/4$, (c) $\varphi = \pi/2$, and (d) $\varphi = 3\pi/4$, where $\varphi = 2\pi\mathrm{St}(tc/U_\infty)$ is the phase angle.

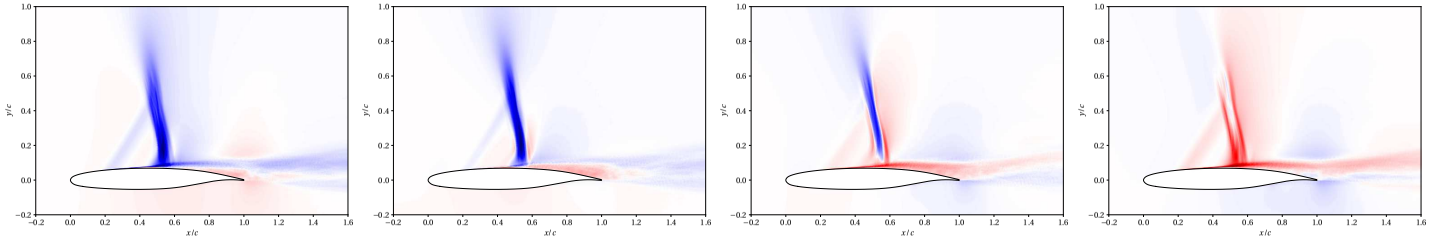

(a) (b) (c) (d)

Figure 6.20: The first SPOD mode of temperature, obtained by the Chu's disturbance energy norm, at the vortex shedding frequency (St_3): (a) $\varphi = 0$, (b) $\varphi = \pi/4$, (c) $\varphi = \pi/2$, and (d) $\varphi = 3\pi/4$, where $\varphi = 2\pi\mathrm{St}(tc/U_\infty)$ is the phase angle.

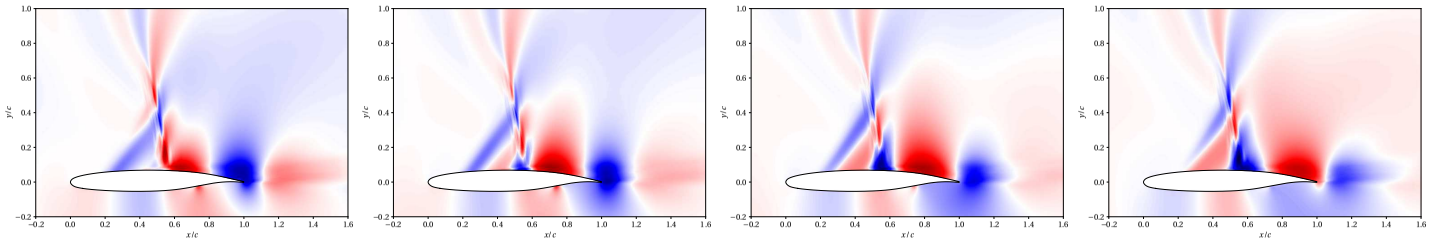

(a) (b) (c) (d)

Figure 6.21: The first SPOD mode of pressure, obtained by the pressure scalar norm, at the vortex shedding frequency (St_3): (a) $\varphi = 0$, (b) $\varphi = \pi/4$, (c) $\varphi = \pi/2$, and (d) $\varphi = 3\pi/4$, where $\varphi = 2\pi St(tc/U_\infty)$ is the phase angle.

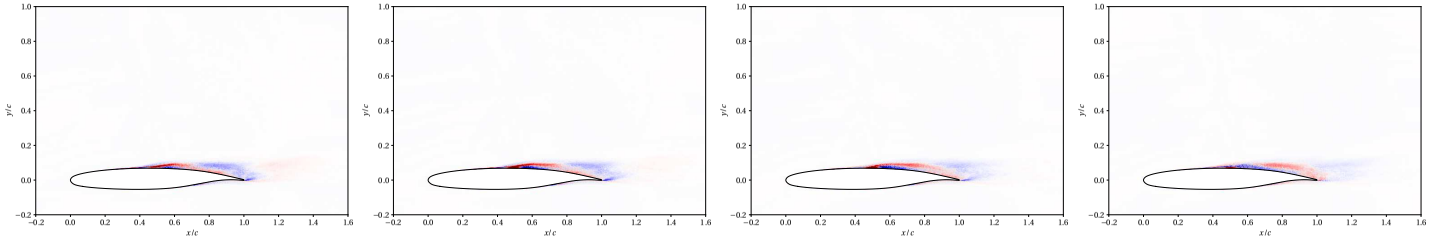

(a) (b) (c) (d)

Figure 6.22: The first SPOD mode of enstrophy, obtained by the enstrophy scalar norm, at the vortex shedding frequency (St_3): (a) $\varphi = 0$, (b) $\varphi = \pi/4$, (c) $\varphi = \pi/2$, and (d) $\varphi = 3\pi/4$, where $\varphi = 2\pi St(tc/U_\infty)$ is the phase angle.

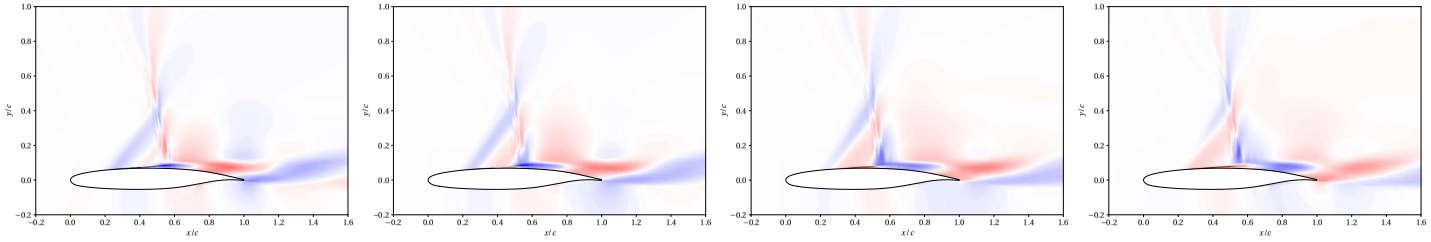

(a) (b) (c) (d)

Figure 6.23: The first SPOD mode of temperature, obtained by the Chu's disturbance energy norm, at the vortex shedding frequency (St_3): (a) $\varphi = 0$, (b) $\varphi = \pi/4$, (c) $\varphi = \pi/2$, and (d) $\varphi = 3\pi/4$, where $\varphi = 2\pi St(tc/U_\infty)$ is the phase angle.

structure is not directly reconstructed. Additionally, the mode evolution also captures the propagation of large-scale acoustic waves. Furthermore, the evolution of the oblique shock / compression wave can be observed. The enstrophy mode primarily captures the near-wall flow behavior. At St_1, the evolution of the enstrophy mode captures the low-frequency boundary layer breathing associated with the movement of the transition point. The evolution of the temperature mode is similar to that of the pressure mode. However, compared to the pressure mode, the temperature mode can clearly capture the laminar boundary layer separation near the leading edge as well as the interaction between the shock and the boundary layer.

At the vortex shedding frequency, $\mathrm{St}_3 \approx 0.554$, the first SPOD modes are shown in Fig. 6.21, Fig. 6.22, and Fig. 6.23, for pressure, enstrophy, and temperature respectively. The enstrophy mode directly captures the periodically detaching vortices associated with the oscillation of the turbulent separation bubble on the suction side near the trailing edge. In contrast, the pressure mode captures the shedding vortices by the non-radiative pseudo-sound propagating with the vortical flow structures. Additionally, the acoustic radiation from the turbulent vortex shedding and shock boundary layer interaction is well-captured. It is observed that the pressure oscillations generated at the shock foot have a wide domain of impact. On the post-shock side, the acoustic waves radiate over a large range of angles. On the pre-shock side, the pressure fluctuations propagate towards the upstream direction below the supersonic region near the wall. The upstream-traveling pressure fluctuations form Mach waves and interact with the main shock and oblique shock / compression wave. In addition, the temperature mode shows the correlation between the laminar separation point and turbulent vortex shedding. The evolution of the mode shape suggests that the fluctuations travel towards the downstream direction.

At both the shock buffet and vortex shedding frequencies, the evolution of the mode shapes shows waves traveling upstream. Globally, these upstream-traveling waves can carry the fluctuations in the post-shock region and bring them back to the pre-shock region, forming feedback paths. On the suction side, the post-shock fluctuations travel back to the upstream region over the shock and above the supersonic region. This phenomenon is also supported by the signal processing of the numerical probes placed above the main shock as shown in Fig. 6.15. Moreover, the upstream-traveling fluctuations also exist on the pressure side of the airfoil. The observations suggest that the upstream-traveling fluctuations originate from the trailing-edge acoustic scattering. The observations of the feedback paths are consistent with the SPOD analysis conducted by Zauner et al. (2023) [180] and resolvent analysis presented in Iwatani et al. (2023) [70].

6.4 Conclusions

A high-resolution wall-resolved LES of transonic flow over the OALT25 laminar supercritical airfoil is performed at $M_\infty = 0.735$, $\mathrm{Re}_c = 1 \times 10^6$, and $\alpha = 4°$. The simulation is conducted using

high-order compact finite difference methods with hybrid central-Riemann fluxes. The use of shock-capturing schemes is controlled by a physics-based shock sensor, and the numerical dissipation from the shock-capturing is not imposed in the turbulence region. Data, including 12288 snapshots over approximately 267 CTUs, are used in the analysis. The instantaneous flow and wave structures are visualized and discussed. The flow conditions are locally sensed on the airfoil surface and at three reference lines created via orthogonal extrusion of the airfoil wall boundary on the suction side during the simulations. A clear shock buffet phenomenon was observed in both flow visualizations and the x-t diagram of velocity dilatation sensed in the freestream above the suction side of the airfoil. Two dominant Strouhal numbers are detected from variations in the integrated aerodynamic coefficients, C_L and C_D. The lower Strouhal number is at $\mathrm{St} \approx 0.1$ and results from shock buffet. The higher Strouhal number is at $\mathrm{St} \approx 0.1$ and is caused by the turbulent vortex shedding. SPOD analysis is conducted using the scalar norms of pressure, density-weighted dilatation, and enstrophy respectively. Both shock buffet and turbulent vortex shedding frequencies are captured by all three energy norms. The SPOD modes at the fundamental frequencies, corresponding to the shock buffet ($\mathrm{St}_1 \approx 0.105$) and turbulent vortex shedding ($\mathrm{St}_3 \approx 0.554$) are visualized. The results imply that the flow fluctuations near the main shock foot associated with periodic movement of the laminar boundary layer separation point, boundary layer transition, etc., play important roles in affecting the shock buffet behavior. Upstream-traveling waves above the supersonic region on the suction side are observed from both SPOD analysis and probe signals, forming a possible feedback mechanism.

Chapter 7

Concluding Remarks

The research work included in this thesis contains three major contributions:

1. A robust and high-resolution simulation framework based on compact numerical schemes for simulations of compressible turbulent flows was developed.

2. A direct parallel linear solver algorithm for solving the cyclic compact banded system arising from the numerical methods used in the simulation framework was developed.

3. Investigations of the fundamental physics of compressible turbulence and transonic aerodynamics were carried out.

The major conclusions of each component are summarized in Sec. 7.1. Discussions of potential future work related to the topics covered in this dissertation are included in Sec. 7.2.

7.1 Conclusions

The basic formulation of the high-resolution simulation framework is presented in Ch. 2. The simulation framework is based on compact finite difference methods. This simulation framework achieves high-resolution simulations of compressible turbulent flows using high-order compact finite difference methods without solution filtering. During the time advancement, the conservative variables are stored at the collocated grid points, and fluxes are assembled at the edge-staggered grid points. The assembly of the nonlinear inviscid fluxes in the compressible Navier-Stokes equations is based on the interpolation of primitive variables, which leads to an effective reduction of aliasing errors. The assembly of viscous fluxes and the calculation of the divergence of fluxes uses staggered derivative schemes. From this treatment, the viscous fluxes gain significantly enhanced spectral resolution in the high-wavenumber regime including at the Nyquist wavenumber. This property is particularly favorable to eddy-resolving simulations of compressible turbulent flows using techniques such

as direct numerical simulations (DNS) and large-eddy simulations (LES). The simulation framework enables robust and high-resolution simulations on both Cartesian and curvilinear meshes. The geometric-law-consistent metric tensor generation specifically for the simulation framework is also presented. The grid convergence test shows that the simulation framework preserves the formal order of convergence of the numerical schemes for simulations on both Cartesian and curvilinear meshes. The simulation framework is compatible with various different shock-capturing methods such as the localized artificial diffusivity (LAD) model and an approximate Riemann solver with nonlinear upwind-biased interpolation. When using the LAD model, solution filtering, as claimed to be previously necessary, can be completely avoided. The application of the approximate Riemann solver with nonlinear shock-capturing interpolation schemes suggests that the use of Riemann fluxes should be highly localized to the shock structures, and in the shock-free region, central fluxes should still be used to maintain simulation resolution by avoiding excessive numerical dissipation. Two physics-based shock sensors are illustrated for central-Riemann flux hybridization, and the demonstrative simulation shows that the shock detection becomes more sensitive while maintaining robustness. An extension of this simulation framework for compressible dense-gas flows is presented in Ch. 3. The simulation uses the Peng-Robinson equation of state to estimate the pressure-volume-temperature relation of CO_2 under transcritical conditions and applies a temperature-pressure-dependent transport model for calculations of viscosity and thermal conductivity. In this work, a proper nondimensionalization of these real-gas models is presented. A DNS of a compressible planar shear layer with unity convective Mach number and a DNS of a zero-pressure-gradient turbulent boundary layer with isothermal-wall-induced heat transfer across the critical temperature are provided as demonstrative simulations. The robustness is achieved for each simulation with large and rapid density changes with respect to small pressure or temperature fluctuations due to the high-speed flow motion or heat transfer.

The simulation framework can be efficiently used for large-scale simulations on modern high-performance computing architectures. The bottleneck computational cost for simulations using compact numerical schemes has been addressed with a direct parallel linear solver algorithm presented in Ch. 4. The algorithm is designed to solve cyclic compact banded systems on heterogeneous computing architectures. The linear solver algorithm uses cyclic reduction and parallel cyclic reduction methods as the elementary elimination patterns and comprehensively considers hierarchical parallelism on shared-memory and distributed-memory. The solution process does not require data-transposes or re-partitioning and has a significantly reduced communication footprint compared to traditional parallel linear solvers. The algorithm also supports flexible grid partitioning and naturally addresses non-zero cyclic entries with arbitrary system size using a method of detaching and reattaching for the block cyclic tridiagonal system formulated across distributed memory partitions during the solution process. The asymptotic scaling of the linear solver algorithm has been justified. The parallel performance has been demonstrated on the *Summit* supercomputer using a

representative fluid mechanics simulation, and the algorithm has achieved scalability of up to 24576 GPUs.

Two studies of compressible turbulent flow physics are presented in Ch. 5 and Ch. 6. The compressibility effects in isotropic turbulence are discussed in Ch. 5. The study uses a set of DNS of solenoidally forced compressible isotropic turbulence with the turbulent Mach number ranging from 0.2 to 0.7. The Reynolds number measured using the longitudinal Taylor microscale is approximately 170 for all cases, and the flow fields demonstrate sufficient large-scale decorrelation across the domain. The size of the computational mesh for all simulations is $1024 \times 1024 \times 1024$, and the analysis of turbulence statistics is based on an ensemble average of statistically stationary data over 10 eddy-turnover times. The Helmholtz decomposition is applied to the velocity field to define solenoidal and dilatational motion. Both energy spectra and normalized probability density functions show that quantities solely related to the solenoidal motion are not sensitive to the turbulent Mach number. However, quantities associated with the dilatational motion strongly depend on the change in turbulent Mach number. The wavenumber scaling of the energy spectra in the inertial subrange and turbulent Mach number scaling of the statistical moments are investigated, and the observations are compared with predictions from an analytical model and other related research work. In addition, a system of budget equations associated with decomposed velocity variances is derived to study the energy exchange between solenoidal and dilatational motions. The statistics of dominant contributing terms are investigated. The numerical study of shock buffet over a laminar supercritical airfoil in transonic flow is illustrated in Ch. 6. The study is based on a wall-resolved LES. The simulation uses hybrid central-Riemann fluxes for shock-capturing and the Vreman subgrid-scale model to account for the effects of under-resolved turbulent flow structures. The airfoil geometry is an OALT25 laminar supercritical airfoil provided by ONERA. In this study, the freestream Mach number is 0.735, and chord-length-based Reynolds number is 1 million. The airfoil is configured at an angle-of-attack of 4 degrees. Simulation data over a range of approximately 267 convective time units (CTUs) are collected after the flow reaches a stationary state. The simulation results show that the boundary layer on the suction side remains laminar near the leading edge, and the boundary layer separates at approximately 30% of the chord length. The flow transitions to turbulence after the laminar separation point due to the growth of the Kelvin-Helmholtz instability. The main shock is located above the turbulent boundary layer near the transition point. Vortex shedding is formed associated with the movement of laminar separation and transition points. The signals of lift and drag coefficients indicate that the flow system has two dominant frequencies at Strouhal numbers of approximately 0.1 and 0.55 respectively. Further data analysis identifies that the two dominant frequencies are associated with shock buffet and turbulent vortex shedding respectively. A modal analysis is conducted using spectral proper orthogonal decomposition (SPOD) to investigate the space-time correlations of the shock buffet system. The SPOD has been conducted using pressure, enstrophy, and Chu's disturbance energy as the energy norms. The spectra of the SPOD eigenvalues

indicate that the flow has low-rank behavior at each dominant frequency. The SPOD modes at the frequencies corresponding to shock buffet and turbulent vortex shedding are computed. Both signal processing sampled by the numerical probes and the evolution of SPOD modes show that the system contains feedback paths.

7.2 Suggested future work

The research outcomes presented in this thesis open many avenues for future exploration in both fundamental studies and engineering applications. First of all, both ideal-gas and real-gas flows have been simulated using the framework outlined in this thesis. This approach can be further extended to simulations of compressible turbulent flows involving multiple components including multi-species and multi-phase flows. Additionally, robustness and accuracy have been achieved in simulations on both Cartesian and curvilinear meshes. To further expand the capability of the simulation framework to address flows with more complex geometries, simulations using multi-block curvilinear meshes or overset structured meshes can be investigated. Furthermore, the simulation framework has shown that it is ready to conduct the state-of-the-art numerical studies of compressible turbulent flows. Beyond demonstrative problems, large-scale high-resolution simulations of various other problems can also be directly configured using the current simulation framework. The simulation framework can also be used as a test bed for studies of numerical schemes such as shock-capturing schemes, positivity preserving methods, shock sensors, compact numerical schemes with further optimization of dispersion relations, and numerical boundary conditions.

Regarding the parallel linear solver algorithm, round-off error propagation can be further investigated from the perspective of numerical linear algebra. To make the solution process more reliable, it is useful to quantify the sensitivity of the round-off error to the condition number, total size of the system, the strategy of grid partitioning, etc. From the perspective of high-performance computing, efficient implementation of the algorithm should be explored. During the solution process, much performance optimization is possible according to the mathematical structure of the linear system as well as the operation patterns. Further performance optimization can be achieved by considering specific computing hardware. Detailed quantification of the computational cost for solving a tridiagonal system and a penta-diagonal system can be conducted.

Associated with the study of compressibility effects in this work, a large amount of DNS data has been generated. These datasets directly enable numerical analysis of compressible isotropic turbulence from many different perspectives. Meanwhile, additional exploration will further advance and strengthen the studies presented in this thesis. As several statistical quantities are provided over a range of turbulent Mach numbers, the change in detailed flow structures can be further investigated. Additionally, the results presented in this thesis are based on DNS of compressible isotropic turbulence with stochastically-evolved low-wavenumber solenoidal forcing. It is valuable to

further provide insight to the research community on how statistical quantities and flow structures change with different forcing methods. The analysis includes solenoidal forcing based on different strategies for flow decomposition, combination of solenoidal and dilatational forcing, effects of the stochastic process, etc.

For the study of transonic shock buffet over a laminar supercritical airfoil, a large amount of time-resolved simulation data are generated which can also directly enable data analysis of various problems using the same flow configuration. In addition, more detailed analysis regarding laminar shock buffet mechanisms needs to be further explored. Along the feedback paths, the SPOD analysis can be used in a quantitative way, and the phase speed can be further measured. Different data-driven approaches, including resolvent analysis and the adjoint method, can be applied along with SPOD analysis to gain a more comprehensive understanding. The linear response of the shock buffet system is another helpful aspect to study. The investigation can be conducted by solving the linearized system representing the perturbation of the LES solution. Furthermore, a simple model can be explored to predict the shock buffet frequencies and amplitude using a significantly reduced amount of simulation data.

Appendix A

Formulation Details in the Simulation Framework

A.1 Calculation of the truncation error of the model linear advection-diffusion system

Considering a one-dimensional linear advection-diffusion process, the modified equation, Eq. (2.20), can be written in the following form.

$$\frac{d\widehat{\phi}}{dt} + \left(ikv' + k^2\nu'\right)\widehat{\phi} = 0 \tag{A.1}$$

where, without loss of generality, k, v' and ν' can be interpreted as the x-component of the wavenumber, modified spectral advective velocity, and modified spectral diffusivity respectively. The complete definitions and explanations of v' and ν' are given in Sec. 2.2. Compared to the exact operations, the truncation error can be quantified in Fourier space.

$$\frac{d\widehat{\phi}}{dt} + \left(ikV + k^2\nu\right)\widehat{\phi} = \widehat{\epsilon}_{\text{adv}} + \widehat{\epsilon}_{\text{dif}} \tag{A.2}$$

where $\widehat{\epsilon}_{\text{adv}}$ and $\widehat{\epsilon}_{\text{dif}}$ denote the spectral truncation error generated from the numerical advection operator and diffusion operator respectively.

$$\widehat{\epsilon}_{\text{adv}} = ikV\left(1 - v'/V\right)\widehat{\phi} \qquad \text{and} \qquad \widehat{\epsilon}_{\text{dif}} = k^2\nu\left(1 - \nu'/\nu\right)\widehat{\phi} \tag{A.3, A.4}$$

For $v'(k\Delta x)$ and $\nu'(k\Delta x)$, when evaluated using a Taylor series about $k\Delta x = 0$, it can be easily shown that $1 - v'(0)/V = 0$ and $1 - \nu'(0)/\nu = 0$ are satisfied for a consistent discretization. Therefore,

the general forms for $\widehat{\epsilon}_{\text{adv}}$ and $\widehat{\epsilon}_{\text{dif}}$ can be denoted as

$$\widehat{\epsilon}_{\text{adv}} = -ikV\widehat{\phi}\sum_{n=1}^{\infty}\left[\frac{1}{n!}\left.\frac{d^n(v'/V)}{d(k\Delta x)^n}\right|_{k\Delta x=0}(k\Delta x)^n\right] \tag{A.5}$$

$$\widehat{\epsilon}_{\text{dif}} = -k^2\nu\widehat{\phi}\sum_{n=1}^{\infty}\left[\frac{1}{n!}\left.\frac{d^n(\nu'/\nu)}{d(k\Delta x)^n}\right|_{k\Delta x=0}(k\Delta x)^n\right] \tag{A.6}$$

which enables calculation of the leading-order truncation error of specific schemes from their spectral behaviors.

For the collocated scheme specified in Eq. (2.1), $v'/V = (k'\Delta x)/(k\Delta x)$ and $\nu'/\nu = (k'\Delta x)^2/(k\Delta x)^2$. The modified wavenumber is given in Eq. (2.13). Considering the constraints on the coefficients given in Eq. (2.2) and Eq. (2.3) for a formally fourth-order derivative approximation, the Taylor-expansion approximations are

$$\widehat{\epsilon}_{\text{adv}} = -V\widehat{\phi}\left\{(ik)^5\frac{3\alpha-1}{30(2\alpha+1)}\Delta x^4 - (ik)^7\frac{18\alpha^2-10\alpha+1}{252(2\alpha+1)^2}\Delta x^6\right\} + \mathcal{O}\left(\Delta x^8\right) \tag{A.7}$$

and

$$\widehat{\epsilon}_{\text{dif}} = \nu\widehat{\phi}\left\{(ik)^6\frac{3\alpha-1}{15(2\alpha+1)}\Delta x^4 - (ik)^8\frac{18\alpha^2-10\alpha+1}{126(2\alpha+1)^2}\Delta x^6\right\} + \mathcal{O}\left(\Delta x^8\right) \tag{A.8}$$

The results indicate that the truncation errors in physical space are

$$\epsilon_{\text{adv}} = -V\left\{\frac{3\alpha-1}{30(2\alpha+1)}\left[\frac{\partial^5\phi}{\partial x^5}\right]\Delta x^4 - \frac{18\alpha^2-10\alpha+1}{252(2\alpha+1)^2}\left[\frac{\partial^7\phi}{\partial x^7}\right]\Delta x^6\right\} + \mathcal{O}\left(\Delta x^8\right) \tag{A.9}$$

and

$$\epsilon_{\text{dif}} = \nu\left\{\frac{3\alpha-1}{15(2\alpha+1)}\left[\frac{\partial^6\phi}{\partial x^6}\right]\Delta x^4 - \frac{18\alpha^2-10\alpha+1}{126(2\alpha+1)^2}\left[\frac{\partial^8\phi}{\partial x^8}\right]\Delta x^6\right\} + \mathcal{O}\left(\Delta x^8\right) \tag{A.10}$$

For staggered derivative and midpoint interpolation schemes specified in Eq. (2.4) and Eq. (2.7) respectively, $v'/V = [T(k\Delta x)]\,(k'\Delta x)\,/(k\Delta x)$ and $\nu'/\nu = (k'\Delta x)^2/(k\Delta x)^2$. The transfer function of the midpoint interpolation scheme, $T(k\Delta x)$, is given in Eq. (2.17), and the modified wavenumber of the staggered derivative scheme is given in Eq. (2.14). For the formally fourth-order discretization, the truncated Taylor series of $\widehat{\epsilon}_{\text{adv}}$ is

$$\begin{aligned}\widehat{\epsilon}_{\text{adv}} = -V\widehat{\phi}\Bigg\{&(ik)^5\frac{212\alpha_D\alpha_I - 14\alpha_D + 66\alpha_I - 27}{960\,(2\alpha_I+1)\,(2\alpha_D+1)}\Delta x^4 - \\ &(ik)^7\frac{1376\alpha_D^2\alpha_I^2 - 52\alpha_D^2\alpha_I + 844\alpha_D\alpha_I^2 + 134\alpha_D^2 - 584\alpha_D\alpha_I + 246\alpha_I^2 + \alpha_D - 111\alpha_I + 9}{4032\,(2\alpha_D+1)^2\,(2\alpha_I+1)^2}\Delta x^6\Bigg\} \\ &+ \mathcal{O}\left(\Delta x^8\right)\end{aligned} \tag{A.11}$$

where the subscripts "D" and "I" are used for the coefficients of staggered derivative and midpoint

interpolation schemes respectively. The truncated Taylor series of $\widehat{\epsilon}_{\text{dif}}$ is

$$\widehat{\epsilon}_{\text{dif}} = \nu\widehat{\phi}\left\{(ik)^6\frac{62\alpha-9}{960\,(2\alpha+1)}\Delta x^4 - (ik)^8\frac{820\alpha^2-244\alpha+9}{16128\,(2\alpha+1)^2}\Delta x^6\right\} + \mathcal{O}\left(\Delta x^8\right) \tag{A.12}$$

The results indicate that the truncation errors in physical space are

$$\epsilon_{\text{adv}} = -V\left\{\frac{212\alpha_D\alpha_I - 14\alpha_D + 66\alpha_I - 27}{960\,(2\alpha_I+1)\,(2\alpha_D+1)}\left[\frac{\partial^5\phi}{\partial x^5}\right]\Delta x^4 - \right.$$
$$\left.\frac{1376\alpha_D^2\alpha_I^2 - 52\alpha_D^2\alpha_I + 844\alpha_D\alpha_I^2 + 134\alpha_D^2 - 584\alpha_D\alpha_I + 246\alpha_I^2 + \alpha_D - 111\alpha_I + 9}{4032\,(2\alpha_D+1)^2\,(2\alpha_I+1)^2}\left[\frac{\partial^7\phi}{\partial x^7}\right]\Delta x^6\right\}$$
$$+\,\mathcal{O}\left(\Delta x^8\right) \tag{A.13}$$

and

$$\epsilon_{\text{dif}} = \nu\left\{\frac{62\alpha-9}{960\,(2\alpha+1)}\left[\frac{\partial^6\phi}{\partial x^6}\right]\Delta x^4 - \frac{820\alpha^2-244\alpha+9}{16128\,(2\alpha+1)^2}\left[\frac{\partial^8\phi}{\partial x^8}\right]\Delta x^6\right\} + \mathcal{O}\left(\Delta x^8\right) \tag{A.14}$$

The same procedure can be applied in combining second-order schemes. The modified wavenumber profiles are $k'\Delta x = \sin(k\Delta x)$ and $k'\Delta x = 2\sin(\frac{1}{2}k\Delta x)$ for the collocated and staggered derivative schemes respectively, and the transfer function for the midpoint interpolation scheme is $T(k\Delta x) = \cos(\frac{1}{2}k\Delta x)$. For fourth-order explicit schemes, α for all schemes is set to 0, and the values of α for sixth-order compact schemes are provided in Tab. 2.1. The leading-order truncation errors of the model equation computed using different combinations of central schemes are shown in Tab. A.1

Order	ϵ_{adv}/V		$\epsilon_{\text{dif}}/\nu$	
	Collocated schemes	Staggered schemes	Collocated schemes	Staggered schemes
2	$-\frac{1}{6}\left[\frac{\partial^3\phi}{\partial x^3}\right]\Delta x^2$	$-\frac{1}{6}\left[\frac{\partial^3\phi}{\partial x^3}\right]\Delta x^2$	$\frac{1}{3}\left[\frac{\partial^4\phi}{\partial x^4}\right]\Delta x^2$	$\frac{1}{12}\left[\frac{\partial^4\phi}{\partial x^4}\right]\Delta x^2$
4	$\frac{1}{30}\left[\frac{\partial^5\phi}{\partial x^5}\right]\Delta x^4$	$\frac{9}{320}\left[\frac{\partial^5\phi}{\partial x^5}\right]\Delta x^4$	$-\frac{1}{15}\left[\frac{\partial^6\phi}{\partial x^6}\right]\Delta x^4$	$-\frac{3}{320}\left[\frac{\partial^6\phi}{\partial x^6}\right]\Delta x^4$
6	$-\frac{1}{2100}\left[\frac{\partial^7\phi}{\partial x^7}\right]\Delta x^6$	$-\frac{59}{89600}\left[\frac{\partial^7\phi}{\partial x^7}\right]\Delta x^6$	$\frac{1}{1050}\left[\frac{\partial^8\phi}{\partial x^8}\right]\Delta x^6$	$\frac{61}{179200}\left[\frac{\partial^8\phi}{\partial x^8}\right]\Delta x^6$

Table A.1: Leading-order truncation errors in calculations of the model one-dimensional linear advection-diffusion equation on a periodic domain.

A.2 Formulations of the subgrid-scale models used in the demonstrative simulations

The large-eddy simulation (LES) system solved in this work is interpreted as the Favre-filtered system with respect to the velocity and temperature fields [46, 52]. No subgrid-scale (SGS) model is applied to mass conservation, Eq. (2.23), and the SGS models in momentum conservation, Eq. (2.24), and energy conservation, Eq. (2.25), are formulated as the turbulent viscosity and conductivity respectively according to the Boussinesq hypothesis [13]. Therefore, the overall dynamic viscosity, μ, and thermal conductivity, κ, used with the Navier-Stokes system are

$$\mu = \check{\mu} + \mu_{\text{SGS}} \qquad \text{and} \qquad \kappa = \check{\kappa} + \kappa_{\text{SGS}} \tag{A.15, A.16}$$

where $\check{\mu}$ and $\check{\kappa}$ are the computable dynamic viscosity and thermal conductivity respectively, and μ_{SGS} and κ_{SGS} are the modeled turbulent viscosity and conductivity respectively.

In this work, μ_{SGS} is calculated using the Vreman SGS model [167]. The calculation method is summarized in the following equations.

$$\mu_{\text{SGS}} = \rho C_{\text{SGS}} \Delta^2 \sqrt{B[\boldsymbol{m}] / \left\|\nabla \boldsymbol{u}\right\|_F^2} \tag{A.17}$$

where Δ is a length scale characterizing the grid spacing. On a uniform Cartesian mesh and curvilinear mesh, Δ are calculated as

$$\Delta = \sqrt[3]{\Delta x \Delta y \Delta z} \qquad \text{and} \qquad \Delta = \sqrt[3]{J}$$

respectively, where Δx, Δy, and Δz are the grid spacings on the uniform Cartesian mesh along the x-, y-, and z-directions respectively, and J is the metric Jacobian assuming the grid spacing of the reference mesh is unity in all directions. For the applications shown in this work, the treatment in the calculation of Δ with respect to the grid anisotropy is ignored. The Frobenius norm of the resolved velocity gradient tensor is computed as

$$\left\|\nabla \boldsymbol{u}\right\|_F^2 = u_{i,j} u_{i,j} \tag{A.18}$$

$\boldsymbol{m}$ is a 3×3 symmetric semi-positive-definite tensor defined as

$$m_{ij} = u_{i,k} u_{j,k} \tag{A.19}$$

Finally, $B[\boldsymbol{m}]$ is a functional defined as

$$B[\boldsymbol{m}] = \frac{1}{2} \delta_{ij} \varepsilon_{ikl} \varepsilon_{jpq} m_{kp} m_{lq} \tag{A.20}$$

where δ_{ij} is the identity tensor, and ε_{ikl} and ε_{jpq} are the Levi-Civita permutation tensors.

κ_{SGS} is calculated based on a constant turbulent Prandtl number, Pr_t

$$\kappa_{\text{SGS}} = c_p \mu_{\text{SGS}} / \text{Pr}_t \tag{A.21}$$

where c_p is the specific heat at a constant pressure.

A.3 Calculation of metrics using compact numerical schemes on a periodic domain

Given a pair of periodic "boundaries," $\partial\mathcal{B}_a$ and $\partial\mathcal{B}_b$, for $\forall \boldsymbol{x}_a \in \partial\mathcal{B}_a$, $\exists \boldsymbol{x}_b \in \partial\mathcal{B}_b$ such that

$$\boldsymbol{x}_b = \boldsymbol{Q}\boldsymbol{x}_a + \boldsymbol{l} \tag{A.22}$$

where $\boldsymbol{Q}$ is an orthogonal tensor denoting rigid rotation, and $\boldsymbol{l}$ represents rigid translation. At the mapped locations in the pair of periodic boundaries, all physical quantities are equivalent. According to the mapping in Eq. (A.22), a scalar quantity field, ϕ, at the pair of periodic boundaries satisfies $\phi(\boldsymbol{x}_b) = \phi(\boldsymbol{x}_a)$, and a vector field, $\boldsymbol{v}$, satisfies $\boldsymbol{v}(\boldsymbol{x}_b) = \boldsymbol{Q}\boldsymbol{v}(\boldsymbol{x}_a)$. $\boldsymbol{Q}$ is an identity tensor for a translationally-periodic boundary.

$$\boldsymbol{x}_b = \boldsymbol{x}_a + \boldsymbol{l} \tag{A.23}$$

As a result, each component in the vector field can be mapped individually, and each component in a tensor field can be smoothed over the entire domain including across the periodic boundary. In this work, only translationally-periodic boundaries are considered with the mapping formulated in Eq. (A.23).

Nevertheless, the physical coordinates may still be discontinuous across the periodic boundary unless $\boldsymbol{l} = \boldsymbol{0}$ as in the demonstrative simulations in Sec. 2.4.5 in the azimuthal direction. Therefore, the compact schemes used for generation of the metric tensor, illustrated in Sec. 2.3.4, require the following modifications along the periodic dimension to avoid discontinuity or inconsistency. The modifications are illustrated using the sixth-order compact differential schemes and interpolation schemes used in this work, and the methods can be easily generalized for different compact schemes.

For staggered differentiation of the coordinate along the periodic dimension, according to

Eq. (2.4), the linear system can be formulated as

$$\begin{bmatrix} 1 & \alpha & 0 & \cdots & 0 & 0 & \alpha \\ \alpha & 1 & \alpha & \cdots & 0 & 0 & 0 \\ 0 & \alpha & 1 & \cdots & 0 & 0 & 0 \\ \vdots & \vdots & \vdots & \ddots & \vdots & \vdots & \vdots \\ 0 & 0 & 0 & \cdots & 1 & \alpha & 0 \\ 0 & 0 & 0 & \cdots & \alpha & 1 & \alpha \\ \alpha & 0 & 0 & \cdots & 0 & \alpha & 1 \end{bmatrix} \begin{bmatrix} (\partial x)_0 \\ (\partial x)_1 \\ (\partial x)_2 \\ \vdots \\ (\partial x)_{N-3} \\ (\partial x)_{N-2} \\ (\partial x)_{N-1} \end{bmatrix} = a \begin{bmatrix} x_{1/2} - x_{-1/2} \\ x_{3/2} - x_{1/2} \\ x_{5/2} - x_{3/4} \\ \vdots \\ x_{N-5/2} - x_{N-7/2} \\ x_{N-3/2} - x_{N-5/2} \\ x_{N-1/2} - x_{N-3/2} \end{bmatrix} + \frac{b}{3} \begin{bmatrix} x_{3/2} - x_{-3/2} \\ x_{5/2} - x_{-1/2} \\ x_{7/2} - x_{1/2} \\ \vdots \\ x_{N-3/2} - x_{N-9/2} \\ x_{N-1/2} - x_{N-7/2} \\ x_{N+1/2} - x_{N-5/2} \end{bmatrix} \tag{A.24}$$

where x represents an arbitrary component of the coordinate system and ∂x denotes a metric component corresponding to x. The mesh spacing in the reference domain is set to be unity. Assuming that there are N grid points along the periodic dimension, the coordinate, with its subscript from 0 to $N-1$, is represented by the computational mesh. Based on a rigid translation, the out-of-bounds coordinates in Eq. (A.24) are calculated as

$$x_{-j} = x_{N-j} - l \qquad \text{and} \qquad x_{N+j} = x_j + l \qquad \text{for} \qquad 0 \leq j < N \tag{A.25, A.26}$$

where l is the translational period in such a dimension.

For periodic coordinate interpolation, according to Eq. (2.7), at the first and last grid points, the equations are

$$\alpha x_{-1/2} + x_{1/2} + \alpha x_{1/2} = \frac{a}{2}(x_0 + x_1) + \frac{b}{2}(x_{-1} + x_2) \tag{A.27}$$

$$\alpha x_{N-3/2} + x_{N-1/2} + \alpha x_{N+1/2} = \frac{a}{2}(x_{N-1} + x_N) + \frac{b}{2}(x_{N-2} + x_{N+1}) \tag{A.28}$$

where the out-of-bounds coordinates on the right-hand side of the equations can still be calculated using the relations given in Eq. (A.25) and Eq. (A.26). However, the out-of-bounds coordinates on the left-hand side of the equations are extra unknowns that are not directly solvable from the linear system. To address this, Eq. (A.25) and Eq. (A.26) are imposed to modify Eq. (A.27) and Eq. (A.28) so that $x_{-1/2}$ and $x_{N+1/2}$ will be substituted with $x_{N-1/2}$ and $x_{1/2}$ respectively. As a

result, the solvable linear system is formulated as

$$\begin{bmatrix} 1 & \alpha & 0 & \cdots & 0 & 0 & \alpha \\ \alpha & 1 & \alpha & \cdots & 0 & 0 & 0 \\ 0 & \alpha & 1 & \cdots & 0 & 0 & 0 \\ \vdots & \vdots & \vdots & \ddots & \vdots & \vdots & \vdots \\ 0 & 0 & 0 & \cdots & 1 & \alpha & 0 \\ 0 & 0 & 0 & \cdots & \alpha & 1 & \alpha \\ \alpha & 0 & 0 & \cdots & 0 & \alpha & 1 \end{bmatrix} \begin{bmatrix} x_{1/2} \\ x_{3/2} \\ x_{5/2} \\ \vdots \\ x_{N-5/2} \\ x_{N-3/2} \\ x_{N-1/2} \end{bmatrix} = \frac{a}{2} \begin{bmatrix} x_0 + x_1 \\ x_1 + x_2 \\ x_2 + x_3 \\ \vdots \\ x_{N-3} + x_{N-2} \\ x_{N-2} + x_{N-1} \\ x_{N-1} + x_N \end{bmatrix} + \frac{b}{2} \begin{bmatrix} x_{-1} + x_2 \\ x_0 + x_3 \\ x_1 + x_4 \\ \vdots \\ x_{N-4} + x_{N-1} \\ x_{N-3} + x_N \\ x_{N-2} + x_{N+1} \end{bmatrix} + \alpha \begin{bmatrix} l \\ 0 \\ 0 \\ \vdots \\ 0 \\ 0 \\ -l \end{bmatrix} \tag{A.29}$$

where the last term on the right-hand side is caused by modifying the out-of-bounds coordinates on the left-hand side.

A.4 Boundary and near-boundary schemes

Along a non-periodic dimension, one-sided schemes are applied. The detailed derivations of one-sided schemes for collocated differentiation, staggered differentiation, and midpoint interpolation are discussed in Ref. [89] and Ref. [107] respectively. In this work, the physical boundary is placed at the first (or last) edge-staggered point, which is a half-grid spacing from the first (or last) nodal point on the interior side. The boundary scheme associated with the collocated sixth-order compact finite difference method shown in Eq. (2.1) is

$$f_0' + 3f_1' = \frac{1}{\Delta\xi}\left(-\frac{17}{6}f_0 + \frac{3}{2}f_1 + \frac{3}{2}f_2 - \frac{1}{6}f_3\right) \tag{A.30}$$

This discretization makes the boundary scheme formally fourth-order accurate. At the first near-boundary point, the most compact fourth-order central discretization is used.

$$\frac{1}{4}f_0' + f_1' + \frac{1}{4}f_2' = \frac{3}{4}\left(f_2 - f_0\right)/\Delta\xi \tag{A.31}$$

At the second near-boundary point, a fourth-order central scheme with a wider stencil is used.

$$\frac{163}{508}f_1' + f_2' + \frac{163}{508}f_3' = \frac{393}{508}\left(f_3 - f_1\right)/\Delta\xi + \frac{3}{127}\left(f_4 - f_0\right)/\Delta\xi \tag{A.32}$$

Starting from the third near-boundary point, the interior scheme is applied. The schematic of boundary and near-boundary stencils associated with the collocated sixth-order compact finite difference method scheme is shown in Fig. A.1.

The boundary scheme of the node-to-edge interpolation associated with the compact interpolation

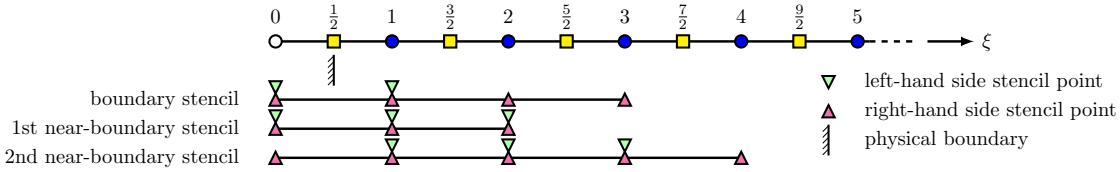

Figure A.1: Schematic of the collocated differentiation near a boundary.

scheme shown in Eq. (2.7) is

$$f^I_{1/2} = \frac{5}{16}f_0 + \frac{15}{16}f_1 - \frac{5}{16}f_2 - \frac{1}{16}f_3 \tag{A.33}$$

This form yields a fourth-order explicit interpolation, and the boundary scheme is one-way coupled with the linear system to determine the interpolated values at near-boundary and interior edge-staggered points. At the first near-boundary point, the scheme is set to be a fourth order scheme.

$$\frac{1}{4}f^I_{1/2} + f^I_{3/2} + \frac{1}{4}f^I_{5/2} = \frac{23}{32}\left(f_2 + f_1\right) + \frac{1}{32}\left(f_3 + f_0\right) \tag{A.34}$$

Starting from the second near-boundary point, the interior scheme is applied. The boundary and near-boundary stencils associated with the interpolation schemes are shown in Fig. A.2.

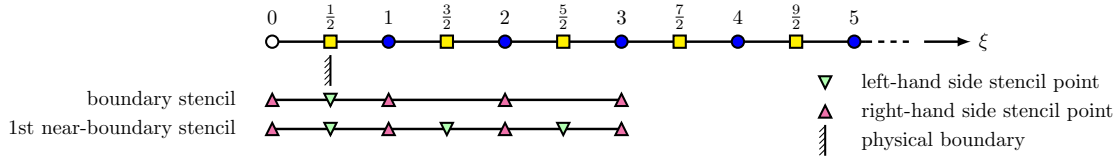

Figure A.2: Schematic of the one-dimensional node-to-edge interpolation near a boundary.

The edge-to-node differentiation that is used for the divergence operator includes a ghost point beyond the physical boundary. The scheme at the ghost point is in an explicit sided form.

$$f'_0 = \frac{1}{\Delta\xi}\left(-\frac{71}{24}f_{1/2} + \frac{47}{8}f_{3/2} - \frac{31}{8}f_{5/2} + \frac{23}{24}f_{7/2}\right) \tag{A.35}$$

The discretization is formally third-order accurate with dissipative leading order truncation error. Similar to the interpolation scheme, by setting the off-diagonal coefficient to zero, the boundary scheme is one-way coupled with the near boundary and interior schemes. The actual boundary scheme uses the most compact fourth-order central difference method as follows:

$$\frac{1}{22}f'_0 + f'_1 + \frac{1}{22}f'_2 = \frac{12}{11}\left(f_{3/2} - f_{1/2}\right)/\Delta\xi \tag{A.36}$$

The combination of Eq. (A.35) and Eq. (A.36) results in a compact one-sided scheme at the boundary

stencil. The scheme at the first near-boundary stencil is

$$\frac{9089}{69564}f_1' + f_2' + \frac{9089}{69564}f_3' = \frac{95257}{92752}\left(f_{5/2} - f_{3/2}\right)/\Delta\xi + \frac{5927}{75888}\left(f_{7/2} - f_{1/2}\right)/\Delta\xi \tag{A.37}$$

Starting from the second near-boundary stencil, the interior scheme is used. The boundary and near-boundary stencils associated with the staggered central differencing schemes are shown in Fig. A.3.

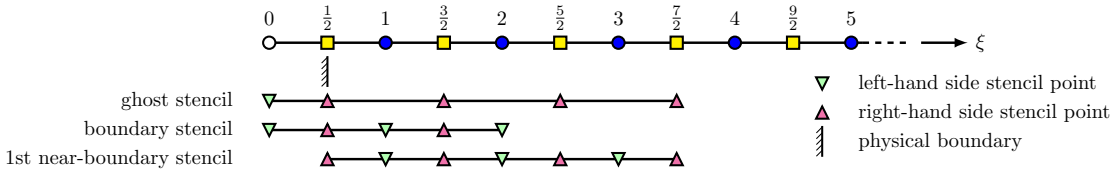

Figure A.3: Schematic of the one-dimensional edge-to-node differentiation near a boundary.

With the physical boundary placed at the edge-staggered points, the boundary conditions are weakly imposed on the Navier-Stokes system via fluxes. This treatment provides extra robustness and the flexibility to impose different types of boundary conditions. In this work, the boundary conditions for the simulations in Sec. 2.4.5 are imposed by setting the variables at the ghost nodal points prior to calculating the variables at the edge-staggered points (cf. Sec. 2.3.2 and Sec. 2.3.3).

A.5 Shock-capturing methods

The methods for shock capturing used in this work are documented in this section. The localized artificial diffusivity (LAD) model is described in A.5.1. The nonlinear interpolation schemes and the approximate Riemann solver are illustrated in A.5.2 and A.5.3 respectively. The LAD model and the nonlinear interpolation scheme combined with an approximate Riemann solver are two independent methods for shock capturing. In this work, these two approaches are not mixed in the same simulation. This work proposes that the latter method be hybridized with central schemes in simulation of compressible turbulent flows. The details are illustrated in Sec. 2.3.5 and Sec. 2.4.5.

A.5.1 Localized artificial diffusivity models

The LAD model used in this work is primarily based on the formulation given in Ref. [75] and Ref. [76]. For shock capturing, only artificial bulk viscosity and thermal conductivity models are used. The artificial diffusivities are added to the overall bulk viscosity, β, and thermal conductivity, κ, in the Navier-Stokes equations described in Sec. 2.3.1.

$$\beta = \check{\beta} + \beta^* \qquad \text{and} \qquad \kappa = \check{\kappa} + \kappa^* \tag{A.38, A.39}$$

where $\check{\beta}$ and $\check{\kappa}$ are calculated using the physical bulk viscosity and thermal conductivity models respectively, and β^* and κ^* are the artificial bulk viscosity and thermal conductivity respectively. On Cartesian meshes, the artificial diffusivities are formulated as

$$\beta^* = C_\beta \mathcal{G}\left\{\rho \mathcal{H}\left(\frac{-\theta\,|\theta|}{\theta^2+\omega_i\omega_i+\varepsilon^2}\right)\left|\mathcal{D}_{mpql}\frac{\partial^4\theta}{\partial x_m\partial x_p\partial x_q\partial x_l}\right|\left(\Delta x_j\frac{\partial\rho}{\partial x_j}\right)^2\left(\frac{\partial\rho}{\partial x_k}\frac{\partial\rho}{\partial x_k}+\varepsilon^2\right)^{-1}\right\} \tag{A.40}$$

$$\kappa^* = C_\kappa \mathcal{G}\left\{\frac{\rho c}{T}\left|\mathcal{D}_{mpql}\frac{\partial^4 e_{\text{th}}}{\partial x_m\partial x_p\partial x_q\partial x_l}\right|\sqrt{\left(\Delta x_j\frac{\partial e_{\text{th}}}{\partial x_j}\right)^2\left(\frac{\partial e_{\text{th}}}{\partial x_k}\frac{\partial e_{\text{th}}}{\partial x_k}+\varepsilon^2\right)^{-1}}\right\} \tag{A.41}$$

where C_β and C_κ are the model constants for β^* and κ^* respectively, $\mathcal{G}(\cdot)$ denotes the truncated Gaussian filter [30], $\mathcal{H}(\cdot)$ denotes the Heaviside step function, ρ is density, c is the speed of sound, T is temperature, e_{th} is internal energy, $\theta = u_{k,k}$ is the velocity dilatation, ω_i is the vorticity vector, $\varepsilon = 1\times10^{-16}$ serves as numerical regulation, and Δx_j is the grid spacing in the j-th dimension. $\mathcal{D}_{mpql}$ is a fourth-order tensor operator. The early version proposed in Ref. [29] uses $\mathcal{D}_{mpql} = (\Delta x\Delta y\Delta z)^{4/3}\,\delta_{mp}\delta_{ql}$. In Ref. [75] and Ref. [76], based on the consideration of the computational cost, especially for curvilinear meshes, the operation of $\mathcal{D}_{mpql}$ is reduced as $\mathcal{D}_{mpql} = \Delta x_m^4$ if $m = p = q = l$, otherwise $\mathcal{D}_{mpql} = 0$. This design makes the operation $\mathcal{D}_{mpql}\partial_{x_m}\partial_{x_p}\partial_{x_q}\partial_{x_l}$ the sum of undivided fourth derivatives in all dimensions. The terms $\sqrt{(\Delta x_j\rho_{,j})^2/(\rho_{,k}\rho_{,k})}$ and $\sqrt{(\Delta x_j e_{\text{th},j})^2/(e_{\text{th},k}e_{\text{th},k})}$ define the length scales considering both grid spacing in different directions and the obliqueness of shock waves indicated by the normalized density and internal energy gradient respectively. The fourth derivative is approximated using the following scheme [89].

$$\alpha f''''_{j-1} + f''''_j + \alpha f''''_{j+1} = a\frac{f_{j-2}-4f_{j-1}+6f_j-4f_{j+1}+f_{j+2}}{\Delta x^4} + b\frac{f_{j-3}-9f_{j-1}+16f_j-9f_{j+1}+f_{j+3}}{6\Delta x^4} \tag{A.42}$$

where f''''_j denotes the numerical evaluation of $\partial_x^4 f$ at x_j. For a formally fourth-order scheme, the coefficients satisfy the following constraints.

$$a = 2(1-\alpha) \qquad \text{and} \qquad b = 4\alpha - 1 \tag{A.43, A.44}$$

If $\alpha = 7/26$, the scheme in Eq. (A.42) becomes formally sixth-order, and $a = 19/13$ and $b = 1/13$. In this work, the sixth-order scheme is used. The truncated Gaussian filter used is given by the following.

$$[\mathcal{G}(f)]_j = \frac{3565}{10368}f_j + \frac{3091}{12960}(f_{j+1}+f_{j-1}) + \frac{1997}{25920}(f_{j+2}+f_{j-2}) + \frac{149}{12960}(f_{j+3}+f_{j-3}) + \frac{107}{103680}(f_{j+4}+f_{j-4}) \tag{A.45}$$

A.5.2 Nonlinear interpolation schemes for shock-capturing

The concept of nonlinear interpolation schemes for shock-capturing referred to in this work is originally introduced in Ref. [73] and known as the weighted essentially non-oscillatory (WENO) method. The five-point-stencil scheme introduced in Ref. [73] is known as the WENO5-JS scheme. Consistent with the higher-order staggered finite difference schemes used for evaluating the flux divergence, the interpolation is used to preserve high-order convergence as opposed to the reconstruction scheme designed for the higher-order finite volume method or the finite difference method referred to in Ref. [141], where the flux difference operation is applied. Since many in literature have provided discussions on the details of the WENO5-JS interpolation scheme and the schemes improved from it, only the key steps are documented.

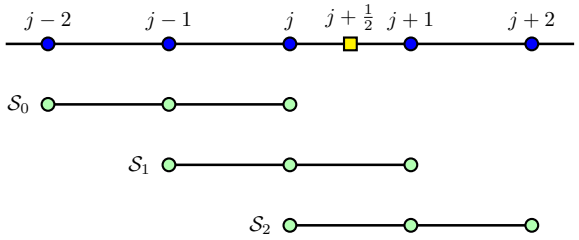

Figure A.4: Candidate sub-stencils of the WENO5-JS interpolation scheme using nodal-point values within the stencil to approximate the edge-staggered value at $j + 1/2$.

The WENO5-JS interpolation scheme evaluates the value at $j + 1/2$ using three candidate sub-stencils, $\mathcal{S}_0$, $\mathcal{S}_1$ and $\mathcal{S}_2$, within a five-point nodal stencil from $j - 2$ to $j + 2$ as shown in Fig. A.4. Each candidate sub-stencil provides an independent evaluation of the interpolated value at $j + 1/2$ using Lagrange interpolation.

$$f^I_{j+\frac{1}{2}}[\mathcal{S}_0] = \frac{1}{8}\left(3f_{j-2} - 10f_{j-1} + 15f_j\right) \tag{A.46}$$

$$f^I_{j+\frac{1}{2}}[\mathcal{S}_1] = \frac{1}{8}\left(-1f_{j-1} + 6f_j + 3f_{j+1}\right) \tag{A.47}$$

$$f^I_{j+\frac{1}{2}}[\mathcal{S}_2] = \frac{1}{8}\left(3f_j + 6f_{j+1} - f_{j+2}\right) \tag{A.48}$$

$$\tag{A.49}$$

where $f^I_{j+\frac{1}{2}}[\mathcal{S}_k]$ denotes the numerically-interpolated value evaluated using the candidate sub-stencil $\mathcal{S}_k$. Optimally, a convex superposition of the interpolated results from all three sub-stencils can form a fifth-order upwind-biased Lagrange interpolation.

$$d_0 f^I_{j+\frac{1}{2}}[\mathcal{S}_0] + d_1 f^I_{j+\frac{1}{2}}[\mathcal{S}_1] + d_2 f^I_{j+\frac{1}{2}}[\mathcal{S}_2] = \frac{1}{128}\left(3f_{j-2} - 20f_{j-1} + 90f_j + 60f_{j+1} - 5f_{j+2}\right) \tag{A.50}$$

where $d_0 = 1/16$, $d_1 = 5/8$, and $d_2 = 5/16$ are known as the linear or optimal weights. In practice,

the convex combination may not use the linear weights especially when the interpolated function is not smooth within the stencil, so a set of nonlinear weights are used to determine the interpolated values.

$$f^I_{j+\frac{1}{2}} = \omega_0 f^I_{j+\frac{1}{2}}[\mathcal{S}_0] + \omega_1 f^I_{j+\frac{1}{2}}[\mathcal{S}_1] + \omega_2 f^I_{j+\frac{1}{2}}[\mathcal{S}_2] \tag{A.51}$$

where the nonlinear weights, ω_0, ω_1, and ω_2, are calculated as

$$\omega_k = \frac{\alpha_k d_k}{\alpha_0 d_0 + \alpha_1 d_1 + \alpha_2 d_2} \quad \text{for} \quad k = 0, 1, 2 \tag{A.52}$$

α_k can be interpreted as a weighting score indicating the quality of the interpolated result from each candidate sub-stencil and is calculated as

$$\alpha_k = (\beta_k + \varepsilon)^{-p} \tag{A.53}$$

where ε and p are model parameters. In the demonstrations, $\varepsilon = 1 \times 10^{-6}$ and $p = 2$ are used. β_k is known as the smoothness indicator measuring the non-smoothness of the discrete profile within the candidate sub-stencil $\mathcal{S}_k$ and is defined as

$$\beta_k = \sum_{l=1}^{2} \Delta x^{2l-1} \int_{x_j - \frac{1}{2}\Delta x}^{x_j + \frac{1}{2}\Delta x} \left(\frac{\partial^l f[\mathcal{S}_k]}{\partial x^l} \right)^2 dx \tag{A.54}$$

The smooth function $f[\mathcal{S}_k]$ is the Lagrange polynomial constructed using all the nodal values within the candidate sub-stencil $\mathcal{S}_k$. For WENO5-JS interpolation, the smoothness indicator of each sub-stencil specified in Fig. A.4 is calculated as follows:

$$\beta_0 = \frac{13}{12}\left(f_{j-2} - 2f_{j-1} + f_j\right)^2 + \frac{1}{4}\left(f_{j-2} - 4f_{j-1} + 3f_j\right)^2 \tag{A.55}$$

$$\beta_1 = \frac{13}{12}\left(f_{j-1} - 2f_j + f_{j+1}\right)^2 + \frac{1}{4}\left(f_{j+1} - f_{j-1}\right)^2 \tag{A.56}$$

$$\beta_2 = \frac{13}{12}\left(f_j - 2f_{j+1} + f_{j+2}\right)^2 + \frac{1}{4}\left(f_{j+2} - 4f_{j+1} + 3f_j\right)^2 \tag{A.57}$$

The targeted essentially non-oscillatory (TENO) method is originally introduced in Ref. [49] and extended from classic WENO schemes. The method generalizes the design of candidate sub-stencils for higher-order methods and calculation of nonlinear weights. Additionally, the interpolation at optimal weights is consistent with central interpolation. These improvements successfully reduce undesirable dissipation and maintain robustness for strong shock capturing in higher-order simulations. Further improvements on the adaptive criterion while calculating nonlinear weights are provided in Ref. [48] for flux reconstruction in a high-order finite volume framework. The coefficients for interpolation are derived in the following context, and the evaluations of some model coefficients are slightly different from those described in Ref. [48].

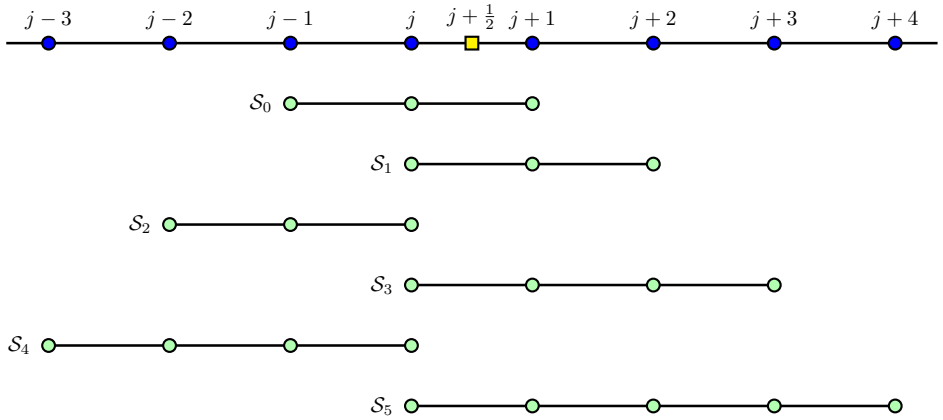

Figure A.5: Candidate sub-stencils of the TENO8-A interpolation scheme using nodal-point values within the stencil to approximate the edge-staggered value at $j + 1/2$.

In this work, the eighth-order adaptive TENO scheme is used and is referred to as the TENO8-A scheme. The scheme contains six candidate sub-stencils from $\mathcal{S}_0$ to $\mathcal{S}_5$ to interpolate the nodal values within an overall 8-point stencil to the edge-staggered point at $j + 1/2$ as shown in Fig. A.5. The individual Lagrange interpolation for each candidate sub-stencil is

$$f^I_{j+\frac{1}{2}}[\mathcal{S}_0] = \frac{1}{8}\left(-f_{j-1} + 6f_j + 3f_{j+1}\right) \tag{A.58}$$

$$f^I_{j+\frac{1}{2}}[\mathcal{S}_1] = \frac{1}{8}\left(3f_j + 6f_{j+1} - f_{j+2}\right) \tag{A.59}$$

$$f^I_{j+\frac{1}{2}}[\mathcal{S}_2] = \frac{1}{8}\left(3f_{j-2} - 10f_{j-1} + 15f_j\right) \tag{A.60}$$

$$f^I_{j+\frac{1}{2}}[\mathcal{S}_3] = \frac{1}{16}\left(5f_j + 15f_{j+1} - 5f_{j+2} + f_{j+3}\right) \tag{A.61}$$

$$f^I_{j+\frac{1}{2}}[\mathcal{S}_4] = \frac{1}{16}\left(-5f_{j-3} + 21f_{j-2} - 35f_{j-1} + 35f_j\right) \tag{A.62}$$

$$f^I_{j+\frac{1}{2}}[\mathcal{S}_5] = \frac{1}{128}\left(35f_j + 140f_{j+1} - 70f_{j+2} + 28f_{j+3} - 5f_{j+4}\right) \tag{A.63}$$

At optimal weights, the convex combination of the interpolated results from the sub-stencils equals the sixth-order central interpolation.

$$\sum_{k=0}^{5} d_k f^I_{j+\frac{1}{2}}[\mathcal{S}_k] = \frac{1225}{2048}\left(f_j + f_{j+1}\right) - \frac{245}{2048}\left(f_{j-1} + f_{j+2}\right) + \frac{49}{2048}\left(f_{j-2} + f_{j+3}\right) - \frac{5}{2048}\left(f_{j-3} + f_{j+4}\right) \tag{A.64}$$

where the optimal weights are $d_0 = 175/384$, $d_1 = 105/384$, $d_2 = 14/384$, $d_3 = 63/384$, $d_4 = 3/384$, and $d_5 = 24/384$. The weighting score, α_k, of each candidate sub-stencil $\mathcal{S}_k$ is calculated in the same way as formulated in Eq. (A.53) with $\varepsilon = 1 \times 10^{-40}$ and $p = 6$. Unlike the WENO method, TENO schemes further normalize α_k to determine a binary pick-up mask function, δ_k, for each candidate

sub-stencil.

$$\delta_k = \mathcal{H}\left(\overline{\alpha}_k - C_T\right) \tag{A.65}$$

where $\mathcal{H}(\cdot)$ denotes the Heaviside step function, $\overline{\alpha}_k = \alpha_k / \left(\sum_{l=0}^{5} \alpha_l\right)$ is a normalized weighting score, and C_T is a cut-off threshold which is dynamically determined for the adaptive method. The nonlinear weights ω_k are determined as

$$\omega_k = \frac{\delta_k d_k}{\sum_{l=0}^{5} \delta_l d_l} \tag{A.66}$$

and the nonlinear interpolated result is calculated as

$$f^I_{j+\frac{1}{2}} = \sum_{k=0}^{5} \omega_k f^I_{j+\frac{1}{2}}[\mathcal{S}_k] \tag{A.67}$$

The smoothness indicator, β_k, needed for calculation of α_k for each candidate sub-stencil in the TENO8-A scheme is calculated as follows:

$$\beta_0 = \frac{1}{4}(f_{j+1} - f_{j-1})^2 + \frac{13}{12}(f_{j-1} - 2f_j + f_{j+1})^2 \tag{A.68}$$

$$\beta_1 = \frac{1}{4}(3f_j - 4f_{j+1} + f_{j+2})^2 + \frac{13}{12}(f_j - 2f_{j+1} + f_{j+2})^2 \tag{A.69}$$

$$\beta_2 = \frac{1}{4}(3f_j - 4f_{j-1} + f_{j-2})^2 + \frac{13}{12}(f_j - 2f_{j-1} + f_{j-2})^2 \tag{A.70}$$

$$\begin{aligned}\beta_3 = {} & \frac{1}{64}(15f_j - 25f_{j+1} + 13f_{j+2} - 3f_{j+3})^2 + \frac{13}{12}(2f_j - 5f_{j+1} + 4f_{j+2} - f_{j+3})^2 \\ & + \frac{61}{720}(f_j - 3f_{j+1} + 3f_{j+2} - f_{j+3})^2\end{aligned} \tag{A.71}$$

$$\begin{aligned}\beta_4 = {} & \frac{1}{64}(15f_j - 25f_{j-1} + 13f_{j-2} - 3f_{j-3})^2 + \frac{13}{12}(2f_j - 5f_{j-1} + 4f_{j-2} - f_{j-3})^2 \\ & + \frac{61}{720}(f_j - 3f_{j-1} + 3f_{j-2} - f_{j-3})^2\end{aligned} \tag{A.72}$$

$$\begin{aligned}\beta_5 = {} & \frac{1}{256}(35f_j - 70f_{j+1} + 56f_{j+2} - 26f_{j+3} + 5f_{j+4})^2 \\ & + \frac{1}{2246400}(4613f_j - 13772f_{j+1} + 15198f_{j+2} - 7532f_{j+3} + 1493f_{j+4})^2 \\ & + \frac{61}{2880}(5f_j - 18f_{j+1} + 24f_{j+2} - 14f_{j+3} + 3f_{j+4})^2 \\ & + \frac{1861}{1310400}(f_j - 4f_{j+1} + 6f_{j+2} - 4f_{j+3} + f_{j+4})^2\end{aligned} \tag{A.73}$$

The cut-off threshold, C_T, in Eq. (A.65) is calculated based on the definition of the local nodal smoothness indicator, μ_j, which is defined as

$$\mu_j = \frac{2\left|(f_{j+1} - f_j)(f_j - f_{j-1})\right| + \varepsilon_\mu}{(f_{j+1} - f_j)^2 + (f_j - f_{j-1})^2 + \varepsilon_\mu} \tag{A.74}$$

where the numerical regularization factor, ε_μ, is determined as

$$\varepsilon_\mu = \frac{0.9c_r}{1-0.9c_r}\varepsilon_{\mu,0} \tag{A.75}$$

ε_μ is statically calculated with tunable model constants c_r and $\varepsilon_{\mu,0}$. As suggested in Ref. [48], $c_r = 0.23$ and $\varepsilon_{\mu,0} = 1 \times 10^{-6}$ are used, which leads to $\varepsilon_\mu = (207/793) \times 10^{-6}$. A complementary indicator, σ, is defined using μ_j in a narrower stencil.

$$\sigma = 1 - \min\left\{1, \min\left\{\mu_{j-1}, \mu_j, \mu_{j+1}, \mu_{j+2}\right\}/c_r\right\} \tag{A.76}$$

Finally, the cut-off threshold, C_T, is calculated as

$$C_T = 10^{-\lfloor c_1 - c_2(1-g(\sigma))\rfloor} \tag{A.77}$$

where $c_1 = 10.5$ and $c_2 = 3.5$ are model constants suggested in Ref. [48], and $g(\cdot)$ is a nonlinear mapping defined as

$$g(\sigma) = (1-\sigma)^4(1+4\sigma) \tag{A.78}$$

A.5.3 Characteristic decomposition on curvilinear meshes and approximate Riemann solver

The use of nonlinear interpolation schemes is combined with the characteristic decomposition for a linearized decoupled system. Considering the inviscid fluxes only, the Navier-Stokes system reduces to an Euler system as follows.

$$\frac{\partial J\boldsymbol{W}}{\partial t} + \frac{\partial \widehat{\boldsymbol{F}}_\xi}{\partial \xi} + \frac{\partial \widehat{\boldsymbol{F}}_\eta}{\partial \eta} + \frac{\partial \widehat{\boldsymbol{F}}_\zeta}{\partial \zeta} = \boldsymbol{0} \tag{A.79}$$

where $\boldsymbol{W}$ is the vector of conservative variables, and $\widehat{\boldsymbol{F}}_\xi$, $\widehat{\boldsymbol{F}}_\eta$, and $\widehat{\boldsymbol{F}}_\zeta$ are the vectors of inviscid contravariant fluxes in ξ, η, and ζ directions respectively. The expressions for $\boldsymbol{W}$, $\widehat{\boldsymbol{F}}_\xi$, $\widehat{\boldsymbol{F}}_\eta$, and $\widehat{\boldsymbol{F}}_\zeta$ are given as

$$\boldsymbol{W} = \begin{pmatrix} \rho \\ \rho u \\ \rho v \\ \rho w \\ \rho e \end{pmatrix} \quad \widehat{\boldsymbol{F}}_\xi = \begin{pmatrix} \rho\widehat{U}_\xi \\ \rho u\widehat{U}_\xi + p\widetilde{g}^{\mathrm{T}}_{x\xi} \\ \rho v\widehat{U}_\xi + p\widetilde{g}^{\mathrm{T}}_{y\xi} \\ \rho w\widehat{U}_\xi + p\widetilde{g}^{\mathrm{T}}_{z\xi} \\ \rho h\widehat{U}_\xi \end{pmatrix} \quad \widehat{\boldsymbol{F}}_\eta = \begin{pmatrix} \rho\widehat{U}_\eta \\ \rho u\widehat{U}_\eta + p\widetilde{g}^{\mathrm{T}}_{x\eta} \\ \rho v\widehat{U}_\eta + p\widetilde{g}^{\mathrm{T}}_{y\eta} \\ \rho w\widehat{U}_\eta + p\widetilde{g}^{\mathrm{T}}_{z\eta} \\ \rho h\widehat{U}_\eta \end{pmatrix} \quad \widehat{\boldsymbol{F}}_\zeta = \begin{pmatrix} \rho\widehat{U}_\zeta \\ \rho u\widehat{U}_\zeta + p\widetilde{g}^{\mathrm{T}}_{x\zeta} \\ \rho v\widehat{U}_\zeta + p\widetilde{g}^{\mathrm{T}}_{y\zeta} \\ \rho w\widehat{U}_\zeta + p\widetilde{g}^{\mathrm{T}}_{z\zeta} \\ \rho h\widehat{U}_\zeta \end{pmatrix}$$

where the components in vector and tensor quantities are explicitly expressed as individual quantities, and the matrix-vector notation denotes the Euler equation system. u, v, and w are the

three-components of the velocity vector in physical space in the x-, y-, and z-directions respectively. Other notation is consistent with that defined in Sec. 2.3.1 and Sec. 2.3.3.

The characteristic decomposition of the contravariant flux Jacobian in the ξ-dimension can be denoted as

$$\frac{\partial \widehat{\boldsymbol{F}}_\xi}{\partial \boldsymbol{W}} = \boldsymbol{R}_\xi \boldsymbol{\Lambda}_\xi \boldsymbol{L}_\xi^{\mathrm{T}} \tag{A.80}$$

where $\boldsymbol{\Lambda}_\xi$ is a diagonal matrix storing the eigenvalues, and the columns in $\boldsymbol{R}_\xi$ and $\boldsymbol{L}_\xi$ are the right and left eigenvectors respectively associated with the eigenvalues stored in $\boldsymbol{\Lambda}_\xi$. A form of characteristic decomposition is provided as follows.

$$\boldsymbol{R}_\xi = \begin{pmatrix} 1 & 0 & 1 & 0 & 1 \\ u - c\overline{g}_{x\xi}^{\mathrm{T}} & \overline{l}_{x\xi} & u & \overline{m}_{x\xi} & u + c\overline{g}_{x\xi}^{\mathrm{T}} \\ v - c\overline{g}_{y\xi}^{\mathrm{T}} & \overline{l}_{y\xi} & v & \overline{m}_{y\xi} & v + c\overline{g}_{y\xi}^{\mathrm{T}} \\ w - c\overline{g}_{z\xi}^{\mathrm{T}} & \overline{l}_{z\xi} & w & \overline{m}_{z\xi} & w + c\overline{g}_{z\xi}^{\mathrm{T}} \\ h - c\overline{U}_\xi & \overline{U}_{l(\xi)} & e_{\mathrm{k}} & \overline{U}_{m(\xi)} & h + c\overline{U}_\xi \end{pmatrix} \tag{A.81}$$

$$\boldsymbol{\Lambda}_\xi = \begin{pmatrix} \widehat{U}_\xi - c\widetilde{g}_{n\xi}^{\mathrm{T}} & 0 & 0 & 0 & 0 \\ 0 & \widehat{U}_\xi & 0 & 0 & 0 \\ 0 & 0 & \widehat{U}_\xi & 0 & 0 \\ 0 & 0 & 0 & \widehat{U}_\xi & 0 \\ 0 & 0 & 0 & 0 & \widehat{U}_\xi + c\widetilde{g}_{n\xi}^{\mathrm{T}} \end{pmatrix} \tag{A.82}$$

$$\boldsymbol{L}_\xi^{\mathrm{T}} = \begin{pmatrix} \frac{\gamma-1}{2c^2}e_{\mathrm{k}} + \frac{\overline{U}_\xi}{2c} & -\frac{\overline{g}_{x\xi}^{\mathrm{T}}}{2c} - \frac{\gamma-1}{2c^2}u & -\frac{\overline{g}_{y\xi}^{\mathrm{T}}}{2c} - \frac{\gamma-1}{2c^2}v & -\frac{\overline{g}_{z\xi}^{\mathrm{T}}}{2c} - \frac{\gamma-1}{2c^2}w & \frac{\gamma-1}{2c^2} \\ -\overline{U}_{l(\xi)} & \overline{l}_{x\xi} & \overline{l}_{y\xi} & \overline{l}_{z\xi} & 0 \\ 1 - \frac{\gamma-1}{c^2}e_{\mathrm{k}} & \frac{\gamma-1}{c^2}u & \frac{\gamma-1}{c^2}v & \frac{\gamma-1}{c^2}w & -\frac{\gamma-1}{c^2} \\ -\overline{U}_{m(\xi)} & \overline{m}_{x\xi} & \overline{m}_{y\xi} & \overline{m}_{z\xi} & 0 \\ \frac{\gamma-1}{2c^2}e_{\mathrm{k}} - \frac{\overline{U}_\xi}{2c} & \frac{\overline{g}_{x\xi}^{\mathrm{T}}}{2c} - \frac{\gamma-1}{2c^2}u & \frac{\overline{g}_{y\xi}^{\mathrm{T}}}{2c} - \frac{\gamma-1}{2c^2}v & \frac{\overline{g}_{z\xi}^{\mathrm{T}}}{2c} - \frac{\gamma-1}{2c^2}w & \frac{\gamma-1}{2c^2} \end{pmatrix} \tag{A.83}$$

where $\widetilde{g}_{n\xi}^{\mathrm{T}} = \sqrt{\left(\widetilde{g}_{x\xi}^{\mathrm{T}}\right)^2 + \left(\widetilde{g}_{y\xi}^{\mathrm{T}}\right)^2 + \left(\widetilde{g}_{z\xi}^{\mathrm{T}}\right)^2}$ is the magnitude of the metrics in ξ dimension. $\overline{g}_{x\xi}^{\mathrm{T}}$, $\overline{g}_{y\xi}^{\mathrm{T}}$, and $\overline{g}_{z\xi}^{\mathrm{T}}$ are the normalized metric components defined as $\overline{g}_{x\xi}^{\mathrm{T}} = \widetilde{g}_{x\xi}^{\mathrm{T}}/\widetilde{g}_{n\xi}^{\mathrm{T}}$, $\overline{g}_{y\xi}^{\mathrm{T}} = \widetilde{g}_{y\xi}^{\mathrm{T}}/\widetilde{g}_{n\xi}^{\mathrm{T}}$, and $\overline{g}_{z\xi}^{\mathrm{T}} = \widetilde{g}_{z\xi}^{\mathrm{T}}/\widetilde{g}_{n\xi}^{\mathrm{T}}$. $[\overline{l}_{x\xi}, \overline{l}_{y\xi}, \overline{l}_{z\xi}]^{\mathrm{T}}$ and $[\overline{m}_{x\xi}, \overline{m}_{y\xi}, \overline{m}_{z\xi}]^{\mathrm{T}}$ are two unit vectors that form a set of orthonormal basis vectors in three-dimensional physical space together with $[\overline{g}_{x\xi}^{\mathrm{T}}, \overline{g}_{y\xi}^{\mathrm{T}}, \overline{g}_{z\xi}^{\mathrm{T}}]^{\mathrm{T}}$. $e_{\mathrm{k}} = (u^2+v^2+w^2)/2$ is the specific kinetic energy. $\overline{U}_\xi$, $\overline{U}_{l(\xi)}$, and $\overline{U}_{m(\xi)}$ are defined as $\overline{U}_\xi = u\overline{g}_{x\xi}^{\mathrm{T}} + v\overline{g}_{y\xi}^{\mathrm{T}} + w\overline{g}_{z\xi}^{\mathrm{T}}$, $\overline{U}_{l(\xi)} = u\overline{l}_{x\xi} + v\overline{l}_{y\xi} + w\overline{l}_{z\xi}$, and $\overline{U}_{m(\xi)} = u\overline{m}_{x\xi} + v\overline{m}_{y\xi} + w\overline{m}_{z\xi}$ respectively. Due to the symmetry of the contravariant flux formulations in different dimensions in the reference domain, the characteristic decompositions in η- and ζ-dimensions are not provided.

For a general equation-of-state model, the following thermodynamic relations are needed.

$$\alpha = \left(\frac{\partial p}{\partial \rho}\right)_{e_{\text{th}}} \quad \text{and} \quad \beta = \left(\frac{\partial p}{\partial e}\right)_{\rho} \tag{A.84, A.85}$$

where e_{th} is the internal energy and satisfies the relation $e = e_{\text{th}} + e_{\text{k}}$. Based on the definitions of α and β and the definition of the speed of sound, c, the following relation holds.

$$c^2 = \alpha + \beta p/\rho^2 \tag{A.86}$$

Correspondingly, the characteristic decomposition, for a real-gas flow, becomes

$$\boldsymbol{R}_\xi = \begin{pmatrix} 1 & 0 & 1 & 0 & 1 \\ u - c\overline{g}^{\mathrm{T}}_{x\xi} & \bar{l}_{x\xi} & u & \overline{m}_{x\xi} & u + c\overline{g}^{\mathrm{T}}_{x\xi} \\ v - c\overline{g}^{\mathrm{T}}_{y\xi} & \bar{l}_{y\xi} & v & \overline{m}_{y\xi} & v + c\overline{g}^{\mathrm{T}}_{y\xi} \\ w - c\overline{g}^{\mathrm{T}}_{z\xi} & \bar{l}_{z\xi} & w & \overline{m}_{z\xi} & w + c\overline{g}^{\mathrm{T}}_{z\xi} \\ h - c\overline{U}_\xi & \overline{U}_{l(\xi)} & h - \frac{\rho c^2}{\beta} & \overline{U}_{m(\xi)} & h + c\overline{U}_\xi \end{pmatrix} \tag{A.87}$$

$$\boldsymbol{L}^{\mathrm{T}}_\xi = \begin{pmatrix} \frac{1}{2} - \frac{\beta(h-2e_{\text{k}})}{2\rho c^2} + \frac{\overline{U}_\xi}{2c} & -\frac{\overline{g}^{\mathrm{T}}_{x\xi}}{2c} - \frac{\beta u}{2\rho c^2} & -\frac{\overline{g}^{\mathrm{T}}_{y\xi}}{2c} - \frac{\beta v}{2\rho c^2} & -\frac{\overline{g}^{\mathrm{T}}_{z\xi}}{2c} - \frac{\beta w}{2\rho c^2} & \frac{\beta}{2\rho c^2} \\ -\overline{U}_{l(\xi)} & \bar{l}_{x\xi} & \bar{l}_{y\xi} & \bar{l}_{z\xi} & 0 \\ \frac{\beta(h-2e_{\text{k}})}{\rho c^2} & \frac{\beta u}{\rho c^2} & \frac{\beta v}{\rho c^2} & \frac{\beta w}{\rho c^2} & -\frac{\beta}{\rho c^2} \\ -\overline{U}_{m(\xi)} & \overline{m}_{x\xi} & \overline{m}_{y\xi} & \overline{m}_{z\xi} & 0 \\ \frac{1}{2} - \frac{\beta(h-2e_{\text{k}})}{2\rho c^2} - \frac{\overline{U}_\xi}{2c} & \frac{\overline{g}^{\mathrm{T}}_{x\xi}}{2c} - \frac{\beta u}{2\rho c^2} & \frac{\overline{g}^{\mathrm{T}}_{y\xi}}{2c} - \frac{\beta v}{2\rho c^2} & \frac{\overline{g}^{\mathrm{T}}_{z\xi}}{2c} - \frac{\beta w}{2\rho c^2} & \frac{\beta}{2\rho c^2} \end{pmatrix} \tag{A.88}$$

The eigenvalue matrix, $\boldsymbol{\Lambda}_\xi$, remains same as shown in Eq. (A.82).

During the numerical solution process, the Euler system is locally linearized in each dimension so that the flux Jacobian is frozen within an interpolation stencil. Based on this assumption, the characteristic variables within a stencil can be calculated as

$$\boldsymbol{Q}_\xi = \left\langle \boldsymbol{L}^{\mathrm{T}}_\xi \right\rangle \boldsymbol{W} \tag{A.89}$$

where $\boldsymbol{Q}_\xi$ is the vector of characteristic variables in the locally linearized Euler system in the ξ-dimension, and the operator $\langle(\cdot)\rangle$ denotes that a quantity remains constant within the stencil. The nonlinear shock-capturing schemes will be applied to interpolate $\boldsymbol{Q}$ to the edge-points using a stencil of nodal points. The nonlinear interpolation scheme is not statically symmetric about the stencil, which provides upwind-biased numerical dissipation in the non-smooth region. For shock-capturing, the nonlinear interpolation needs to be applied using both backward-biased and forward-biased stencils to obtain the characteristic variables that are potentially carried by the "right-" traveling waves, $\boldsymbol{Q}^+_\xi$, interpolated from the "left" side (which is commonly denoted by "L") and the "left-" traveling waves, $\boldsymbol{Q}^-_\xi$, interpolated from the "right" side (which is commonly denoted

by "R") respectively. After interpolation, the characteristic variables obtained on the edge-points are converted back to the conservative variables using the right eigenvectors.

$$\boldsymbol{W}_{\xi}^{+} = \langle \boldsymbol{R}_{\xi} \rangle \, \boldsymbol{Q}_{\xi}^{+} \quad \text{and} \quad \boldsymbol{W}_{\xi}^{-} = \langle \boldsymbol{R}_{\xi} \rangle \, \boldsymbol{Q}_{\xi}^{-} \tag{A.90, A.91}$$

where $\boldsymbol{W}_{\xi}^{+}$ and $\boldsymbol{W}_{\xi}^{-}$ are the volume weighted conservative variables converted from the interpolated characteristic variables, $\boldsymbol{Q}_{\xi}^{+}$ and $\boldsymbol{Q}_{\xi}^{-}$. In this work, the elements in the locally averaged eigenvectors, $\left\langle \boldsymbol{L}_{\xi}^{\mathrm{T}} \right\rangle$ and $\langle \boldsymbol{R}_{\xi} \rangle$, are assembled by the Roe-Pike averaged quantities [131, 130] which are calculated using the first nodal values on both sides of each targeted edge-point location.

With $\boldsymbol{W}_{\xi}^{+}$ and $\boldsymbol{W}_{\xi}^{-}$ obtained, the approximate Riemann flux can be calculated. In this work, the Rusanov flux [132, 157] is used.

$$\widehat{\boldsymbol{F}}_{\xi}^{\mathrm{Riemann}} = \frac{1}{2}\left(\widehat{\boldsymbol{F}}_{\xi}^{-} + \widehat{\boldsymbol{F}}_{\xi}^{+}\right) - \frac{1}{2} S \left(\boldsymbol{W}_{\xi}^{-} - \boldsymbol{W}_{\xi}^{+}\right) \tag{A.92}$$

where $\widehat{\boldsymbol{F}}_{\xi}^{\mathrm{Riemann}}$ is the Rusanov type of approximate Riemann flux, $\widehat{\boldsymbol{F}}_{\xi}^{-}$ and $\widehat{\boldsymbol{F}}_{\xi}^{+}$ are the contravariant fluxes assembled by $\boldsymbol{W}_{\xi}^{-}$ and $\boldsymbol{W}_{\xi}^{+}$ respectively, and S is an approximate wave speed calculated as

$$S = \max\left\{ \left|\widehat{U}_{\xi}^{+}\right| + c_{\xi}^{+} \widetilde{g}_{n\xi}^{\mathrm{T}}, \left|\widehat{U}_{\xi}^{-}\right| + c_{\xi}^{-} \widetilde{g}_{n\xi}^{\mathrm{T}} \right\} \tag{A.93}$$

where c_{ξ}^{+} and c_{ξ}^{-} are the speeds of sound calculated using $\boldsymbol{W}_{\xi}^{+}$ and $\boldsymbol{W}_{\xi}^{-}$ respectively. For hybrid central-Riemann flux assembly, the hybridization is applied in constructing the primitive variables after the calculation of $\boldsymbol{W}_{\xi}^{+}$ and $\boldsymbol{W}_{\xi}^{-}$, and the volume weighted conservative variables and contravariant fluxes are calculated using blended primitive variables. If only primitive variables that are interpolated using central compact schemes are used, $\boldsymbol{W}_{\xi}^{+} = \boldsymbol{W}_{\xi}^{-}$ and $\widehat{\boldsymbol{F}}_{\xi}^{+} = \widehat{\boldsymbol{F}}_{\xi}^{-}$. In this scenario, $\widehat{\boldsymbol{F}}_{\xi}^{\mathrm{Riemann}}$ is same as the central flux.

Appendix B

Real-Gas Thermodynamic and Transport Properties

This chapter documents the derivations and calculations used in the computational code for simulations of dense-gas flows and the corresponding data post-processing related to this thesis work. The novelty of the work documented in this chapter is not claimed, the author conducted the derivations based on well-developed theories that were present in the community. In this chapter, the derivations of thermodynamic relations are presented in detail. Alternatively, the derivations can be also conducted using existing formulas for convenience, such as the Bridgman's derivation [14]. The derivations of thermodynamic relations based on the first and second laws of thermodynamics and definitions are summarized in Sec. B.1. The calculations of the thermodynamic properties based on the Peng-Robinson model [119] are documented in Sec. B.2 where the modeling of the temperature-dependent specific heat at constant volume is particularly suitable for CO_2. The calculations of temperature- and pressure-dependent viscosity and thermal conductivity based on the Chung et al. (1988) transport models [25] are documented in Sec. B.3.

B.1 Fundamentals of pure-substance thermodynamics

Starting from the first law of thermodynamics,

$$de = \delta q - \delta w \tag{B.1}$$

where e is the specific internal energy, q is the specific heat exchange, and w is the specific work done by the substance. Only considering the work due to changes in volume, the variation in work can be expressed as $\delta w = pdv$ where p and v are the pressure and specific volume respectively. Let

density be ρ so that $\rho = 1/v$. The specific enthalpy, h, is defined as

$$h = e + pv \tag{B.2}$$

Then, the specific heat capacity at constant volume, c_v, and constant pressure, c_p, can be defined as

$$c_v = \left(\frac{\partial e}{\partial T}\right)_v \qquad \text{and} \qquad c_p = \left(\frac{\partial h}{\partial T}\right)_p \tag{B.3, B.4}$$

where T is the temperature. For an isochoric process, $\delta q = de = c_v dT$, and for an isobaric process, $\delta q = dh = c_p dT$. As the identification of thermodynamic states, in general, using reversible process from a reference state, $e = e(T, v)$ and $h = h(T, p)$, and correspondingly, $c_v = c_v(T, v)$ and $c_p = c_p(T, p)$. The calculation from e_{ref} to e assumes a process of isochoric heat exchange from T_{ref} to T and then an isothermal expansion/compression from v_{ref} to v; and the calculation from h_{ref} to h assumes a process of isobaric heat exchange from T_{ref} to T and then an isothermal expansion/compression from p_{ref} to p.

$$de = c_v dT + \left(\frac{\partial e}{\partial v}\right)_T dv \qquad \text{and} \qquad dh = c_p dT + \left(\frac{\partial h}{\partial p}\right)_T dp \tag{B.5, B.6}$$

$(\partial e/\partial v)_T$ in Eq. (B.5) is known as the energy of imperfection of a real gas that induces the heat effects due to intermolecular interactions. For an ideal gas, molecules are assumed to be sufficiently far from each other and result in no interaction. Therefore, $(\partial e/\partial v)_T = 0$, which also leads to $(\partial h/\partial p)_T = 0$. Then e and h are determined by T only. However, this may not hold for real gases. Using the definition of the specific enthalpy in Eq. (B.2), Eq. (B.4) leads to

$$c_p = \left(\frac{\partial h}{\partial T}\right)_p = \left(\frac{\partial e}{\partial T}\right)_p + p\left(\frac{\partial v}{\partial T}\right)_p \tag{B.7}$$

where

$$\left(\frac{\partial e}{\partial T}\right)_p = \left(\frac{\partial e}{\partial T}\right)_v + \left(\frac{\partial e}{\partial v}\right)_T \left(\frac{\partial v}{\partial T}\right)_p$$

Substituting into Eq. (B.7) and combining with Eq. (B.3), the following relation can be obtained

$$c_p = c_v + \left[\left(\frac{\partial e}{\partial v}\right)_T + p\right]\left(\frac{\partial v}{\partial T}\right)_p \tag{B.8}$$

From the second law of thermodynamics, for a reversible process, $\delta q = Tds$, where s is the specific entropy. Combined with Eq. (B.1), it can be shown that

$$Tds = de + pdv \tag{B.9}$$

Combining Eq. (B.9) and Eq. (B.2), an alternative form can be obtained as

$$Tds = dh - vdp \tag{B.10}$$

From Eq. (B.9), for an isothermal process and an isochoric process the following two relations hold respectively.

$$\left(\frac{\partial e}{\partial v}\right)_T = T\left(\frac{\partial s}{\partial v}\right)_T - p \qquad \text{and} \qquad T\left(\frac{\partial s}{\partial T}\right)_v = \left(\frac{\partial e}{\partial T}\right)_v \tag{B.11, B.12}$$

Differentiate Eq. (B.11) with respect to T along an isochoric process, and differentiate Eq. (B.12) with respect to v along an isothermal process respectively.

$$\left[\frac{\partial}{\partial T}\left(\frac{\partial e}{\partial v}\right)_T\right]_v = T\left[\frac{\partial}{\partial T}\left(\frac{\partial s}{\partial v}\right)_T\right]_v + \left(\frac{\partial s}{\partial v}\right)_T - \left(\frac{\partial p}{\partial T}\right)_v \tag{B.13}$$

$$T\left[\frac{\partial}{\partial v}\left(\frac{\partial s}{\partial T}\right)_v\right]_T = \left[\frac{\partial}{\partial v}\left(\frac{\partial e}{\partial T}\right)_v\right]_T \tag{B.14}$$

The mixed second derivatives in Eq. (B.13) and Eq. (B.14) are commutable.

$$\left[\frac{\partial}{\partial T}\left(\frac{\partial e}{\partial v}\right)_T\right]_v = \left[\frac{\partial}{\partial v}\left(\frac{\partial e}{\partial T}\right)_v\right]_T \quad \text{and} \quad \left[\frac{\partial}{\partial T}\left(\frac{\partial s}{\partial v}\right)_T\right]_v = \left[\frac{\partial}{\partial v}\left(\frac{\partial s}{\partial T}\right)_v\right]_T$$

Therefore, Eq. (B.13) combined with Eq. (B.14) can be reduced to the following relation which is known as one of the Maxwell relations [100].

$$\left(\frac{\partial s}{\partial v}\right)_T = \left(\frac{\partial p}{\partial T}\right)_v \tag{B.15}$$

Eq. (B.15) enables replacing $(\partial s/\partial v)_T$ in Eq. (B.11) to obtain the specific energy imperfection in terms of p, v and T.

$$\left(\frac{\partial e}{\partial v}\right)_T = T\left(\frac{\partial p}{\partial T}\right)_v - p \tag{B.16}$$

Eq. (B.16) can be used to evaluate the energy imperfection, cf. Eq. (B.5), with a pressure-volume-temperature (p-v-T) relation, an identified reference state, and a model of $c_v(T, v_{\text{ref}})$. The internal energy can be calculated by integrating Eq. (B.5) from the reference state following a path that has an isothermal process and an isochoric process.

$$e = e_{\text{ref}} + \int_{T_{\text{ref}}}^{T} c_v(T, v_{\text{ref}})dT + \int_{v_{\text{ref}}}^{v}\left[T\left(\frac{\partial p}{\partial T}\right)_v - p\right]dv \tag{B.17}$$

Combining Eq. (B.8) and Eq. (B.16), an alternative expression of c_p is

$$c_p = c_v + T\left(\frac{\partial p}{\partial T}\right)_v \left(\frac{\partial v}{\partial T}\right)_p \tag{B.18}$$

Furthermore, given a thermodynamic process described by the p-v-T relation,

$$dp = \left(\frac{\partial p}{\partial T}\right)_v dT + \left(\frac{\partial p}{\partial v}\right)_T dv \tag{B.19}$$

for an isobaric process, $dp = 0$, the following relation holds.

$$\left(\frac{\partial v}{\partial T}\right)_p = -\left(\frac{\partial p}{\partial T}\right)_v \left(\frac{\partial p}{\partial v}\right)_T^{-1} \tag{B.20}$$

Substituting this relation into Eq. (B.18), another calculation of c_p can be obtained as

$$c_p = c_v - T\left(\frac{\partial p}{\partial T}\right)_v^2 \left(\frac{\partial p}{\partial v}\right)_T^{-1} \tag{B.21}$$

In the compressible Navier-Stokes solver, T needs to be calculated iteratively from e during the conversion from conservative variables to primitive variables if an explicit expression is not accessible. The iterative solution process can be denoted as follows.

$$T^{(m+1)} = T^{(m)} - \alpha \frac{e(T^{(m)}, v)}{c_v(T^{(m)}, v)} \tag{B.22}$$

where α is a relaxation factor, and for the standard Newton-Raphson method, $\alpha = 1$; the superscripts on T represent the iteration step counts.

The speed of sound, c, that is required in the flow solver, is defined as

$$c^2 = \left(\frac{\partial p}{\partial \rho}\right)_s = -v^2 \left(\frac{\partial p}{\partial v}\right)_s \tag{B.23}$$

where the derivative $(\partial p/\partial v)_s$ can be calculated using the chain rule.

$$\left(\frac{\partial p}{\partial v}\right)_s = \left(\frac{\partial p}{\partial T}\right)_s \left(\frac{\partial T}{\partial v}\right)_s \tag{B.24}$$

where the derivatives $(\partial p/\partial T)_s$ and $(\partial T/\partial v)_s$ can be calculated using the thermodynamic processes defined by

$$ds = \left(\frac{\partial s}{\partial T}\right)_p dT + \left(\frac{\partial s}{\partial p}\right)_T dp \qquad \text{and} \qquad ds = \left(\frac{\partial s}{\partial T}\right)_v dT + \left(\frac{\partial s}{\partial v}\right)_T dv$$

respectively by imposing an isentropic constraint $ds = 0$. The results are

$$\left(\frac{\partial p}{\partial T}\right)_s = -\left(\frac{\partial s}{\partial T}\right)_p \left(\frac{\partial s}{\partial p}\right)_T^{-1} \qquad \text{and} \qquad \left(\frac{\partial T}{\partial v}\right)_s = -\left(\frac{\partial s}{\partial v}\right)_T \left(\frac{\partial s}{\partial T}\right)_v^{-1}$$

Substituting these two results into Eq. (B.24) yields

$$\left(\frac{\partial p}{\partial v}\right)_s = \left(\frac{\partial s}{\partial T}\right)_p \left(\frac{\partial T}{\partial s}\right)_v \left(\frac{\partial p}{\partial v}\right)_T \tag{B.25}$$

Combining Eq. (B.9) and Eq. (B.5) the thermodynamic relation can be obtained as

$$Tds - pdv = c_v dT + \left(\frac{\partial e}{\partial v}\right)_T dv$$

For an isochoric process, $dv = 0$, the derivative, $(\partial s/\partial T)_p$, is calculated as

$$\left(\frac{\partial s}{\partial T}\right)_p = \frac{c_p}{T} \tag{B.26}$$

Similarly, combining Eq. (B.10) and Eq. (B.6), an alternative relation is obtained as

$$Tds + vdp = c_p dT + \left(\frac{\partial h}{\partial p}\right)_T dp$$

For an isobaric process, $dp = 0$, and the derivative, $(\partial T/\partial s)_v$, is calculated as

$$\left(\frac{\partial T}{\partial s}\right)_v = \frac{T}{c_v} \tag{B.27}$$

Substituting the results obtained in Eq. (B.26) and Eq. (B.27) into Eq. (B.25), the derivative, $(\partial p/\partial v)_s$ can be calculated as

$$\left(\frac{\partial p}{\partial v}\right)_s = \frac{c_p}{c_v}\left(\frac{\partial p}{\partial v}\right)_T$$

Combining with Eq. (B.23), the speed of sound, c, can be calculated as

$$c^2 = -v^2 \frac{c_p}{c_v}\left(\frac{\partial p}{\partial v}\right)_T = \frac{c_p}{c_v}\left(\frac{\partial p}{\partial \rho}\right)_T \tag{B.28}$$

An equivalent form of the speed of sound calculated based on the formulation of thermodynamic model, $p = p(\rho, e)$, can be derived similarly to the procedure provided above. The right-hand side of Eq. (B.24) can be modified using e as the intermediate variable.

$$\left(\frac{\partial p}{\partial v}\right)_s = \left(\frac{\partial p}{\partial e}\right)_s \left(\frac{\partial e}{\partial v}\right)_s \tag{B.29}$$

where skipping the steps of setting up the thermodynamic processes, the derivatives, $(\partial p/\partial e)_s$ and $(\partial e/\partial v)_s$, on the right-hand side of Eq. (B.29) are evaluated as

$$\left(\frac{\partial p}{\partial e}\right)_s = -\left(\frac{\partial s}{\partial e}\right)_p \left(\frac{\partial s}{\partial p}\right)_e^{-1} \qquad \text{and} \qquad \left(\frac{\partial e}{\partial v}\right)_s = -\left(\frac{\partial s}{\partial v}\right)_e \left(\frac{\partial s}{\partial e}\right)_v$$

Substituting these results into Eq. (B.29), the derivative, $(\partial p/\partial v)_s$, can be further expressed as

$$\left(\frac{\partial p}{\partial v}\right)_s = \left(\frac{\partial s}{\partial e}\right)_p \left(\frac{\partial p}{\partial v}\right)_e \left(\frac{\partial e}{\partial s}\right)_v \tag{B.30}$$

The derivative, $(\partial s/\partial e)_p$, on the right-hand side of Eq. (B.30) can be calculated using the identity

$$\left(\frac{\partial s}{\partial e}\right)_p = \left(\frac{\partial s}{\partial e}\right)_v + \left(\frac{\partial v}{\partial e}\right)_p \left(\frac{\partial s}{\partial v}\right)_e \tag{B.31}$$

Eq. (B.9) is used to compute the derivatives, $(\partial e/\partial s)_v$ and $(\partial s/\partial v)_e$, by imposing the constraints $dv = 0$ and $de = 0$, respectively.

$$\left(\frac{\partial e}{\partial s}\right)_v = T \qquad \text{and} \qquad \left(\frac{\partial s}{\partial v}\right)_e = \frac{p}{T}$$

Combining all the results, Eq. (B.30) becomes

$$\left(\frac{\partial p}{\partial v}\right)_s = \left[1 + p\left(\frac{\partial v}{\partial e}\right)_p\right] \left(\frac{\partial p}{\partial v}\right)_e \tag{B.32}$$

where using the relation

$$dv = \left(\frac{\partial v}{\partial e}\right)_p de + \left(\frac{\partial v}{\partial p}\right)_e dp$$

it can be obtained, based on the identity for $dv = 0$, that

$$\left(\frac{\partial v}{\partial e}\right)_p \left(\frac{\partial p}{\partial v}\right)_e = -\left(\frac{\partial p}{\partial e}\right)_v$$

Therefore, combining Eq. (B.23), the speed of sound can be also calculated as

$$c^2 = -v^2\left[\left(\frac{\partial p}{\partial v}\right)_e - p\left(\frac{\partial p}{\partial e}\right)_v\right] = \left(\frac{\partial p}{\partial \rho}\right)_e + \frac{p}{\rho^2}\left(\frac{\partial p}{\partial e}\right)_\rho \tag{B.33}$$

Besides the calculation of the speed of sound using Eq. (B.33), the derivatives, $(\partial p/\partial \rho)_e$ and $(\partial p/\partial e)_\rho$, are also needed for the characteristic decomposition in the application of a shock-capturing scheme. For specific internal energy modeled with the form $e = e(T, \rho)$, the derivatives can be

evaluated using the mathematical identities combined with the definition of c_v in Eq. (B.3).

$$\left(\frac{\partial p}{\partial \rho}\right)_e = \left(\frac{\partial p}{\partial \rho}\right)_T + \left(\frac{\partial T}{\partial \rho}\right)_e \left(\frac{\partial p}{\partial T}\right)_\rho \qquad \text{and} \qquad \left(\frac{\partial p}{\partial e}\right)_\rho = \frac{1}{c_v}\left(\frac{\partial p}{\partial T}\right)_\rho \tag{B.34, B.35}$$

where the following identity can be applied to calculate the derivative, $(\partial T/\partial \rho)_e$, more conveniently.

$$\left(\frac{\partial T}{\partial \rho}\right)_e = -\frac{1}{c_v}\left(\frac{\partial e}{\partial \rho}\right)_T$$

Therefore, Eq. (B.34) can be rewritten as

$$\left(\frac{\partial p}{\partial \rho}\right)_e = \left(\frac{\partial p}{\partial \rho}\right)_T - \frac{1}{c_v}\left(\frac{\partial p}{\partial T}\right)_\rho \left(\frac{\partial e}{\partial \rho}\right)_T \tag{B.36}$$

Furthermore the following equation holds according to the definition of v as $v = 1/\rho$.

$$\left(\frac{\partial x}{\partial \rho}\right)_T = -v^2\left(\frac{\partial x}{\partial v}\right)_T \qquad \text{and} \qquad \left(\frac{\partial x}{\partial T}\right)_\rho = \left(\frac{\partial x}{\partial T}\right)_v$$

where x can be either p or e for the related derivatives in Eq. (B.35) and Eq. (B.36).

The specific Gibbs free energy is also needed in general to determine the physical solution among multiple roots obtained from the thermodynamic model. The definition of the specific Gibbs free energy, g, is

$$g = h - Ts \tag{B.37}$$

Combining Eq. (B.37) with Eq. (B.10), the variation in the specific Gibbs free energy can be expressed as

$$dg = vdp - sdT \tag{B.38}$$

Eq. (B.38) implies the identity that

$$\left(\frac{\partial g}{\partial p}\right)_T = v \tag{B.39}$$

According to the chain rule,

$$\left(\frac{\partial g}{\partial p}\right)_T = \left(\frac{\partial g}{\partial v}\right)_T \left(\frac{\partial v}{\partial p}\right)_T \tag{B.40}$$

Therefore, the derivative, $(\partial g/\partial v)_T$, which is useful to the derivations in the following sections, can be calculated using the p-v-T relation as

$$\left(\frac{\partial g}{\partial v}\right)_T = v\left(\frac{\partial p}{\partial v}\right)_T \tag{B.41}$$

B.2 Calculations of thermodynamic properties

The thermodynamic behavior of a real-gas near the critical condition is calculated using the Peng-Robinson equation of state (EOS) model [119]. The Peng-Robinson model proposes a p-v-T relation formulated as a cubic EOS. The expression of the Peng-Robinson model is

$$p = \frac{RT}{v-b} - \frac{a\alpha(T_r)}{v^2+2vb-b^2} \tag{B.42}$$

where R is the specific gas constant; a and b are constant parameters determined by the critical condition, with values

$$a = 0.45723553\frac{R^2T_c^2}{p_c} \qquad \text{and} \qquad b = 0.07779607\frac{RT_c}{p_c} \tag{B.43, B.44}$$

where T_c and p_c are the critical temperature and pressure respectively. α is a function of the reduced temperature, $T_r = T/T_c$, defined as

$$\alpha = \left[1+\kappa\left(1-\sqrt{T_r}\right)\right]^2 \tag{B.45}$$

where κ is a model parameter calculated using the acentric factor of the gas molecule, ω,

$$\kappa = \begin{cases} 0.37464 + 1.54226\omega - 0.26992\omega^2 & \text{for } \omega \leq 0.49 \\ 0.379642 + 1.48503\omega - 0.164423\omega^2 + 0.016666\omega^3 & \text{for } \omega > 0.49 \end{cases} \tag{B.46}$$

The p-v-T relation requires the following model parameters: ω, T_c, p_c and R. The derivatives based on the p-v-T relation are calculated as

$$\left(\frac{\partial p}{\partial T}\right)_v = \frac{R}{v-b} + \frac{a\left[1+\kappa\left(1-\sqrt{T_r}\right)\right]}{v^2+2vb-b^2}\left(\frac{\kappa}{T_c\sqrt{T_r}}\right) \tag{B.47}$$

$$\left(\frac{\partial p}{\partial v}\right)_T = -\frac{RT}{(v-b)^2} + \frac{2a\,(v+b)\left[1+\kappa\left(1-\sqrt{T_r}\right)\right]^2}{\left(v^2+2vb-b^2\right)^2} \tag{B.48}$$

The calculation of internal energy is based on Eq. (B.17) with the reference state set to the ideal-gas limit at the critical temperature, $v_{\text{ref}} \to \infty$ and $T_{\text{ref}} = T_c$. In the ideal-gas limit, the temperature-dependent specific heat at constant volume, $c_v(T,\infty)$, is modeled using a power law.

$$c_v(T,\infty) = c_v(T_c,\infty)\left(\frac{T}{T_c}\right)^n = \frac{R}{\gamma_{c,\infty}-1}\left(\frac{T}{T_c}\right)^n \tag{B.49}$$

where n is a dimensionless model parameter and $\gamma_{c,\infty}$ is the ratio of specific heats in the ideal-gas limit at the critical temperature.

B.2.1 Calculation of density from the Peng-Robinson model

Eq. (B.42) is explicit in p but implicit in T and v (or ρ). Define a compressibility factor Z as

$$Z = \frac{pv}{RT} \tag{B.50}$$

An equivalent expression of Eq. (B.42) is formulated in terms of a cubic equation with respect to Z instead of v [26].

$$Z^3 - (1-B)Z^2 + (A - 2B - 3B^2)Z + B(B^2 + B - A) = 0 \tag{B.51}$$

where A and B are temporally defined for convenience as

$$A = \frac{\alpha a p}{R^2 T^2} \qquad \text{and} \qquad B = \frac{bp}{RT}$$

Eq. (B.51) has the form

$$Z^3 + a_2 Z^2 + a_1 Z + a_0 = 0$$

Transform Eq. (B.51) to a depressed form by a change of variables, $Z = y - a_2/3$,

$$y^3 + b_1 y + b_0 = 0 \tag{B.52}$$

where

$$b_1 = a_1 - \frac{1}{3}a_2^2 \qquad b_0 = \frac{2}{27}a_2^3 - \frac{1}{3}a_2 a_1 + a_0$$

The discriminant of Eq. (B.52), Δ_y, is given as

$$\Delta_y = \frac{b_0^2}{4} + \frac{b_1^3}{27}$$

For $\Delta_y > 0$, Eq. (B.52) has one real root and two complex conjugate roots, and the valid solution is the real root.

$$y = \left(-\frac{b_0}{2} + \sqrt{\Delta_y}\right)^{1/3} + \left(-\frac{b_0}{2} - \sqrt{\Delta_y}\right)^{1/3} \tag{B.53}$$

For $\Delta_y < 0$, Eq. (B.52) has three distinct real roots,

$$\begin{cases} y_1 = r\cos(\phi) \\ y_2 = r\cos(\phi + 2\pi/3) \\ y_3 = r\cos(\phi - 2\pi/3) \end{cases} \tag{B.54}$$

where

$$r = 2\sqrt{-b_1/3} \qquad \text{and} \qquad \phi = \frac{1}{3}\arccos\left(\frac{-b_0/2}{\sqrt{-b_1^3/27}}\right)$$

When multiple real roots are present, the solution is the positive root that corresponds to the lowest specific Gibbs free energy [26]. The specific Gibbs free energy can be formally calculated by integrating along an isothermal compression / expansion process.

$$\Delta g = g(T, v) - g(T, v_{\text{ref}}) = \int_{v_{\text{ref}}}^{v} \left(\frac{\partial g}{\partial v}\right)_T dv \tag{B.55}$$

For the Peng-Robinson EOS model, and according to the derivation in Eq. (B.41), the specific Gibbs free energy can be calculated as

$$\Delta g = \int_{v_{\text{ref}}}^{v} \left\{ \frac{-RTv}{(v-b)^2} + \frac{2Bv(v+b)}{\left(v^2+2vb-b^2\right)^2} \right\} dv \tag{B.56}$$

Since the objective is to select a physically valid root for the specific volume, v, the common constant terms in the evaluations of Δg for different values of v can be neglected. Therefore, the calculation can be simplified to

$$\Delta g = \Delta g_0 + \frac{RTb}{v-b} - \frac{a\alpha v}{v^2+2vb-b^2} - RT\ln(v/b-1) + \frac{a\alpha}{2\sqrt{2}b}\ln\left[\frac{v-(\sqrt{2}-1)b}{v+(\sqrt{2}+1)b}\right] \tag{B.57}$$

where Δg_0 contains all the common constant terms that are not relavant to the calculation of the specific Gibbs free energy to select the root of v, and $\alpha = \alpha(T/T_c)$ is implied as defined based on the Peng-Robinson EOS in Eq. (B.45).

B.2.2 Calculation of temperature from the Peng-Robinson model

The Peng-Robinson EOS, Eq. (B.42), is a quadratic equation for $\sqrt{T_r}$, which can be written as

$$\left(A - B\kappa^2\right) T_r + 2B\kappa(\kappa+1)\sqrt{T_r} - B(\kappa+1)^2 - p = 0 \tag{B.58}$$

where A and B here are temporally defined as

$$A = \frac{RT_c}{v-b} \qquad \text{and} \qquad B = \frac{a}{v^2+2vb-b^2}$$

Therefore, the temperature can be calculated as

$$T = T_c\left[\frac{B\kappa(\kappa+1) + \sqrt{AB(\kappa+1)^2 + (A-B\kappa^2)p}}{(A-B\kappa^2)}\right]^2 \tag{B.59}$$

B.2.3 Calculations of internal energy, specific heats, and other relations

The calculation of the internal energy is based on Eq. (B.17), where $v_{\text{ref}} \to \infty$ and $T_{\text{ref}} = T_c$. The calculation of $c_v(T, v_{\text{ref}})$ is given in Eq. (B.49). Combined with the Peng-Robinson p-v-T relation, the specific internal energy can be calculated as

$$e(T_r, v) = \frac{RT_c(T_r^{n+1} - 1)}{(\gamma_{c,\infty} - 1)(n+1)} + \frac{a}{2\sqrt{2}b}(\kappa + 1)\left(\kappa - \kappa\sqrt{T_r} + 1\right)\ln\left(\frac{v + (1 - \sqrt{2})b}{v + (1 + \sqrt{2})b}\right) \tag{B.60}$$

where n is introduced in Eq. (B.49) for the calculation of the temperature dependent specific heat in the ideal-gas limit. The specific heat at constant volume in the dense-gas regime is calculated based on its definition given in Eq. (B.3).

$$c_v(T_r, v) = c_v(T_r, \infty) - \left(\frac{a\kappa(\kappa + 1)}{4\sqrt{2}bT_c\sqrt{T_r}}\right)\ln\left[\frac{v - (\sqrt{2} - 1)b}{v + (\sqrt{2} + 1)b}\right] \tag{B.61}$$

The specific heat at constant pressure, c_p, can be calculated using Eq. (B.21) combining with the calculation of c_v in Eq. (B.61), where the derivatives based on the p-v-T relation, $(\partial p/\partial T)_v$ and $(\partial p/\partial v)_T$, are given in Eq. (B.47) and Eq. (B.48) respectively. The energy of imperfection, $(\partial e/\partial v)_T$, is calculated as

$$\left(\frac{\partial e}{\partial v}\right)_T = \frac{a(\kappa + 1)(\kappa - \kappa\sqrt{T_r} + 1)}{v^2 + 2vb - b^2} \tag{B.62}$$

B.3 Calculations of transport properties

The calculations of the transport properties of a fluid considering the effects of temperature and pressure are calculated using the transport models proposed by Chung et al. (1988) [25]. The detailed calculations documented in this section also largely reference the work published in Ref. [125]. The original Chung et al. (1988) model involves dimensional model parameters so that specific physical units are required with the given formulas during calculation. In addition to the model that is formulated in a dimensional form, the derivation provided in this section also contains the nondimensional form of the transport models converted from Chung et al. (1988) [25] as proposed in Ch. 3.

Given a Lennard-Jones potential curve, a dimensionless temperature, T^*, is defined as

$$T^* = kT/\epsilon$$

where k is the Boltzmann constant, and ϵ is the depth of the potential well. It is reported by Chung et al. that

$$kT_c/\epsilon = 1.2593 \tag{B.63}$$

Therefore, T^* can be calculated using the reduced temperature T_r.

$$T^* = 1.2593 T_r \tag{B.64}$$

The collision integral from a gas-dynamics point of view, Ω_v, is calculated based on an empirical relation proposed by Neufeld et al. [108]. For $0.3 \leq T^* \leq 100$, Ω_v can be calculated as

$$\Omega_v(T^*) = A{T^*}^{-B} + C\exp(-DT^*) + E\exp(-FT^*) \tag{B.65}$$

where A, B, C, D, E, and F are constant dimensionless model coefficients whose values are provided in Tab. B.1. The scaled electric dipole moment, μ_r, is calculated as

$$\mu_r = \frac{131.3\mu[\text{debyes}]}{\sqrt{V_c[\text{cm}^3/\text{mol}] \times T_c[\text{K}]}} \tag{B.66}$$

where μ is the dimensional electric dipole moment given in units of debyes, V_c is the molar volume given in units of cm^3/mol, and T_c is the critical temperature given in units of K.

A	B	C	D	E	F
1.16145	0.14874	0.52487	0.77320	2.16178	2.43787

Table B.1: Coefficients for the calculation of Ω_v in Eq. (B.65).

B.3.1 Calculation of dynamic viscosity

According to the method of Chung et al. (1988), the dynamic viscosity of a pure gas, η, can be calculated as

$$\eta = \eta_c \eta^* / \eta_c^* \tag{B.67}$$

where η_c is the dynamic viscosity at the critical condition, $\eta_c = \eta(T_c, p_c)$. η^* is a function of temperature and density, and η_c^* is η^* at the critical condition. η^* is calculated as

$$\eta^* = \frac{\sqrt{T^*}}{\Omega_v} F_c \left(\frac{1}{G_2} + E_6 y \right) + \eta^{**} \tag{B.68}$$

where the variables, y, F_c, G_2, and η^{**} are calculated following the equations below.

$$y = \rho v_c / 6 \tag{B.69}$$

$$F_c = 1 - 0.2756\omega + 0.059035\mu_r^4 + \kappa_p \tag{B.70}$$

$$G_1 = (1 - 0.5y)/(1 - y)^3 \tag{B.71}$$

$$G_2 = \frac{E_1\left(1 - e^{-E_4 y}\right)/y + E_2 G_1 e^{E_5 y} + E_3 G_1}{E_1 E_4 + E_2 + E_3} \tag{B.72}$$

$$\eta^{**} = E_7 G_2 y^2 \exp\left(E_8 + E_9 {T^*}^{-1} + E_{10} {T^*}^{-2}\right) \tag{B.73}$$

In the equations from Eq. (B.68) to Eq. (B.73), y is a dimensionless density, G_1 and G_2 are functions of y, η^{**} is a function of T^* and y, and F_c accounts for the molecular shapes and polarities of dilute gases. Ω_v is calculated using Eq. (B.65). v_c is the specific volume at the critical condition; ω is the acentric factor; μ_r is the scaled electric dipole moment (cf. Eq. (B.66)); and κ_p is a special correction for highly polar substances such as alcohols and acids. The dimensionless coefficients E_i are calculated as

$$E_i = a_i + b_i\omega + c_i\mu_r^4 + d_i\kappa_p \tag{B.74}$$

where the coefficients a_i, b_i, c_i, and d_i are listed in Tab. B.2. Note that all E_i's only depend on the molecular structure. According to the calculation process, at the critical point $T^* = 1.2593$ and $y = 1/6$, which can be used to calculate η_c^*. The input arguments for the solver initialization are μ_r, κ_p, ω, p_c, T_c, and η_c. Then given p and T with the procedure introduced in this sub-section, η can be uniquely calculated.

i	a_i	b_i	c_i	d_i
1	6.3240E+00	5.04120E+01	-5.1680E+01	1.189E+03
2	1.2100E-03	-1.15400E-03	-6.2570E-03	3.728E-02
3	5.2830E+00	2.54209E+02	-1.6848E+02	3.898E+03
4	6.6230E+00	3.80960E+01	-8.4640E+00	3.142E+01
5	1.9745E+01	7.63000E+00	-1.4354E+01	3.153E+01
6	-1.9000E+00	-1.25370E+01	4.9850E+00	-1.815E+01
7	2.4275E+01	3.45000E+00	-1.1291E+01	6.935E+01
8	7.9720E-01	1.11700E+00	1.2350E-02	-4.117E+00
9	-2.3820E-01	6.77000E-02	-8.1630E-01	4.025E+00
10	6.8630E-02	3.47900E-01	5.9260E-01	-7.270E-01

Table B.2: Coefficients for the calculation of E_i for dynamic viscosity calculation in Eq. (B.74).

B.3.2 Calculation of thermal conductivity

According to the method of Chung et al. [25], the thermal conductivity of a pure gas, λ, can be calculated as

$$\lambda = R\eta_c\left\{3.75256\eta_r^{\ominus}\Psi\left(\frac{1}{G_2} + E_6 y\right) + q^* E_7 G_2 y^2\sqrt{T_r}\right\} \tag{B.75}$$

where the superscript "$\ominus$" denotes the quantity that is evaluated at a low pressure, i.e., $\eta^{\ominus} = \eta(T, p^{\ominus})$ and $\eta_r^{\ominus} = \eta^{\ominus}/\eta_c$ for $p^{\ominus}/p_c \ll 1$. The definitions of y and G_2 in Eq. (B.75) are the same as those for the calculation of dynamic viscosity associated with G_1, E_i (cf. Eq. (B.69), Eq. (B.71), Eq. (B.72),

and Eq. (B.74)), whereas the coefficient matrix used to calculate E_i is different from those used for the calculation of viscosity. The coefficients a_i, b_i, c_i, and d_i for the calculation of thermal conductivity are listed in Tab. B.3.

i	a_i	b_i	c_i	d_i
1	2.4166E+00	7.4824E-01	-9.1858E-01	1.2172E+02
2	-5.0924E-01	-1.5094E+00	-4.9991E+01	6.9983E+01
3	6.6107E+00	5.6207E+00	6.4760E+01	2.7039E+01
4	1.4543E+01	-8.9139E+00	-5.6379E+00	7.4344E+01
5	7.9274E-01	8.2019E-01	-6.9369E-01	6.3173E+00
6	-5.8634E+00	1.2801E+01	9.5893E+00	-6.5529E+01
7	9.1089E+01	1.2811E+02	-5.4217E+01	5.2381E+02

Table B.3: Coefficients for the calculation of E_i for the thermal conductivity calculation in Eq. (B.74).

Consistent with the method of Chung et al. the low-pressure viscosity can be calculated as

$$\eta^{\ominus} = \eta_c^{\ominus} \frac{\Omega_{vc}}{\Omega_v} \sqrt{T_r} \tag{B.76}$$

where $\eta_c^{\ominus}$ denotes the dynamic viscosity at the critical temperature but at a low-pressure, i.e., $\eta_c^{\ominus} = \eta(T_c, p^{\ominus})$, and Ω_{vc} is the collision integral at the critical condition calculated from Eq. (B.65) for $T^* = 1.2593$.

The function Ψ in Eq. (B.75) is calculated as

$$\Psi(T_r, p_r) = 1 + \alpha' \frac{0.215 + 0.28288\alpha' - 1.061\beta' + 0.26665z}{0.6366 + \beta' z + 1.061\alpha'\beta'} \tag{B.77}$$

where the dimensionless factor α' is calculated as

$$\alpha' = \frac{c_v}{R} - \frac{3}{2} \tag{B.78}$$

where c_v and R are the specific heat at constant volume and the specific gas constant. $c_v(T, v)$ can be calculated from the thermodynamic equation of state. β' is an empirical correlation. For nonpolar molecules, β' is calculated as

$$\beta' = 0.7862 - 0.7109\omega + 1.3168\omega^2 \tag{B.79}$$

while for polar gas molecules, β' is species dependent. For a type of polar gas molecule whose β' is not available, the default value to use is $\beta' = 0.758$. z characterizes the number of collisions required to interchange between quantum of rotational energy and translational energy, which is calculated as

$$z = 2.0 + 10.5T_r^2 \tag{B.80}$$

In Eq. (B.75), the dimensionless factor q^* is defined as

$$q^* = q/(R\eta_c) \tag{B.81}$$

where the calculation of the dimensional quantity, q, is given as an empirical correlation in dimensional form [125].

$$q[\mathrm{W/(m \cdot K)}] = 3.586 \times 10^{-3} \frac{\sqrt{T_c[\mathrm{K}] \div M[\mathrm{kg/mol}]}}{(V_c[\mathrm{cm^3/mol}])^{2/3}} \tag{B.82}$$

where M is the molar mass of the molecules, and V_c is molar volume of the fluid at the critical condition. in Eq. (B.82), the critical temperature T_c is specified in K, the molar mass, M, is specified in kg/mol, the molar volume, V_c, is specified in $\mathrm{cm^3/mol}$, and the result, q, is obtained in the unit of $\mathrm{W/(m \cdot K)}$.

Appendix C

Formulation of the Taylor-Green Vortex Used in the Performance Test of the Parallel Linear Solver

C.0.1 Problem description

The Taylor-Green vortex problem is a well-established fluid mechanics problem defined on a 3D periodic domain, $\boldsymbol{x} \in [0, 2\pi l) \times [0, 2\pi l) \times [0, 2\pi l)$, where l is a characteristic length. The tests used in this work were conducted by solving the compressible Navier-Stokes equations.

$$\frac{\partial \boldsymbol{\phi}}{\partial t} + \nabla \cdot \boldsymbol{F} + \nabla \cdot \boldsymbol{G} = 0 \tag{C.1}$$

where $\boldsymbol{\phi}$ is the set of the conservative variables; $\boldsymbol{F}$ is the set of inviscid fluxes; and $\boldsymbol{G}$ is the set of diffusive fluxes. They are defined as

$$\boldsymbol{\phi} = \begin{bmatrix} \rho \\ \rho \boldsymbol{u} \\ \rho(e + \boldsymbol{u} \cdot \boldsymbol{u}/2) \end{bmatrix} \tag{C.2}$$

$$\boldsymbol{F} = \begin{bmatrix} \rho \boldsymbol{u} \\ \rho \left(\boldsymbol{u} \otimes \boldsymbol{u} \right) + P \boldsymbol{I} \\ \boldsymbol{u} \left(\rho e + \rho \boldsymbol{u} \cdot \boldsymbol{u}/2 + P \right) \end{bmatrix} \tag{C.3}$$

$$\boldsymbol{G} = \begin{bmatrix} 0 \\ -\boldsymbol{\sigma} \\ \boldsymbol{q} - \boldsymbol{u} \cdot \boldsymbol{\sigma} \end{bmatrix} \tag{C.4}$$

where ρ is the density; $\boldsymbol{u} = [u, v, w]^T$ is the velocity vector; P is the pressure; $\boldsymbol{I}$ is the identity tensor; e is the specific internal energy, $\boldsymbol{\sigma}$ is the viscous stress tensor; and $\boldsymbol{q}$ is the heat flux. The fluid is treated as an ideal gas with the following equation of state.

$$P = \rho R T \tag{C.5}$$

where R is the specific gas constant; and T is the temperature. Accordingly, the internal energy is

$$e = \frac{RT}{\gamma - 1} \tag{C.6}$$

where γ is the ratio of specific heat. The viscous stress tensor is modeled as

$$\boldsymbol{\sigma} = \mu \left[(\nabla \boldsymbol{u}) + (\nabla \boldsymbol{u})^T \right] + \left(\beta - \frac{2}{3}\mu \right) (\nabla \cdot \boldsymbol{u}) \, \boldsymbol{I} \tag{C.7}$$

where μ is the dynamic shear viscosity; and β is the bulk viscosity. For the simulations used in this work, $\beta = 0$, and μ is set to be a constant determined from the Reynolds number, Re.

$$\mathrm{Re} = \frac{\rho_0 V l}{\mu} \tag{C.8}$$

where ρ_0 is the mean density as well as the initial density of the fluid, and V is a characteristic velocity. The heat flux $\boldsymbol{q}$ is computed based on Fourier's law

$$\boldsymbol{q} = -\kappa \nabla T \tag{C.9}$$

where κ is the heat conductivity controlled by the Prandtl number, Pr, defined as the following.

$$\mathrm{Pr} = \frac{\gamma R \mu}{(\gamma - 1)\kappa} \tag{C.10}$$

The initial velocity, $[u_0, v_0, w_0]^T$, and pressure, P_0, fields are set as [19]

$$u_0 = V \sin(x/l) \cos(y/l) \cos(z/l) \tag{C.11}$$

$$v_0 = -V \cos(x/l) \sin(y/l) \cos(z/l) \tag{C.12}$$

$$w_0 = 0 \tag{C.13}$$

$$P_0 = P_{\mathrm{ref}} + \frac{\rho_0 V^2}{16} \left[\cos(2x/l) + \cos(2y/l) \right] \left[\cos(2z/l) + 2 \right] \tag{C.14}$$

where $l = 1$, $V = 1$, $\rho_0 = 1$, and $P_{\mathrm{ref}} = 100$. The Reynolds number and Prandtl number are set to $\mathrm{Re} = 1600$ and $\mathrm{Pr} = 0.7$, respectively. The specific gas constant is set to unity, and the specific heat ratio $\gamma = 5/3$, so that the Mach number, Ma, consistent with the initial conditions, is approximately

0.08, calculated based on the following based on its definition:

$$\mathrm{Ma} = \frac{V}{\sqrt{\gamma P_{\mathrm{ref}}/\rho_0}} \tag{C.15}$$

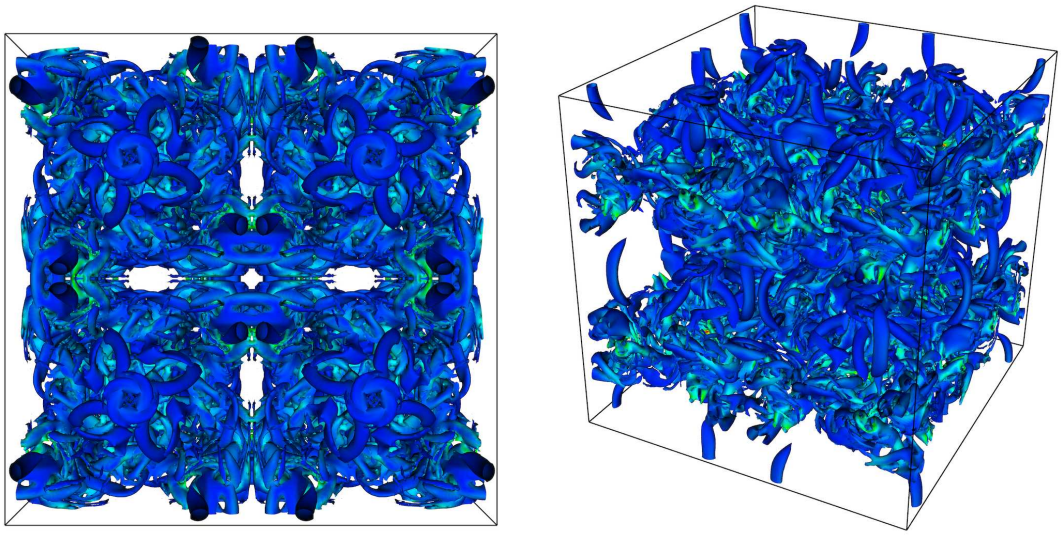

(a) (b)

Figure C.1: Q-criterion iso-surface colored by enstrophy in the Taylor-Green vortex problem using 256^3 points.

C.0.2 Numerical schemes

The problem is numerically computed on a 3D Cartesian uniform mesh using the staggered sixth order compact finite difference schemes and the sixth order compact interpolators [89, 107], as shown in the following two equations.

$$\frac{9}{62}f'_{i-1} + f'_i + \frac{9}{62}f'_{i+1} = \frac{63}{62}\left(\frac{f_{i+1/2} - f_{i-1/2}}{\Delta}\right) + \frac{17}{62}\left(\frac{f_{i+3/2} - f_{i-3/2}}{3\Delta}\right) \tag{C.16}$$

$$\frac{3}{10}f^I_{i-1} + f^I_i + \frac{3}{10}f^I_{i+1} = \frac{3}{2}\left(\frac{f_{i+1/2} + f_{i-1/2}}{2}\right) + \frac{1}{10}\left(\frac{f_{i+3/2} + f_{i-3/2}}{2}\right) \tag{C.17}$$

where f, f', and f^I represent the original field, first derivative, and interpolated field, respectively; the subscripts indicate the grid indices in the corresponding direction; and Δ is the grid spacing in the corresponding direction. The primitive variables are all stored at the collocated grid points, and all the fluxes in $\boldsymbol{F}$ and $\boldsymbol{G}$ are constructed at the edge-staggered locations in the corresponding directions. The time advancement uses the standard fourth order Runge-Kutta method.

Bibliography

[1] Yoshiaki Abe, Taku Nonomura, Nobuyuki Iizuka, and Kozo Fujii. Geometric interpretations and spatial symmetry property of metrics in the conservative form for high-order finite-difference schemes on moving and deforming grids. *Journal of Computational Physics*, 260:163–203, 2014.

[2] Yoonhan Ahn, Seong Jun Bae, Minseok Kim, Seong Kuk Cho, Seungjoon Baik, Jeong Ik Lee, and Jae Eun Cha. Review of supercritical CO_2 power cycle technology and current status of research and development. *Nuclear Engineering and Technology*, 47(6):647–661, 2015.

[3] Hussein Aluie. Scale decomposition in compressible turbulence. *Physica D: Nonlinear Phenomena*, 247(1):54–65, 2013.

[4] Ponnampalam Balakumar, Prahladh S Iyer, and Mujeeb R Malik. Turbulence simulations of transonic flows over an NACA-0012 airfoil. In *AIAA SciTech 2023 Forum*, AIAA 2023-0254, 2023.

[5] B Benoit and I Legrain. Buffeting prediction for transport aircraft applications based on unsteady pressure measurements. In *5th Applied Aerodynamics Conference*, AIAA 1987-2356, 1987.

[6] Iván Bermejo-Moreno, Johan Larsson, and Sanjiva K Lele. LES of canonical shock-turbulence interaction. *Annual Research Briefs*, pages 209–222, 2010.

[7] Jean-Pierre Bertoglio, Françoise Bataille, and Jean-Denis Marion. Two-point closures for weakly compressible turbulence. *Physics of Fluids*, 13(1):290–310, 2001.

[8] GA Blaisdell, ET Spyropoulos, and JH Qin. The effect of the formulation of nonlinear terms on aliasing errors in spectral methods. *Applied Numerical Mathematics*, 21(3):207–219, 1996.

[9] Gregory Allan Blaisdell. *Numerical Simulation of Compressible Homogeneous Turbulence*. PhD thesis, Stanford University, 1991.

[10] Daniel J Bodony and Sanjiva K Lele. On using large-eddy simulation for the prediction of noise from cold and heated turbulent jets. *Physics of Fluids*, 17(8):085103, 2005.

[11] Rafael Borges, Monique Carmona, Bruno Costa, and Wai Sun Don. An improved weighted essentially non-oscillatory scheme for hyperbolic conservation laws. *Journal of Computational Physics*, 227(6):3191–3211, 2008.

[12] Sanjeeb T Bose, Parviz Moin, and Donghyun You. Grid-independent large-eddy simulation using explicit filtering. *Physics of Fluids*, 22(10):105103, 2010.

[13] Joseph Boussinesq. Essai sur la théorie des eaux courantes. *Mémoires présentés par divers savants à l'Académie des Sciences*, pages 1–680, 1877.

[14] Percy Williams Bridgman. *A Condensed Collection of Thermodynamic Formulas*. Harvard University Press, 1925.

[15] V Brion, J Dandois, J-C Abart, and P Paillart. Experimental analysis of the shock dynamics on a transonic laminar airfoil. *Progress in Flight Physics–Volume 9*, 9:365–386, 2017.

[16] Jens Brouwer, Julius Reiss, and Jörn Sesterhenn. Conservative time integrators of arbitrary order for skew-symmetric finite-difference discretizations of compressible flow. *Computers & Fluids*, 100:1–12, 2014.

[17] Vincent Brunet. Computational study of buffet phenomenon with unsteady rans equations. In *21st AIAA Applied Aerodynamics Conference*, AIAA 2003-3679, 2003.

[18] Gerd Brunner. Applications of supercritical fluids. *Annual Review of Chemical and Biomolecular Engineering*, 1:321–342, 2010.

[19] Jonathan R Bull and Antony Jameson. Simulation of the Taylor–Green vortex using high-order flux reconstruction schemes. *AIAA Journal*, 53(9):2750–2761, 2015.

[20] Oscar Buneman. A compact non-iterative Poisson solver. *SUIPR report*, 294, 1969.

[21] Billy L Buzbee, Gene H Golub, and Claire W Nielson. On direct methods for solving Poisson's equations. *SIAM Journal on Numerical Analysis*, 7(4):627–656, 1970.

[22] Alessandro Ceci and Sergio Pirozzoli. Natural grid stretching for dns of compressible wall-bounded flows. *Journal of Computational Physics: X*, 17:100128, 2023.

[23] Boa-Teh Chu. On the energy transfer to small disturbances in fluid flow (part i). *Acta Mechanica*, 1(3):215–234, 1965.

[24] Boa-Teh Chu and Leslie SG Kovásznay. Non-linear interactions in a viscous heat-conducting compressible gas. *Journal of Fluid Mechanics*, 3(5):494–514, 1958.

[25] Ting Horng Chung, Mohammad Ajlan, Lloyd L Lee, and Kenneth E Starling. Generalized multiparameter correlation for nonpolar and polar fluid transport properties. *Industrial & Engineering Chemistry Research*, 27(4):671–679, 1988.

[26] L. Coleman. *Distillation Science*. LibreTexts, 2022.

[27] Tim Colonius and Sanjiva K Lele. Computational aeroacoustics: progress on nonlinear problems of sound generation. *Progress in Aerospace Sciences*, 40(6):345–416, 2004.

[28] Tim Colonius, Sanjiva K Lele, and Parviz Moin. Sound generation in a mixing layer. *Journal of Fluid Mechanics*, 330:375–409, 1997.

[29] Andrew W Cook. Artificial fluid properties for large-eddy simulation of compressible turbulent mixing. *Physics of Fluids*, 19(5):055103, 2007.

[30] Andrew W Cook and William H Cabot. A high-wavenumber viscosity for high-resolution numerical methods. *Journal of Computational Physics*, 195(2):594–601, 2004.

[31] Richard Courant, Kurt Friedrichs, and Hans Lewy. Über die partiellen differenzengleichungen der mathematischen physik. *Mathematische Annalen*, 100(1):32–74, 1928.

[32] JD Crouch, A Garbaruk, and D Magidov. Predicting the onset of flow unsteadiness based on global instability. *Journal of Computational Physics*, 224(2):924–940, 2007.

[33] Julien Dandois, Ivan Mary, and Vincent Brion. Large-eddy simulation of laminar transonic buffet. *Journal of Fluid Mechanics*, 850:156–178, 2018.

[34] Sébastien Deck. Numerical simulation of transonic buffet over a supercritical airfoil. *AIAA Journal*, 43(7):1556–1566, 2005.

[35] Vedang M Deshpande, Raktim Bhattacharya, and Diego A Donzis. A unified framework to generate optimized compact finite difference schemes. *Journal of Computational Physics*, 432:110157, 2021.

[36] Alexander Doehring, T Kaller, SJ Schmidt, and NA Adams. Large-eddy simulation of turbulent channel flow at transcritical states. *International Journal of Heat and Fluid Flow*, 89:108781, 2021.

[37] Diego A Donzis and Shriram Jagannathan. Fluctuations of thermodynamic variables in stationary compressible turbulence. *Journal of Fluid Mechanics*, 733:221–244, 2013.

[38] Diego A Donzis and John Panickacheril John. Universality and scaling in homogeneous compressible turbulence. *Physical Review Fluids*, 5(8):084609, 2020.

[39] F Ducros, F Laporte, Th Soulères, V Guinot, Ph Moinat, and B Caruelle. High-order fluxes for conservative skew-symmetric-like schemes in structured meshes: application to compressible flows. *Journal of Computational Physics*, 161(1):114–139, 2000.

[40] H. Carter Edwards, Christian R. Trott, and Daniel Sunderland. Kokkos: Enabling manycore performance portability through polymorphic memory access patterns. *Journal of Parallel and Distributed Computing*, 74(12):3202 – 3216, 2014. Domain-Specific Languages and High-Level Frameworks for High-Performance Computing.

[41] Albert Einstein. Die grundlage der allgemeinen relativitätstheorie. In *Das Relativitätsprinzip*, pages 81–124. Springer, 1923.

[42] Vinayak Eswaran and Stephen B Pope. An examination of forcing in direct numerical simulations of turbulence. *Computers & Fluids*, 16(3):257–278, 1988.

[43] Gerald Farin. *Curves and Surfaces for Computer-Aided Geometric Design: a Practical Guide*. Elsevier, 2014.

[44] Gauthier Fauchet and Jean-Pierre Bertoglio. A two-point closure for compressible turbulence. *Comptes Rendus de l'Académie des Sciences - Series IIB - Mechanics-Physics-Astronomy*, 327(7):665–671, 1999.

[45] AJ Favre. *The Equations of Compressible Turbulent Gases*. Defense Technical Information Center, 1965.

[46] Alexandre Favre. Turbulence: Space-time statistical properties and behavior in supersonic flows. *Physics of Fluids*, 26(10):2851–2863, 1983.

[47] H Foysi, S Sarkar, and R Friedrich. Compressibility effects and turbulence scalings in supersonic channel flow. *Journal of Fluid Mechanics*, 509:207–216, 2004.

[48] Lin Fu, Xiangyu Hu, and Nikolaus A Adams. A targeted ENO scheme as implicit model for turbulent and genuine subgrid scales. *Communications in Computational Physics*, 26(2):311–345, 2019.

[49] Lin Fu, Xiangyu Y Hu, and Nikolaus A Adams. A family of high-order targeted ENO schemes for compressible-fluid simulations. *Journal of Computational Physics*, 305:333–359, 2016.

[50] Yuma Fukushima and Soshi Kawai. Wall-modeled large-eddy simulation of transonic airfoil buffet at high reynolds number. *AIAA Journal*, 56(6):2372–2388, 2018.

[51] Walter Gander and Gene H Golub. Cyclic reduction—history and applications. *Scientific Computing (Hong Kong, 1997)*, pages 73–85, 1997.

[52] Eric Garnier, Nikolaus Adams, and Pierre Sagaut. *Large Eddy Simulation for Compressible Flows*. Springer Science & Business Media, 2009.

[53] Niranjan S Ghaisas, Akshay Subramaniam, and Sanjiva K Lele. A unified high-order Eulerian method for continuum simulations of fluid flow and of elastic–plastic deformations in solids. *Journal of Computational Physics*, 371:452–482, 2018.

[54] Aditya S Ghate and Sanjiva K Lele. Subfilter-scale enrichment of planetary boundary layer large eddy simulation using discrete Fourier–Gabor modes. *Journal of Fluid Mechanics*, 819:494–539, 2017.

[55] Nicholas F Giannelis, Gareth A Vio, and Oleg Levinski. A review of recent developments in the understanding of transonic shock buffet. *Progress in Aerospace Sciences*, 92:39–84, 2017.

[56] Konrad Goc, Rahul Agrawal, Parviz Moin, and Sanjeeb Bose. Studies of transonic aircraft flows and prediction of initial buffet onset using large-eddy simulations. In *AIAA Aviation 2023 Forum*, AIAA 2023-4338, 2023.

[57] David Gottlieb and Steven A Orszag. *Numerical Analysis of Spectral Methods: Theory and Applications*. SIAM, 1977.

[58] Rick E Graves and Brian M Argrow. Bulk viscosity: past to present. *Journal of Thermophysics and Heat Transfer*, 13(3):337–342, 1999.

[59] Fernando Grossi, Marianna Braza, and Yannick Hoarau. Prediction of transonic buffet by delayed detached-eddy simulation. *AIAA Journal*, 52(10):2300–2312, 2014.

[60] Ohad Gur, Joseph A Schetz, and William H Mason. Aerodynamic considerations in the design of truss-braced-wing aircraft. *Journal of Aircraft*, 48(3):919–939, 2011.

[61] Francis H Harlow and J Eddie Welch. Numerical calculation of time-dependent viscous incompressible flow of fluid with free surface. *The physics of fluids*, 8(12):2182–2189, 1965.

[62] Jean-Pierre Hickey, Peter C Ma, Matthias Ihme, and Siddharth S Thakur. Large eddy simulation of shear coaxial rocket injector: Real fluid effects. In *49th AIAA/ASME/SAE/ASEE Joint PropulsionConference*, page 4071. AIAA Aerospace Research Center, 2013.

[63] Steven P Hirshman, Kalyan S Perumalla, Vickie E Lynch, and Raul Sanchez. BCYCLIC: A parallel block tridiagonal matrix cyclic solver. *Journal of Computational Physics*, 229(18):6392–6404, 2010.

[64] Roger W Hockney. A fast direct solution of Poisson's equation using Fourier analysis. *Journal of the ACM (JACM)*, 12(1):95–113, 1965.

[65] RW Hockney and CR Jesshope. Parallel computers: Architecture. *Programming and Algorithms, Adam Hilger, Bristol*, 1981.

[66] Gerhard A Holzapfel. Nonlinear solid mechanics: a continuum approach for engineering science. *Meccanica*, 37(4):489–490, 2002.

[67] Julian CR Hunt, Alan A Wray, and Parviz Moin. Eddies, streams, and convergence zones in turbulent flows. In *Center for Turbulence Research Proceedings of the Summer Program*, 1988.

[68] M Yousuff Hussaini and Thomas A Zang. Spectral methods in fluid dynamics. *Annual Review of Fluid Mechanics*, 19(1):339–367, 1987.

[69] Michael Iovnovich and Daniella E Raveh. Reynolds-averaged Navier-Stokes study of the shock-buffet instability mechanism. *AIAA Journal*, 50(4):880–890, 2012.

[70] Yuta Iwatani, Hiroyuki Asada, Chi-An Yeh, Kunihiko Taira, and Soshi Kawai. Identifying the self-sustaining mechanisms of transonic airfoil buffet with resolvent analysis. *AIAA Journal*, pages 1–12, 2023.

[71] Laurent Jacquin, Pascal Molton, Sebastien Deck, Bernard Maury, and Didier Soulevant. Experimental study of shock oscillation over a transonic supercritical profile. *AIAA Journal*, 47(9):1985–1994, 2009.

[72] Shriram Jagannathan and Diego A Donzis. Reynolds and Mach number scaling in solenoidally-forced compressible turbulence using high-resolution direct numerical simulations. *Journal of Fluid Mechanics*, 789:669–707, 2016.

[73] Guang-Shan Jiang and Chi-Wang Shu. Efficient implementation of weighted ENO schemes. *Journal of Computational Physics*, 126(1):202–228, 1996.

[74] Eric Johnsen, Johan Larsson, Ankit V Bhagatwala, William H Cabot, Parviz Moin, Britton J Olson, Pradeep S Rawat, Santhosh K Shankar, Björn Sjögreen, Helen C Yee, et al. Assessment of high-resolution methods for numerical simulations of compressible turbulence with shock waves. *Journal of Computational Physics*, 229(4):1213–1237, 2010.

[75] Soshi Kawai and Sanjiva K Lele. Localized artificial diffusivity scheme for discontinuity capturing on curvilinear meshes. *Journal of Computational Physics*, 227(22):9498–9526, 2008.

[76] Soshi Kawai, Santhosh K Shankar, and Sanjiva K Lele. Assessment of localized artificial diffusivity scheme for large-eddy simulation of compressible turbulent flows. *Journal of Computational Physics*, 229(5):1739–1762, 2010.

[77] Soshi Kawai, Hiroshi Terashima, and Hideyo Negishi. A robust and accurate numerical method for transcritical turbulent flows at supercritical pressure with an arbitrary equation of state. *Journal of Computational Physics*, 300:116–135, 2015.

[78] Shigeo Kida and Steven A Orszag. Energy and spectral dynamics in forced compressible turbulence. *Journal of Scientific Computing*, 5(2):85–125, 1990.

[79] Željko Knez, Elena Markočič, Maja Leitgeb, Mateja Primožič, M Knez Hrnčič, and Mojca Škerget. Industrial applications of supercritical fluids: A review. *Energy*, 77:235–243, 2014.

[80] Andrey Nikolaevich Kolmogorov. The local structure of turbulence in incompressible viscous fluid for very large Reynolds numbers. *Cr Acad. Sci. URSS*, 30:301–305, 1941.

[81] Leslie SG Kovásznay. Turbulence in supersonic flow. *Journal of the Aeronautical Sciences*, 20(10):657–674, 1953.

[82] Robert H Kraichnan. The structure of isotropic turbulence at very high reynolds numbers. *Journal of Fluid Mechanics*, 5(4):497–543, 1959.

[83] AG Kravchenko and Parviz Moin. On the effect of numerical errors in large eddy simulations of turbulent flows. *Journal of Computational Physics*, 131(2):310–322, 1997.

[84] Arthur G Kravchenko and Parviz Moin. Numerical studies of flow over a circular cylinder at $\mathrm{Re_D}$= 3900. *Physics of fluids*, 12(2):403–417, 2000.

[85] Sylvain Laizet and Eric Lamballais. High-order compact schemes for incompressible flows: A simple and efficient method with quasi-spectral accuracy. *Journal of Computational Physics*, 228(16):5989–6015, 2009.

[86] BHK Lee. Oscillatory shock motion caused by transonic shock boundary-layer interaction. *AIAA Journal*, 28(5):942–944, 1990.

[87] BHK Lee. Self-sustained shock oscillations on airfoils at transonic speeds. *Progress in Aerospace Sciences*, 37(2):147–196, 2001.

[88] Sangsan Lee, Sanjiva K Lele, and Parviz Moin. Eddy shocklets in decaying compressible turbulence. *Physics of Fluids A: Fluid Dynamics*, 3(4):657–664, 1991.

[89] Sanjiva K Lele. Compact finite difference schemes with spectral-like resolution. *Journal of Computational Physics*, 103(1):16–42, 1992.

[90] Sanjiva K Lele. Compressibility effects on turbulence. *Annual Review of Fluid Mechanics*, 26(1):211–254, 1994.

[91] Peter J Linstrom and William G Mallard. The NIST Chemistry WebBook: A chemical data resource on the internet. *Journal of Chemical & Engineering Data*, 46(5):1059–1063, 2001.

[92] Richard Liska and Burton Wendroff. Comparison of several difference schemes on 1D and 2D test problems for the Euler equations. *SIAM Journal on Scientific Computing*, 25(3):995–1017, 2003.

[93] LM Lourenco and C Shin. Characteristics of the plate turbulent near wake of a circular cylinder. a particle image velocimetry study. *Unpublished, results taken from Beaudan and Moin*, 1994.

[94] Calvin Lui and Sanjiva Lele. Direct numerical simulation of spatially developing, compressible, turbulent mixing layers. In *39th Aerospace Sciences Meeting and Exhibit*, AIAA 2001-0291, 2001.

[95] John Leask Lumley. The structure of inhomogeneous turbulent flows. *Atmospheric turbulence and radio wave propagation*, pages 166–178, 1967.

[96] Ali Mani. Analysis and optimization of numerical sponge layers as a nonreflective boundary treatment. *Journal of Computational Physics*, 231(2):704–716, 2012.

[97] Ali Mani, Johan Larsson, and Parviz Moin. Suitability of artificial bulk viscosity for large-eddy simulation of turbulent flows with shocks. *Journal of Computational Physics*, 228(19):7368–7374, 2009.

[98] NN Mansour, P Moin, WC Reynolds, and JH Ferziger. Improved methods for large eddy simulations of turbulence. In *Turbulent Shear Flows I: Selected Papers from the First International Symposium on Turbulent Shear Flows, The Pennsylvania State University, University Park, Pennsylvania, USA, April 18–20, 1977*, pages 386–401. Springer, 1979.

[99] L Masini, S Timme, and AJ Peace. Analysis of a civil aircraft wing transonic shock buffet experiment. *Journal of Fluid Mechanics*, 884:A1, 2020.

[100] J.C. Maxwell. *Theory of Heat*. D. Appleton and Company, 1872.

[101] John B McDevitt and Arthur F Okuno. Static and dynamic pressure measurements on a NACA 0012 airfoil in the ames high reynolds number facility. Technical report, NASA, 1985.

[102] Davide Modesti and Sergio Pirozzoli. Reynolds and mach number effects in compressible turbulent channel flow. *International Journal of Heat and Fluid Flow*, 59:33–49, 2016.

[103] P Moin and R Verzicco. On the suitability of second-order accurate discretizations for turbulent flow simulations. *European Journal of Mechanics-B/Fluids*, 55:242–245, 2016.

[104] Parviz Moin, Kyle Squires, W Cabot, and Sangsan Lee. A dynamic subgrid-scale model for compressible turbulence and scalar transport. *Physics of Fluids A: Fluid Dynamics*, 3(11):2746–2757, 1991.

[105] VM Molochnikov, NI Mikheev, AN Mikheev, AA Paereliy, NS Dushin, and OA Dushina. Siv measurements of flow structure in the near wake of a circular cylinder at Re= 3900. *Fluid Dynamics Research*, 51(5):055505, 2019.

[106] VS Murthy and WC Rose. Detailed measurements on a circular cylinder in cross flow. *AIAA Journal*, 16(6):549–550, 1978.

[107] Santhanam Nagarajan, Sanjiva K Lele, and Joel H Ferziger. A robust high-order compact method for large eddy simulation. *Journal of Computational Physics*, 191(2):392–419, 2003.

[108] Philip D Neufeld, AR Janzen, and R_A Aziz. Empirical equations to calculate 16 of the transport collision integrals ω (l, s)* for the Lennard-Jones (12–6) potential. *The Journal of chemical physics*, 57(3):1100–1102, 1972.

[109] Franck Nicoud, Hubert Baya Toda, Olivier Cabrit, Sanjeeb Bose, and Jungil Lee. Using singular values to build a subgrid-scale model for large eddy simulations. *Physics of Fluids*, 23(8):085106, 2011.

[110] Taku Nonomura, Nobuyuki Iizuka, and Kozo Fujii. Increasing order of accuracy of weighted compact nonlinear scheme. *AIAA Paper*, 893, 2007.

[111] Taku Nonomura, Nobuyuki Iizuka, and Kozo Fujii. Freestream and vortex preservation properties of high-order WENO and WCNS on curvilinear grids. *Computers & Fluids*, 39(2):197–214, 2010.

[112] Britton J Olson, Johan Larsson, Sanjiva K Lele, and Andrew W Cook. Nonlinear effects in the combined Rayleigh-Taylor/Kelvin-Helmholtz instability. *Physics of Fluids*, 23(11):114107, 2011.

[113] Lawrence Ong and J Wallace. The velocity field of the turbulent very near wake of a circular cylinder. *Experiments in Fluids*, 20(6):441–453, 1996.

[114] Steven A Orszag. Analytical theories of turbulence. *Journal of Fluid Mechanics*, 41(2):363–386, 1970.

[115] Steven A Orszag. On the elimination of aliasing in finite-difference schemes by filtering high-wavenumber components. *Journal of Atmospheric Sciences*, 28(6):1074–1074, 1971.

[116] Steven A Orszag. Comparison of pseudospectral and spectral approximation. *Studies in Applied Mathematics*, 51(3):253–259, 1972.

[117] S.V Patankar and D.B Spalding. A calculation procedure for heat, mass and momentum transfer in three-dimensional parabolic flows. *International Journal of Heat and Mass Transfer*, 15(10):1787–1806, 1972.

[118] GS Patterson Jr and Steven A Orszag. Spectral calculations of isotropic turbulence: Efficient removal of aliasing interactions. *The Physics of Fluids*, 14(11):2538–2541, 1971.

[119] Ding-Yu Peng and Donald B Robinson. A new two-constant equation of state. *Industrial & Engineering Chemistry Fundamentals*, 15(1):59–64, 1976.

[120] Sergio Pirozzoli. Numerical methods for high-speed flows. *Annual Review of Fluid Mechanics*, 43(1):163–194, 2011.

[121] Sergio Pirozzoli. Stabilized non-dissipative approximations of euler equations in generalized curvilinear coordinates. *Journal of Computational Physics*, 230(8):2997–3014, 2011.

[122] Sergio Pirozzoli and Paolo Orlandi. Natural grid stretching for dns of wall-bounded flows. *Journal of Computational Physics*, 439:110408, 2021.

[123] R Placek and M Miller. Wind tunnel tests of laminar–turbulent transition influence on basic aerodynamic characteristics of laminar airfoil in transonic flow regime. *Inst. of Aviation TR D-5.2*, 2, 2016.

[124] Robert Placek and Paweł Ruchała. The flow separation development analysis in subsonic and transonic flow regime of the laminar airfoil. *Transportation Research Procedia*, 29:323–329, 2018.

[125] Bruce E Poling, John M Prausnitz, John P O'connell, et al. *The Properties of Gases and Liquids*, volume 5. Mcgraw-hill New York, 2001.

[126] Stephen B Pope. Turbulent flows. *Measurement Science and Technology*, 12(11):2020–2021, 2001.

[127] T Pulliam and J Steger. On implicit finite-difference simulations of three-dimensional flow. In *16th Aerospace Sciences Meeting*, AIAA 1978-10, 1978.

[128] JR Ristorcelli. A pseudo-sound constitutive relationship for the dilatational covariances in compressible turbulence. *Journal of Fluid Mechanics*, 347:37–70, 1997.

[129] Donald P Rizzetta, Miguel R Visbal, and Philip E Morgan. A high-order compact finite-difference scheme for large-eddy simulation of active flow control. *Progress in Aerospace Sciences*, 44(6):397–426, 2008.

[130] Philip L Roe. Characteristic-based schemes for the Euler equations. *Annual Review of Fluid Mechanics*, 18(1):337–365, 1986.

[131] PL Roe and J Pike. Efficient construction and utilisation of approximate Riemann solutions. In *Proc. of the Sixth Int'l. Symposium on Computing Methods in Applied Sciences and Engineering, VI*, pages 499–518, 1985.

[132] Viktor Vladimirovich Rusanov. The calculation of the interaction of non-stationary shock waves with barriers. *Zhurnal Vychislitel'noi Matematiki i Matematicheskoi Fiziki*, 1(2):267–279, 1961.

[133] Jaiyoung Ryu and Daniel Livescu. Turbulence structure behind the shock in canonical shock–vortical turbulence interaction. *Journal of Fluid Mechanics*, 756, 2014.

[134] Pierre Sagaut and Claude Cambon. *Homogeneous Turbulence Dynamics*, volume 15. Springer, 2008.

[135] Sutanu Sarkar, Gordon Erlebacher, M Yousuff Hussaini, and Heinz Otto Kreiss. The analysis and modelling of dilatational terms in compressible turbulence. *Journal of Fluid Mechanics*, 227:473–493, 1991.

[136] Oliver T Schmidt and Tim Colonius. Guide to spectral proper orthogonal decomposition. *AIAA Journal*, 58(3):1023–1033, 2020.

[137] Thomas Schmitt, Laurent Selle, Anthony Ruiz, and Bénédicte Cuenot. Large-eddy simulation of supercritical-pressure round jets. *AIAA Journal*, 48(9):2133–2144, 2010.

[138] Sudip K Seal, Kalyan S Perumalla, and Steven P Hirshman. Revisiting parallel cyclic reduction and parallel prefix-based algorithms for block tridiagonal systems of equations. *Journal of Parallel and Distributed Computing*, 73(2):273–280, 2013.

[139] JS Shang. High-order compact-difference schemes for time-dependent maxwell equations. *Journal of Computational Physics*, 153(2):312–333, 1999.

[140] Claude E Shannon. Communication in the presence of noise. *Proceedings of the IRE*, 37(1):10–21, 1949.

[141] Chi-Wang Shu. High order weighted essentially nonoscillatory schemes for convection dominated problems. *SIAM Review*, 51(1):82–126, 2009.

[142] Chi-Wang Shu and Stanley Osher. Efficient implementation of essentially non-oscillatory shock-capturing schemes. *Journal of Computational Physics*, 77(2):439–471, 1988.

[143] Mark P Simens, Javier Jiménez, Sergio Hoyas, and Yoshinori Mizuno. A high-resolution code for turbulent boundary layers. *Journal of Computational Physics*, 228(11):4218–4231, 2009.

[144] Joseph Smagorinsky. General circulation experiments with the primitive equations: I. the basic experiment. *Monthly Weather Review*, 91(3):99–164, 1963.

[145] Hang Song, Aditya S Ghate, Steven Dai, Anjini Chandra, and Sanjiva K Lele. Conservative and robust compact finite difference approach for simulations of dense gas flows. In *AIAA Aviation 2023 Forum*, AIAA 2023-3690, 2023.

[146] Hang Song, Aditya S Ghate, Kristen Matsuno, Jacob West, Akshay Subramaniam, Lucy J Brown, and Sanjiva K Lele. Robust high-resolution simulations of compressible turbulent flows without filtering. In *AIAA Aviation 2022 Forum*, AIAA 2022-4122, 2022.

[147] Hang Song, Kristen V Matsuno, Jacob R West, Akshay Subramaniam, Aditya S Ghate, and Sanjiva K Lele. Scalable parallel linear solver for compact banded systems on heterogeneous architectures. *Journal of Computational Physics*, 468:111443, 2022.

[148] Hang Song, Man Long Wong, Aditya S Ghate, and Sanjiva K Lele. Numerical study of transonic laminar shock buffet on the OALT25 airfoil. In *AIAA SciTech 2024 Forum*, AIAA 2024-2148, 2024.

[149] Akshay Subramaniam. *Simulations of Shock Induced Interfacial Instabilities Including Materials With Strength*. Stanford University, 2018.

[150] Akshay Subramaniam, Man Long Wong, and Sanjiva K Lele. A high-order weighted compact high resolution scheme with boundary closures for compressible turbulent flows with shocks. *Journal of Computational Physics*, 397:108822, 2019.

[151] Takao Suzuki and Sanjiva K Lele. Shock leakage through an unsteady vortex-laden mixing layer: application to jet screech. *Journal of Fluid Mechanics*, 490:139–167, 2003.

[152] Paul N Swarztrauber. A direct method for the discrete solution of separable elliptic equations. *SIAM Journal on Numerical Analysis*, 11(6):1136–1150, 1974.

[153] Roland A Sweet. A generalized cyclic reduction algorithm. *SIAM Journal on Numerical Analysis*, 11(3):506–520, 1974.

[154] Roland A Sweet. A cyclic reduction algorithm for solving block tridiagonal systems of arbitrary dimension. *SIAM Journal on Numerical Analysis*, 14(4):706–720, 1977.

[155] Kunihiko Taira, Steven L Brunton, Scott TM Dawson, Clarence W Rowley, Tim Colonius, Beverley J McKeon, Oliver T Schmidt, Stanislav Gordeyev, Vassilios Theofilis, and Lawrence S Ukeiley. Modal analysis of fluid flows: An overview. *AIAA Journal*, 55(12):4013–4041, 2017.

[156] PD Thomas and CK Lombard. Geometric conservation law and its application to flow computations on moving grids. *AIAA Journal*, 17(10):1030–1037, 1979.

[157] Eleuterio F Toro. *Riemann Solvers and Numerical Methods for Fluid Dynamics: a Practical Introduction*. Springer Science & Business Media, 2013.

[158] Aaron Towne, Oliver T Schmidt, and Tim Colonius. Spectral proper orthogonal decomposition and its relationship to dynamic mode decomposition and resolvent analysis. *Journal of Fluid Mechanics*, 847:821–867, 2018.

[159] VK Tritschler, BJ Olson, SK Lele, Stefan Hickel, XY Hu, and Nikolaus Andreas Adams. On the richtmyer–meshkov instability evolving from a deterministic multimode planar interface. *Journal of Fluid Mechanics*, 755:429–462, 2014.

[160] Christian R. Trott, Damien Lebrun-Grandié, Daniel Arndt, Jan Ciesko, Vinh Dang, Nathan Ellingwood, Rahulkumar Gayatri, Evan Harvey, Daisy S. Hollman, Dan Ibanez, Nevin Liber, Jonathan Madsen, Jeff Miles, David Poliakoff, Amy Powell, Sivasankaran Rajamanickam, Mikael Simberg, Dan Sunderland, Bruno Turcksin, and Jeremiah Wilke. Kokkos 3: Programming model extensions for the exascale era. *IEEE Transactions on Parallel and Distributed Systems*, 33(4):805–817, 2022.

[161] Ali Uzun and Mujeeb R Malik. Large-eddy simulation of flow over a wall-mounted hump with separation and reattachment. *AIAA Journal*, 56(2):715–730, 2018.

[162] Milton Van Dyke. *An Album of Fluid Motion*, volume 176. Parabolic Press Stanford, 1982.

[163] Sudharshan S Vazhkudai, Bronis R de Supinski, Arthur S Bland, Al Geist, James Sexton, Jim Kahle, Christopher J Zimmer, Scott Atchley, Sarp Oral, Don E Maxwell, et al. The design, deployment, and evaluation of the coral pre-exascale systems. In *SC18: International Conference for High Performance Computing, Networking, Storage and Analysis*, pages 661–672. IEEE, 2018.

[164] Miguel R Visbal and Datta V Gaitonde. High-order-accurate methods for complex unsteady subsonic flows. *AIAA Journal*, 37(10):1231–1239, 1999.

[165] Miguel R Visbal and Datta V Gaitonde. On the use of higher-order finite-difference schemes on curvilinear and deforming meshes. *Journal of Computational Physics*, 181(1):155–185, 2002.

[166] Theodore Von Karman. Progress in the statistical theory of turbulence. *Proceedings of the National Academy of Sciences*, 34(11):530–539, 1948.

[167] AW Vreman. An eddy-viscosity subgrid-scale model for turbulent shear flow: Algebraic theory and applications. *Physics of Fluids*, 16(10):3670–3681, 2004.

[168] Jianchun Wang, Toshiyuki Gotoh, and Takeshi Watanabe. Shocklet statistics in compressible isotropic turbulence. *Physical Review Fluids*, 2(2):023401, 2017.

[169] Jianchun Wang, Toshiyuki Gotoh, and Takeshi Watanabe. Spectra and statistics in compressible isotropic turbulence. *Physical Review Fluids*, 2(1):013403, 2017.

[170] Jianchun Wang, Yipeng Shi, Lian-Ping Wang, Zuoli Xiao, XT He, and Shiyi Chen. Effect of compressibility on the small-scale structures in isotropic turbulence. *Journal of Fluid Mechanics*, 713:588–631, 2012.

[171] Jianchun Wang, Yipeng Shi, Lian-Ping Wang, Zuoli Xiao, XT He, and Shiyi Chen. Scaling and statistics in three-dimensional compressible turbulence. *Physical Review Letters*, 108(21):214505, 2012.

[172] Jianchun Wang, Minping Wan, Song Chen, Chenyue Xie, Lian-Ping Wang, and Shiyi Chen. Cascades of temperature and entropy fluctuations in compressible turbulence. *Journal of Fluid Mechanics*, 867:195–215, 2019.

[173] Peter Welch. The use of fast fourier transform for the estimation of power spectra: a method based on time averaging over short, modified periodograms. *IEEE Transactions on Audio and Electroacoustics*, 15(2):70–73, 1967.

[174] David C Wilcox. *Turbulence Modeling for CFD*. DCW Industries, Inc., 3rd edition, 2006.

[175] William R Wolf, João Luiz F Azevedo, and Sanjiva K Lele. Convective effects and the role of quadrupole sources for aerofoil aeroacoustics. *Journal of Fluid Mechanics*, 708:502, 2012.

[176] Man Long Wong and Sanjiva K Lele. High-order localized dissipation weighted compact nonlinear scheme for shock-and interface-capturing in compressible flows. *Journal of Computational Physics*, 339:179–209, 2017.

[177] Pui-Kuen Yeung and Stephen B Pope. Lagrangian statistics from direct numerical simulations of isotropic turbulence. *Journal of Fluid Mechanics*, 207:531–586, 1989.

[178] Ming Yu, Chun-Xiao Xu, and Sergio Pirozzoli. Genuine compressibility effects in wall-bounded turbulence. *Physical Review Fluids*, 4(12):123402, 2019.

[179] Rozie Zangeneh. Parametric study of separation and reattachment in transonic airfoil flows. *AIAA Journal*, 59(11):4465–4474, 2021.

[180] Markus Zauner, Pradeep Moise, and Neil D Sandham. On the co-existence of transonic buffet and separation-bubble modes for the OALT25 laminar-flow wing section. *Flow, Turbulence and Combustion*, 110(4):1023–1057, 2023.

[181] Markus Zauner and Neil D Sandham. Modal analysis of a laminar-flow airfoil under buffet conditions at Re = 500,000. *Flow, Turbulence and Combustion*, 104(2):509–532, 2020.

[182] Shuhai Zhang, Shufen Jiang, and Chi-Wang Shu. Development of nonlinear weighted compact schemes with increasingly higher order accuracy. *Journal of Computational Physics*, 227(15):7294–7321, 2008.

[183] Yao Zhang, Jonathan Cohen, and John D Owens. Fast tridiagonal solvers on the GPU. *ACM Sigplan Notices*, 45(5):127–136, 2010.